CRANFIELD UNIVERSITY

Nicholas Grech

Gas Turbine Sub-Idle Performance Modelling; Groundstart, Altitude Relight, and Windmilling

School of Engineering

Ph.D. Thesis

SCHOOL OF ENGINEERING
DEPARTMENT OF POWER AND PROPULSION

Full Time Ph.D.

Academic Year 2010 – 2013

Nicholas Grech

Gas Turbine Sub-Idle Performance Modelling; Groundstart, Altitude Relight, and Windmilling

Supervisors: Dr V. Pachidis, Dr P.K. Zachos
Industrial Advisors: Mr A. Rowe, Mr S. Brown, Mr R. Tunstall

January 2013

This report is submitted in partial fulfilment of the requirements for the degree of Doctorate of Philosophy

Abstract

Engine performance modelling is a major part of the engine design process, in which specialist solvers are employed to predict, understand and analyse the engine's behaviour at various operating conditions. Sub-idle whole engine performance synthesis solvers are not as reliable and accurate as design point solvers. Lack of knowledge and data result in component characteristics being reverse-engineered or extrapolated from above-idle data. More stringent requirements on groundstart and relight capabilities, has prompted the need to advance the knowledge on low-speed engine performance, thereby requiring more robust sub-idle performance synthesis solvers.

The objective of this study, was to improve the accuracy and reliability of a current aero gas turbine sub-idle performance solver by studying each component in isolation through numerical simulations. Areas researched were: low-speed and locked-rotor compressor characteristics, low-power combustion efficiency, air blast atomizer and combustor performance at sub-idle, torque-based whole engine sub-idle performance synthesis, and mixer performance at far off-design conditions.

The observations and results from the numerical simulations form the contribution to knowledge of this research. Numerical simulations of compressor blades under highly negative incidence angles show the complex nature of the flow, with the results used to determine a suitable flow deviation model, a method to extract blade aerodynamic characteristics in highly separated flows, and measure the blockage caused by highly separated flow with operating condition and blade geometry. The study also concluded that the use of Blade Element Theory is not accurate enough to be used at such far off-design conditions. The linearised parameter-based whole engine performance solver was converted

to used torque-based parameters, which validated against engine test data, shows that it is suitable for low-power simulations with the advantage of having the potential to start engine simulations from static conditions.

A study of air-blast atomization at windmilling relight conditions has shown that current established correlations used to predict spray characteristics are not suitable for altitude relight studies, tending to overestimate the atomization quality. Also discovered is the highly influential interaction of compressor wakes with the combustor and atomizer under altitude relight conditions, resulting in more favourable lighting conditions than previous assumptions and models have shown. This is a completely new discovery which will result in a change in the way combustors are designed and sized for relight conditions, and the way combustion rig tests are conducted.

The study also has valuable industrial contributions. The locked-rotor numerical data was used within a stage-stacking compressible flow code to estimate the compressor sub-idle map, of which results were used within a whole engine performance solver and results validated against actual engine test data. The atomization studies at relight were used to factor in the insensitivity of current spray correlations, which together with a newly developed sub-idle combustion efficiency sub-routine, are used to determine the combustion efficiency at low-power settings. The interaction of compressor wakes with the atomizer showed that atomizer performance at relight is underestimated, resulting in oversized combustors. By using the knowledge gained within this research, combustor size can be reduced, resulting in lower NO_x at take-off and a smaller and lighter core, with a combustor requiring less cooling air.

The component research has advanced the knowledge and modelling capability of sub-idle performance solvers, increasing their reliability and encouraging their use for future aero gas turbine engines.

Contents

Acknowledgements

It's hard to imagine how I would have lasted throughout these three years without the support and dedication of the people with whom I shared this period of time. Words don't always reflect the depth of my gratitude towards such friendships, but I'll try my best....

I would like to first and foremost, acknowledge my appreciation towards Prof Riti Singh and Dr Vassilios Pachidis for giving me the opportunity to undertake my studies within the Cranfield Rolls-Royce University Technology Centre. It has without doubt provided a unique opportunity to work close with the industry. As for my industrial supervisors, I would like to thank Arthur Rowe, Stephen Brown and Richard Tunstall for their advice, and for sharing their knowledge and experience. A great deal of support and collaboration was shown by the Aerothermal Methods team in Derby, especially Dr Marco Zedda and Chris Goddard, who despite their busy schedule, patiently helped and provided resources for the combustion numerical modelling. Much is also owed to Owen Cumpson in Bristol, and Roy Meads and Nick Balkota in Derby, who helped with getting software up and running, compiling and troubleshooting the source codes.

Dr Pavlos Zachos has been a pillar of support. He was my mentor and my friend through the good and the difficult times. He guided me through every step of the way, with invaluable advice and constructive feedback. His success as an academic was of great inspiration. Thank you for everything Pavlos! The new friends I made during my studies: Ahad, Serena, Domenico, Grant and Carlos, a big thank you for the time we spent together and the fond memories that I will cherish.

My appreciation also goes to the M.Sc students who produced high quality work and contributed towards this research project: Hugo, Charlie, Daniele, Tommaso, Enric, Alexandre and Maxime.

My family has always been a pillar of support. I doubt I would be anywhere where I am now without the continuous support of my parents Helen and Joseph. A big thank you also goes to my brother Keith, who supports me even now and with whom I have shared my wonderful childhood. It is also thanks to the continuous efforts of my grandparents Carmelo, Adelina, Giacondo and Rosaria that I have such a close family to go back to, which is ever so rare nowadays and that I greatly treasure.

Finally, I cannot but show enormous gratitude towards my wife Claire, who has patiently supported me all the way through such demanding times. Her support, love, understanding, and the occasional cup of tea have helped me get through this experience.

To my parents Joseph and Helen for their unconditional support, love, and encouragement.

List of Figures

List of Tables

Nomenclature

Symbols

Symbol	Description	Units/Value
A	Area	m^2
a	Position of maximum blade camber	
B	Transfer number	$-$
c	Chord or Velocity	m or m/s
c	Specific heat capacity	kJ/kgK
C_{12}	Convert torque to power (33,000 ft.lbf/min)/(2π rad/rev)	5252.11
C_{15}	Convert CHU/s to hp	2.54674
C_p	Static pressure coefficient	$-$
C_l	Lift coefficient	$-$
Cd	Nozzle discharge coefficient	$-$
C_d	Drag coefficient	$-$
C_f	Tangential force coefficient	$-$
c_m	Mean axial velocity	m/s
Cv	Nozzle thrust coefficient	$-$
D	Diameter	m
D_{32}	Sauter Mean Diameter	m
d_q	Quenching distance	m
E_{min}	Minimum ignition energy	J
f_c	Fraction of air used in combustion	$-$
G_θ	Axial flux of angular momentum	kgm^2/s^2
G_x	Axial flux of linear momentum	kgm/s^2

H	Total enthalpy	J
i	Incidence	$^{\circ}$
k	Thermal conductivity	J/msK
L	Latent heat of vaporization	kJ/kg
N	Rotational speed	rpm
P	Total pressure	Pa or psi
p	Static pressure	Pa or psi
Q	Flow parameter $\left(\frac{W\sqrt{T}}{AP}\right)$	$-$
q	Rosin-Rammler drop size distribution parameter	$-$
r	Radius	m
Re	Reynolds number	$-$
s	Pitch	m
s/c	Solidity	$-$
S_N	Swirl number	$-$
T	Total temperature	K
t	Static temperature	K
U	Blade velocity	m/s
V	Flow velocity	m/s
W	Mass flow rate	kg/s or lb/s
W	Angular velocity	m/s
X	Axial force	N
Y	Tangential force	N
Z_{max}	Guess maximum value	$-$
Z_{min}	Guess minimum value	$-$
y^+	Dimensionless wall distance	$-$
y_p	First cell size (boundary layer mesh)	m
Y_{As}	Air surface mass fraction	$-$
Y_{Ar}	Air reference mass fraction	$-$
Y_{Fs}	Fuel surface mass fraction	$-$
Y_{Fr}	Fuel reference mass fraction	$-$
$Y_{F\infty}$	Ambient fuel mass fraction	$-$

Greek Symbols

Symbol	Description	Units
α	Flow angle	$^\circ$
β	Beta parameter or metal angle	$-$ or $^\circ$
Δ	Difference	$-$
δ	Deviation	$^\circ$
ϵ	Deflection	$^\circ$
γ	Ratio of specific heats	$-$
ρ	Density	kg/m^3
η	Efficiency	%
λ	Evaporation constant	m^2/s
μ	Dynamic viscosity	kg/ms
ϕ	Flow coefficient $\left(\frac{W\sqrt{T}/P}{N/\sqrt{T}}\right)$	$-$
ψ	Work coefficient $\left(\frac{\Delta H/T}{(N/\sqrt{T})^2}\right)$	$-$
ψ_{is}	Pressure coefficient $\left(\eta_{is}\frac{\Delta H/T}{(N/\sqrt{T})^2}\right)$	$-$
σ	Surface tension	kg/s^2
τ	Torque	$lb.ft$
τ_w	Wall shear stress	Pa
θ	Blade camber angle or Combustion Loading	$^\circ$ or $-$
ξ	Stagger	$^\circ$
ζ	Total pressure loss coefficient	$-$

Acronyms

Symbol	Description
AFR	Air-to-Fuel Ratio
APU	Auxiliary Power Unit
ATF	Altitude Test Facility
BET	Blade Element Theory
BPR	Bypass Ratio
BSL	Baseline

CAS	Corrected Air Speed
CDF	Cycle Definition File
CFD	Computational Fluid Dynamics
CH	Scaling factor for ψ
CHI	Scaling factor for ψ_{is}
CN	Scaling factor for quasi non-dimensional speed ($N/\sqrt{T}$)
CT	Scaling factor for specific torque (τ/P)
CTRZ	Central Torodial Recirculation Zone
CW	Scaling factor for quasi non-dimensional mass flow
DPM	Discrete Phase Model
DNS	Direct Numerical Simulation
FAR	Fuel-to-Air Ratio
FTB	Flying Test Bed
HP	High Pressure
HPC	High Pressure Compressor
HPT	High Pressure Turbine
HTSK	Heat Soakage
IP	Intermediate Pressure
IPC	Intermediate Pressure Compressor
IPT	Intermediate Pressure Turbine
ISA	International Standard Atmosphere
LES	Large-Eddy Simulations
LP	Low Pressure
LPC	Low Pressure Compressor
LPT	Low Pressure Turbine
LUFF	Light Up Fuel Flow
NCP	Nozzle Charging Plane
NH	HP spool speed
NI	IP spool speed
NL	LP spool speed
NPR	Nozzle Pressure Ratio

NrT	Non-dimensional speed
OEI	One Engine Inoperative
OGV	Outlet Guide Vane
PR	Pressure Ratio
QUICK	Quadratic Upwind Interpolation
RANS	Reynolds Averaged Navier-Stokes
RMSE	Root Mean Square Error
RNG	Re-Normalisation Group
RSM	Reynolds Stress Model
SFC	Specific Fuel Consumption
SMD	Sauter Mean Diameter
SPC	Shaft Power Coupling
SSG	Speziale-Sarkar-Gatski
SST	Shear-Stress Transport
TLC	Top Left Corner (Relight envelope)
TMPR	Total Mixer Pressure Ratio
TOC	Top Of Climb
TR	Temperature Ratio
TRC	Top Right Corner (Relight envelope)
VIGV	Variable Inlet Guide Vane
VSV	Variable Stator Vane
WrTP	Non-dimensional mass flow
XNH	High pressure shaft speed
XNI	Intermediate pressure shaft speed
XNL	Low pressure shaft speed

Subscripts

Symbol	Description
1	Inlet
2	Outlet
3	Nozzle inlet
4	Nozzle exit
26	HP compressor intlet
30	HP compressor outlet / Combustor inlet
31	Combustor flame tube
32	Sauter Mean Diameter
40	Combustor outlet / HP turbine inlet
42	HP turbine outlet
a	Air
atm	Atmospheric
amb	Ambient
bn	Boiling
bypass	Bypass duct or flow
d	Droplet based
eff	Effective
f	Fuel
g	Gas
geom	Geometrical
h	Hub
h	Hydraulic
is	Isentropic
ce	Evaporation-rate based combustion
$c\theta$	Reaction-rate based combustion
cmix	Mixing-rate based combustion
core	Core duct or flow
m	Mean

ref	Reference
res	Reservoir
rc	Recirculation
surf	Surface
sw	Swirler
st	Stoichiometric
θ	Tangential
∞	Ambient
L	Liquid
M	Mass transfer
T	Heat transfer
p	Pressure or Pre-filming
pz	Primary zone
v	Vapour
x	Axial
y	Tangential

Superscripts

Symbol	**Description**
$*$	Design point value
$'$	Angle of attack

Chapter 1

Introduction

In 1940, Stanley Hooker introduced Frank Whittle's novel engine concept to Works Manager at Rolls-Royce, Ernest W. Hives, describing it as a very simple machine (at least relative to the large piston aero engines of the time). The reply he got was, "Don't worry, we will design the bloody simplicity out of it!" [41]. The aero-gas turbine is indeed a very complex and fine example of engineering achievement. In just over seventy years, it has thoroughly revolutionised our mode of transport and our access to global air travel. Through investment in research and development, its performance has greatly improved. Performance is what a manufacturer effectively sells to the customer, and it determines the engine's competitiveness. Walsh and Fletcher [1] define performance within the gas turbine context as "*the thrust or shaft power delivered for a given fuel flow, life, weight, emissions, engine diameter and cost. This must be achieved while ensuring stable and safe operation throughout the operational envelope, under all steady state and transient conditions*". Engines are optimised to operate at the high efficiency at cruise conditions to achieve the least Specific Fuel Consumption (SFC) possible. This is known as the engine's design point. A compromise in the design is required to ensure adequate performance at other conditions such as starting, take-off, top-of-climb (TOC), taxiing and altitude relight (restarting following an inflight engine flameout). These are off-design operations for which reliable performance is also required by both contractual (with the client) and certification (with the certifying authority) obligations, including ever more stringent noise, emissions and safety regulations [42].

The sub-idle operating region

The lowest power setting for a gas turbine is its idle speed. At idle the engine produces negligible thrust. Most of the fuel is used to maintain the thermodynamic cycle by overcoming any losses (such as bearing friction), inefficiencies and power off-takes (such as electrical and hydraulic power, and air conditioning). Any operation below this power setting is within the engine's sub-idle region, generally having a shaft rotational speed below 40-70% [1] of the design speed. Figure 1.1 shows the transient working line of a compressor as it accelerates from zero-speed to idle. Such an operation occurs all within the compressor's sub-idle region. Sub-idle encompasses engine operations such as: groundstart, altitude relight and windmilling. Windmilling occurs when a compressor rotates mainly not through the energy provided by the turbine, but by a flow of air forced through it, such as a gust of wind (when on ground), or a spent engine on an aircraft travelling at high speed. These terms are all explained in further detail in Chapter 2. The engine's performance during these sub-idle operations has to satisfy a number of certification requirements. It is therefore as critical as the design point performance.

Sub-idle is a far off-design operating area where conventional methods for performance prediction are less accurate [5], mainly due to the lack of understanding of the complex physical phenomena that take place, and the lack of engine and component performance data available.

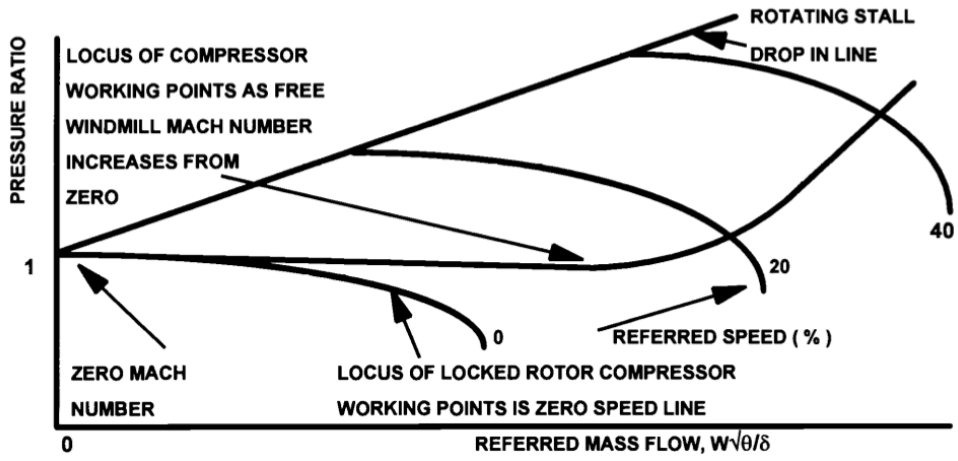

Figure 1.1: Compressor sub-idle operating region [1]

1.1 Gas turbine performance modelling

In an attempt to improve fuel consumption, emissions and efficiency, novel engine cycles and aircraft designs are envisaged for the future. Designers are trying to extract every possible percentage point of efficiency out of the traditional turbofan, pushing concepts far from the baseline design. Significant changes in engine configuration and architecture are being made such as electric starting, geared fans and intercooling, apart from improvements in turbomachinery design. Such changes influence the engine's overall performance, including the sub-idle operations.

To estimate the performance of a new design or the effect of introducing novel technology, aero-thermal models of the engine are developed within performance solvers. Recent publications on developing performance models for novel gas turbine concepts include Alexiou et al [43] on the geared turbofan.

Such engine performance simulation solvers use component characteristics and models derived from empirical correlations, test rig data, experience, and scaling of previous engines' component data if these are of a similar design. Without such tools, new engine architectures and designs would be too costly and risky to prototype. The reliability of such solvers rests on the accuracy of the component characteristics and the validity of the correlations used, assuming all the aerodynamic and thermodynamic phenomena such as pressure losses, heat soakage and chemical kinetics are accounted for. Heat soakage is the heat transfer between the working fluid and the engine metal during transients. The combustor has the largest effect due to the large temperature changes, large surface area and thermal mass.

1.2 Sub-idle performance modelling

Due to the particular and complex nature of sub-idle operations, performance solvers used to tackle this area are specifically designed for such purposes. As described below, whilst there are significant benefits in using such solvers, predicting accurately the sub-idle performance is not easy.

1.2.1 Benefits from sub-idle modelling

An aero-engine has to first meet the minimum certification requirements, and secondly have competitive overall performance, reliability and running costs. In terms of sub-idle, this involves mainly the engine's altitude relight capability and the groundstart performance. To estimate whether an engine design can satisfy the certification and contractual requirements, a sub-idle performance solver can, amongst other things, be used for:

Starting:

- Estimate starter sizing and starter supply requirements. This directly influences the demand on the Auxiliary Power Unit (APU) and battery size in case of electric starters.
- Analysis of parasitic losses which are the largest contributor to power consumption during starting. Estimate of low oil temperature or cold soaked engine on the breakaway torque.
- Tuning of the fuel schedule and limiters to avoid hung starts, failed starts or overfuelling (which can cause a stalled start) whilst guaranteeing the adequate time-to-idle.
- Determining the start bleed and variable geometry (variable inlet guide vane (VIGV) and variable stator vane (VSV)) schedule requirement to maintain compressor stability while minimising fuel consumption.
- Analyse the influence of retrofitting more advanced components, such as higher pressure ratio compressors.

Windmilling:

- Estimate the power off-take capability, i.e. how much power can be extracted from windmilling engine. This information is also required by the aircraft systems designers to estimate the hydraulic, pneumatic and electric power available following a flameout.
- Estimate the engine drag. This would influence directly the aircraft design, sizing and performance under One-Engine-Inoperative (OEI) conditions.

Relight:

- Prediction of the engine's windmilling flow, pressure and temperature characteristics; the combustor design team requires an estimate of these parameters to, amongst other studies such as cooling requirement, size the combustor for adequate altitude relight capability.

1.2.2 Difficulties in modelling low-speed engine operations

For design point simulations, performance solvers are widely used and are considered reliable, with up to 1-2% accuracy [23]. Good agreement with test data is due to the experience, accurate correlations and reliable data fed into such performance simulation solvers. This is however not the case for far off-design conditions, where the aero-thermal phenomena within the components are highly complex and are neither fully understood yet, nor easy to model. Sub-idle is one such far off-design condition. Some of the main difficulties are:

- Lack of accurate data and component characteristics:
  - Experimental test rigs are expensive to run. Consequently, the low speed characteristics of turbomachinery are not experimentally determined since stall at such low power is not a great risk for the engine.
  - Apart from the cost, certain tests cannot be run due to environmental restrictions. This is especially true for low power combustor tests where the low

Air-to-Fuel Ratio (AFR) results in unburnt fuel being released into the atmosphere. Such tests can only be done in highly specialised rigs, which were setup only recently and are expensive to run.

  - At low power, instrumentation errors become more significant. Any measured data is prone to a high level of uncertainty and susceptible to even the smallest fluctuations which otherwise would go unnoticed during high power tests. For low power tests, the instrumentation on a component or a whole engine often needs to be changed.
  - Data representation at low power can be a problem, especially for the compressor, as explained in Chapter 3.

- Transient simulation

  - Sub-idle operations are generally transient, increasing the level of complexity of the solver. Factors such as heat soakage, inertia (not just that of the main shafts, but also the attached accessories) and volume packing, need to be accounted for.

In an attempt to improve the reliability of sub-idle performance solvers, the first step is to fully understand the underlying physical phenomena in order to create models or derive correlations that can be subsequently used to improve the sub-idle performance solver's reliability. This is the strategy followed for this project, relying on numerical studies and fundamental theory to understand the components' behaviour at sub-idle, as illustrated in Fig. 1.2.

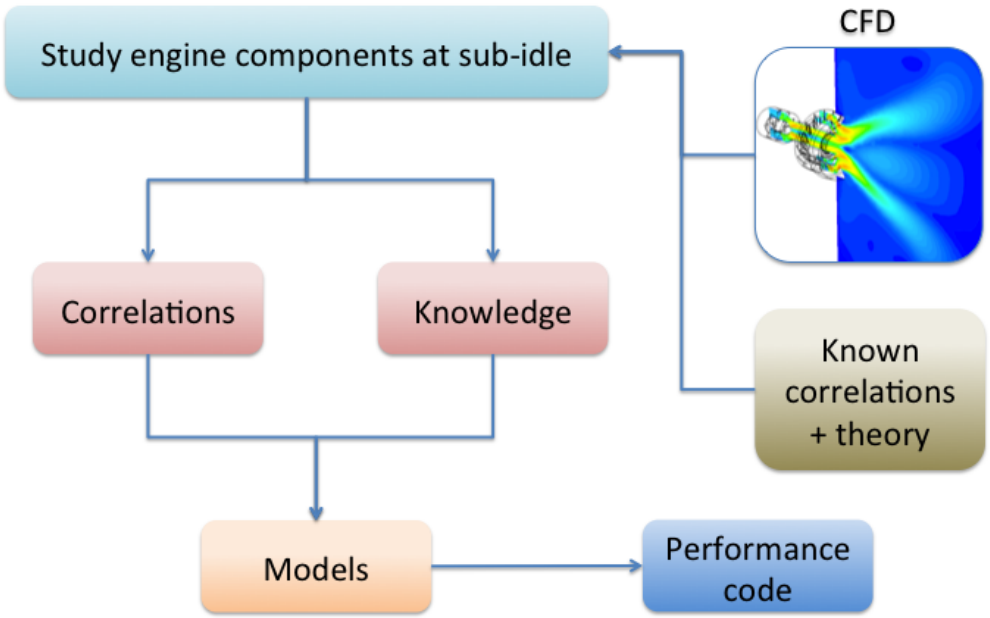

Figure 1.2: Strategy followed to improve the sub-idle performance solver

1.3 Scope of work

Sub-idle engine performance solvers produce reasonably good results but not good enough to confidently use them as a design tool. Instead, the predicted performance is validated against test rig data to identify potential sections of the solver that need improvement. Ideally, such solvers will reach a level of maturity at which they can be effectively used as design tools. The scope of this research project is to improve the accuracy and reliability of sub-idle performance solvers, pushing them closer to that level of maturity. Previous work by Jones [44], Howard [37] and Zachos [5], identified four areas of potential improvement. An overview is given here whilst further detail on each topic is given in its respective chapter.

- **Low-speed compressor characteristics**

  As described in section 1.2.2, compressor low-speed characteristics are often not available. Extrapolation has been used to generate the missing data. This method however relies highly on engineering judgement and is inaccurate at speeds close to zero, as explained in further detail in Chapter 3. The interpolation methodology developed by Zachos [5], based on cascade experimental and numerical data, produces promising results in generating physics-based locked-rotor and low speed compressor characteristics.

  The concept relies on understanding the flow's properties and behaviour at locked rotor conditions. At such conditions the blade is subject to high negative incidence angles, thus operating at a highly off-design condition for which most correlations do not apply. The flow is dominated by large areas of recirculation and high pressure losses. Further studies and understanding of the flow's behaviour can improve the method's accuracy, especially in terms of the flow deviation, the aerodynamic properties at high inlet Mach numbers and the reduction in effective flow area due to the recirculation zones.

- **Engine performance matching methodology**

  The parameters with which turbine and compressor characteristics are currently represented (ϕ, ψ and ψ_{is} as functions of $N/\sqrt{T}$) in sub-idle performance solvers, are

not adequate for low-speed simulations, as clearly explained in Riegler et al [45] due to their value, by definition, asymptoting towards infinity when speed approaches zero. Further details on low-speed compressor characteristics are given in Chapter 3. Specific torque (τ/P) was identified as a good substitute for the ambiguous efficiency parameter. This would theoretically allow transient accelerations from zero speed. The sub-idle performance solver had to be modified to use the proposed parameters, thus improving its low-speed performance prediction capability.

- **Sub-idle combustion efficiency prediction**

  Whilst combustion efficiency is almost 100% at design point, and generally above 95% at idle, at sub-idle it can be significantly less - as low as 30%. This is due to the low pressure and air flow rates at such low engine speeds. The value of combustion efficiency at such conditions is also difficult to estimate due to the influence of different phenomena, mainly the rate of mixing of fuel and air, the fuel evaporation rate, and the reaction rate (further details can be found in Chapter 5). Currently, this problem is overcome by crudely estimating the reduction in combustion efficiency through an 'inefficiency factor', which is adjusted until the modelled performance matches the experimental data. A more reliable and predictive sub-idle combustion efficiency model is therefore required to be plugged into the current performance solver.

- **Off-design mixer performance**

  Some turbofan engines are designed with a single mixed exhaust system rather than separate exhausts due to a small increase in cycle efficiency. The mixer mixes the bypass and core air, exhausting them from a single nozzle. At design point, the mixing process is easily modelled using a constant momentum and enthalpy balance together with a small percentage fundamental total pressure loss. It is safe to assume that the total and static pressures of the bypass and core streams are similar to minimise mixing losses.

  Under far off-design conditions such as windmilling, the air tends to flow mostly through the bypass duct due to the high blockage imposed by the core's turbo-

machinery. This causes the bypass ratio (BPR) to increase drastically, and leads to mixing of highly dissimilar streams at the exhaust mixing plane. Consequently turbulent mixing occurs in the jet pipe, leading to large total pressure losses. These losses are not accounted for in the current solver and are difficult to model. A surrogate model of the mixer characteristics at off-design can be used to represent this component's performance within the solver, thereby increasing the accuracy of the simulations.

1.4 Research objectives

1.4.1 Concept

The inaccuracy of sub-idle performance solvers lies within the modelling of each engine components' performance at low power. To address this issue, systematic research into each individual component was carried out. The main project objective was to improve the whole engine sub-idle performance solver by introducing better models and correlations derived from studying each component individually, either analytically or through Computational Fluid Dynamics (CFD). Additionally, the compressor and turbine sections of the performance solver were modified to run on torque based parameters. The main topics covered by this research are:

1.4.2 Low-speed compressor characteristics

- Study through experimentally validated numerical simulations, the flow properties and aerodynamic coefficients of a high pressure compressor blade at high negative incidences to further understand the underlying physical phenomena of the flow at locked-rotor conditions, mainly:
  - A far off-design flow deviation model and verify validity of current empirical correlations
  - Blade aerodynamic coefficients (C_p and C_f) for both low and high inlet flow Mach numbers
  - Reduction of blade channel effective area due to highly separated flows
  - Effect of incidence angle on the compressor zero-speed choking point
  - Verify the use of Blade Element Theory (BET) for flows at high negative incidence
- Update the sub-idle compressor map generating code according to the observations made from the above mentioned numerical studies. In particular, areas of improvement include:

  - Upgrade the flow deviation prediction model to one more suitable for far off-design conditions
  - Update the blade coefficient database for both low and high flow Mach numbers
  - Include changes in channel effective flow area to calculate the choking mass flow as a function of the blade operating condition
  - Provision for use of Blade Element Theory to upgrade from meanline to 3D analysis

1.4.3 Torque-based sub-idle engine performance solver

- Convert the sub-idle performance engine matching method from using linearised parameters (ϕ, ψ and ψ_{is} as explained in Chapter 3) to torque-based conventional parameters
- Convert the compressor and turbine map characteristics from linearised parameters to torque-based conventional parameters
- Extrapolate the compressor and turbine characteristics down to zero speed
- Run groundstart and altitude relight transients from zero-speed (static) condition

1.4.4 Sub-idle combustion efficiency

- Develop a sub-idle combustion efficiency model in the form of a sub-routine for implementation within the performance solver
- Understand and identify the key changes in the flow field and atomization performance of an airblast atomizer (an atomizer utilising high velocity air to break down fuel into droplets to form a fine spray) at sub-idle conditions. Determine whether current empirical correlations are suitable for modelling the spray characteristics during an altitude relight
- Determine whether large wakes from the compressor outlet guide vanes (OGV) during an altitude relight influence significantly the airblast atomizer and combustor's performance

1.4.5 Off-design mixer performance modelling

- Extract, from numerical simulations, the total pressure loss map of a mixer as a function of the far-off design operating conditions
- Analyse the difference between a lobed and plain type mixer in terms of flow field, mixing and total pressure loss at far-off design conditions
- Implement a sub-routine within the performance solver to utilize the numerically-derived total pressure loss map

1.5 Thesis structure and overview

In the introduction, an overall view of the area of study, the scope of work, and objectives, were given for all the topics covered within this study. The importance of good sub-idle engine performance was emphasised since this is usually thought of as of secondary importance. Consequently, the need to have adequate sub-idle performance solvers was underlined, highlighting the rationale of the project. To acquaint better the reader with what sub-idle engine operations consist of, these are listed and described in sufficient detail in Chapter 2.

This is then followed by each topic of work described in a separate chapter. Each chapter is self-contained, with a brief introduction, literature review, methodology, results, discussion and main conclusions. First the compressor work is described in Chapter 3 to serve as groundwork for the solver conversion work in Chapter 4, to which it is closely related.

The combustion efficiency study (Chapter 5) describes the development of a sub-idle combustion efficiency model, whilst Chapters 6 and 7 describe the numerical work undertaken to understand better the phenomena that take place within a combustor during a relight manoeuvre. The mixer studies are described in Chapter 8, followed by a ground-start performance data analysis of an intermediate (IP) start engine in Chapter 9. Where required, description of how results from the work undertaken were implemented into the main sub-idle performance solver, is also given within the chapter.

The conclusions are finally discussed in Chapter 10, which also highlights the main achievements and deliverables of this work. The report concludes with a more managerial aspect of the project in Chapter 11. Here an overview of how the project was managed is given, including the coordination with the supervisor, MSc students and the industrial sponsor. A list of journal and conference publications resulting from this study is given in Appendix A.

Chapter 2

Sub-Idle Operations

2.1 Groundstarting

An engine's groundstart performance is dictated by the contractual obligations that the manufacturer agrees to with the customer, in addition to the certification requirements. It includes the time required to reach idle (usually 45 - 60 seconds with Auxiliary Power Unit (APU) power at sea level International Standard Atmosphere (ISA) [46]) and the ability to start under adverse weather conditions. Further details can be found in [46] and [42].

In a groundstart transient, as shown in Fig. 2.1, the engine's starters (generally pneumatic, but electric starters are also being used), crank the high-pressure (HP) shaft until the right conditions for light-up in the combustion chamber are achieved. The igniter is then switched on and the fuel injected. A step increase in the HP compressor exit pressure indicates that ignition has occurred. The engine then accelerates to idle following a predetermined fuel schedule. The starters are de-coupled after the self-sustaining speed is surpassed.

The complexity lies in the fuel and variable geometry scheduling (variable stator vanes (VSV), variable inlet guide vanes (VIGV), and bleed valves), which are fine-tuned during prototype groundstart tests. Variable geometry allows the compressor to operate reliably and efficiently at off-design conditions; further details can be found in [1]. The light-up fuel flow (LUFF) needs to be carefully selected since high values will cause a high pressure

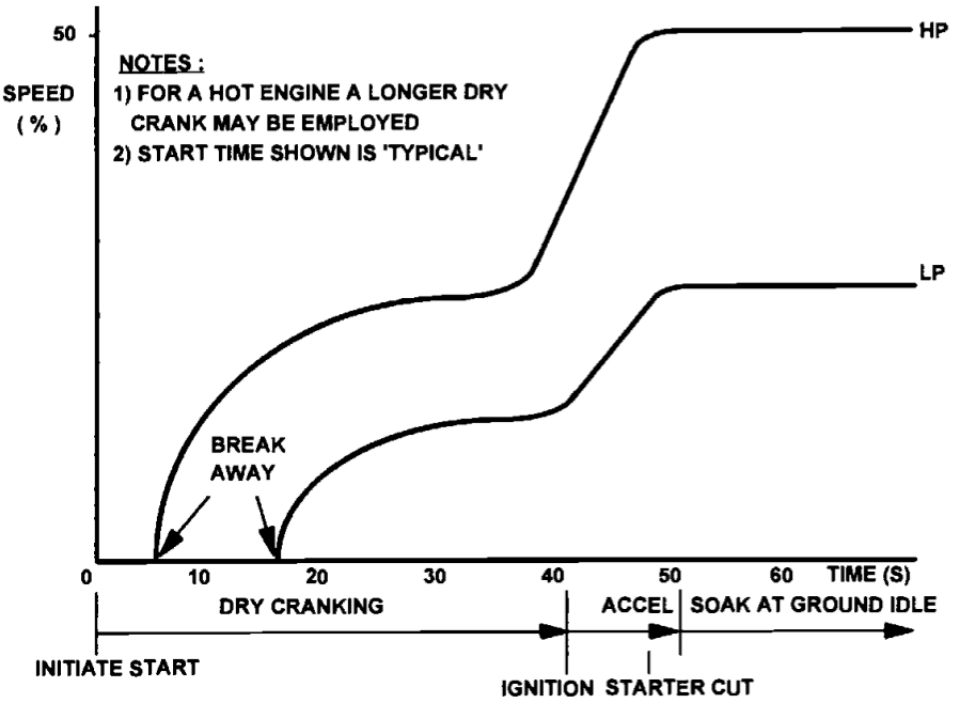

Figure 2.1: Typical groundstart sequence and speeds [1]

rise in the combustor. This in turn increases the pressure ratio across the high-pressure compressor (HPC), pushing it towards stall. High LUFF may cause stalled starts. The maximum acceptable time for starts under extreme conditions is about 2 minutes, with 90 seconds being a good design aim. Problems may be encountered on very cold days due to poor combustion and high viscous drags due to the lubricating oil, and on hot days due to low starter air pressure [46]. Following a start, engines are momentarily held at idle to allow time for thermal soakage to preserve cyclic life.

2.2 Altitude relight

Though uncommon, in-flight engine flame-outs do occur. It is estimated that one in every 100,000 flights will experience a flame-out [47]; a small number but not insignificant. Causes for a flame-out are various: pilot error, hail or rain ingestion, foreign object ingestion, and volcanic ash, to name the most common. The engine's ability to relight at altitude has always been a design challenge for manufacturers, especially the combustor design. It is however a critical aspect of the certification process for which a relight envelope (in terms of altitude and flight Mach number) is agreed upon and must be met.

A successful relight may be limited by combustor stability (at high air velocities and a low pressure and temperature), compressor stall (at low airspeeds and high altitudes), and poor cycle performance giving hot and slow restarts at low Mach numbers. The maximum time acceptable for relights is about 2 minutes, with 90 seconds being a reasonable target [46].

The combustor volume is sized specifically for a reliable altitude relight capability. Larger combustors improve the relight capability, but are otherwise oversized for nominal operating conditions. A large combustor is not desirable. The larger wetted surface area creates higher cold pressure losses, reducing the overall engine efficiency. It also requires more cooling air to maintain the metal temperature below melting, and generally longer shafts are required, adding weight. The minimum required volume for a reliable relight can be calculated. However, uncertainties due to the limited knowledge on the combustion phenomena at such conditions forces designers to include a safety margin and make the combustor bigger. An expensive price to pay, considering that the engine will have to suffer the added complexity and weight throughout its entire operational life, for an event that will rarely, if ever, happen.

Different possible types of relight are: windmilling, quick and starter-assisted. Their operational envelope is illustrated in Fig. 2.2, and a brief description is given in the following sections.

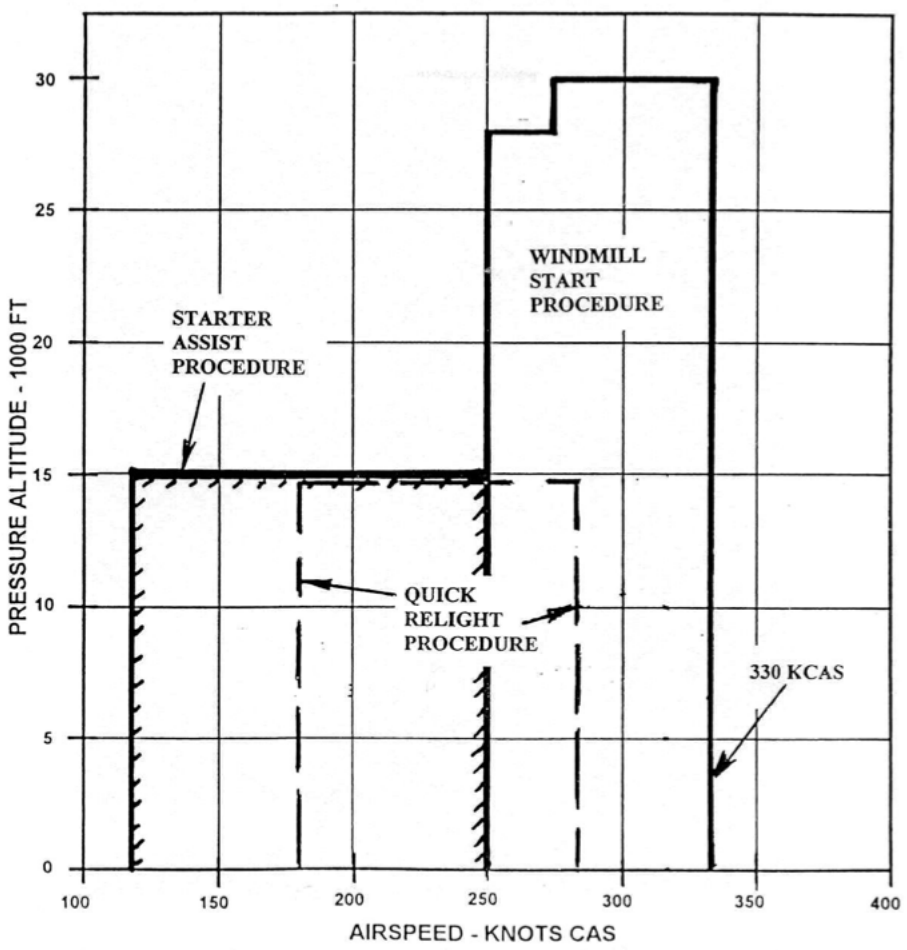

Figure 2.2: Different types of altitude relight as a function of corrected air speed (CAS) (Rolls-Royce data)

2.3 Windmilling

When air flows through an unlit engine, it forces the spools to rotate. This behaviour, known as windmilling, occurs mostly in aircraft engines due to the ram pressure caused by the flight velocity. The direction of rotation is the same as for normal operation. Two types of windmilling are possible: all the engine spools rotate freely (*free windmilling*) and the HP (or in some engines the IP) spool is mechanically prevented from rotating (*locked-rotor windmilling*). Locked-rotor generally occurs when the torque required by the accessories attached to the shaft is higher than the torque generated through the shaft by the incoming ram air. Engine malfunction and damage can also cause locked-rotor windmilling. The compressor's operation for both locked and free windmilling conditions was previously illustrated in Fig. 1.1 .

If during free windmilling the spools are rotating fast enough and there is enough flow going through the combustor, it is possible to restart the engine without any assistance. This will depend on the flight conditions (altitude and Mach number) and the amount of power extracted by the accessories which, as shown in Fig. 2.3, will influence the steady-state windmilling rotational speed of the shafts. If the windmilling shaft speeds are too low, the starter may be used to increase the rotational speed of the shaft (starter-assisted relight - as explained later in section 2.5).

2.4 Quick windmilling relight

Following a flame-out, the lack of thrust and increased drag from the flamed-out engine will cause the aircraft to lose considerable altitude. A flame-out may occur at low altitude, for example due to a bird strike during take-off. Rowe [46], mentions at least one case of a pilot inadvertently shutting down both engines of a twin engined aircraft on initial climbout (below 5000 ft). This type of incident has led to a new 'quick relight' requirement - which is a windmill restart at low altitude, low airspeed (200 kts) initiated up to 30 seconds following engine shutdown.

Relighting within such a short time is only possible if the engine carcass maintains a certain temperature during the brief windmilling phase - and therefore the time restriction. Oil temperature, and therefore viscosity, needs to remain high to reduce the power absorbed by bearing friction. A high temperature within the combustor also helps fuel vaporisation, increasing combustion efficiency and improving the chances of relight whilst enabling rapid acceleration.

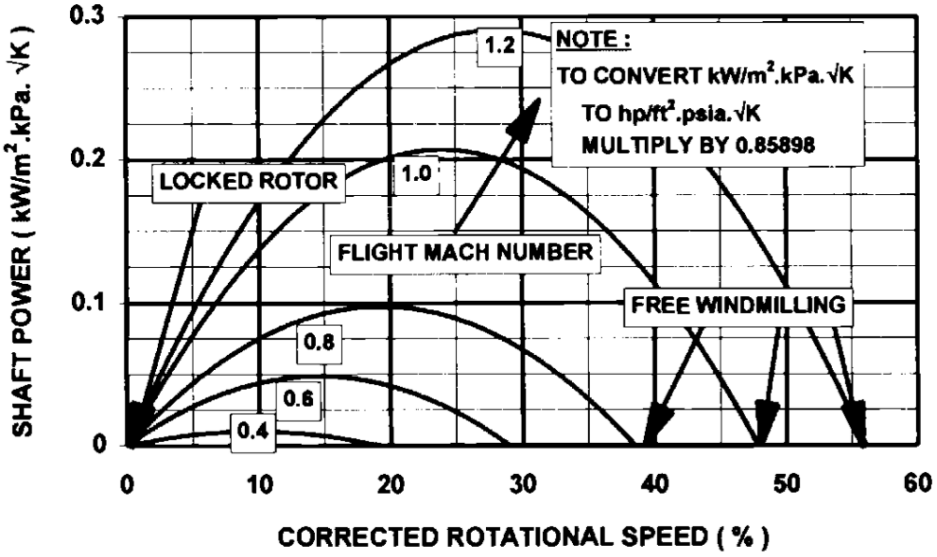

Figure 2.3: Effect of power extraction on windmilling [1]

2.5 Starter-assisted relight

At low windmilling speeds there is a chance that conditions inside the combustion chamber are unfavourable for ignition. As mentioned, the cause may be excessive power required by the accessories and low ram pressure rise at the compressor face due to low flight velocities (as shown in Fig. 2.2). In such a situation, additional rotational power can be provided via the starter motor. This can be done through bleed air from the other engine or the APU, or from the electrical power supply in the case of an electric starter. In the extreme case when starter power is not available, some of the other accessories such as the hydraulic pumps may have to be off-loaded from the system.

2.6 Concluding remarks

The overview given of the operating conditions categorised within the sub-idle operating condition of the aero gas turbine engine, highlights the requirement to predict its performance at such far off-design conditions. Though most of these operations, such as altitude relight and quick windmilling relight, will never be experienced by an engine during its operation life, the safety and certification requirement obliges manufacturers to guarantee that even during these rare events, the engine behaves predictably and safely. Groundstarts form a small percentage of the engine's operation time, but are still bound by contractual obligations such as time-to-idle. Groundstart is also a critical operation since the engine is sensitive to the fuel schedule and most of the variable geometry (bleeds, VIGVs and VSVs) are activated as the engine spools up.

The research undertaken focuses primarily on the groundstart and windmilling performance. By studying the performance of each component at low power, the aim is to improve the reliability of sub-idle performance code, increasing the confidence in their predictions and reducing design iterations and tests.

Chapter 3

Sub-Idle Compressor Performance

3.1 Introduction

One of the main limitations in building sub-idle engine performance models, is the lack of compressor low-speed characteristic data. Due to the expensive rig tests required, such data is very scattered if available, generally obtained from ATF (Altitude Test Facility) experiments. Over the years, researchers (Kurzke [2], Riegler [45], Jones [48] [49], Aslanidou [50] and Leitges [6]) have studied various methods to predict the compressor's sub-idle characteristics in an effort to provide more accurate data for performance solvers.

The following chapter presents the research undertaken to predict more accurately the compressor sub-idle map through studying the underlying flow physics. The methodology followed was first conceptualised by Zachos [5] [50] in the form of a stage-stacking compressor sub-idle map generation code, based on blade aerodynamic coefficients derived from experimentally validated numerical simulations. The improvements made to the compressor sub-idle characteristics generation code, are all based on knowledge gained from the numerical studies undertaken within this research and described in this chapter. The numerical studies were run to shed more light on the flow behaviour within an axial compressor at locked rotor and low-speed conditions, and how to model it. The numerical studies undertaken and described herein, address the following issues associated with highly separated flows: change in flow outlet angle, measurement of blade aerodynamic coefficients, restriction of the flow, and the use of blade element theory.

3.2 Literature review

3.2.1 Working modes and flow characteristics

At high speed, an axial compressor will convert work into a total temperature and pressure rise, thereby acting as a compressor. However, as explained in Walsh and Fletcher [1], at low-speed a compressor may act as a stirrer (or paddle) or even as a turbine. As a paddle, any compressor work available is converted into a total temperature rise. However the compressor's low-speed relative to the air flow rate, results in an off-design velocity triangle on the blade. The flow experiences a total pressure loss due to the blade operating in a far off-design condition, resulting in flow separation and large wakes. The compressor can also act as a turbine [1], in which case the flow will experience a total pressure and temperature drop. This behaviour means that at some point the work done will be equal to the work output and the total temperature ratio across the compressor will become unity. Using the standard definition for isentropic efficiency (Eqn. (3.1)), this means that efficiency will asymptote up to infinity, as illustrated in Fig. 3.1. The different compressor working modes are illustrated in Fig. 3.2.

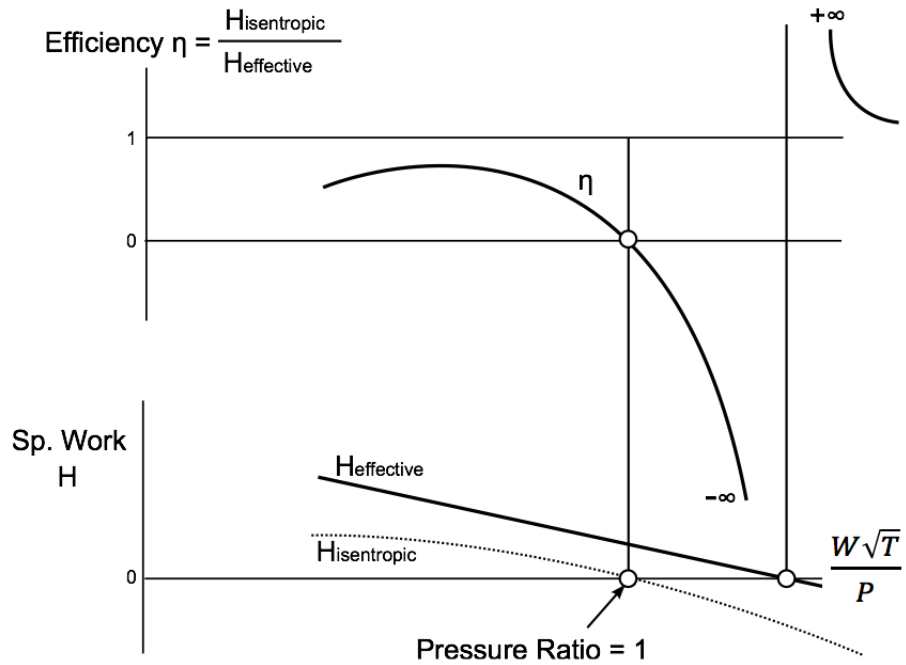

Figure 3.1: Specific work (H) and isentropic efficiency (η) as a function of quasi non-dimensional mass flow ($\frac{W\sqrt{T}}{P}$) [2]

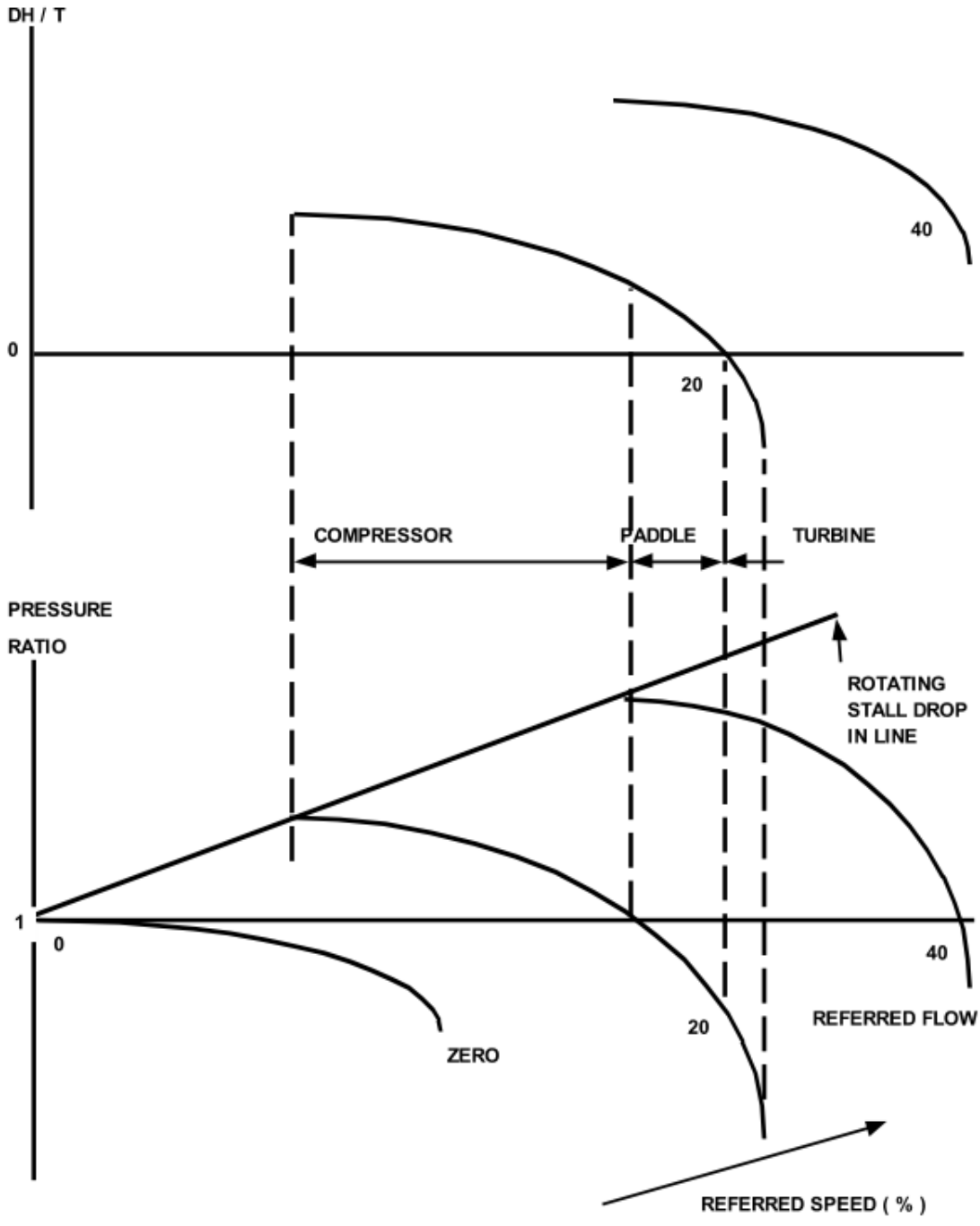

Figure 3.2: Axial compressor working modes at sub-idle conditions [1]

During a start-up, the compressor will go through each of the working modes described. Generally the high high pressure compressor (HPC) is cranked using a starter motor and will therefore start immediately in a compression working mode as shown in Fig. 3.3 where the pressure ratio is always above unity. However the intermediate pressure compressor (IPC) and low pressure compressor (LPC) will rotate only when enough flow is being forced through the core by the high pressure (HP) spool. Therefore during the first few seconds of a start-up, the LPC and IPC will not be rotating (zero-speed) and act as cascades. A total pressure drop is experienced across the turbomachinery.

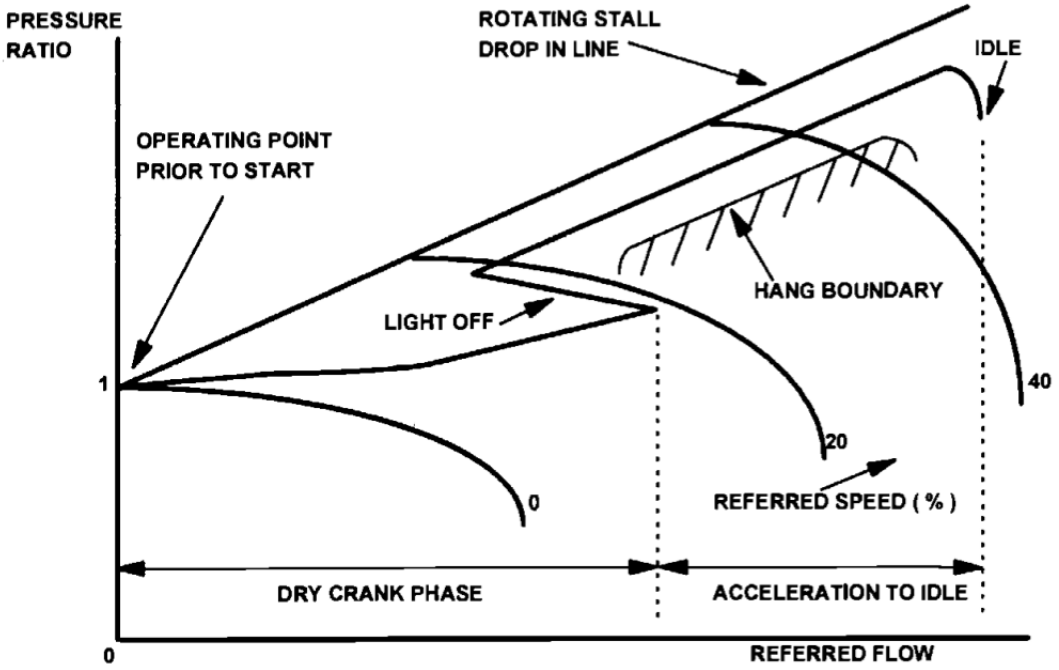

Figure 3.3: HP compressor transient working line during startup [1]

Eventually the torque generated by the flow on the blades overcomes the bearing friction and the IP and LP shafts start rotating. However, as previously described and as observed in Fig. 3.4, the compressor is still operating at off-design and is not capable of compressing the flow. Once light-up occurs, the rotational speed is high enough for compression to take place. The transient line in Fig. 3.4 is also valid for the HPC in the case of an altitude relight starting from a locked-rotor condition.

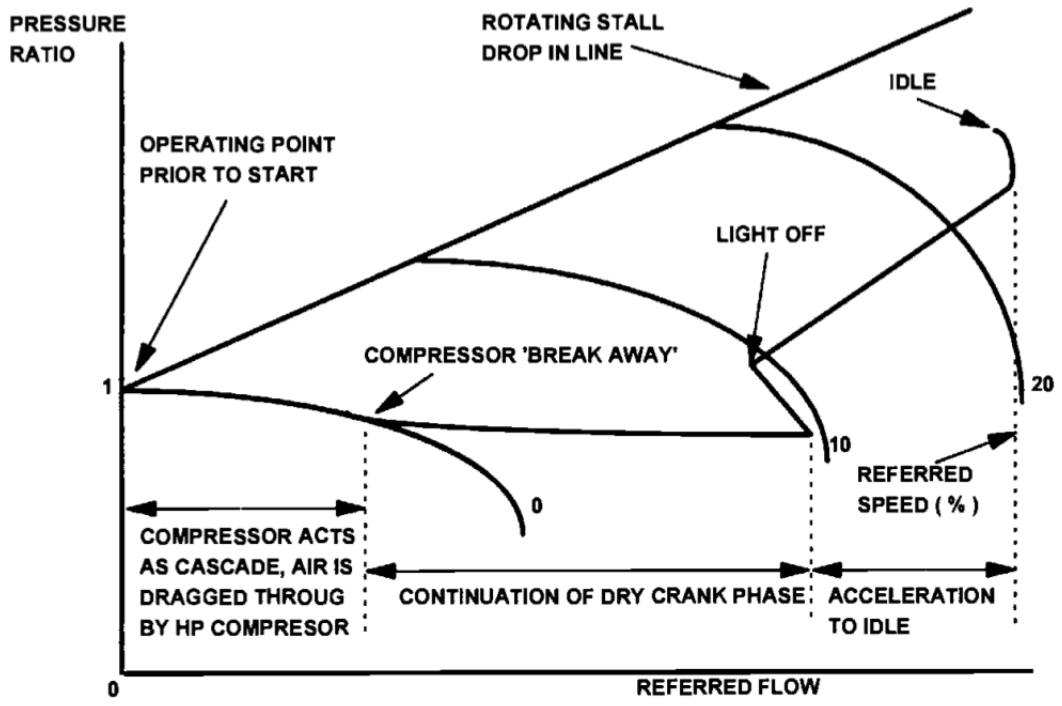

Figure 3.4: Fan, IP or LP compressor transient working line during startup [1]

At zero spool speed, the flow impinges on the rotor axially resulting in a severely negative incidence angle. Separation effects occur on the pressure surface of the blade, also characterised by low Reynolds number values. Approximate incidences (i) for a modern HPC blade operating at locked rotor conditions are -50° to -60°. Stator blades operating downstream of steady-state windmilling rotors experience lower values of incidence (i), up to -20° but of course still negative. A representative example of the incidence angle distribution in a modern engine under windmilling conditions can be found in Hatton [51]. The highest negative incidence angle blade performance data is found in Howell [3], and reproduced in [7]. Howell [3] reports experimentally derived compressor characteristics at incidences from -23° to +10°; mainly pressure loss coefficients (w), lift coefficients (C_l) and flow outlet angles (α_2) (Fig. 3.5). Highly negative incidence data is provided also by Hawthorne in [4] who reproduced Howell's results reported in [52] and presented in Fig. 3.6. However as outlined by Zachos [5] and Howard [37], such studies could not be applied to windmilling and locked rotor conditions since the change in the axial velocity through the stage is not taken into account; an invalid assumption for the low Reynolds number typical of windmilling conditions.

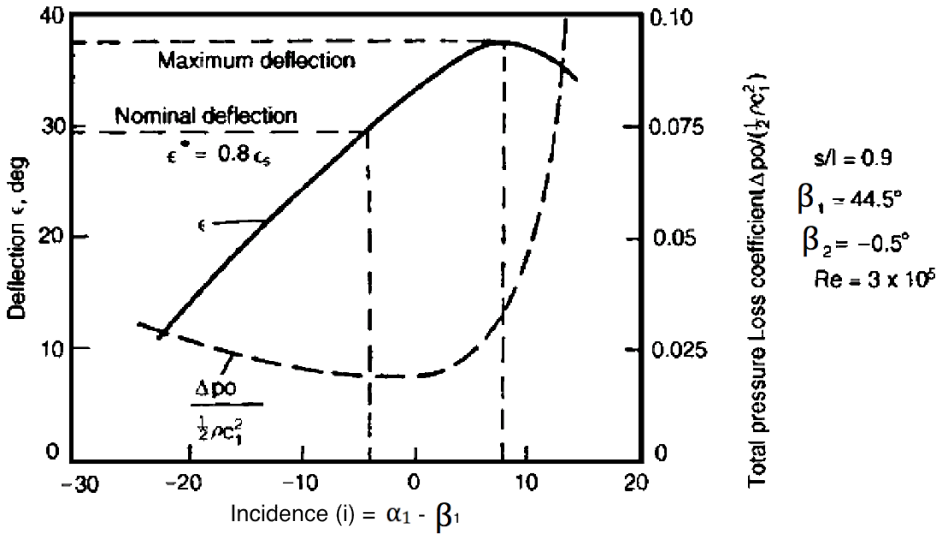

Figure 3.5: Total pressure loss coefficient (w) and deflection (ϵ) for various incidence angles (i) [3]

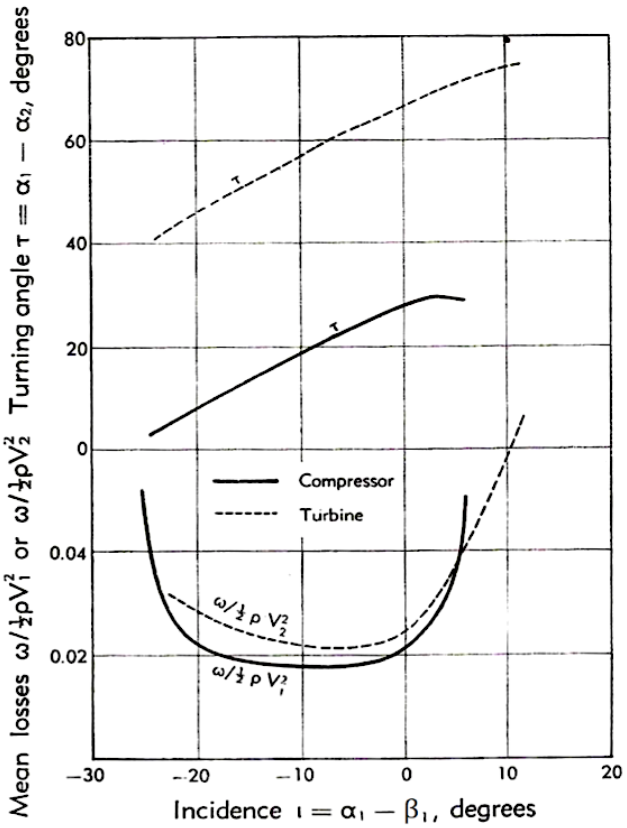

Figure 3.6: Pressure loss ($w/\frac{1}{2}\rho V^2$) and turning angle blade characteristics for negative incidences (i) [4]

3.2.2 Compressor map representation

As long as the compressor characteristics are the same, the map format is usually of secondary importance. However, this applies only for nominal conditions. As shown in the previous section, at sub-idle the compressor can operate in different working modes. At such conditions, the parameters used to represent the map become critical. A brief overview is here given on compressor map representation, whilst further reading can be found in Jones [49], Kurzke [2], Zachos [5][50] and Riegler [45].

Conventional parameters

When compressor characteristics are represented in a conventional map format, this usually consists of pressure ratio plotted against corrected flow (representing flow Mach number), for lines of corrected speed (representing the rotational Mach number of the blades). Lines (or 'islands') of constant efficiency (η) are also plotted within the same map. This format is generally used for above-idle performance simulations but for sub-idle, efficiency creates a problem.

As described in section 3.2.1, due to the definition of isentropic efficiency (η) (Eqn. (3.1)), the value of compressor efficiency asymptotes up to infinity when the actual work done approaches zero since the temperature ratio approaches unity. This discontinuity prohibits the use of efficiency as a parameter within sub-idle performance solvers since the solver would not be able to converge to a solution.

$$\eta_{is} = \frac{1 - \left(\frac{P_2}{P_1}\right)^{\left(\frac{\gamma-1}{\gamma}\right)}}{1 - \frac{T_2}{T_1}} \tag{3.1}$$

Pressure ratio and non-dimensional mass flow do not experience such a discontinuity and therefore do not create convergence problems.

Use of Beta (β) lines

The conventional map format can cause some ambiguity in the areas of the map close to choking, since for a value of corrected speed and corrected flow, there are multiple values of pressure ratio. Additionally, a co-linearity of pressure ratio values exists in the low-speed region of the map, for the same corrected speed but different flow values as illustrated in Fig. 3.7.

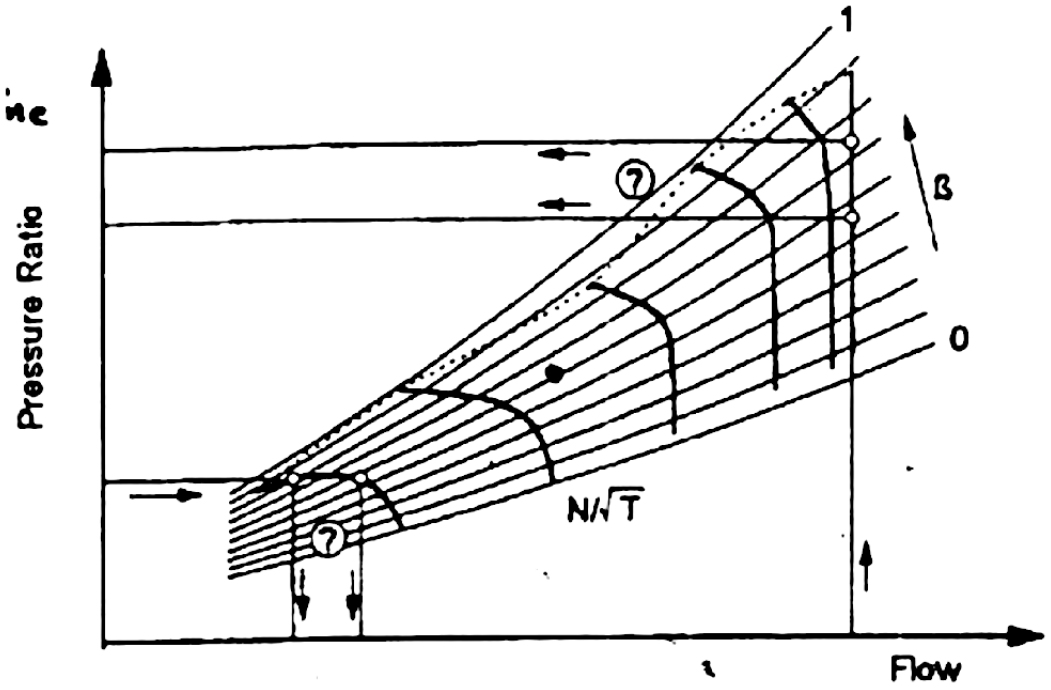

Figure 3.7: Pressure ratio and flow ambiguity at low and high speeds [2]

The Beta (β) parameter is introduced onto the compressor map as illustrated in Fig. 3.7 to avoid problems of horizontal and vertical positions of the speed line. In general, β lines are arbitrary lines equispaced and parallel to the surge line. Though of no physical meaning, the β grid can be carefully applied over the map such that lines of constant β will be close to a constant position of the exit throttle valve in a compressor rig test. Such a parameter is useful since it eliminates the areas of ambiguity previously mentioned. Kurzke [2] shows how the β lines can be used for interpolation.

Linearised parameters

To overcome the problem with the discontinuity in efficiency when using conventional parameters, most sub-idle performance solvers resort to using linearised parameters: the flow (ϕ), work (ψ), and pressure coefficients (ψ_{is}) as defined in Eqns. (3.2), (3.3) and (3.4). Each coefficient is given as a function of the non-dimensional speed ($N/\sqrt{T}$) and β line.

$$\phi = \frac{V_x}{U} \propto \frac{W\sqrt{T}/P}{N/\sqrt{T}} \tag{3.2}$$

$$\psi = \frac{\Delta H}{U^2} \propto \frac{\Delta H/T}{(N/\sqrt{T})^2} \tag{3.3}$$

$$\psi_{is} = \eta_{is}\frac{\Delta H}{U^2} \propto \eta_{is}\frac{\Delta H/T}{(N/\sqrt{T})^2} \tag{3.4}$$

where V_x is the flow axial velocity, U is the blade speed, W is the mass flow, T is the total temperature, P is the total pressure, N is the rotational speed of the compressor, H is the enthalpy, and η_{is} is the isentropic efficiency.

Using this format, the sub-idle map can be generated through extrapolation. There are disadvantages to this methodology however; mainly that the map cannot be extended down to zero speed since by definition Eqns. (3.2), (3.3) and (3.4) will asymptote up to infinity as shown in Fig. 3.8. Such a system for representing compressor characteristics cannot be used to run transient accelerations from static conditions.

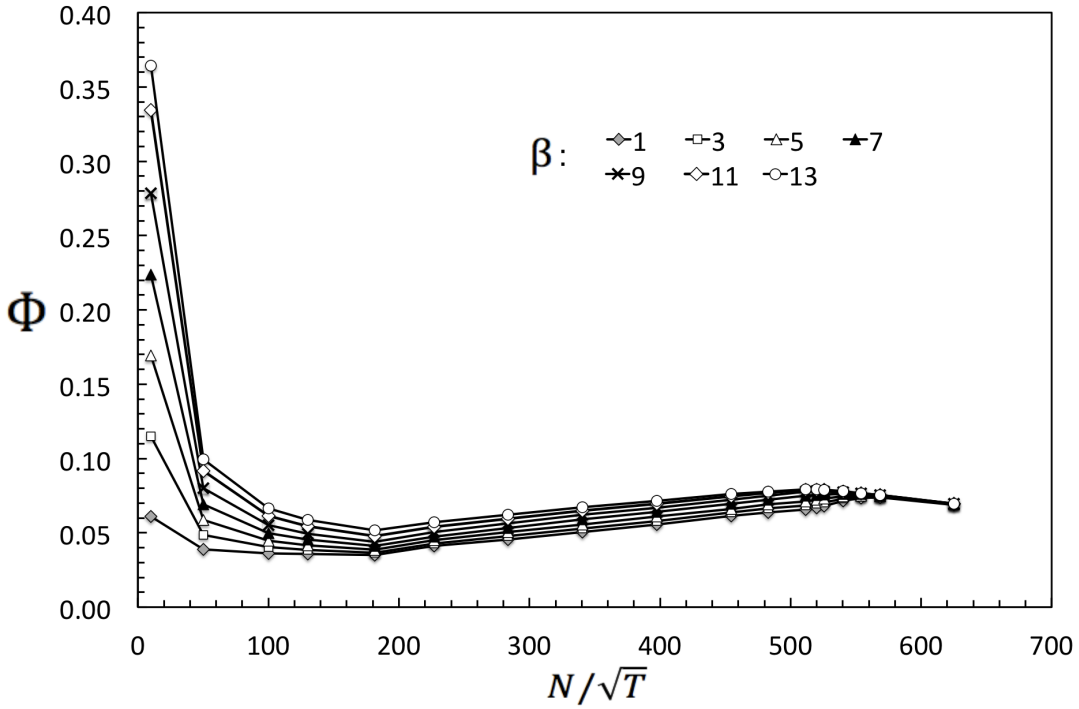

Figure 3.8: Flow (ϕ) characteristic at very low speeds ($N/\sqrt{T}$) for different values of β [5]

Specific torque

A possible alternative that permits good map representation even at low and zero speeds is the use of corrected (or specific) torque (τ/P). Specific torque maintains a finite value over the entire operating range of the compressor, even at low and zero speeds. This is due to the tangential force that the flow applies on the rotor blades as it passes through the stages, caused by the change in angular momentum, as predicted by Euler's equation (Eqn. (3.5)), even if the rotor is static.

$$\tau = W\left(r_2 V_{\theta 2} - r_1 V_{\theta 1}\right) \tag{3.5}$$

where τ is the torque, r is the radius, and V_θ is the tangential velocity.

It is therefore a physical parameter. It can be measured in a test rig with relative ease and has no discontinuity when the total temperature ratio is unity. As mentioned in Riegler [45], a universally applicable map would consist of the corrected flow, pressure ratio and corrected torque. The quasi non-dimensional torque group defined in Eqn. (3.6) is proposed by Zachos [5], and used throughout this study to represent the compressor torque.

$$\frac{\tau}{P} = \phi.\psi.\left(\frac{N}{\sqrt{T}}\right)^2.\frac{60}{2\pi} \tag{3.6}$$

The use of torque as a compressor characteristic requires significant modification of the performance solver. The compressor and turbine routines need to be adapted. The engine matching scheme is to be converted so that it matches the torque (or alternatively power) of the compressor, the turbine and any other source that adds or reduces shaft power (Fig. 3.9). This is explained in Chapter 4.

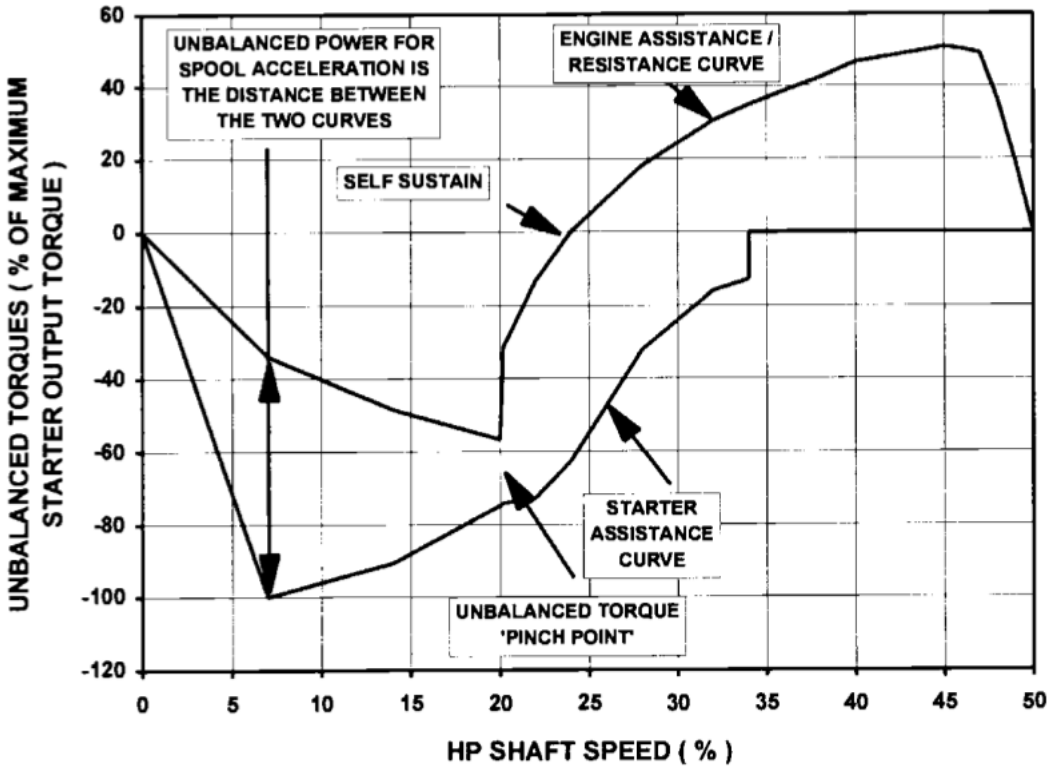

Figure 3.9: Torque balance during a starting transient operation [1]

3.2.3 Sub-idle characteristics prediction methods

Numerous authors have over the years developed different methods to try and predict the sub-idle compressor characteristics. A good review is given by Jones [48] and Zachos [5]. The current study focuses on two different methods: extrapolation as described by Leitges [6], and interpolation as described by Zachos [5][50].

Extrapolation

This extrapolation method for low-speed characteristics most commonly used involves converting the compressor characteristics into linearized parameter format, to overcome the efficiency discontinuity problem, as explained in section 3.2.2. Each parameter is plotted as a function of $N/\sqrt{T}$ with lines of constant β. The extrapolation is performed for each β-line and each parameter using a parabola with an end boundary condition of a horizontal slope at $N/\sqrt{T} = 0$. However this is not possible due to the definition of the linearized parameters, so a very low speed is selected instead, as illustrated in Fig. 3.10.

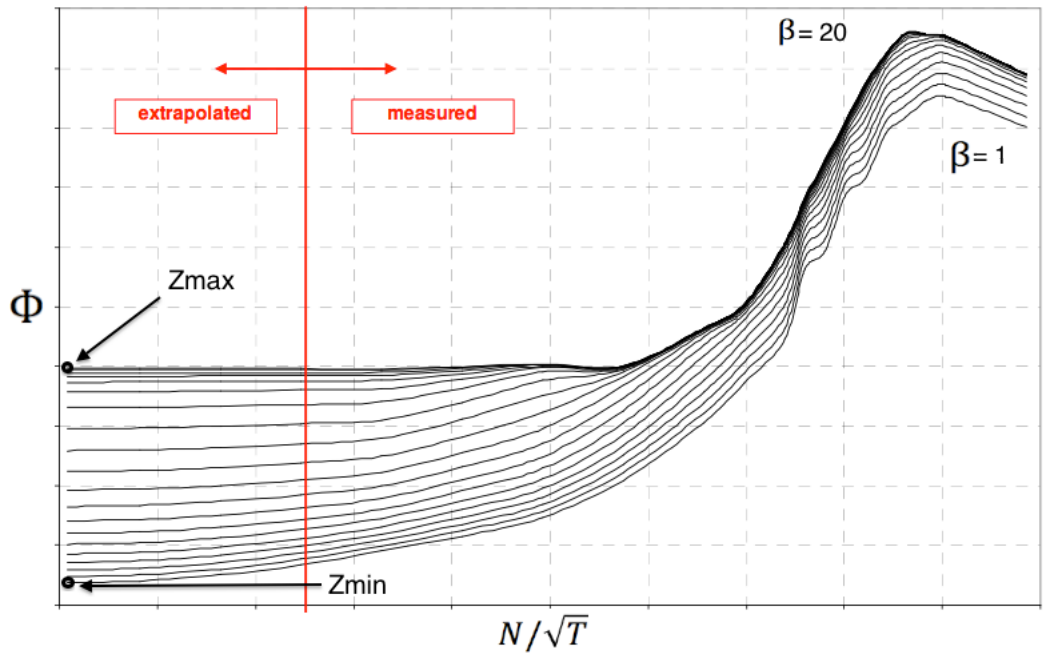

Figure 3.10: Extrapolation of above-idle compressor *phi* characteristic down to low-speed [6]

At the lowest speed line, the value of the parameter to which the parabolic interpolation is done, is not known. A 'level adjustment' system is therefore introduced. This consists of two steps: determine (or rather guess) the minimum (Z_{min}) and maximum value (Z_{max}) of the parameter at the lowest speed line being used, and assume that the values in between are distributed in the same way as for the lowest measured (from test data) speed line. The choice of Z_{min} and Z_{max} is down to engineering judgement, but physical soundness can be checked by choosing values so that no discontinuities in the curvature are present between the original and extrapolated map, and by plotting the $\psi - \phi$, $\psi_{is} - \phi$, and $\psi - \psi_{is}$ characteristics. In all such diagrams, the extrapolated lines for low speeds should collapse onto a single line due to the incompressibility of the air (therefore low flow Mach numbers are assumed) as illustrated in Fig. 3.11 and 3.12. The whole process has therefore a trial-and-error approach to it and is based on engineering judgement. It is hence not fully generic.

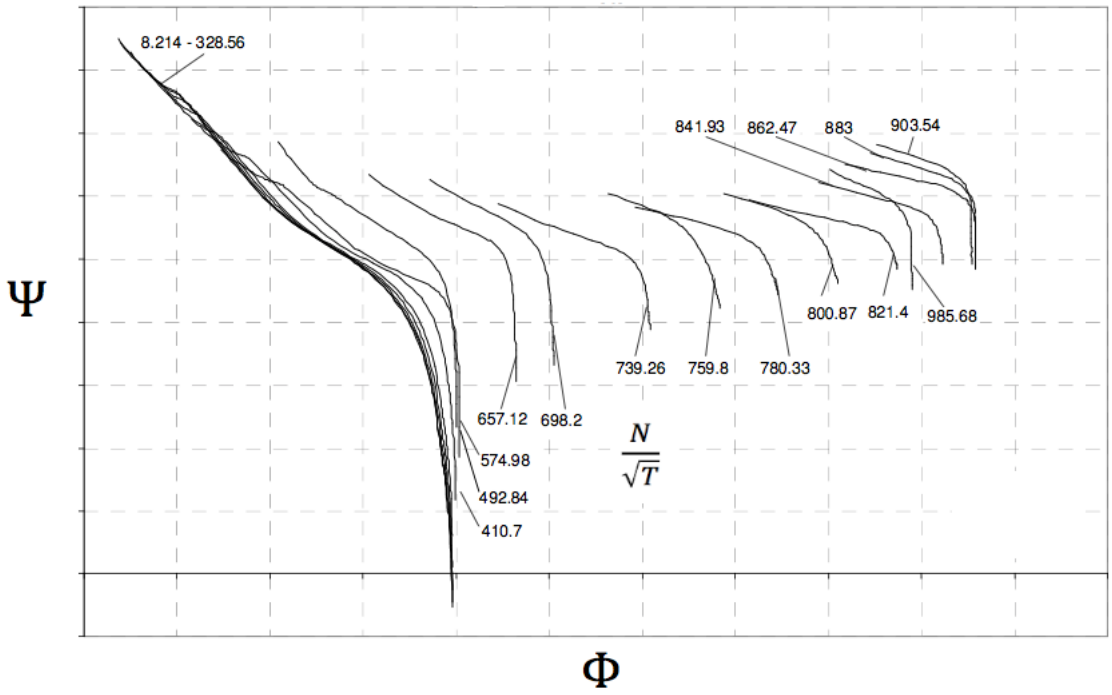

Figure 3.11: ψ - ϕ extrapolated characteristics at low speed ($N/\sqrt{T}$) [6]

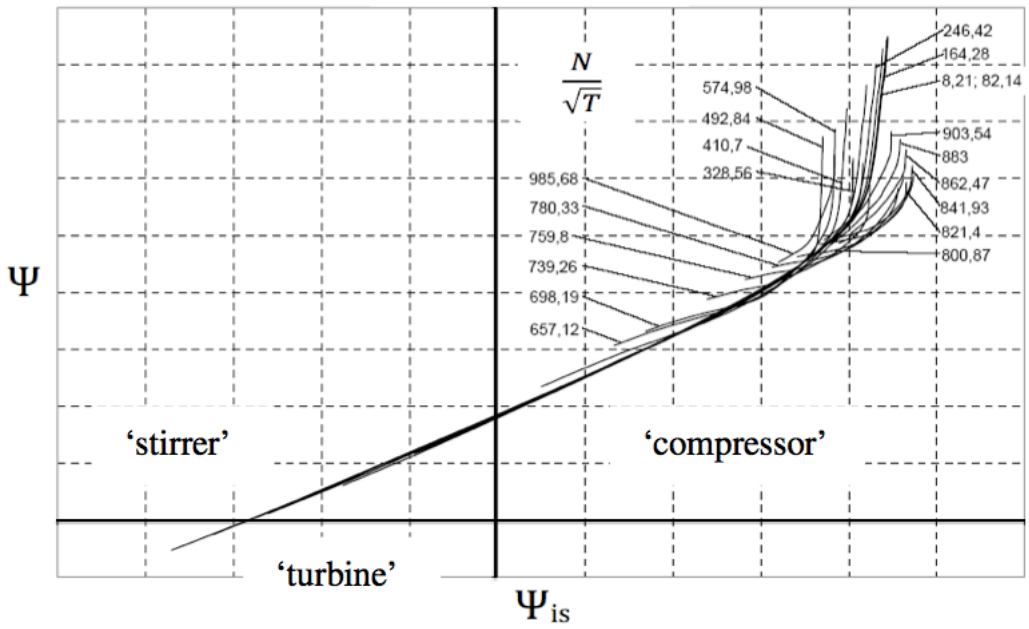

Figure 3.12: ψ - ϕ_{is} extrapolated characteristics [6]. The figure also shows the three working modes of the compressor.

Interpolation

A more physics based alternative to extrapolation is interpolation, firstly introduced by Howard [37] and implemented by Zachos [5]. The principle lies in first predicting the zero-speed line through analysis of the flow in a locked-rotor case. Once the zero speed curve is known, the map can be generated through interpolation, providing a much better definition of the low-speed curves. For the overall compressor characteristic at locked-rotor condition to be generated, a stage-stacking method is applied as firstly introduced by Howard [37]. The applied methodology was originally developed by McKenzie [53] and is used by other authors such as Song et al [54]. Stage-stacking allows the single-stage experimental and numerical studies to be expanded to calculate multi-stage compressor characteristics. However for a locked-rotor case, the changes in flow characteristics in between stages is more difficult to predict and the interstage gap may need to be taken into account as a separate geometrical parameter.

The calculation by Zachos [5] of the zero-speed curve is based on two main assumptions. The first is that the total temperature of the gas remains unchanged since there is no work and therefore no increase in the enthalpy of the gas. The second is that the density remains constant throughout the compressor. This is not entirely accurate, but because only low flow Mach numbers were considered, the change in pressure and temperature of the gas stream is too small to cause significant changes in the density. The new version of the compressor sub-idle map generation code, written as part of the current study, aims to predict the zero-speed line characteristics up to the choking point, and therefore compressibility needs to be accounted for. This is more thoroughly explained in section 3.4.1. In the previous section (3.2.2) it was concluded that specific torque, pressure ratio and non-dimensional mass flow are the best characteristics to represent the sub-idle compressor map.

In order to predict the zero-speed characteristics in terms of these parameters, Zachos [5] and Aslanidou [13], undertook experimental and numerical studies to determine the blade static pressure rise (C_p) and tangential force (C_f) aerodynamic coefficients operating at high negative incidence. These were extracted using Eqns. (3.7) and (3.8), which as-

sume incompressible flow [7]. Similarly, the lift (C_l) and drag (C_d) coefficients, as defined in Eqns. (3.9) and (3.10), were also extracted. The coefficients were used to determine the static pressure drop and tangential force across each blade row.

Once the torque and static pressure losses on the blade are known, they can be summed up to give the characteristic of the entire compressor using the stage-stacking technique. The total torque exerted on the blades is the sum of the torque exerted on all the rotor blades while the total pressure loss is calculated from the static pressure loss and the dynamic pressure at inlet and outlet. More details can be found in Zachos [5] [50], Aslanidou [13] and Rulke [12].

$$C_p = \frac{p_2 - p_1}{\frac{1}{2}\rho c_x^2} \tag{3.7}$$

$$C_f = 2(\tan\,\alpha_1 - \tan\,\alpha_2) \tag{3.8}$$

where p_1 and p_2 are the inlet and outlet static pressures across the blade, α_1 and α_2 are the inlet and outlet flow angles, and c_x is the average axial velocity across the blade, as defined in Figs. 3.13 and 3.14.

$$C_l = \frac{s}{c}\cos\alpha_m \left(C_f - \zeta \frac{\sin 2\alpha_m}{2} \right) \tag{3.9}$$

$$C_d = \zeta \frac{s}{c}\cos^3\alpha_m \tag{3.10}$$

where ζ is the total pressure loss coefficient, defined as:

$$\zeta = \frac{\Delta P}{\frac{1}{2}\rho c_x^2} \tag{3.11}$$

and α_m is defined as:

$$\alpha_m = \tan^{-1}\left(\frac{1}{2}\left[\tan\alpha_1 + \tan\alpha_2\right] \right) \tag{3.12}$$

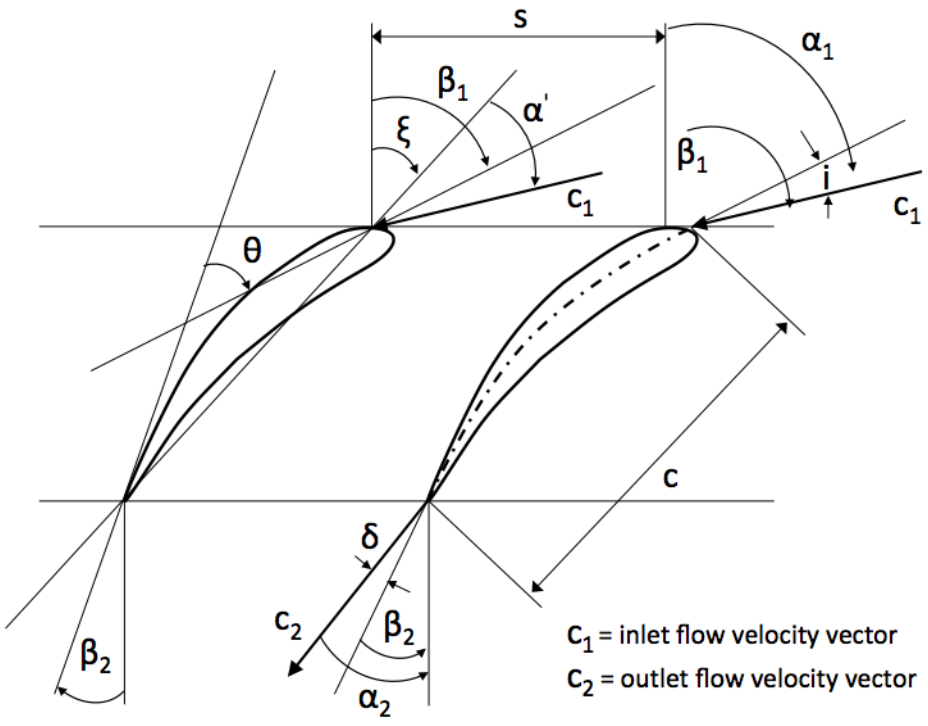

Figure 3.13: Flow and blade angle notations used

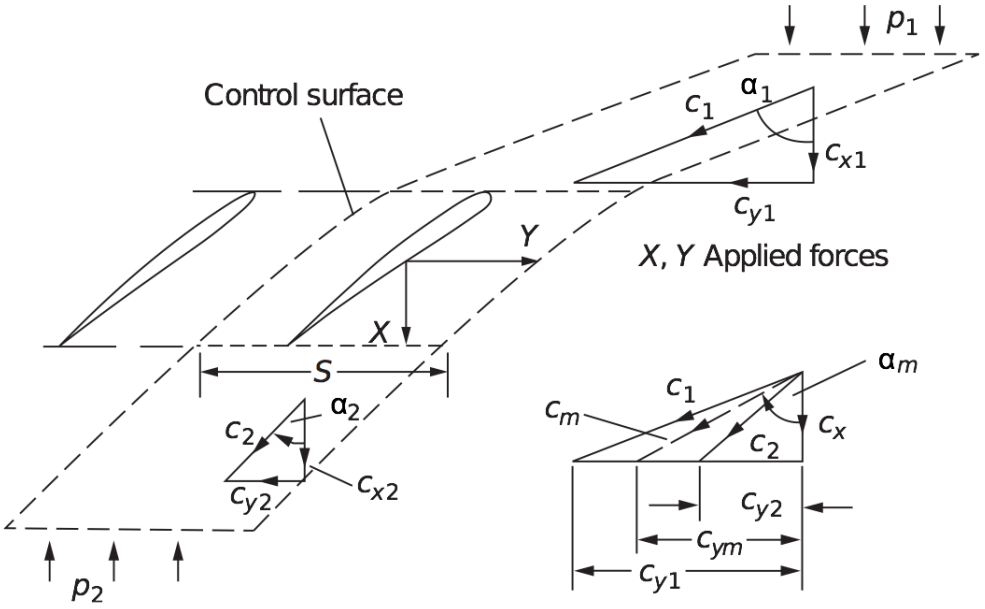

Figure 3.14: Cascade forces, flow and angle notations used, based on Dixon [7]

3.2.4 Numerical modelling of blades at negative incidence

Previous work carried out within the sub-idle performance modelling group by former researchers was fundamental for the current research, especially the validation against experimental data of the numerical model for blades at high negative incidence. A brief overview is given herein whilst further details can be found in Zachos [5] [55] [10], Pengue [8], Rulke [12] and Aslanidou [13].

Validation of numerical solver

All the analysis of the flow's behaviour at locked-rotor conditions is based on numerical studies. It is therefore fundamental for the numerical solver to be validated. Zachos [5] [55] [10], Pengue [8] and Rulke [12] validated the numerical solver against experimental data using 3-hole and 5-hole pneumatic probe measurements of a high pressure compressor blade linear cascade, of which geometry is illustrated in Fig. 3.15.

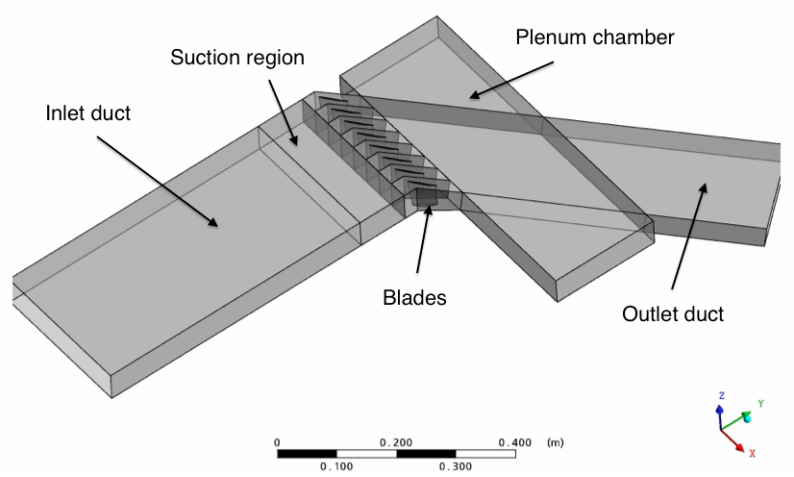

Figure 3.15: Numerical model cascade geometry used for validation [8]

Mesh and near wall treatment - The y^+ is a non-dimensional parameter used to define the size of the first cell next to the wall. The choice of y^+ depends on the case being run. The near-wall region can be largely subdivided into three layers, as illustrated in Fig. 3.16. In the innermost layer, called the "viscous sublayer", the flow is almost laminar, and the molecular viscosity plays a dominant role in momentum and heat or mass transfer. In the outer layer, called the fully-turbulent layer, turbulence plays a major role. The middle region is where the effects of molecular viscosity and turbulence are equally important.

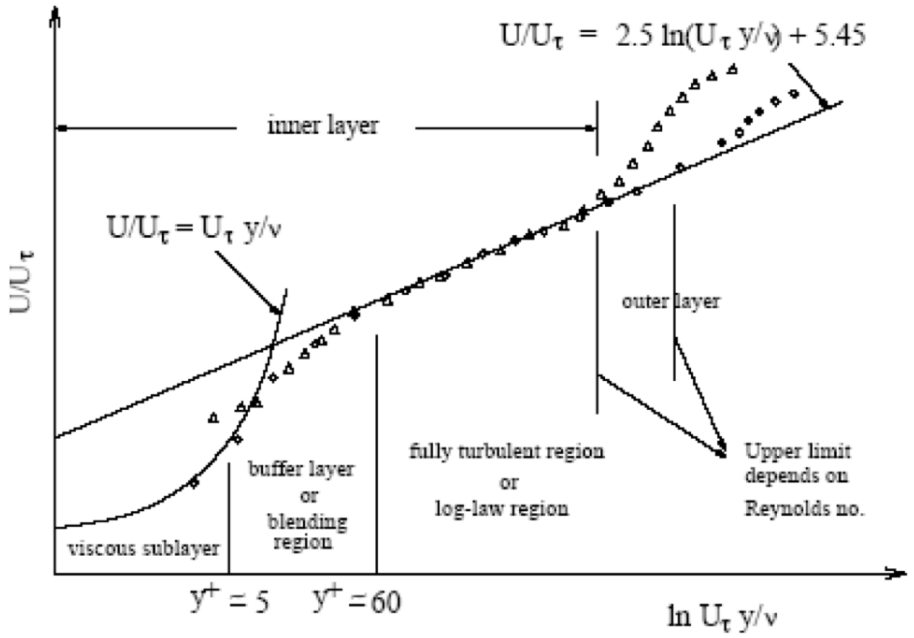

Figure 3.16: y^+ for the boundary layer where u_τ is the friction velocity, defined as $\sqrt{\tau_w}/\rho$ [9]

There are two approaches to modelling the near-wall region. In one approach, the viscosity-affected inner region is not resolved. Instead, semi-empirical wall functions are used to bridge the viscosity-affected region between the wall and the fully-turbulent region. To apply this method, the first node has to be out of the viscous sublayer, which implies a $y^+ > 30$. In most high-Reynolds-number flows, the wall function approach substantially saves computational resources, is robust, and can be reasonably accurate. However, it is inadequate in situations where the low Reynolds number effects are dominant and the assumptions underlying the wall functions cease to be valid.

In the other approach, the turbulence models are modified to enable the viscosity-affected region to be resolved with a mesh all the way to the wall, including the viscous sublayer, sometimes termed as the "near-wall modelling" approach. Such situations require near-wall models that are valid in the viscosity-affected region. For near-wall modelling, the solver requires a number of elements within the boundary layer, primarily the centroid of the first cell has to lie within the viscous sub-layer, requiring a $y^+ < 2$ from the wall. To estimate the first cell size (y_p), the following definitions are used:

$$y^+ = \frac{y_p \; u_r}{v} \tag{3.13}$$

where u_r can be obtained using:

$$u_r = \sqrt{\frac{\tau_w}{\rho}} = U_e \sqrt{\frac{C_f}{2}} \tag{3.14}$$

where τ_w is the wall sheer stress and C_f is the friction coefficient. C_f can be defined as:

$$\frac{C_f}{2} \approx 0.037 \; Re_L^{-1/3} \tag{3.15}$$

for flat plates where L is the characteristic length, or

$$\frac{C_f}{2} \approx 0.039 \; Re_D^{-1/4} \tag{3.16}$$

for ducts where D is the duct diameter

The computational grid by Pengue [8] and Zachos [5] [10] [11], was generated separately for each one of the domains. All the regions apart from the blade boundary layer sectors were meshed using a hexahedral unstructured approach. A structured mesh was used for the boundary layer sections. The enhanced wall treatment was utilized, so y^+ was kept below 2 in the blade boundary layer region. The O-mesh configuration employed for the near the wall region in the blade block is illustrated in Fig. 3.17. A mesh sensitivity study using three different mesh size was carried out, using the mesh densities tabulated in Table 3.1. The results obtained with the three meshes were compared in terms of the total pressure loss coefficient and flow exit angle. The mesh sensitivity assessment showed that the three meshes produce results within a 0.5% range of difference, especially regarding the pressure loss. The medium mesh size was selected as the most suitable as a compromise between computational time and accuracy of the results

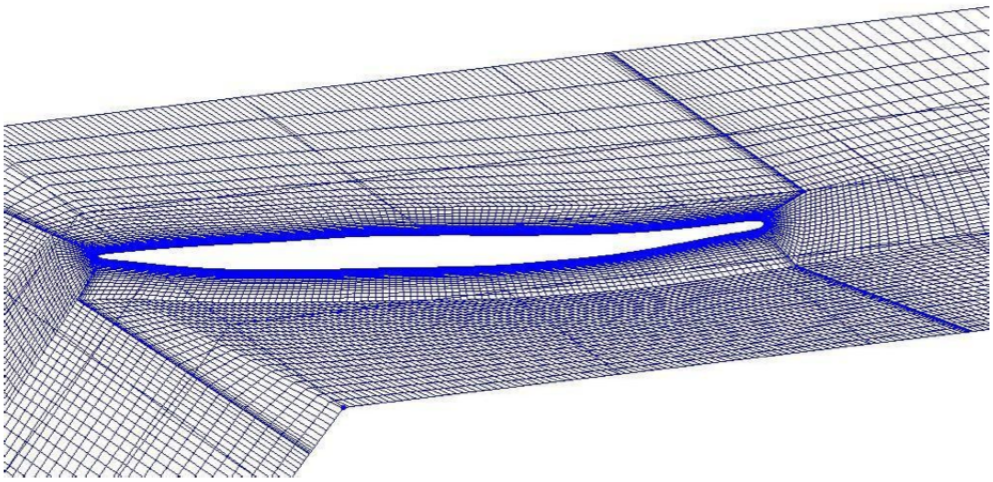

Figure 3.17: Mesh used for validation of numerical solver [10]

Grid	Inlet	Blade	Plenum	Total
1	402,343	3,911,520	956,087	5,269,950
2	511,576	6,984,456	1,336,018	8,832,050
3	645,719	9,577,920	1,715,949	11,939,588

Table 3.1: Mesh sizes used for grid sensitivity assessment [8] [11]

Turbulence model and boundary conditions - All the numerical simulations by Pengue [8] and Rulke [12] were carried out using ANSYS CFX solver. A high resolution (second order) level of accuracy was used for the solution of the RANS equations. A total pressure inlet and mass flow outlet boundary condition was used. Experimental values of the total and static pressure in the region between the blades and the boundary layer suction block were available from the rig calibration process carried out [55]. Mass was calculated through density and inlet area. The total pressure at the inlet was kept constant in all simulations, while the mass flow rate at the outlet was calculated, varying as a function of the inlet Mach number.

The turbulence closure set was considered to be of major importance due to the extremely challenging nature of the flow patterns developed around the high incidence blades. The turbulence parametric research focused on the non-algebraic two-equation eddy-viscosity models $k-\epsilon$ and $k-\omega$. A detailed review on turbulence models and their applicability for highly separated flows is given in Pengue [8]. The initial conclusion, based on Menter [56] [57], was that the $k-\omega$ Shear-Stress Transport (SST) model is the most suitable turbulence model, since the high negative incidence angle at which the blades are tested will result in a significant separation.

The $k-\omega$ SST model was found to perform well in the test cases. A number of runs were performed using the Zierke and Deutsch [58] cascade geometry, a case study widely documented and available in the open literature. A parametrical analysis regarding the turbulence modelling has been carried out by comparing the numerical results against the experimental data at three different positions downstream of the blades: 105%, 110% and 153% chords. The capability of the solver to predict wake propagation was verified in this way. Results for the 105.4% chords downstream obtained with all the different turbulence models is shown in Fig. 3.18. The study concluded that the $k-\epsilon$ model demonstrates poor performance both in the center of the wakes as well as on the peripheral regions. This behavior of the $k-\epsilon$ model can be observed at all the three locations analyzed. The $k-\omega$ SST model and the SSG (Speziale-Sarkar-Gatski) model have a similar behaviour in the peripheral zones, even if they estimate a lower velocity in respect to the experiments.

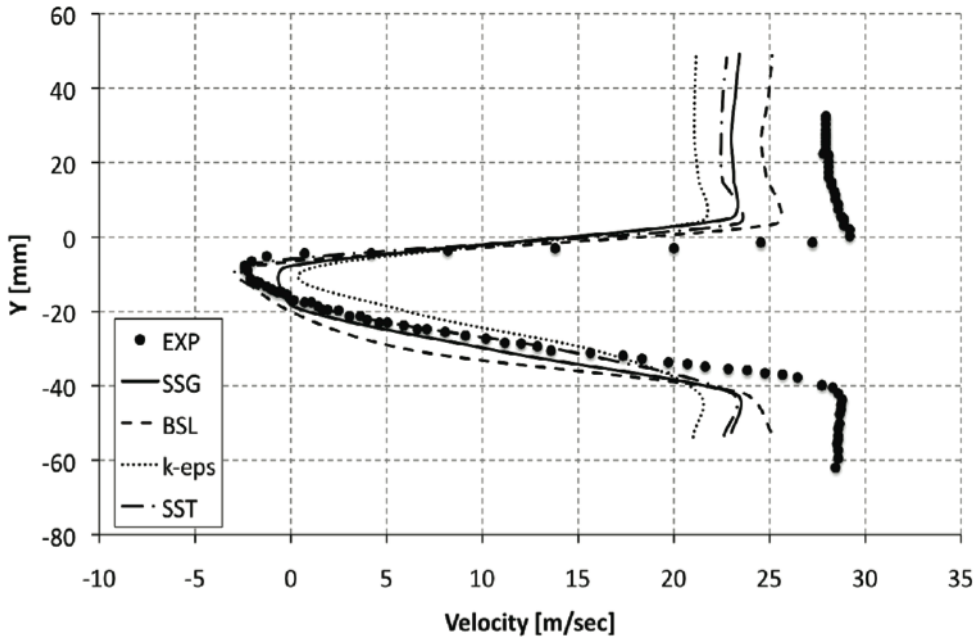

Figure 3.18: Wake profiles at 105.4% chords downstream [11]

However the two models behave in different ways when they have to predict the central region of the wake. The Shear Stress Model is the one that predicts better the low velocity region both at 105.4% chord and at 152.5% chord. The baseline (BSL) model has the same performance of the SST model at 105.4% chord but then its predictability degrades further downstream. Therefore, the turbulence model that can predict the most accurate separation pattern seems to be the Shear Stress Transport model and that was the applied turbulence closure scheme selected for the numerical study.

Unsteadiness - Due to the extremely negative flow incidence it is highly possible that unsteady effects would dominate the flowfield downstream of the blades. A number of unsteady numerical simulations were carried out by Pengue [8] and published in Zachos et al [10] [11] to evaluate whether their periodicity could be captured with a steady state approach. Time averaged unsteady results were compared with those of steady simulations in the span and pitch-wise direction.

The results shown in Fig. 3.19 for the pitch-wise direction, indicate that there is little difference between steady and unsteady simulation results for the points compared, probably due to the fact that the unsteadiness is highly periodic. A percentage error however is not given. Zachos [5] [10] [11] and Pengue [8] concluded that a very similar flow solution as far as the pressure loss through the cascade is concerned can be obtained equally well by the steady state numerical approach.

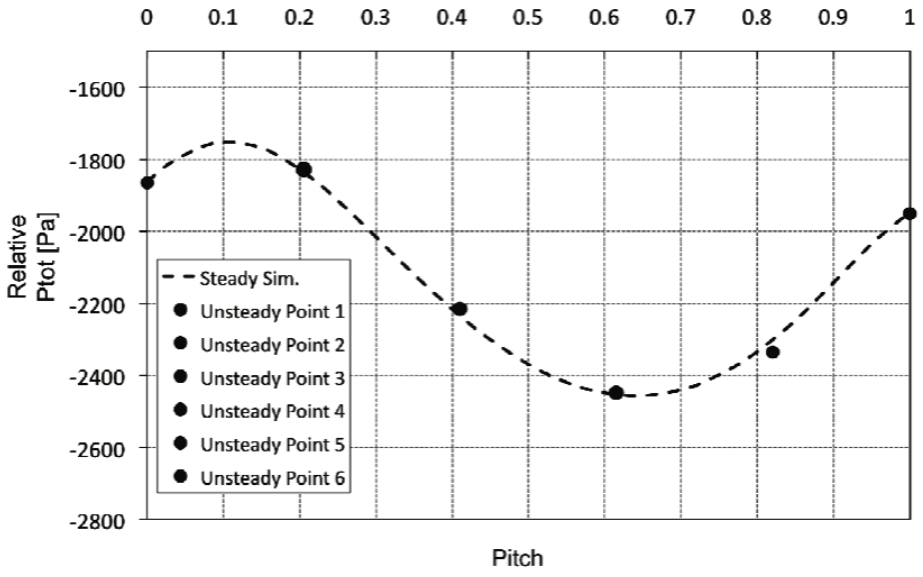

Figure 3.19: Comparison between steady and unsteady results in the pitch-wise direction [11]

Comparison against experimental data - A detailed comparison between the CFD and experimental data is given in Pengue [8], Zachos [5] and Zachos et al [10], [11]. Figure 3.20 shows a sample of this comparison for an inlet flow Mach number of 0.1. The total pressure loss is captured within 1% deviation from the 5-hole probe experimental data. The flow outlet angle has significantly more error, up to 8° of error when the flow is at -50°. However, considering the unsteadiness of the flow and the difficulty in both numerically modelling and experimentally measurement such flow features, the comparison is deemed acceptable.

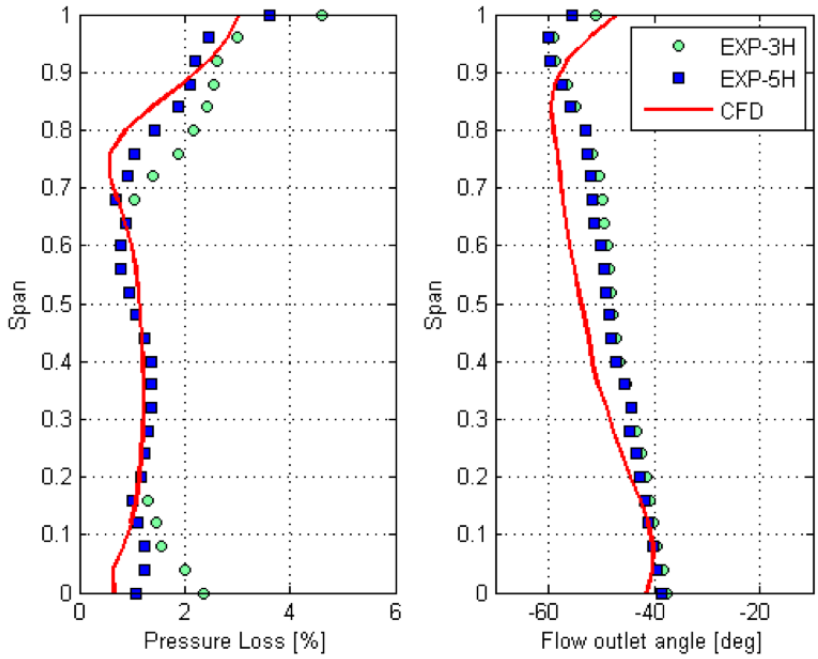

Figure 3.20: Numerical and experimental results for the linear cascade at inlet M=0.1 measured at 1.5 chords downstream [5]

To maintain this validation, the same modelling strategies, including the use of an O-grid mesh around the blade with $y^+ < 2$ to compute the boundary layer, and boundary conditions for incompressible flow, were used by Rulke [12], Zachos [5], Zachos et al [11], and the numerical simulations within this study. Further details on the numerical model setup used within this study are given in section 3.3.1.

3.2.5 Blade aerodynamic coefficients

The blade aerodynamic coefficients are fundamental to predict the zero-speed characteristic of the compressor. Following the validation of the numerical solver with cascade test data, Rulke [12] simulated various blade operating conditions (stagger (ξ) of 0° and 46°, solidity ($\frac{s}{c}$) 0.5 and 1.0, incidence angle (i) from 0° to -60°) to build the database of coefficients required by the code. Figure 3.21 shows a sample of the results for the blade coefficients at a solidity of 0.5 and stagger 0°.

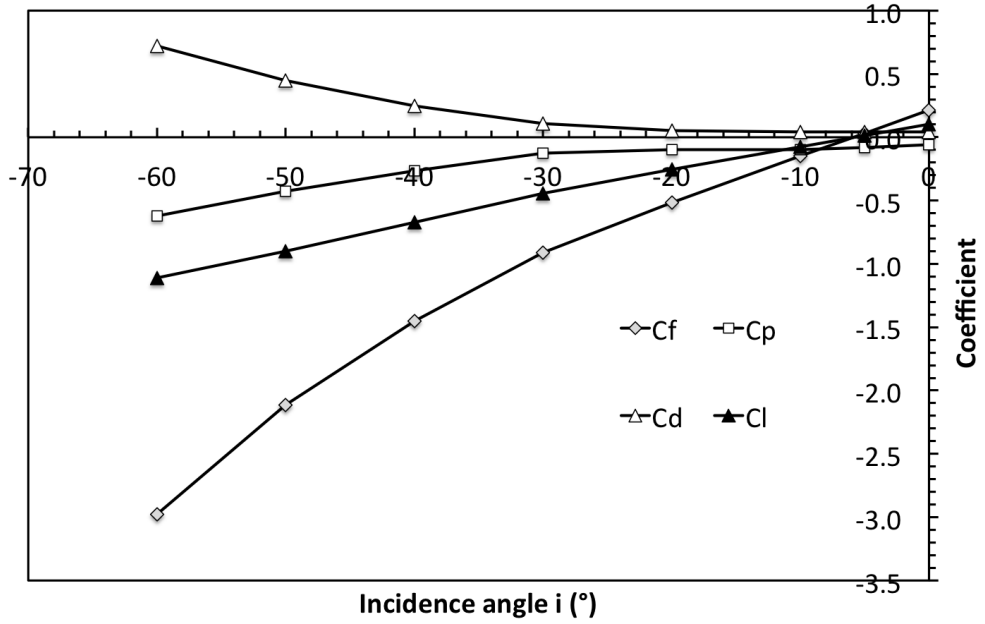

Figure 3.21: Blade aerodynamic coefficients (C_f, C_p, C_d and C_l) for 0.5 solidity ($\frac{s}{c}$), stagger (ξ) of 0° at flow inlet Mach 0.1 [12]

3.2.6 Zero-speed characteristic

With the methodology defined and the blade characteristics extracted, the prediction of the zero-speed line and the generation of the sub-idle compressor characteristics through interpolation was carried out by Aslanidou [13] and Zachos [5] (Fig. 3.22 and 3.23).

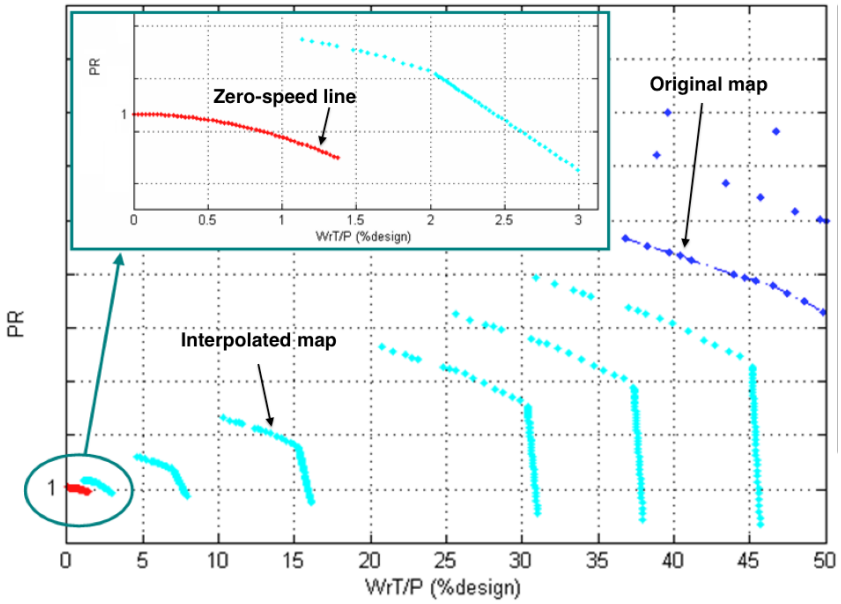

Figure 3.22: Sub-idle compressor map by Aslanidou [13] and Zachos [5]

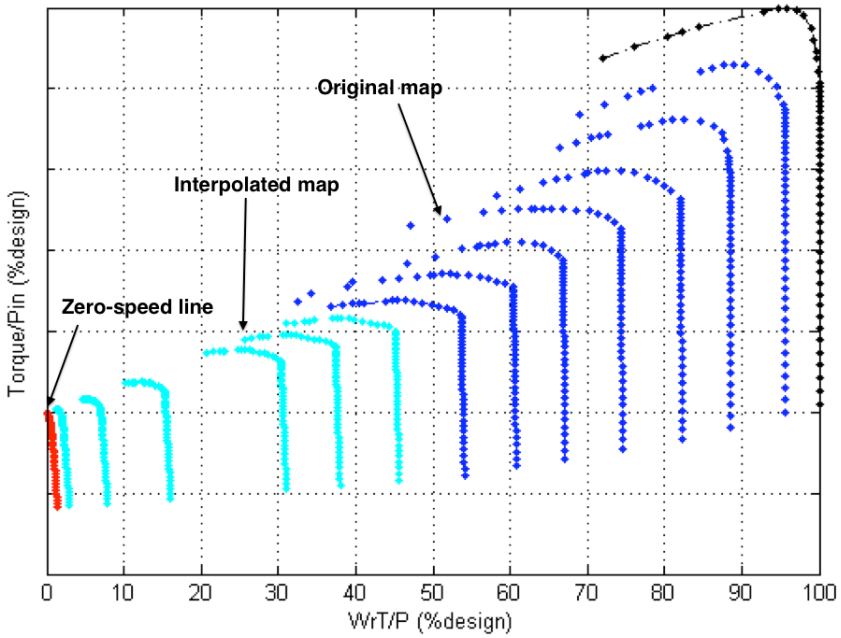

Figure 3.23: Sub-idle torque map by Aslanidou [13] and Zachos [5]

3.2.7 Blade Element Theory

When tackling an axial flow compressor design problem, it is necessary to prescribe the desirable velocity distributions at each radius of the compressor that will eventually fulfil the design requirements. The appropriate blade sections are selected at each radial position and stacked in proper relation to each other. The blade-element approach to compressor design is discussed in detail in Lieblein [59].

The concept of Blade Element Theory consists of the idea that axial flow compressor blades are evolved from a process of radial stacking of individual aerofoil shapes called blade elements [14] as illustrated in Fig. 3.24. These elements are assumed to be along surfaces of revolution generated by rotating a streamline about the compressor axis. Each element along the height of the blade is designed to direct the flow of air in a certain direction as required by the design velocity diagram of the blade row. This means that the flow is resolved in only two dimensions, whilst the radial flow is omitted. However, even assuming this can be done with relatively good accuracy, Robbins [14] shows how significant differences exist when the linear cascade is subsequently converted into an annular one. The three-dimensional effects influence the magnitude of the design incidence angle, the loss in total pressure, and the deviation angle.

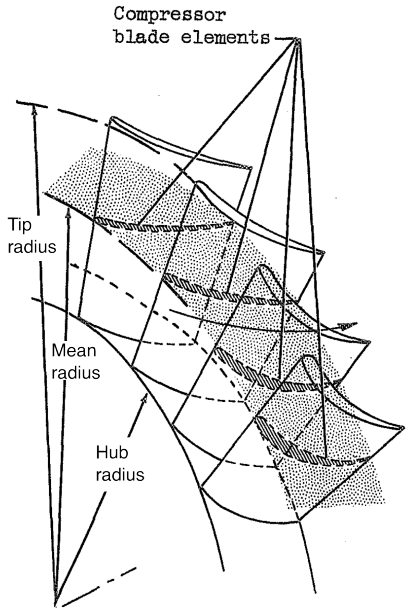

Figure 3.24: Compressor blade elements shown along control surface of revolution [14]

In a two-dimensional cascade at subsonic conditions, the magnitude of the loss in total pressure across the blade element is determined from the growth of the blade-surface boundary layer (profile loss). In an actual subsonic flow compressor, the loss in total pressure is determined not only by the profile loss, but also by losses induced by the three-dimensional nature of the flow, resulting from secondary motions and disturbances generated by the casing wall boundary layers, blade tip clearance and interaction with adjacent blade rows. Further details are found in Robbins [14] and Lieblein [59]. In an attempt to analyse the far off-design flow characteristics in three-dimensions rather just at midspan, Rulke [12] compared the blade aerodynamic coefficients at the hub (10%), midspan (50%) and tip (90%) positions of a 3D blade and the equivalent 2D profile. The results, as shown in Fig 3.25, indicate that the 2D results are close to the averaged values of the 3D blade. The study was however conducted only for a single incidence angle (i) of -60°.

The objective of the current project within this area of study, described in section 3.3.7, was to confirm these results for the entire range of incidences and determine the relative errors.

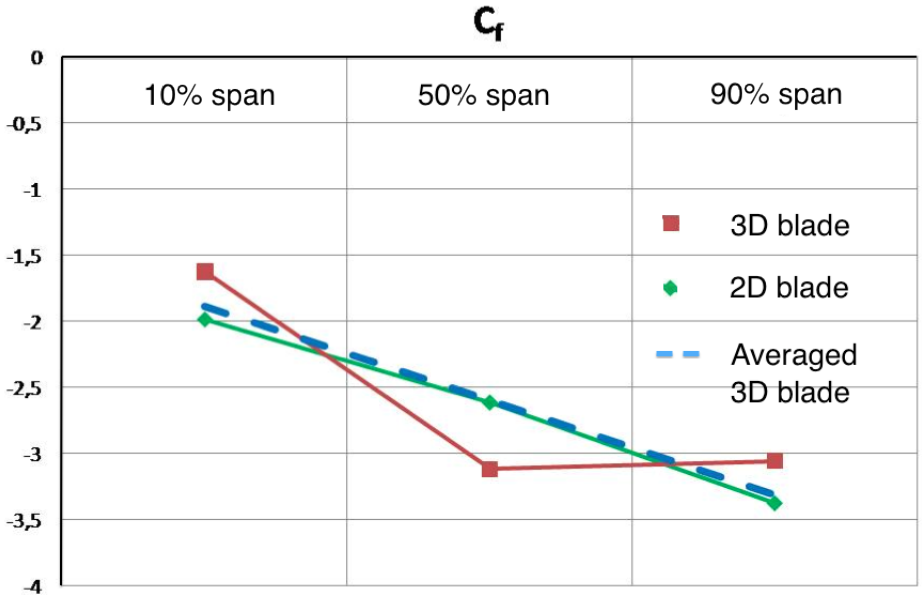

Figure 3.25: Comparison of tangential force coefficient (C_f) measured from numerical simulations at inlet Mach 0.1 for fully 3D blade and equivalent 2D sections at 10%, 50% and 90% span height [12]

3.2.8 Concluding remarks

The literature review on sub-idle compressor performance highlighted the differences between turbomachinery flow characteristics at very low speed and nominal conditions. The changes in compressor working modes influence the choice of parameters used to map the characteristics at low speeds. Efficiency is not a suitable parameter, due to the compressor acting as a stirrer and a turbine at such far off-design conditions. The literature suggests torque-based parameters since torque is not affected by discontinuities in the low speed region and is a physical measurable parameter. Linearised parameters are unsuitable at speeds close to zero.

An overview of available compressor sub-idle characteristics prediction methods showed that even though a number of checks can be made to ensure the physical soundness of the result, extrapolation is based on engineering guesses. Zero-speed characteristics cannot be evaluated since the method is based on linearised parameters. Interpolation is suggested as a more physics based approach where pressure ratio and torque characteristics are interpolated to a zero-speed line, which in turn is derived by analysing the flow through the compressor at locked-rotor condition. A stage-stacking technique is used, together with blade characteristics that can be derived from cascade tests, or numerical simulations. Previous research validated against cascade test data, the use of steady-state numerical solvers for predicting the blade characteristics at high negative incidences, where the flow is highly separated. Blade characteristics at low Mach number flows were derived from numerical simulations and used as input data for a stage-stacking code to predict the zero-speed line.

The current research described in the following sections, build on this method, using the validated numerical solver to extend the numerical simulations up to high inlet Mach numbers and derive blade aerodynamic coefficients including compressibility effects. Flow deviation and blockage due to highly separated flows is also investigated, with results implemented in a new version of the compressor sub-idle map generation code, based on isentropic flow equations and Q-curves to cater for compressibility.

3.3 Locked-rotor numerical studies

3.3.1 Cascade numerical model

All the numerical studies described in this chapter were run using the same set of blade numerical models, consisting of the same high pressure compressor blade profile at different solidities, stagger angles (ξ) and incidences (i).

Mesh and boundary layer treatment

The guidelines set by Pengue [8] and Rulke [12] for the numerical model mesh and setup were used. A mesh dependency study and turbulence model assessment was therefore not required since the numerical modelling methodology was already validated against experimental data, as described in section 3.2.4. The geometry is illustrated in Fig. 3.26. The mesh was refined to reduce cell skewness using ANSYS Gambit. It has a refined structured O-grid around the blade surface with $y^+ < 2$, as recommended by the solver's user guide [60] and illustrated in Fig. 3.27. The rest of the domain is then unstructured. The final mesh consists of 2.8 million cells. The process was repeated for the other models for which different stagger angles (0°, 23° and 46°) and solidities (0.5, 0.75, 1.0, 1.25) are used.

Velocity inlet and mass flow outlet boundary conditions were used, with the incidence angle set by dictating the flow inlet angle into the domain. Simulations were run with ANSYS CFX using the k-ω SST turbulence model. The solver was set to a pressure-based implicit steady state scheme, starting with first order upwind simulations, followed by higher resolution. The fluid was treated as incompressible with the temperature set at 300 K and ambient pressure of 101325 Pa. Convergence criteria were set to an RMS level of $1.0e^{-5}$ but generally the RMS turbulent kinetic energy could only reach a minimum level of around $1.0e^{-4}$.

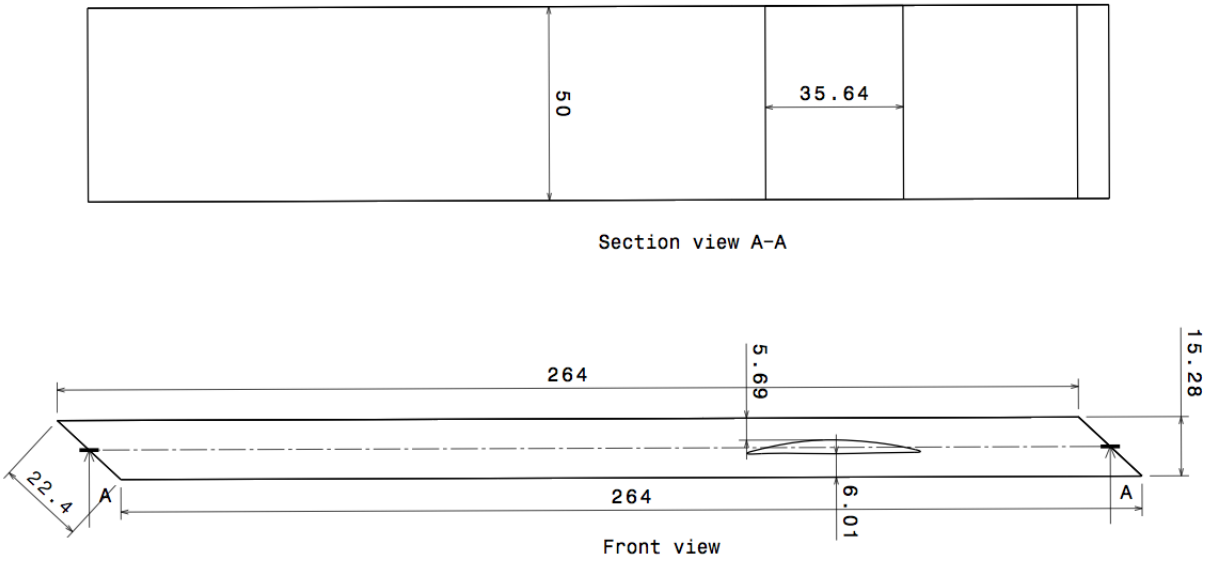

Figure 3.26: Domain dimensions for solidity ($\frac{s}{c}$) 0.5 (mm) [15]

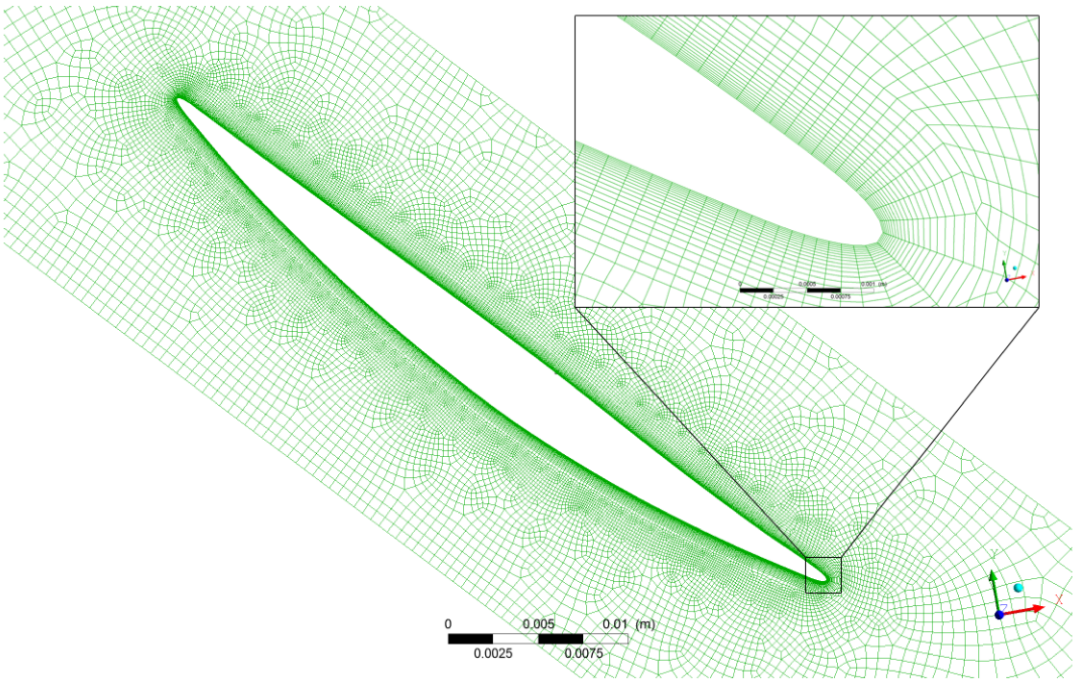

Figure 3.27: Updated cascade mesh showing O-grid around the blade [15]

3.3.2 Flow behaviour at high negative incidence

Little is known of the flow behaviour at low-speed and locked-rotor conditions. The following section describes the numerical work undertaken within this research on flow deviation at high negative incidence, together with important observations from the results. Simulations were run in collaboration with H. Larcher [15], as part of his MSc project. The objective was to understand better the nature and magnitude of the flow phenomena that dominate this far off-design area of the compressor characteristics. Where possible, comparison with other experimental and numerical results from the literature is highlighted to demonstrate confidence in the numerical work and the respective results.

Velocity profile characteristics

There are very few studies on blade aerodynamics at highly negative incidence angles. However, a certain degree of similarity can be observed with blades under stalled conditions. At both highly positive and highly negative incidences, the shape of the blade is no longer influential. Yocum and O'Brien [16] [61] experimentally studied fully stalled blades to provide more fundamental understanding of separated flows in cascades. For a solidity of unity, three stagger angles (ξ) were tested at highly positive incidences, well into the stalled flow regime. The study determined the large influence that the blade stagger has on the separated flow. As illustrated in Fig. 3.28, the flow detaches from the blade surface and forms a region of reverse flow. This creates a restriction in the blade channel. To maintain mass flow continuity, the rest of the flow is forced to accelerate.

It is noticeable from Fig. 3.28 that as the stagger increases, the region of reverse flow decreases in size. Consequently the velocity of the rest of the flow decreases, relative to the cases with lower stagger (ξ). For highly negative incidences, the flow characteristics are similar to the stalled case except that the reverse flow region increases with increasing stagger. The numerical model described in section 3.3.1 was run at negative incidences (i) ranging from 0° to -60° and at stagger angles of 0°, 23° and 46° for solidities ($\frac{s}{c}$) 0.5 - 1.5. The velocity profiles were extracted from the numerical simulations at the blade's mid-span, and are illustrated in Figs. 3.29 and 3.30. The similarity with the profiles for stalled blades in Fig. 3.28 is evident.

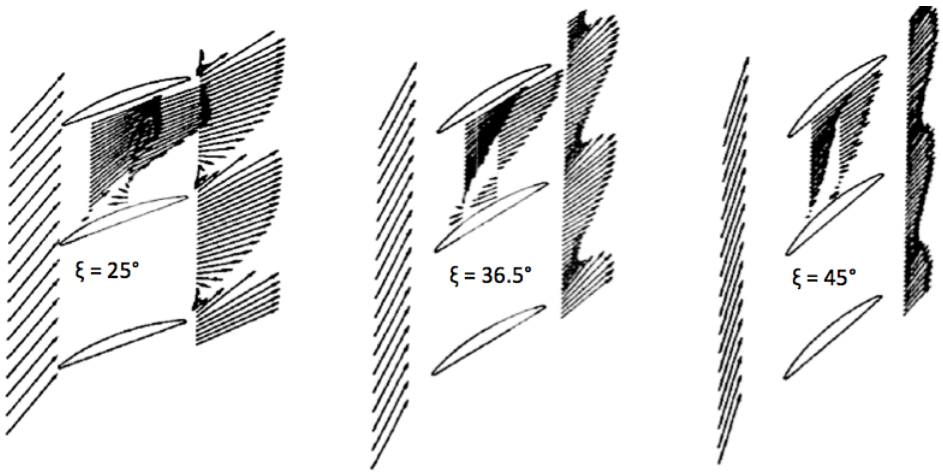

Figure 3.28: Experimental flow velocity profiles at blade inlet, blade-to-blade and outlet sections for stagger (ξ) 25°, 36.5° and 45° for an angle of attack (α') of 20° [16]

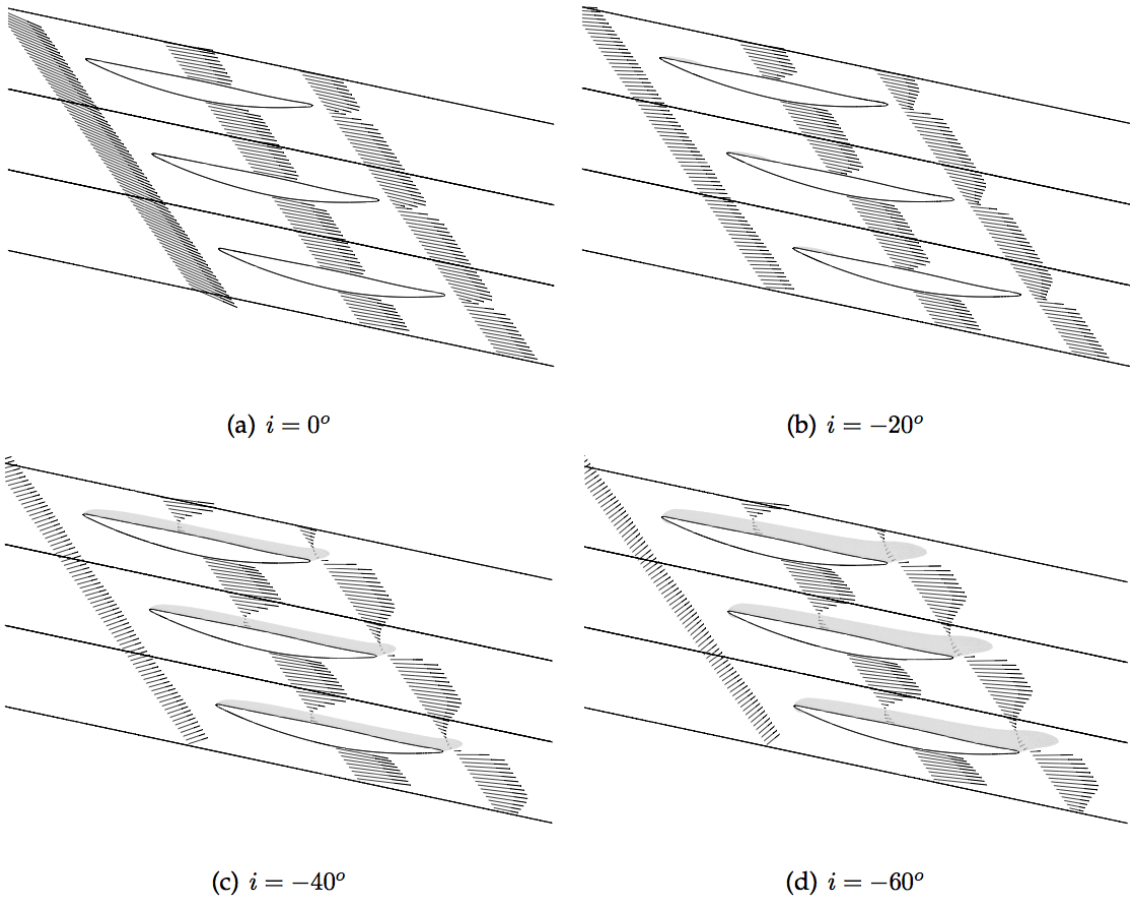

Figure 3.29: Inlet, mid-chord and trailing edge velocity profiles for solidity ($\frac{s}{c}$) 0.5, stagger (ξ) of 46° and incidence (i) of 0°, −20°, −40° and −60°. Recirculation zone highlighted if present [15]

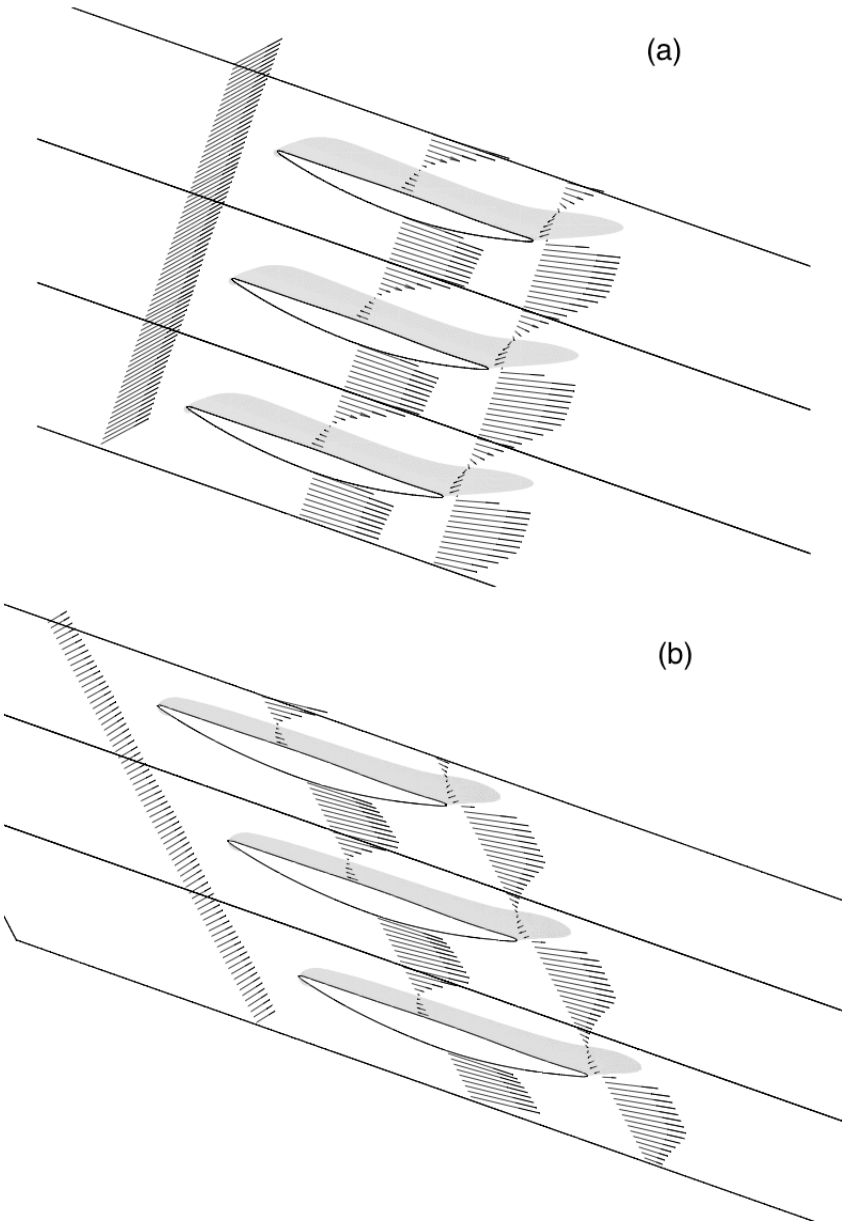

Figure 3.30: Velocity profiles at incidence (i) $-60°$, solidity ($\frac{s}{c}$) 0.5 for (a) stagger (ξ) = $0°$ (b) stagger (ξ) = $46°$ [15]

Change in flow direction downstream of the blade

An important parameter when studying blade flow characteristics is flow deviation. However the presence of highly separated flows which extend downstream of the blade, makes measurement of the flow outlet angle for high negative incidence cases, quite difficult. An analysis of the velocity contours in Rulke [12] indicated that the flow does not maintain a constant direction as it leaves the blade trailing edge. Rather it tends to turn and stabilise only at a significant distance downstream. For cases run, the flow angle was measured at various positions downstream, as shown in Fig. 3.31.

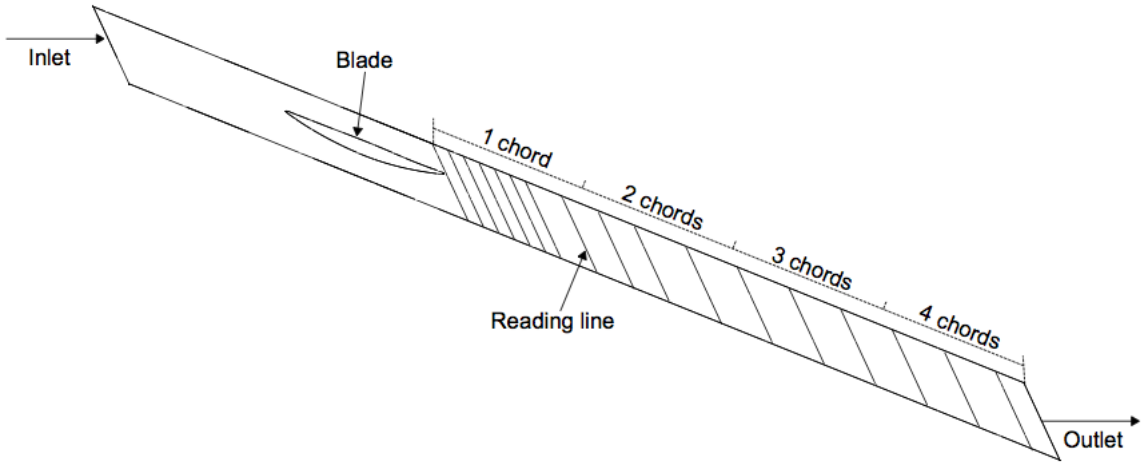

Figure 3.31: Flow angle (α_2) reading locations downstream of the blade - stagger (ξ) 46°, solidity ($\frac{s}{c}$) 0.5

A sample of the results is given in Figs. 3.32 and 3.33 for a stagger angle (ξ) of 46°, and Figs. 3.34 - 3.36 for a stagger angle of 0°. At low incidences ($i \geq -20°$), flow outlet angle remains fairly constant, reaching a stable value quickly. Flow separation in these cases is low and the blade maintains its aerodynamic characteristics. As the incidence becomes more negative (i $\leq$ -30°), the final flow angle (α_2) tends to deviate from the design point value. For example, in Figs. 3.32 and 3.33 for solidity 0.5, at low incidence ($i \geq -30°$) the final flow angle (α_2) is approximately 46°. As the incidence decreases past -30°, the final flow angle increases to 48°, 52.5°, 55° and 56° for incidences (i) of -30°, -40°, -50° and -60° respectively. The flow requires more distance downstream of the trailing edge to reach a final stable value. Similar behaviour is observed in Figs. 3.34 - 3.36.

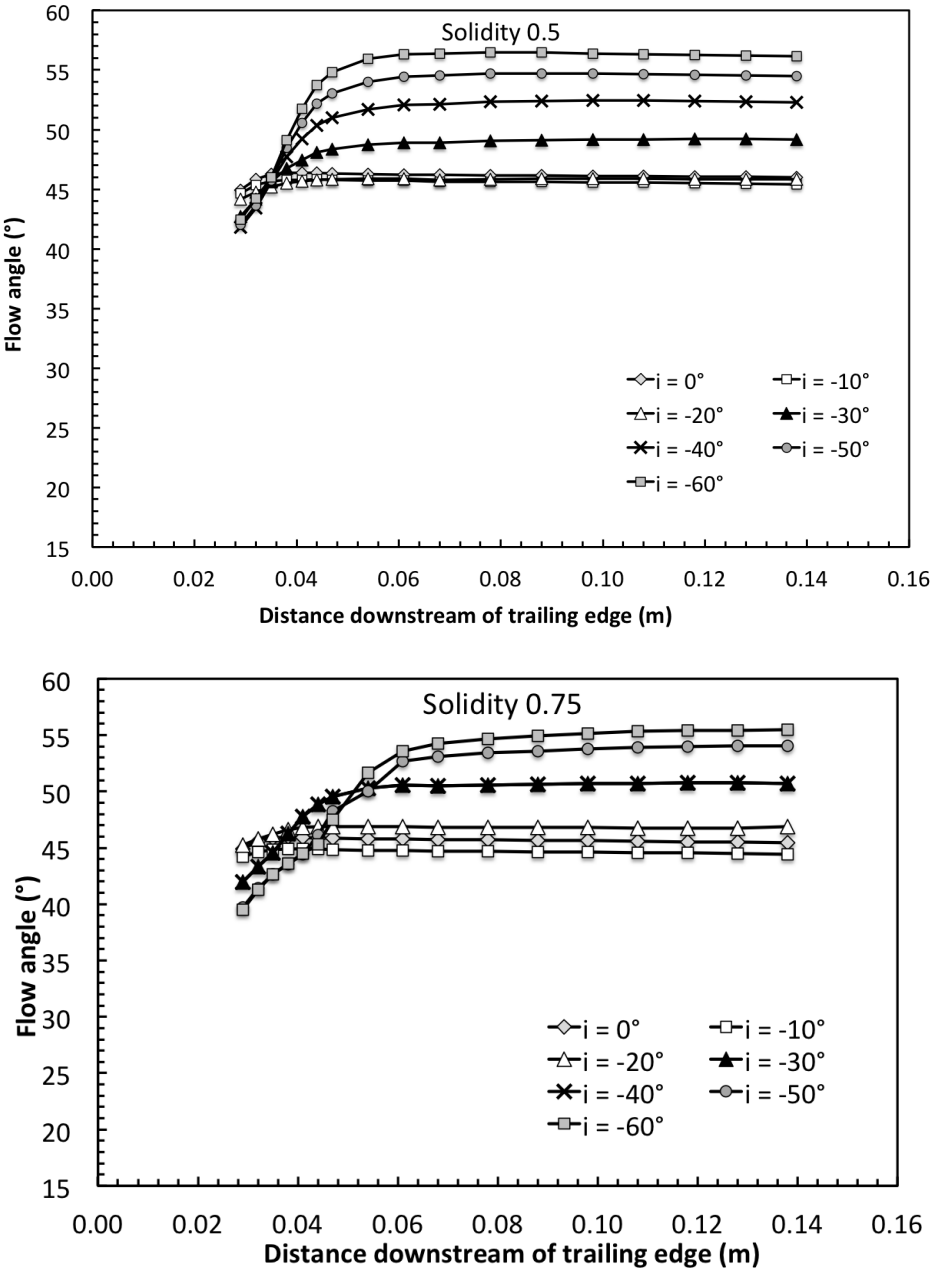

Figure 3.32: Velocity averaged flow angle measured at different positions downstream (as shown in Fig. 3.31) of the blade at 46° stagger (ξ) for different incidence angles (i = 0° to -60°) and solidities ($\frac{s}{c}$) 0.5 and 0.75 [15]

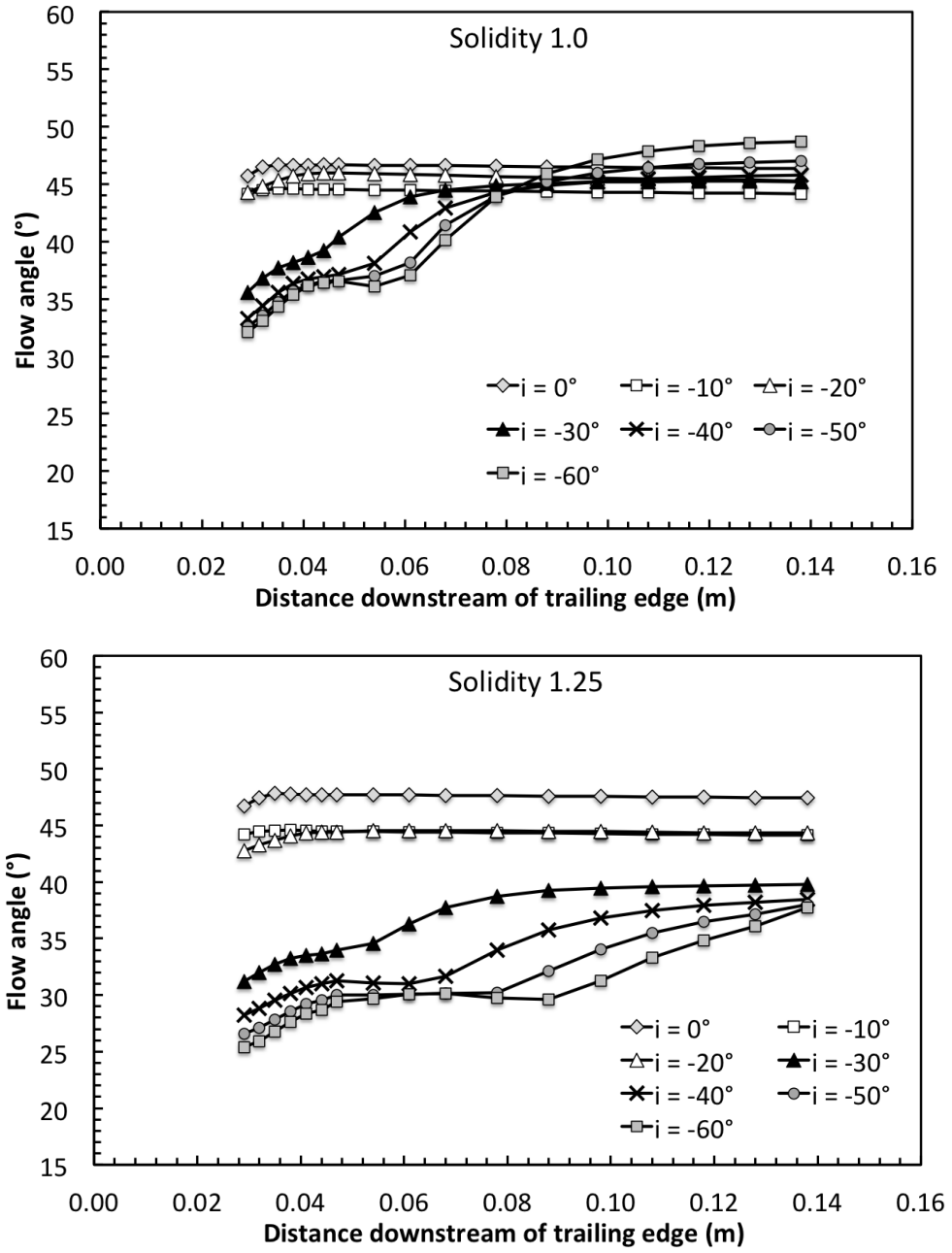

Figure 3.33: Velocity averaged flow angle measured at different positions downstream (as shown in Fig. 3.31) of the blade at 46° stagger (ξ) for different incidence angles (i = 0° to -60°) and solidities ($\frac{s}{c}$) 1.0 and 1.25 [15]

It is likely that this change in flow angle is due to the presence of the separated and recirculating flow on the blade surface, caused by the high negative incidence. This effectively changes the blade channel shape, forcing the flow into a particular direction dictated by the separated zone's shape relative to the other blade. On leaving this region, the flow will tend to follow the direction of least deflection from the inlet angle. The effect of solidity ($\frac{s}{c}$) is very significant on the flow characteristics downstream of the blade when the incidence is very negative. This is evident in Fig. 3.37 where at an incidence (i) of -50°, the change in flow direction with distance downstream is highly dependent on the solidity. The results suggest that a low solidity forces ($\frac{s}{c} \approx 0.5$) the flow to stabilise more quickly, most probably since the blades are closer together and therefore the flow is controlled better. For high solidities ($\frac{s}{c} \geq 1.0$) where the blades are far apart, the flow takes much longer to stabilise. At low negative incidences ($i \geq -30°$) the effect is less pronounced, probably since at such conditions the blade still maintains its aerodynamic properties and flow deviation is closer to the design point value.

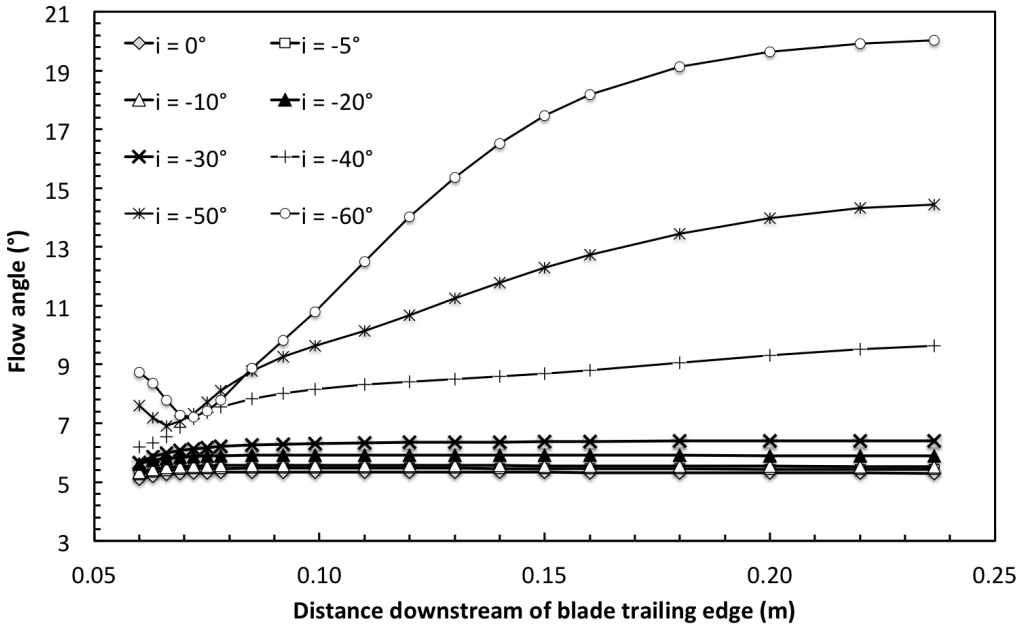

Figure 3.34: Velocity averaged flow angle measured at different positions downstream of the blade at 0° stagger (ξ) for different incidence angles (i = 0° to -60°) and solidity 0.5 [15]

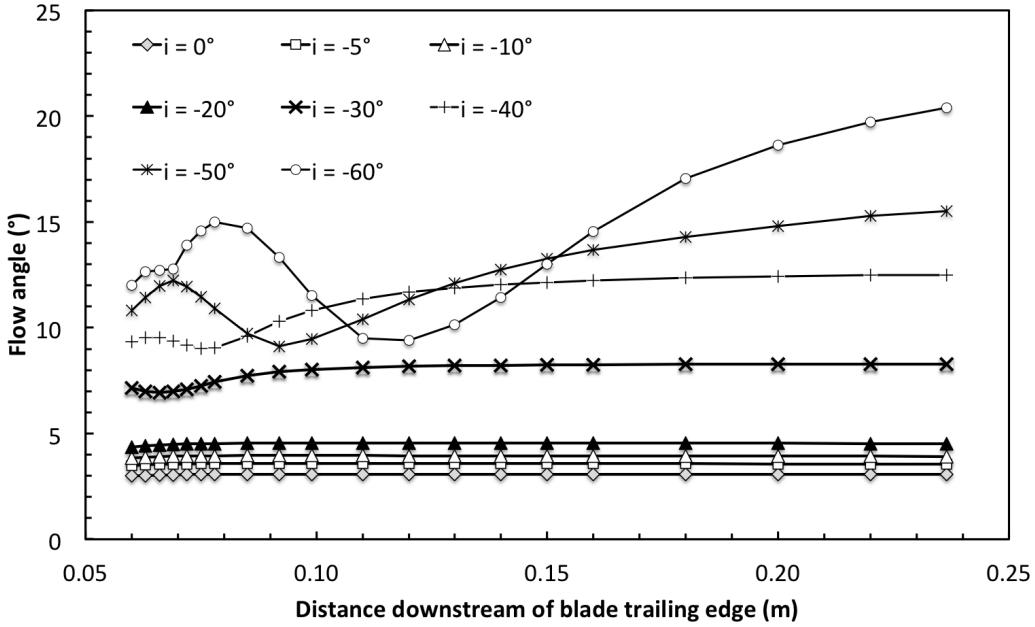

Figure 3.35: Velocity averaged flow angle measured at different positions downstream of the blade at 0° stagger (ξ) for different incidence angles (i = 0° to -60°) and solidity ($\frac{s}{c}$) 1.0 [15]

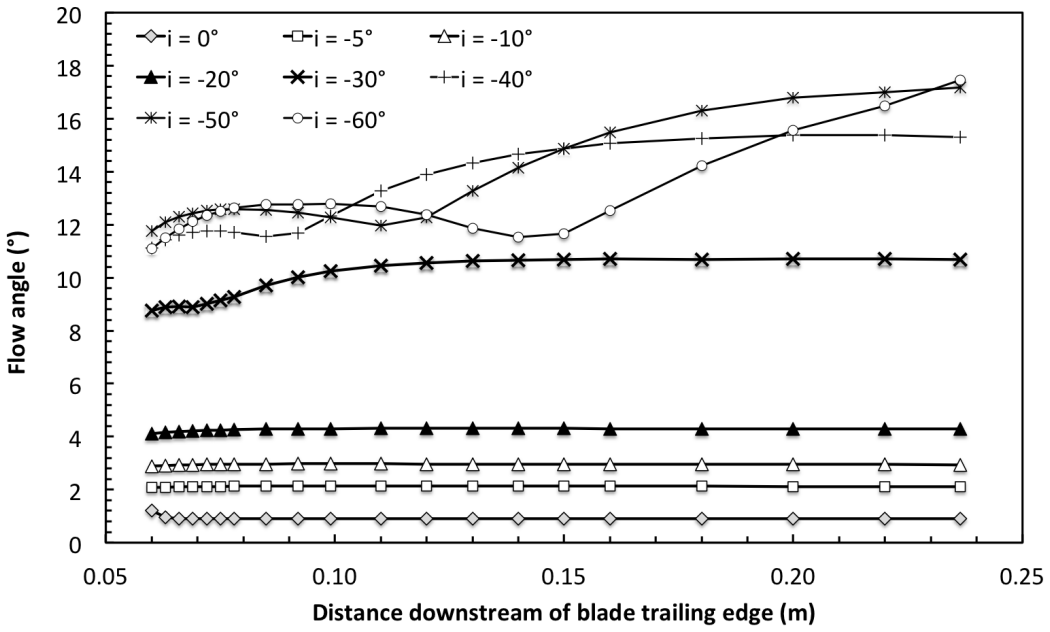

Figure 3.36: Velocity averaged flow angle measured at different positions downstream of the blade at 0° stagger (ξ) for different incidence angles (i = 0° to -60°) and solidity ($\frac{s}{c}$) 1.5 [15]

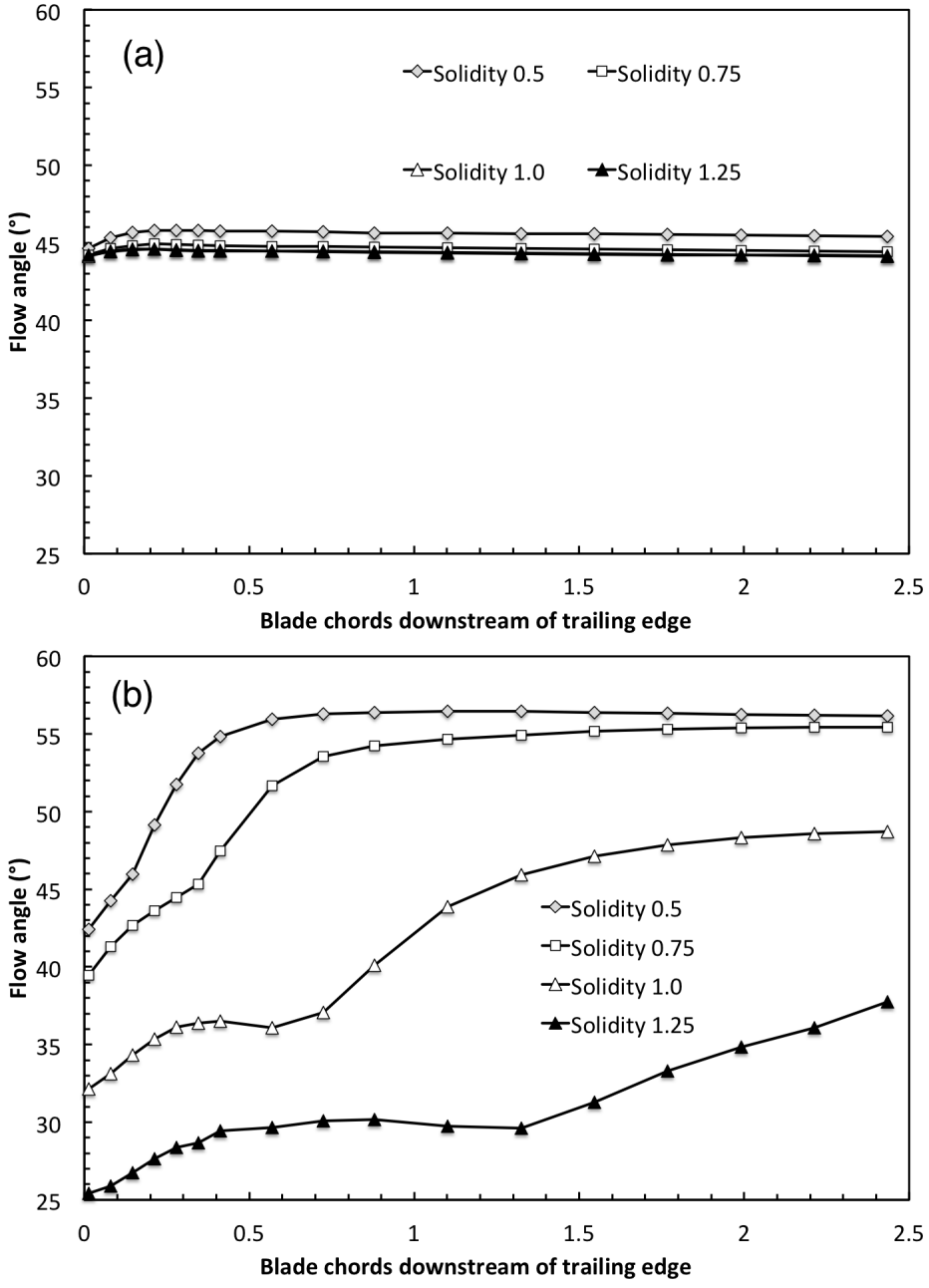

Figure 3.37: Influence of solidity ($\frac{s}{c}$ = 0.5, 0.75, 1.0 and 1.25) for incidence (a) i = -10° and (b) i = -50° incidence, on the flow angle (α_2) at different positions downstream

3.3.3 Estimation of blade coefficients in highly separated flows

The compressor code developed depends on the blade aerodynamic coefficients C_p and C_f to estimate the total pressure loss across it and the torque it produces. A good estimate of this value for each blade as a function of its operating condition (incidence (i), solidity ($\frac{s}{c}$) and stagger (ξ)) is therefore very important.

Due to the complex and turbulent flow at high negative incidence, it is difficult to extract a good representative value for the coefficients (C_p, C_f, C_d, C_l) since these change with the distance downstream as the flow angle changes. One therefore has to take measurements at various positions downstream of the blade until the position where the flow has stabilised is identified. However, since this may be a fair distance downstream (more than 3 chords), the additional viscous losses due to the cascade walls is included with the static pressure coefficient. An alternative methodology is proposed based on measuring the force experienced by the blade. The static pressure (C_p) and tangential force (C_f) coefficients can be expressed in terms of the axial and tangential forces acting on the blade, as defined in Eqns. (3.17) and (3.18), according to notations in Fig. 3.14.

$$C_p = \frac{X}{\frac{1}{2}\rho c_x^2} \tag{3.17}$$

$$C_f = \frac{Y}{\frac{1}{2}\rho c_x^2} \tag{3.18}$$

where X and Y are respectively the axial and tangential force per unit length.

By measuring the forces on the blade, the coefficients can be easily reverse engineered if the density and average axial velocity are known. The result is a unique value for the coefficients which is independent of the position at which measurements are taken and that captures the actual characteristics of the blade assuming a fully mixed out flow. The axial and tangential forces were extracted from the numerical simulations using a polyline around the blade at midspan to extract the force per unit length directly. The results are summarised in Figs. 3.38 and 3.39. For the tangential force coefficient (C_f)

it is evident how solidity plays a significant role on the downstream flow characteristics. For low solidity, there is very little difference between the values of C_f for one and two chords downstream and for the mixed out solution (forces). This indicates that the flow stabilises very quickly at less than one chord downstream of the blade. Similar behaviour is observed for solidity 1.0, where however there is some difference starting at an incidence of -30°. This would indicate that as the solidity increases, the flow takes longer to stabilise and large flow separations are induced at a lower negative incidence.

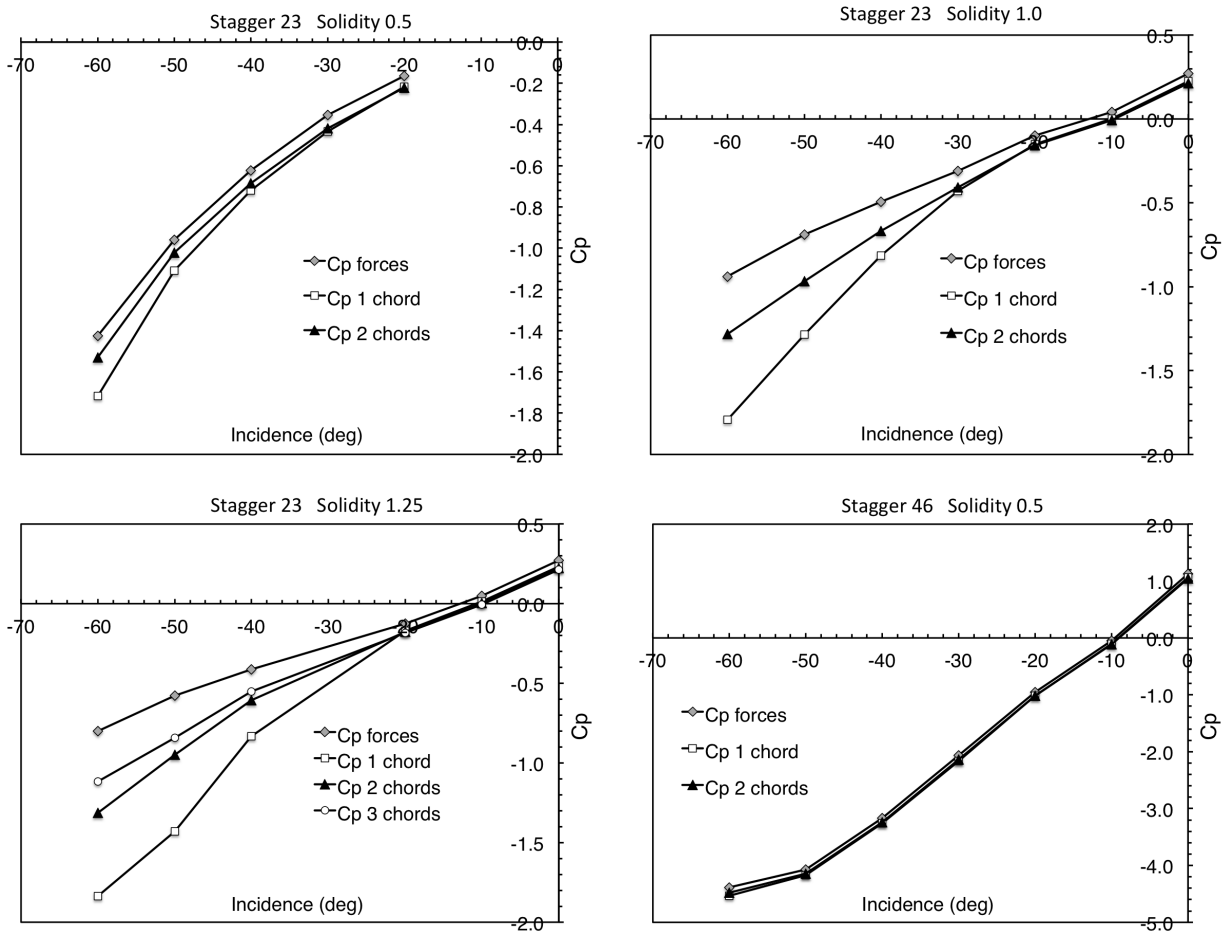

Figure 3.38: Comparison of static pressure rise coefficient (C_p) derived from the axial force and from the flow at one, two and three chords downstream for flow inlet Mach 0.1, various stagger angles (ξ) and solidities ($\frac{s}{c}$)

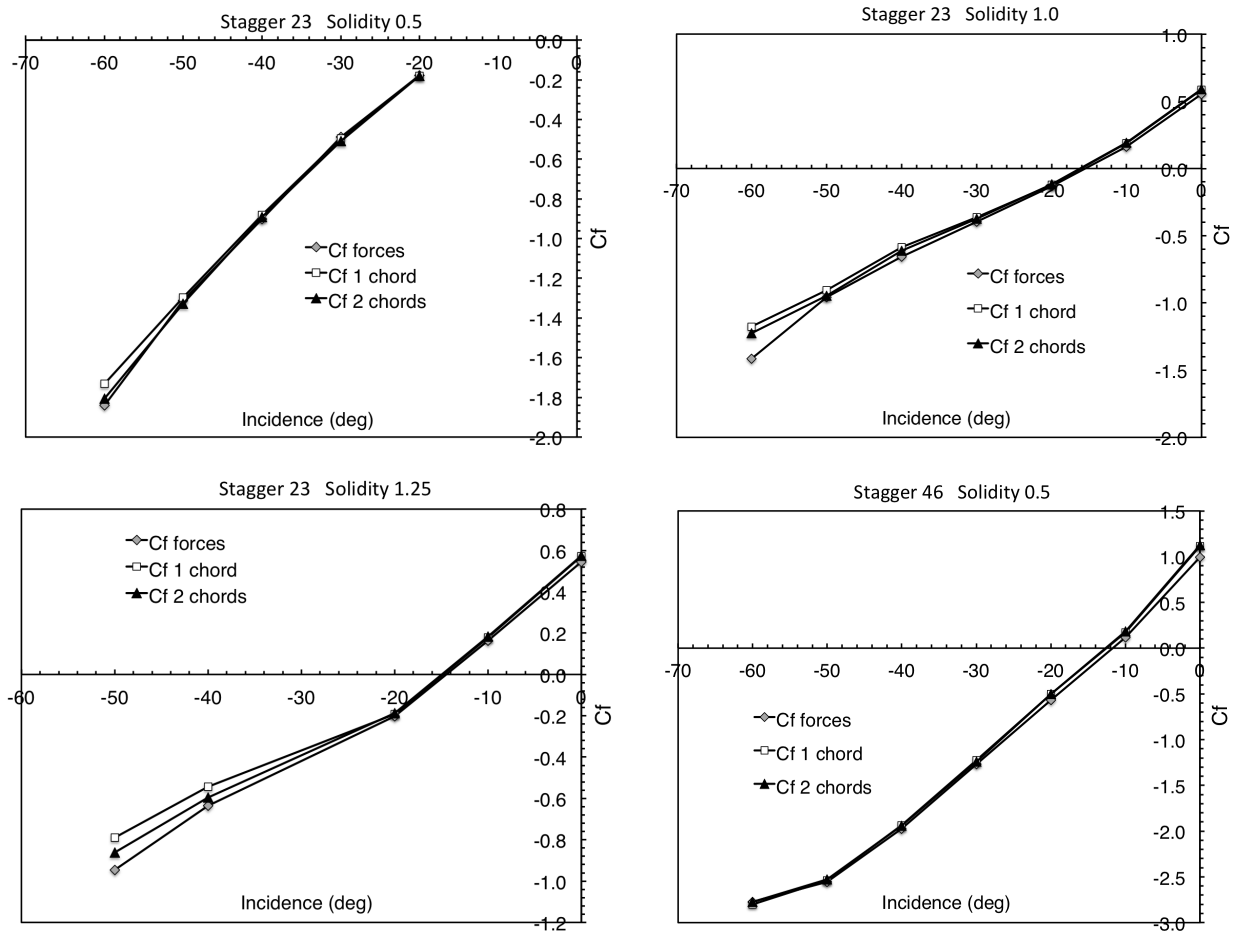

Figure 3.39: Comparison of tangential force coefficient (C_f) derived from the tangential force and from the flow at one and two chords downstream for flow inlet Mach 0.1, various stagger angles (ξ) and solidities ($\frac{s}{c}$)

The results for solidity ($\frac{s}{c}$) of 1.25 confirm this observation. The results measured at two chords downstream are closer to the fully mixed out solution. However there is still some difference at the most negative incidences, indicating that the flow actually requires more than two chords downstream to reach the stable condition. Again, the incidence where the results diverge is lower due to the higher solidity, this time starting at -20°.

In retrospect, this behaviour is expected since by increasing the solidity, the flow is relatively unrestricted, whereas with a low solidity the flow is forced to follow a fixed path, thereby stabilising very quickly and is less prone to changes in incidence. Changing the solidity from 0.5 to 1.25 results in the flow stabilising from a distance less than one chord downstream, to requiring more than two chords.

The behaviour is similar for the static pressure coefficient (C_p). At low solidity, the difference between the three measurements taken is much smaller compared to the higher solidities.

3.3.4 Flow deviation at high negative incidence

Flow deviation is defined as the difference between the blade's metal outlet angle and the angle which the flow takes when leaving the blade's trailing edge (as given in Eqn. (3.19)). This discrepancy is mostly a potential flow effect as explained in Cumpsty [19].

$$\alpha_2 = \delta + \beta_2 \tag{3.19}$$

where α_2 is the outlet flow angle, β_2 is the blade metal outlet angle, and δ is the flow deviation, as annotated in Fig. 3.13

Several correlations for predicting the flow deviation were derived over the years. Carter's [62] rule (Eqn. (3.20)), based on the Constant's [63] work, is one of the most popular correlations for design point deviation calculations. Other variants are given by Howell [3] and McKenzie [64]. A review is found in Larcher [15]. Carter's rule is given as:

$$\delta^*_{Carter} = m\theta\sqrt{\frac{s}{c}} \tag{3.20}$$

where θ is the blade camber, s/c is the solidity, and the value of m depends on the shape of the camber line and the blade setting, as outlined in Dixon [7] and defined using Eqn. (3.21).

$$m = 0.23(2a/c)^2 + \alpha^*_2/500 \tag{3.21}$$

where a/c is the position of maximum camber, and α^*_2 is the design point outlet flow angle

A comparison between different flow deviation (δ) correlations and experimental results is given in McKenzie [64], indicating that for solidities ($\frac{s}{c}$) less than 1.5, Carter's rule gives the lowest deviation angle, with the other results being up to double that amount. These equations are however inaccurate for off-design conditions since the blade's behaviour is very different. The effect of this inaccuracy on the performance solver is through the calculation of the incidence angle on the blade downstream, which in turn is used to estimate the blade coefficients C_p and C_f. Cetin et al [65] propose a modified version of Carter's

rule (Eqn. (3.22)), which generally tends to align better with experimental data.

$$\delta^* = -1.099379 + 3.0186(\delta^*_{Carter}) - 0.1988(\delta^*_{Carter})^2 \tag{3.22}$$

Various authors have adapted or used such equations, of which Al-Daini [66], Templalexis et al [67] and Boyer [68] were analysed. A number of off-design deviation models are also available, however these are based on stalled blade studies, i.e. highly positive incidences. Creveling and Carmody [17] propose the relationship given in Eqn. (3.23), where the first parameter is a polynomial function of the second as shown in Fig. 3.40. Whilst for both highly negative and highly positive incidences the flow will be so highly separated that the shape of the blade will be of little influence, the applicability of such correlations for sub-idle conditions was never verified.

$$\frac{\delta - \delta^*}{\epsilon_{ref}} = f\left(\frac{i - i^*}{\epsilon_{ref}}\right) \tag{3.23}$$

where i is the angle of incidence, i^* is the angle of incidence at design point, and ϵ_{ref} is the reference deflection, as defined in Eqn. (3.24)

$$\epsilon_{ref} = (\beta_1 + i^*) - (\beta_2 + \delta^*) \tag{3.24}$$

where β_1 and β_2 are the inlet and outlet blade metal angles, as illustrated in Fig. 3.13

In an attempt to come up with an off-design flow deviation model for blades at highly negative incidence ($i \leq -30°$), the simulations run in section 3.3.3 were analysed using Creveling and Carmody's [17] correlation. Since the flow changes direction with the distance downstream, the deviation angle was measured through the tangential force by reverse engineering the outlet angle through Eqn. (3.8). This gives the flow deviation of the fully mixed-out solution. As shown in Figs. 3.41 and 3.42, the flow behaves according to the correlation. A third order polynomial fit was found to capture well the deviation parameter from which the constants, tabulated in Table 3.2, were derived.

$$\frac{\delta - \delta^*}{\epsilon_{ref}} = a\left(\frac{i - i^*}{\epsilon_{ref}}\right)^3 + b\left(\frac{i - i^*}{\epsilon_{ref}}\right)^2 + c\left(\frac{i - i^*}{\epsilon_{ref}}\right) + d \tag{3.25}$$

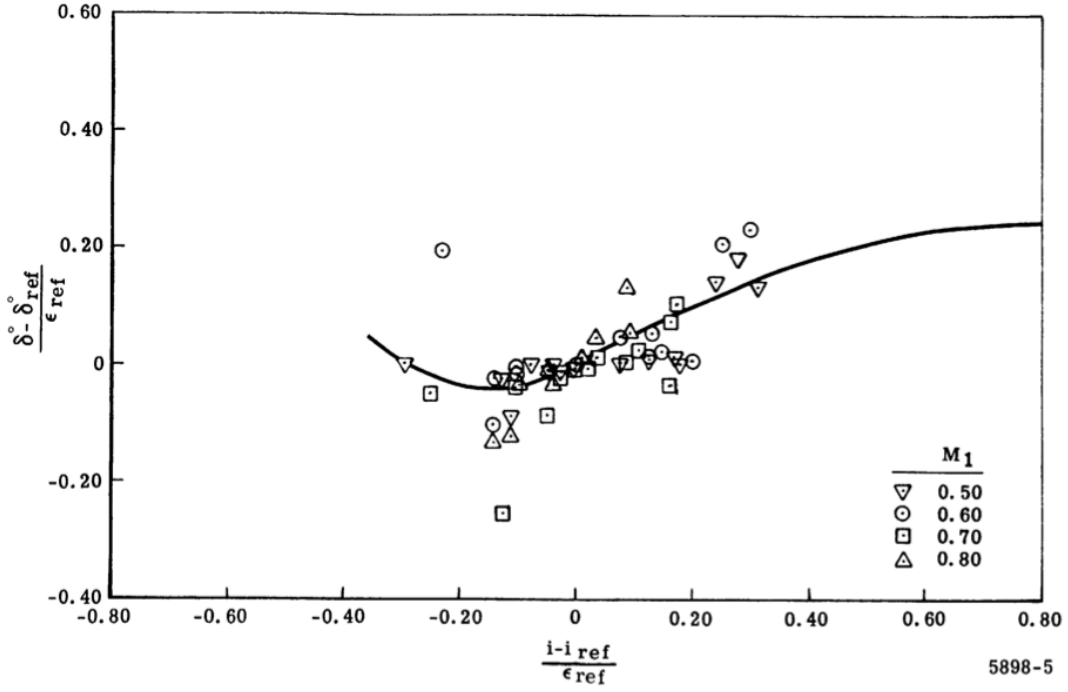

Figure 3.40: Creveling and Carmody's [17] off-design flow deviation correlation

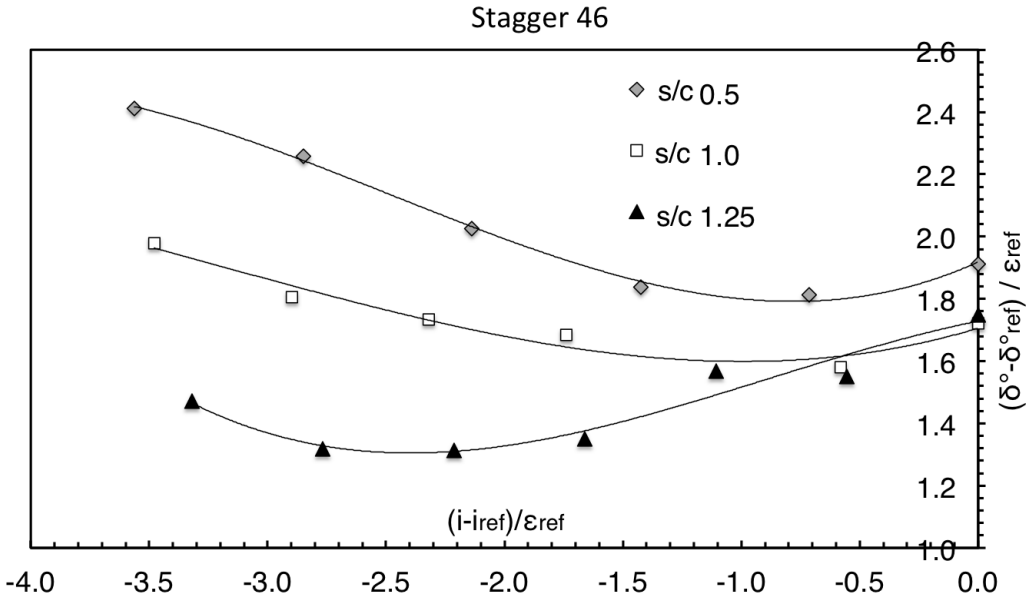

Figure 3.41: Flow deviation for different staggers (ξ) and solidities ($\frac{s}{c}$) using Creveling and Carmody's [17] relationship [18]

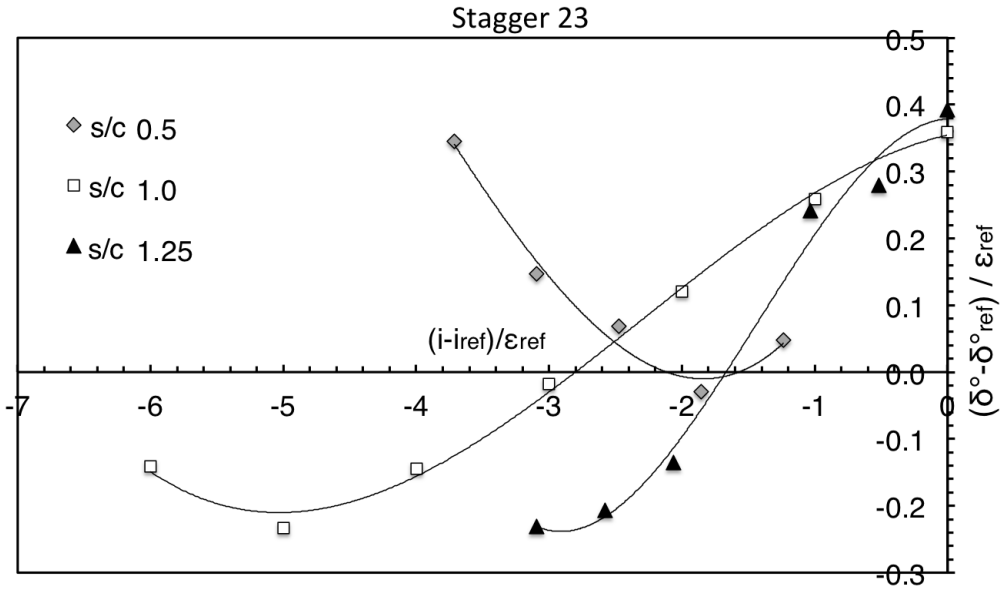

Figure 3.42: Flow deviation for different staggers (ξ) and solidities ($\frac{s}{c}$) using Creveling and Carmody's [17] relationship [18]

Stagger (ξ)	Solidity ($\frac{s}{c}$)	a	b	c	d
	0.5	0.019	0.24	0.6898	0.565
23	1.0	-0.01	-0.0492	0.0443	0.3544
	1.25	-0.05	-0.02112	0.0106	0.3787
	0.5	0.035	0.2603	0.3434	0.2798
46	1.0	0.014	0.1368	0.2296	0.3725
	1.25	-0.03	-0.0919	0.1548	0.4556

Table 3.2: Polynomial constants for Creveling and Carmody's [17] correlation applied to highly negative incidence flow

3.3.5 Blockage due to flow separation

The previous version of the compressor sub-idle map generation method does not consider the choked region of the zero-speed line. It also does not take into account the variation in flow effective area for different operating conditions. Preliminary studies, shown in Fig. 3.43 and 3.44, indicated that this parameter changes significantly and can lead to choking of the rear compressor stages at low-speed high flow conditions.

The axial velocity for the -60° incidence case could be twice as high as for the 0° case, depending on the blade geometry. In reality it is unlikely that a locked compressor will ever choke during any engine operation. However identifying the zero-speed choking point can help in the interpolation process, serving as an anchor that can be related to the above-idle choking points.

Introduction and Objective

In order to calculate the choking mass flow of a compressor at locked-rotor conditions, the smallest flow area has to be identified. The smallest metal area will be within the last downstream blade row. However since the flow is dominated by large separated and recirculation regions, the actual effective flow area will be smaller than the physical area. If this reduction in effective area is not taken into account, the choking mass flow of the locked-rotor compressor is overestimated.

The objective of the study presented in this section was to map the change in flow effective area within the blade channel, as a function of the operating condition and the compressor geometry. Different solidities ($\frac{s}{c}$), stagger (ξ) and incidence (i) angles, and air mass flow rates, were run to create a database of effective area ratios that can be used by the compressor code to more accurately predict the zero-speed choking point. The numerical simulations were run and post-processed with the help of Enric Illana [69], a Thermal Power MSc student.

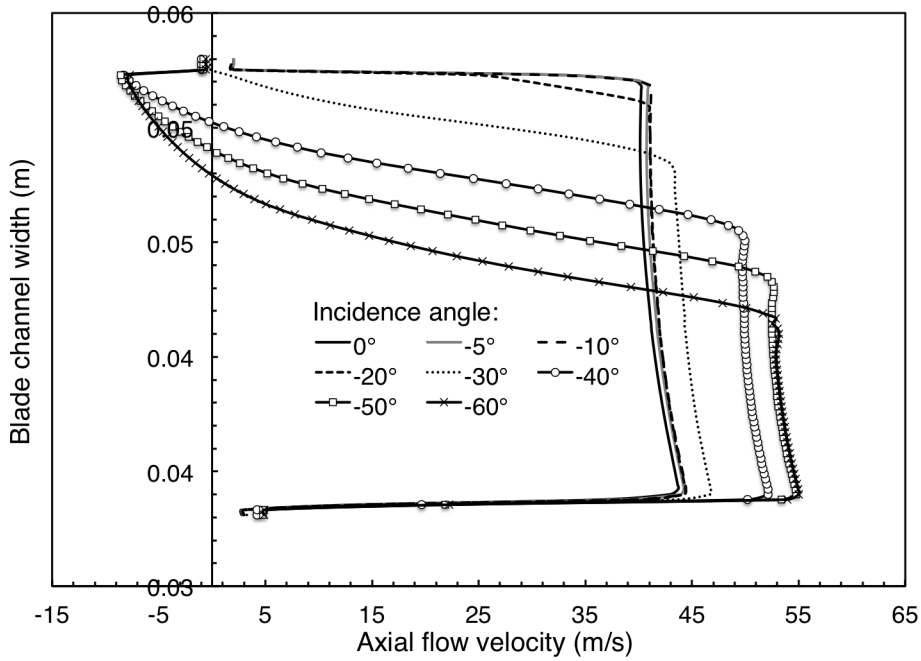

Figure 3.43: Axial velocity profile across blade channel at inlet Mach 0.1 and negative incidence (i) angles from $i = 0°$ to $-60°$

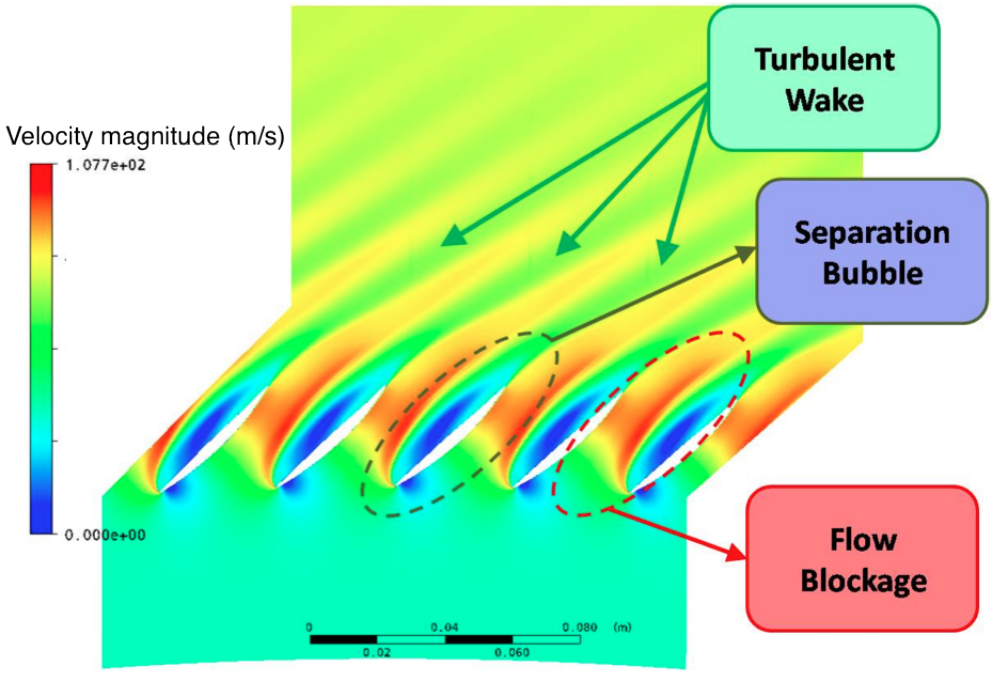

Figure 3.44: Velocity magnitude contours showing the velocity defect due to the flow separation, resulting in a reduction of flow effective area [12]

Definition of blockage

In the simulations undertaken, three main types of losses can be identified: profile, end-wall and shock losses. These losses have an impact on the cascade performance as they generate an increase in entropy. However, according to Suder [70], only the profile and end-wall losses are considered as 'blockage related losses' because they generate regions of substantial velocity defect such as boundary layers or recirculation bubbles. The term 'blockage' is generally related to the reduction of the free stream effective area resulting from the existence of such regions.

The definition for effective area, relative to the geometrical one, is given in Eqn. (3.26). A procedure to estimate the blockage in a compressor blade row is described in [70], which consists of obtaining density and axial velocity distributions at an axial plane, in the radial and pitch-wise directions. The parameters ρ_e and u_e are determined from such distributions by removing the regions of low momentum, which are delimited by regions of high velocity gradient, followed by interpolation at the wake zone and extrapolation at the end-walls. In this way, the effective area can be estimated by integrating Eqn. (3.26) numerically. This procedure is however arduous to undertake and is not practical when a large amount of simulations have to be evaluated. Furthermore, the effective area depends on the axial position where measurements are taken and therefore is not necessarily the minimum effective area of the blade channel.

$$\frac{A_{eff}}{A_{geom}} = (1 - B) = \frac{1}{A_{geom}} \int \int \frac{\rho u}{(\rho_{eff} u_{eff})} dA \tag{3.26}$$

where B is the blockage, and ρ_{eff} and u_{eff} are respectively the density and axial velocity at the plane being investigated

Another way of estimating the effective area is by using the flow parameter. To do so an axial plane is considered, at which averaged values of the total pressure and Mach number are estimated. As the flow parameter (Q) depends only on the Mach number, by measuring the mass flow through the cascade, the effective flow area can be calculated (assuming constant total temperature). In this case however, the effective area cannot

be related to the geometrical area since by definition of the flow parameter, the flow area is perpendicular to the streamlines. Thus, the effective flow area is related to the one at inlet by Eqn. (3.27).

$$\frac{A_{eff}}{A_{eff,in}} = \frac{Q_{in}}{Q}\frac{\sqrt{\text{Total temperature ratio}}}{\text{Total pressure ratio}} \tag{3.27}$$

Taking measurements on a plane which are not perpendicular to the direction of the streamlines may introduce errors in the value of the effective area calculated, especially in the cases of cascades with high stagger angles. However, it is not practical to obtain the plane perpendicular to the flow direction because it changes with the cascade geometry, the incidence and the ΔP. Furthermore, due to the translational periodicity, it is difficult to define such a plane when conducting the post-processing. Figure 3.45 illustrates where the measurement plane should be placed and the actual plane considered. The minimum effective area, using Eqn. (3.27), is located in the position where the product of the total pressure and the Q parameter is maximum. In order to determine its position, a sweep of the passage was conducted.

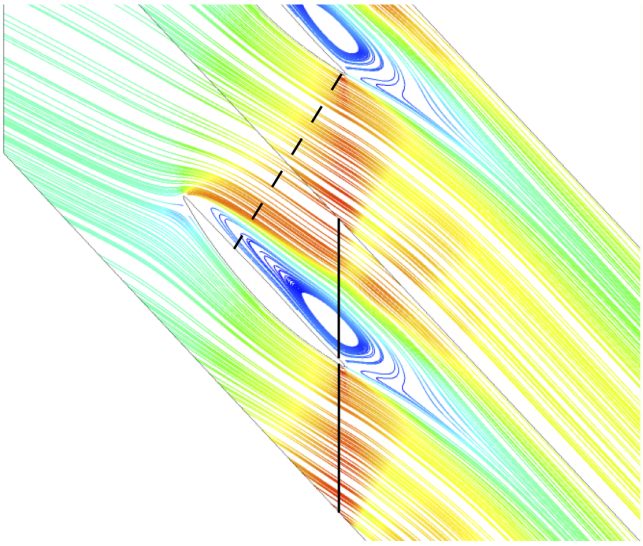

Figure 3.45: Ideal (dashed line) and actual (solid line) plane to get the effective area

Other work on flow blockage due to stalled flow can be found in Weber et al [71], Khalid et al [72] and Khalid [73]. A detailed review is also given in Illana [69].

Numerical model setup

The domain is based on the one used for the flow separation studies described in section 3.3.1 and the one validated by Zachos [5] and Rulke [12]. It consists of a 3D blade with a uniform 2D profile standing one chord downstream of the inlet, with the outlet at three chords downstream to allow the solution to stabilise and improve convergence. The domain is translationally periodic. The meshing strategy and the use of the $k-\omega$ SST (Shear Stress Transport) turbulence model was based on the validation against experimental cascade tests from Zachos [5] and Rulke [12] described in section 3.2.4.

An O-grid around the blade was set to resolve the boundary layer whilst the rest of the domain is hexahedral mesh structure. This resulted in a value of $y^+ < 2$ for the blade surface and a total of 4 million cells within the whole domain. A total inlet pressure and outlet static pressure boundary condition configuration was used since neither the mass flow, nor the maximum inlet Mach number were known. The incidence angle on the blade was set by imposing the inlet flow direction vector as shown in Fig. 3.46 which illustrates a plan view of the 3D model. A constant total temperature of 285 K was used throughout. The aim of the simulations was to achieve choking conditions by increasing the inlet total pressure until the choking inlet Mach number was reached, simulating a blowdown rig.

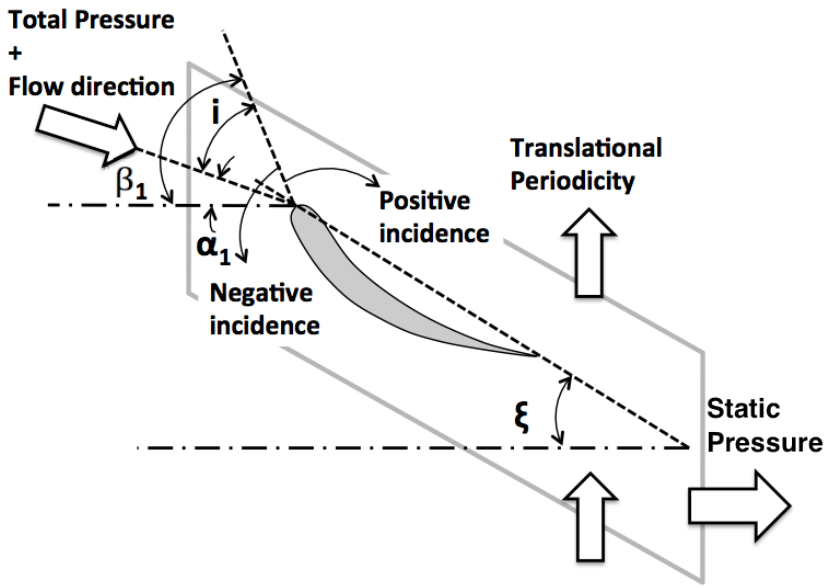

Figure 3.46: Boundary conditions imposed on the numerical domain

The simulations were run with ANSYS CFX, with a pressure-based implicit scheme and higher resolution scheme. The ideal gas law was used for the fluid, whilst viscosity was set using Sutherland's formula with reference viscosity at 18.27μPas at a reference temperature of 291.15 K with Sutherland's constant as 120 K, which are values typically used for air.

Simulations were run as steady state cases. Zachos et al [10], as was explained in further detail in section 3.2.4, confirm that under such conditions, the error between steady and time-averaged unsteady simulations is negligible, probably due to the fact that the unsteadiness is highly periodic. In addition, the main interest of this study is the evaluation of the blade characteristics at high incidence angle, while the zooming into the unsteady flow structure and its analysis is an issue of secondary significance and outside the scope of the research.

Different models for a stagger (ξ) angle of 23° and 46° degrees were used. Each model was run at an incidence (i) of 0°, -10°, -20°, -30° and -60°. Different total pressure drops were required to choke the different models, depending on the level of separation. As with previous simulations, convergence criteria for the simulations were set to an RMS level of $1.0e^{-5}$ but RMS turbulent kinetic energy could only reach a minimum level of around $1.0e^{-4}$.

Results

The pressure loss characteristics of the half-stage studies were first analysed. A sample of the results is shown in Fig. 3.47. It is noticeable that the low negative incidences result in lower total pressure drops for the same non-dimensional mass flow. For a stagger angle of 23° and $Q = 0.02$, the total pressure ratio drops from 0.99 at i = -10°, to 0.91 at i = -60°. This is expected since at low negative incidences, the blade is still operating at an incidence not too far from design point and the flow is still attached to the blade. The zero-speed line is very shallow, but then chokes relatively quickly.

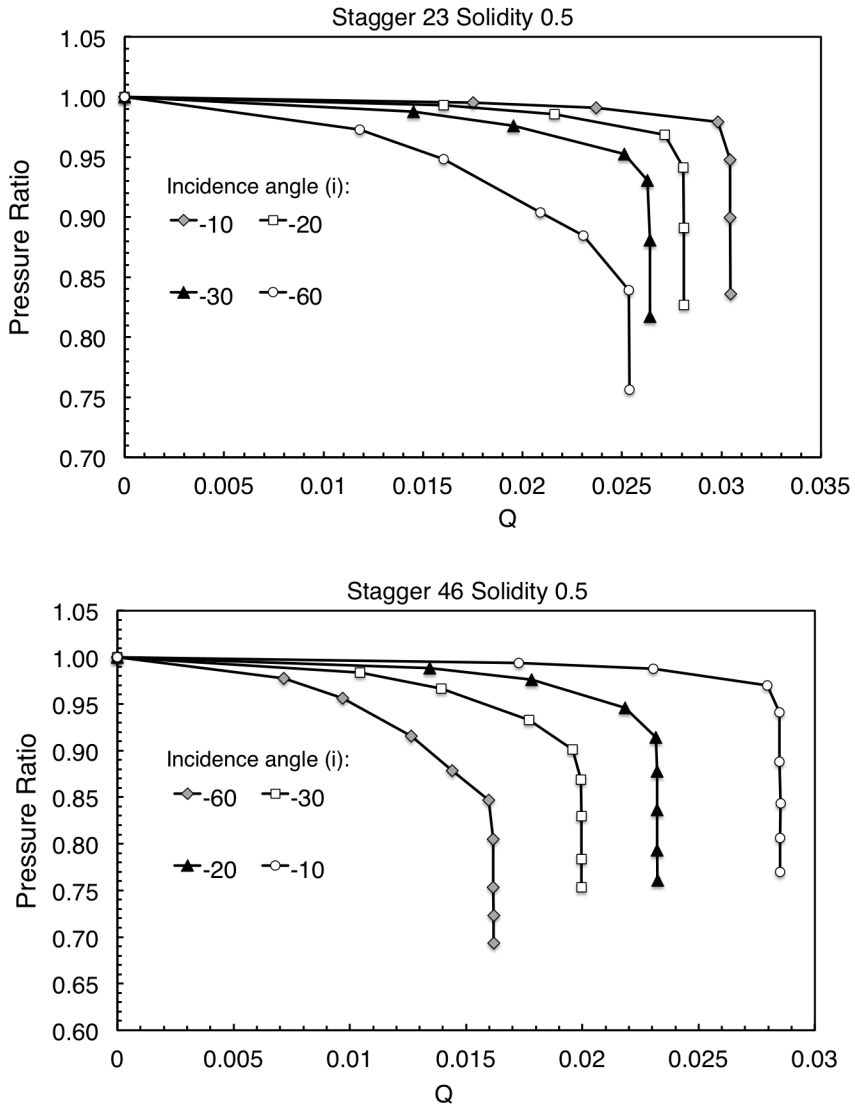

Figure 3.47: Cascade total pressure ratio (P_2/P_1) characteristics showing choking points for each incidence (i) run

As the incidence becomes more negative, the pressure losses increase due to the detachment of the flow from the blade surface, the region of recirculation caused by the high incidence, and the large wakes downstream of the trailing edge. However the transition to the choked condition is more gradual, probably dampened by the presence of the recirculation bubble on the blade's pressure surface. The effect of solidity ($\frac{s}{c}$) and stagger (ξ) is noticeable in Fig. 3.48 for a constant incidence (i) of -30°. High stagger angles with low solidity tend to choke the earliest and have the highest pressure losses, thereby resulting in a relatively steep zero-speed line. These trends are also observed in section 3.3.6 where the blade aerodynamic coefficients are analysed.

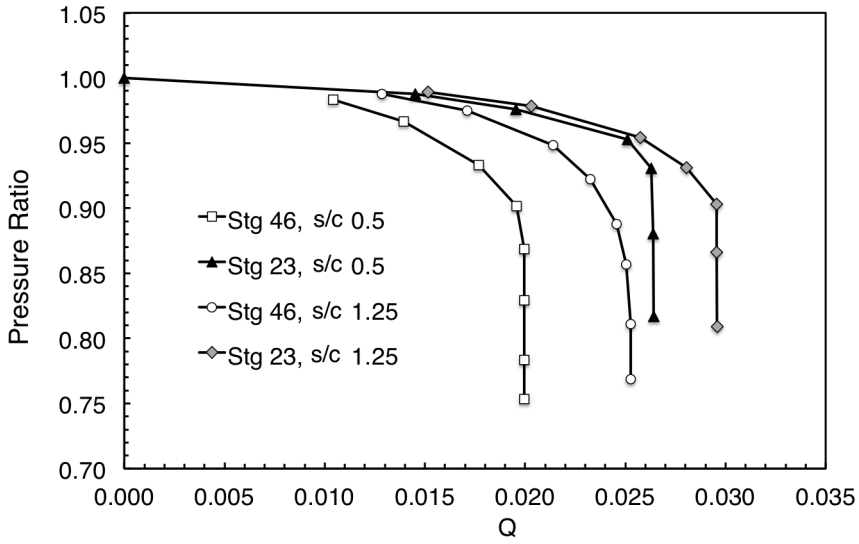

Figure 3.48: Effect of stagger (ξ) and solidity ($\frac{s}{c}$) on the blade total pressure ratio (P_2/P_1) characteristics at a constant incidence (i) of -30°

The change in flow effective area with incidence and total pressure drop for the two stagger angles analysed is shown in Fig. 3.49. Overall, the larger stagger has a smaller effective area, even at low negative incidence. This is probably due to the degree of overlap that higher stagger (ξ) angles have. In both cases of stagger, at low negative incidence the change in effective area with ΔP is very small, indicating that there is very little volume occupied by the separated flow. This is reasonable since the incidence is not negative enough for the flow to detach from the blade surface. As the incidence becomes more negative at low total pressure drops, the effective area decreases drastically, down to

values as low as 35% for stagger 46°. As the total pressure drop is increased, the effective area increases, indicating that the volume of separated region is decreasing and the flow is reattaching itself to the blade. This is confirmed by visualisations of the flow, shown in Figs. 3.50 - 3.52. For a stagger (ξ) of 46° and incidence (i) -60°, the effective area increases from 35% up to 48% when the total pressure drop across the half-stage is increased. For a stagger of 23°, the change is from 55% up to 73%.

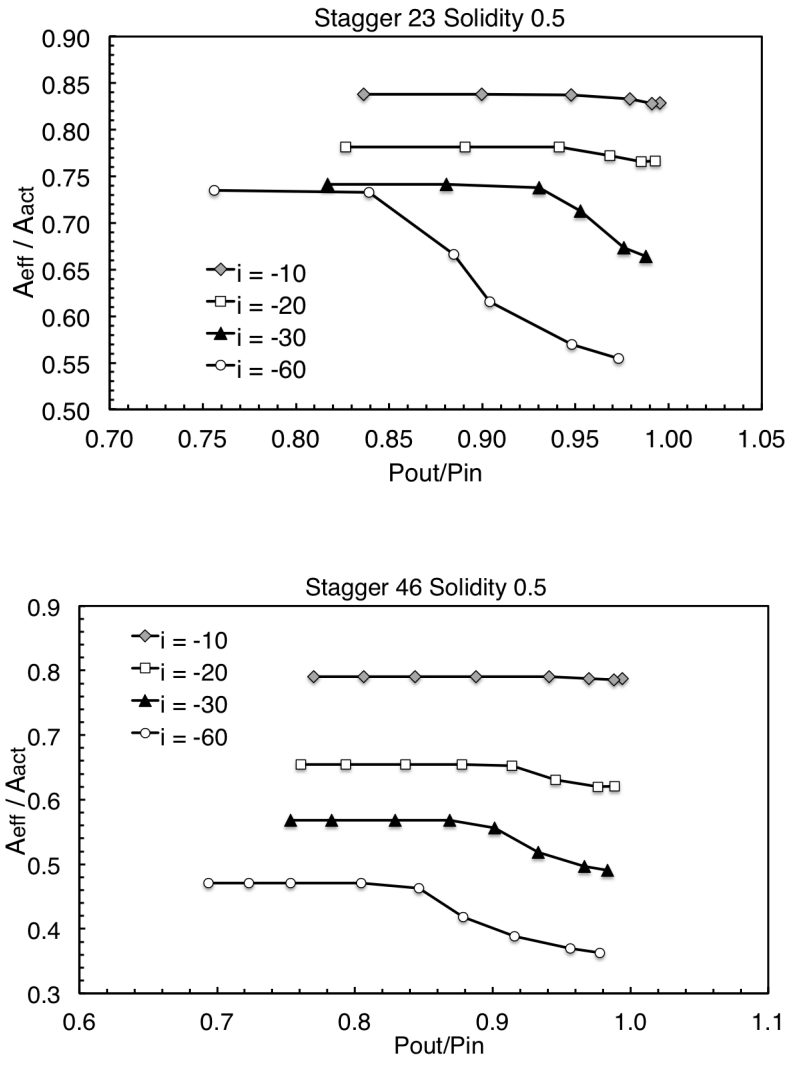

Figure 3.49: Flow effective (A_{eff}) relative to geometric area (A_{geom}) as a function of incidence angle (i) and total pressure ratio (P_2/P_1) across the numerical domain, for different blade geometrical characteristics - stagger (ξ) and solidity ($\frac{s}{c}$)

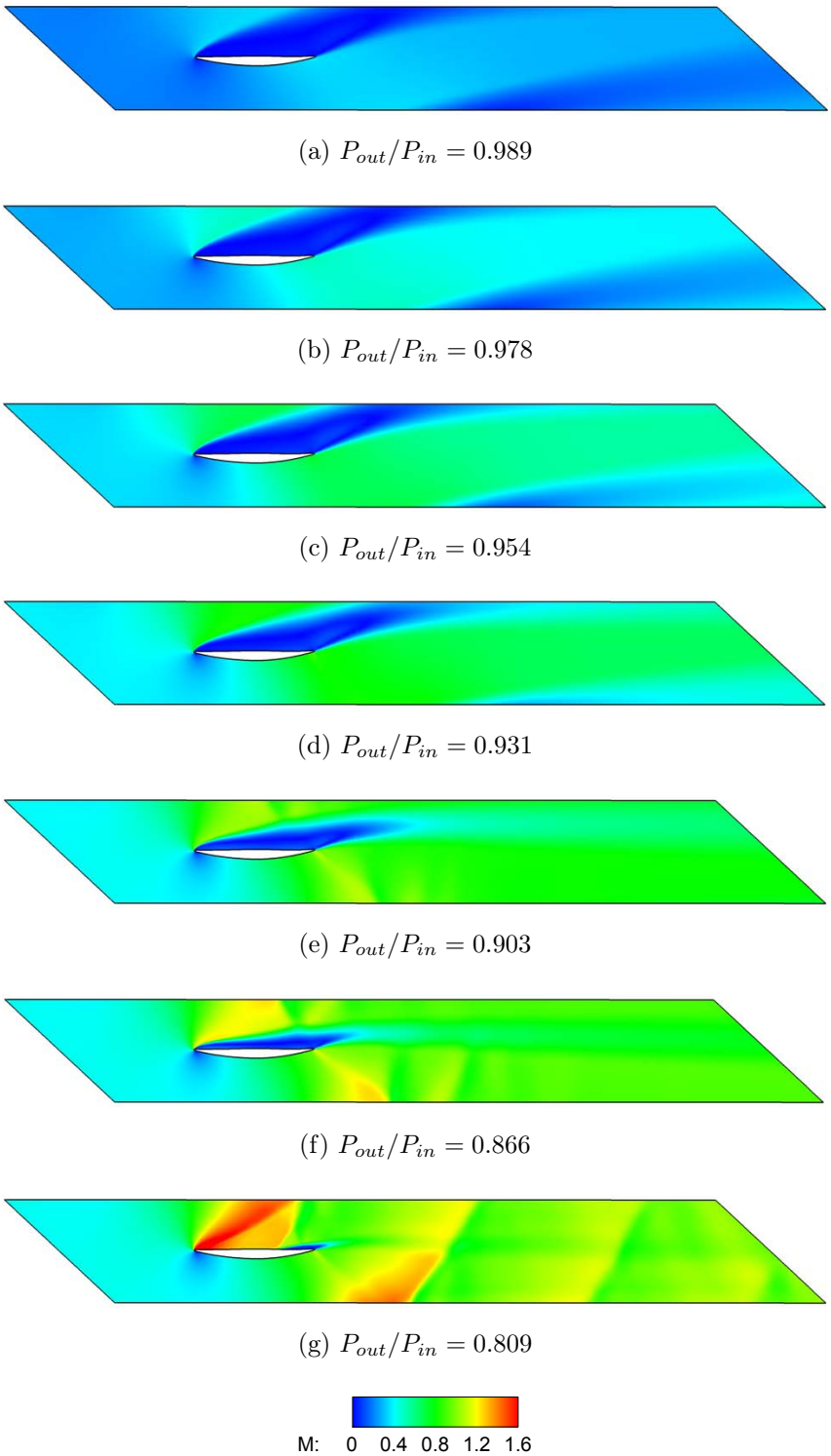

(a) $P_{out}/P_{in} = 0.989$

(b) $P_{out}/P_{in} = 0.978$

(c) $P_{out}/P_{in} = 0.954$

(d) $P_{out}/P_{in} = 0.931$

(e) $P_{out}/P_{in} = 0.903$

(f) $P_{out}/P_{in} = 0.866$

(g) $P_{out}/P_{in} = 0.809$

Figure 3.50: Mach number contours up to choking for incidence (i) $-30°$, solidity ($\frac{s}{c}$) 1.25, stagger (ξ) 46°

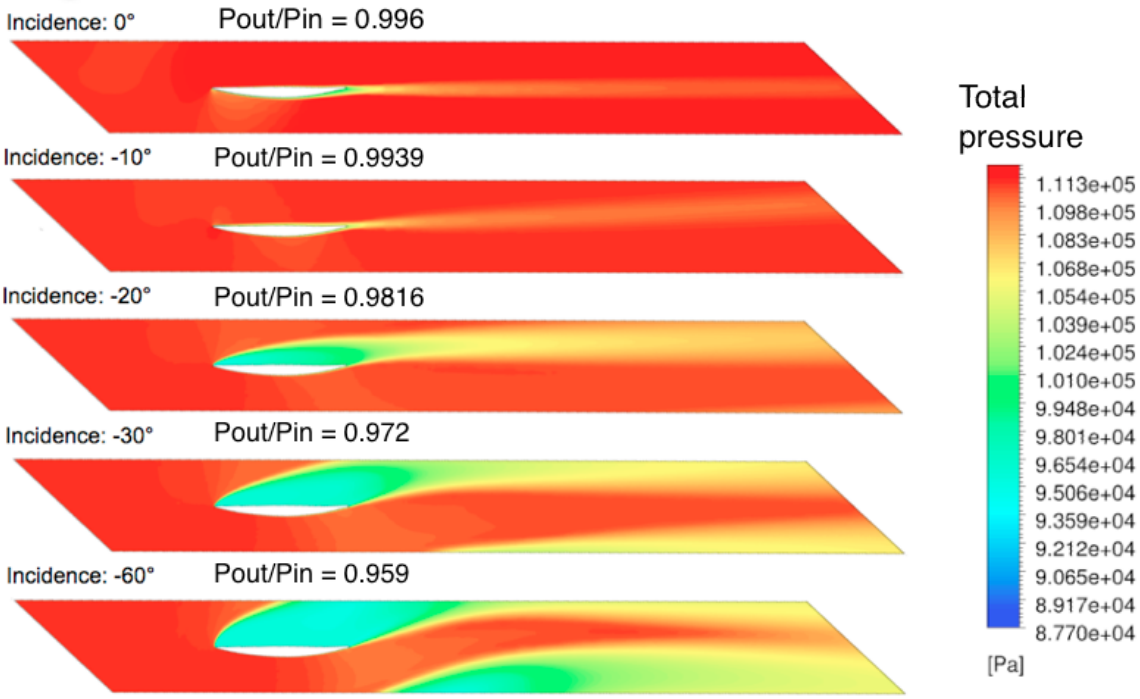

Figure 3.51: Total pressure for incidence angle (i); stagger (ξ) 46°, solidity ($\frac{s}{c}$) 1.0

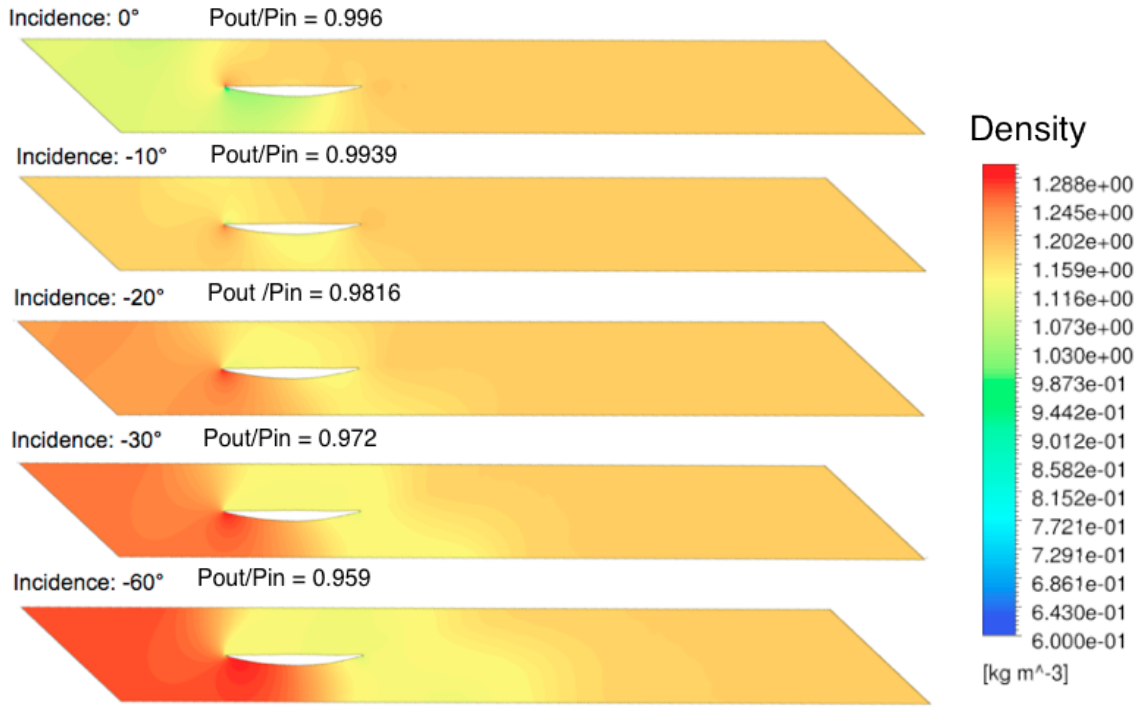

Figure 3.52: Density for incidence angle (i); stagger (ξ) 46°, solidity ($\frac{s}{c}$) 1.0

3.3.6 Blade aerodynamic coefficients at high Mach number

Introduction and Objective

Work done so far by previous researchers [5] [12] extracted the coefficients at an inlet Mach number of 0.1. Since at low flow Mach numbers the coefficients are fairly constant, the values extracted at this condition were used throughout the code. However the code has been updated to predict the compressor's choking point, and therefore this assumption is no longer valid, as shown in Fig. 3.53. In order to estimate more accurately the zero-speed characteristics close to the choking point, the coefficients at high inlet Mach numbers had to be extracted. The work was carried out with the help of Enric Illana [69], a Thermal Power MSc student. The same models as those used for the flow blockage study described in section 3.3.5 were used, including the variations in ΔP, incidence (i), stagger (ξ) and solidity ($\frac{s}{c}$). To calculate the aerodynamic coefficients, the methodology described in section 3.3.3 was used.

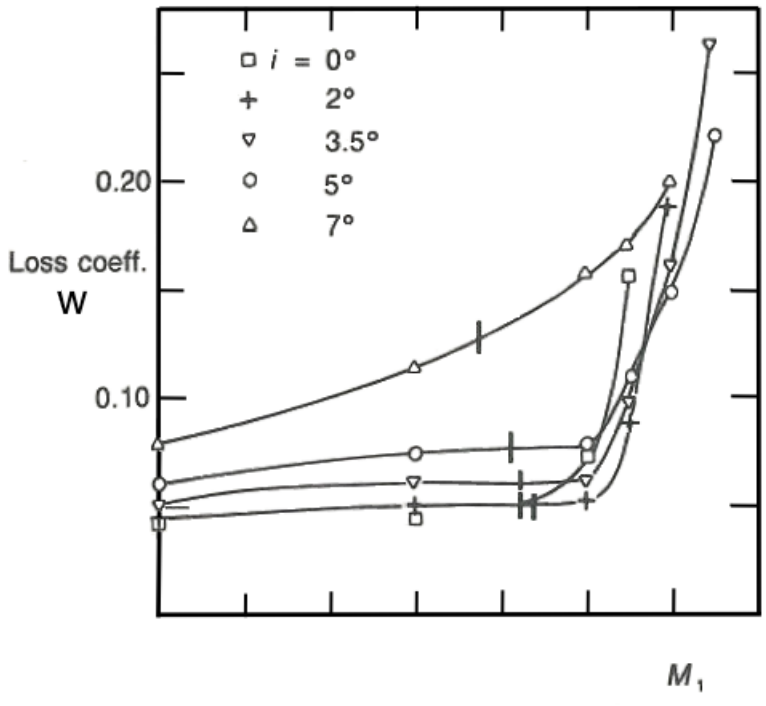

Figure 3.53: Total pressure loss coefficient (w) as a function of incidence (i) and flow Mach number [19]

Results

The static pressure (C_p) and tangential force (C_f) coefficients for a constant blade geometry but various incidence angles, are illustrated in Fig. 3.54 to highlight the effect of incidence. Results, are similar in principle to those in Fig. 3.53 where the lowest incidences have a flatter profile, followed by an increase in the coefficient. It is clear that especially for the highest negative incidences ($i \leq -30°$), coefficients cannot be assumed constant. As expected, the highest negative incidence ($i = -60°$) creates the largest pressure loss. The smaller negative incidences have a lower pressure loss since the size and magnitude of the separated flow on the pressure side of the blade is smaller.

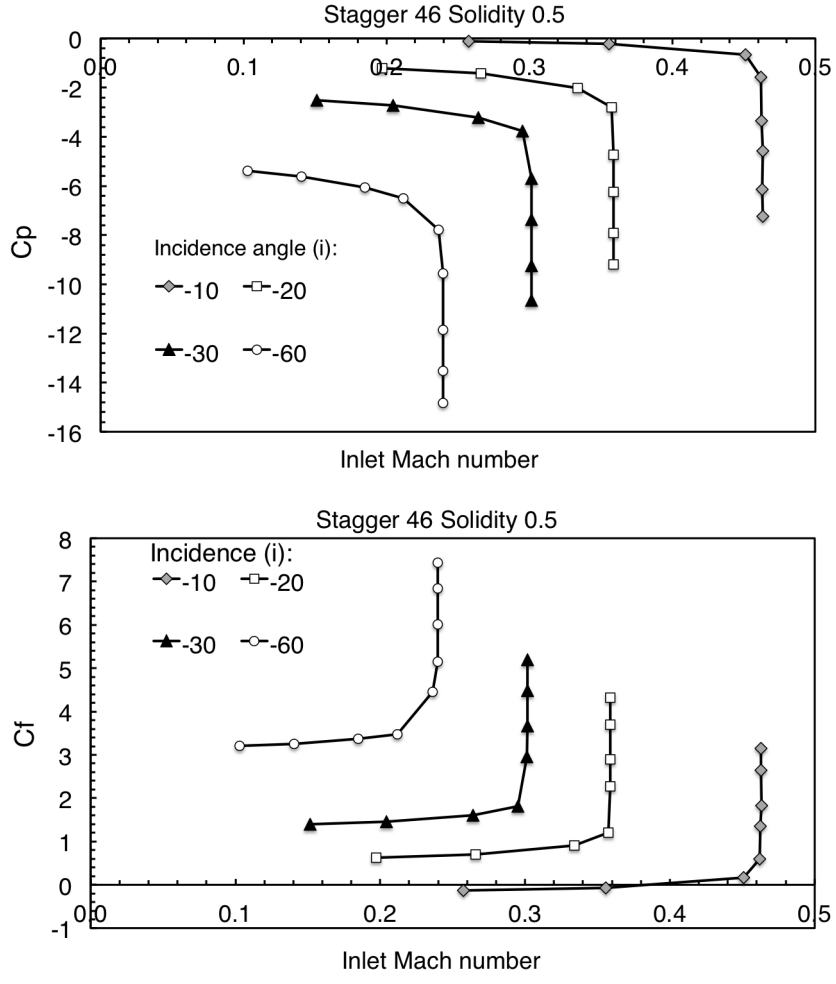

Figure 3.54: Blade static pressure (C_p) and tangential force (C_f) aerodynamic coefficients for stagger (ξ) 46° and solidity ($\frac{s}{c}$) 0.5 as a function of the incidence (i) angle and the inlet flow Mach number

Stagger (ξ) and solidity ($\frac{s}{c}$) have a large influence on the blade characteristics, as shown in Fig. 3.55. For the same solidity, when the stagger increases from 23° to 46°, the blade tends to choke at lower inlet Mach number. The value of C_p starts from a lower value than for the smaller stagger, even for low inlet Mach numbers. This indicates that the losses are greater at high stagger, even if the incidence angle on the blade is the same. In turn, the tangential force coefficient (C_f) is higher for the 46° stagger, suggesting that the flow turning angle is larger for the higher staggers.

Similar behaviour is noticeable when the solidity is increased. At low solidity, the half-stage chokes at a lower inlet Mach number and the C_p is more negative throughout the range of incidences run. However the difference in characteristics between solidities but for the same stagger (ξ), increase when the stagger increases. This is very noticeable in Fig. 3.55 where for stagger 23° the difference in characteristics between solidity 0.5 and 1.25 is very low, relative to those for stagger 46°.

Summarising, at these conditions, the pressure losses increase with stagger (ξ) and decrease with solidity ($\frac{s}{c}$). A compressor having blades of low stagger and high solidity would therefore have a shallower zero-speed line relative to one with high-stagger and low-solidity blades. In terms of torque, a compressor with high-stagger and low-solidity blading would impose the most torque on the shaft at zero-speed.

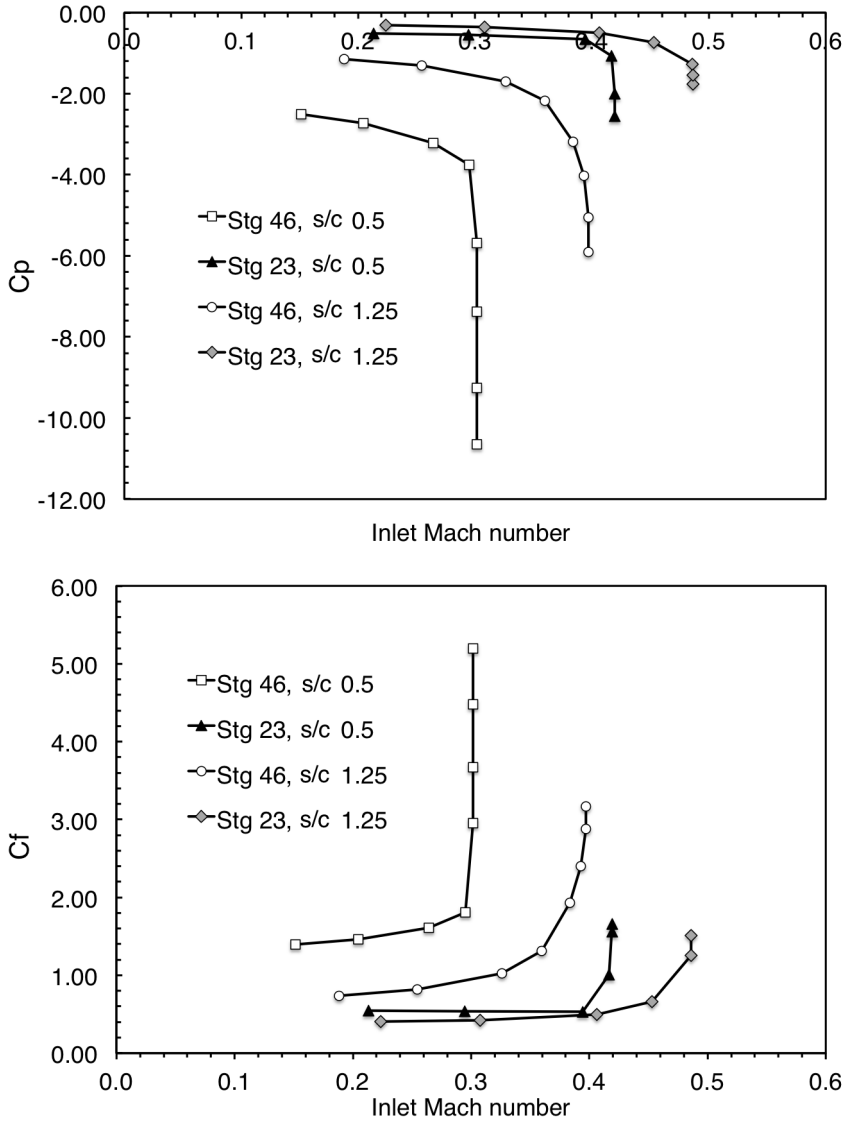

Figure 3.55: Effect of stagger (ξ) and solidity ($\frac{s}{c}$) on blade static pressure (C_p) and tangential force (C_f) aerodynamic coefficients for a constant incidence (i) of -30°

3.3.7 Validity of Blade Element Theory at high negative incidence

To verify whether using blade elements to represent a full 3D blade is applicable to high negative incidence cascade flows, the work undertaken by Rulke [12] was expanded to include more incidence angles, ranging from 0° to -60°. The same numerical models described in section 3.3.1 were used. The values of C_p, C_f, C_d and C_l were calculated from readings taken at two chords downstream of the blade at the tip (90%), midspan (50%) and hub (10%), using Eqns. (3.7) and (3.8).

The results shown in Fig. 3.56 give the averaged values across the entire blade length, comparing the 2D and 3D blade results. In general, the coefficients of the averaged 2D and 3D blade are significantly different, by up to 50% in certain cases. The major difference lies with C_d and C_p, both associated with the pressure loss. The trend is similar, but the absolute values are dissimilar and there does not seem to be a correlation or factor that can be added to the 2D characteristics to approximate the 3D blade's aerodynamic behaviour.

Similarly, comparing the total pressure loss coefficient shown in Fig. 3.57, again averaged across the entire blade length, it is clear how the 2D blade underestimates the total pressure loss across the blade row for the entire range of incidence angles run. Again this can be attributed to the three-dimensional, hub and tip effects, which as mentioned in Robbins [14], are not present in a 2D simulation. The measurements from the 2D simulation were taken at midspan, thus avoiding the end-wall effects resulting in the loss measured being only the 2D profile loss.

Concluding, it seems evident that the known limitations of the BET reduce it's effectiveness in representing a fully 3D blade at high negative incidence. Therefore, whilst the code was updated to use BET (see section 3.4.1) this must be used cautiously, keeping these limitations in mind.

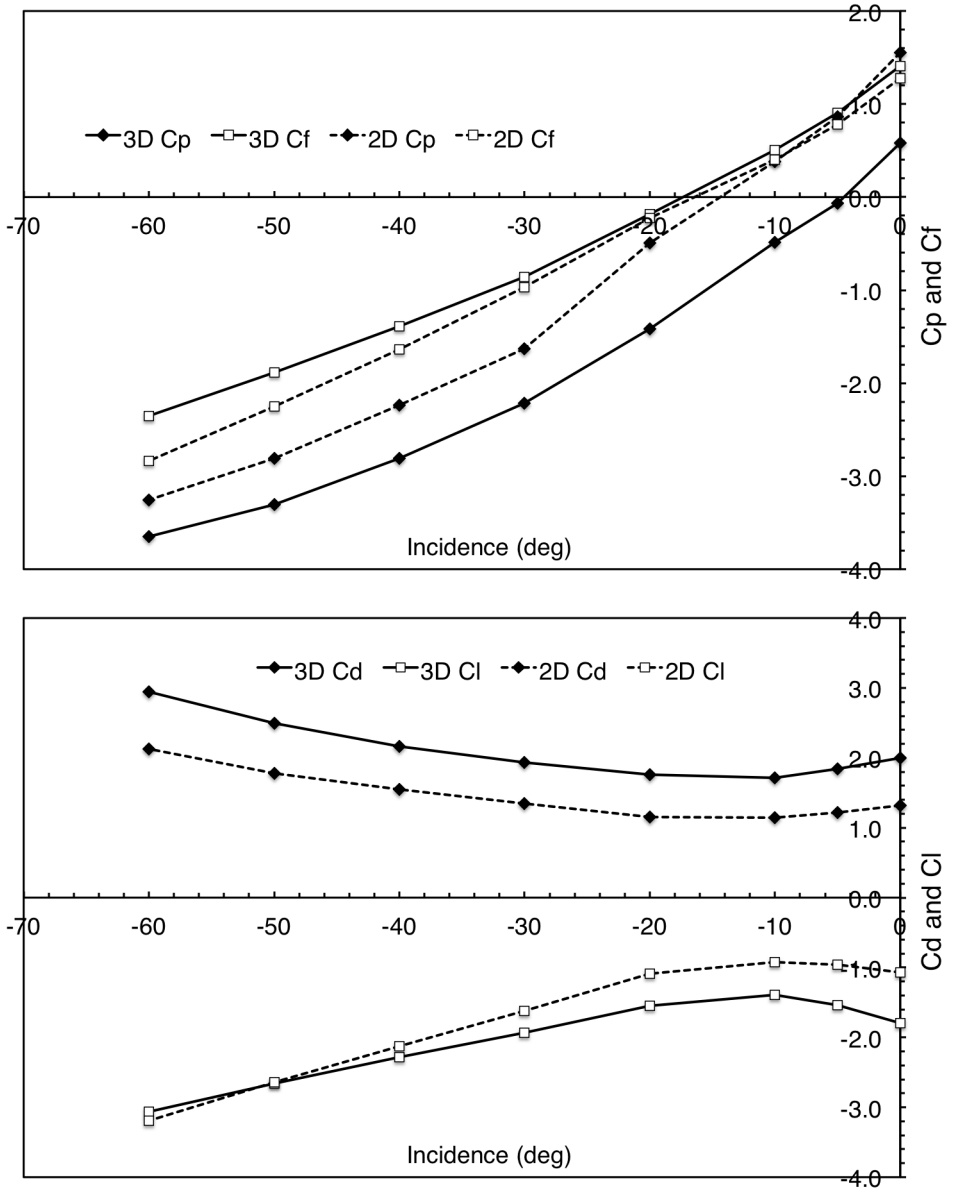

Figure 3.56: Averaged blade aerodynamic coefficients C_p, C_f, C_d and C_l for the 2D and 3D cases as a function of incidence (i)

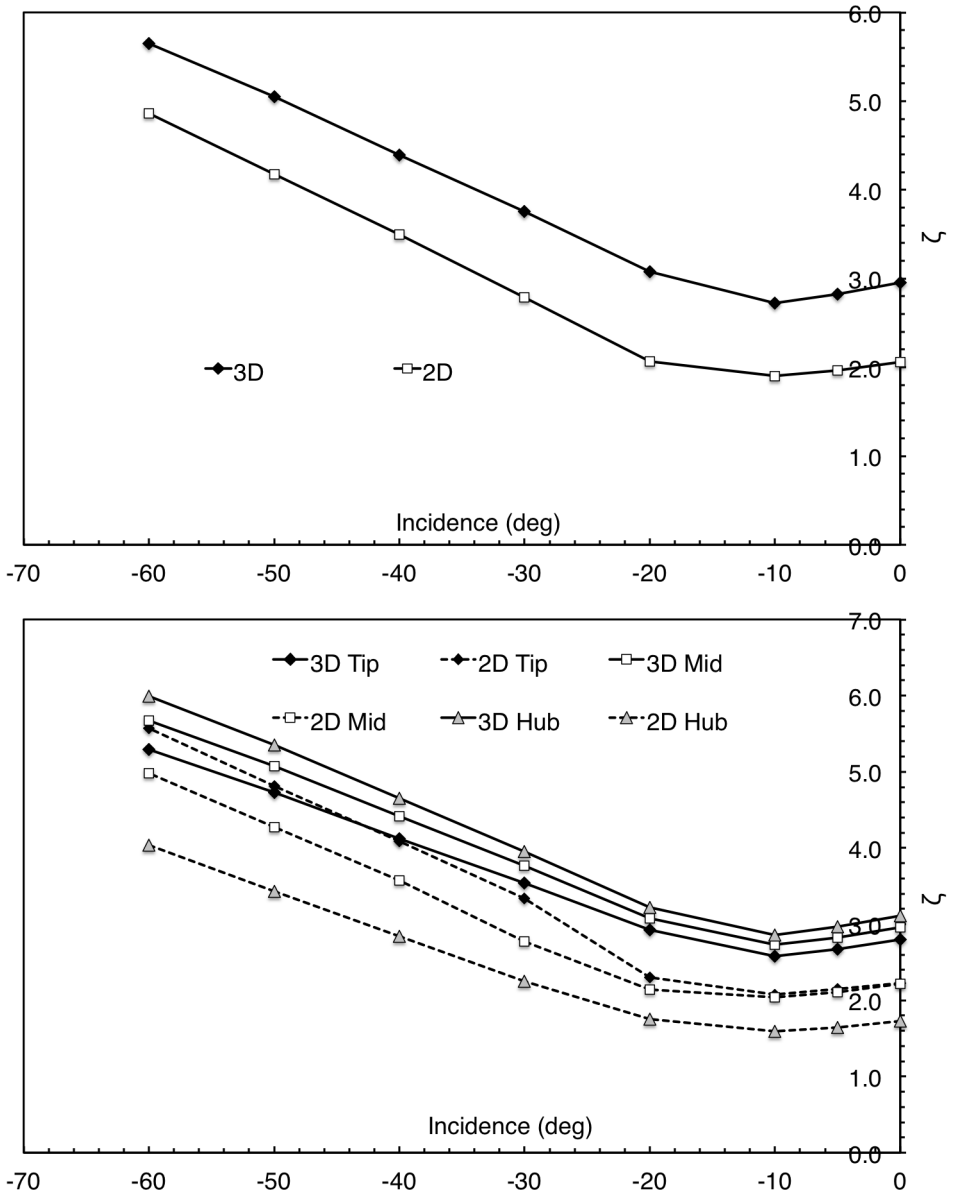

Figure 3.57: Averaged, and hub, tip and midspan total pressure loss coefficients for the 2D and 3D cases as a function of incidence (i)

3.3.8 Interpolation methodology

The sub-idle map generation code developed by Zachos [5] and Aslanidou [13] [50] uses a simple second order interpolation to generate the sub-idle speed lines between the estimated zero-speed line and the test rig-derived idle-speed line. The interpolation methodology is used for both the pressure ratio and the quasi non-dimensional mass flow, in addition to the torque characteristics.

This methodology was not validated, so one of the aims during this study was to explore the relationship between characteristics and speed to validate the interpolation method. From the model of a high-pressure compressor stage, it was possible to generate the zero-speed (locked-rotor) curve and other low-speed lines. The numerical simulations were set up and run by Tommaso Ferroglio [20] and analyzed by Hugo Larcher [15], both MSc students for whom the author was their thesis advisor. A brief description of the numerical model is given in next section, whilst further details can be found in Ferroglio [20]. Figure. 3.58 shows the numerical model used for this investigation which consisted of a single rotor and stator passage. Different rotational speeds were simulated to extract the low-speed lines of the stage.

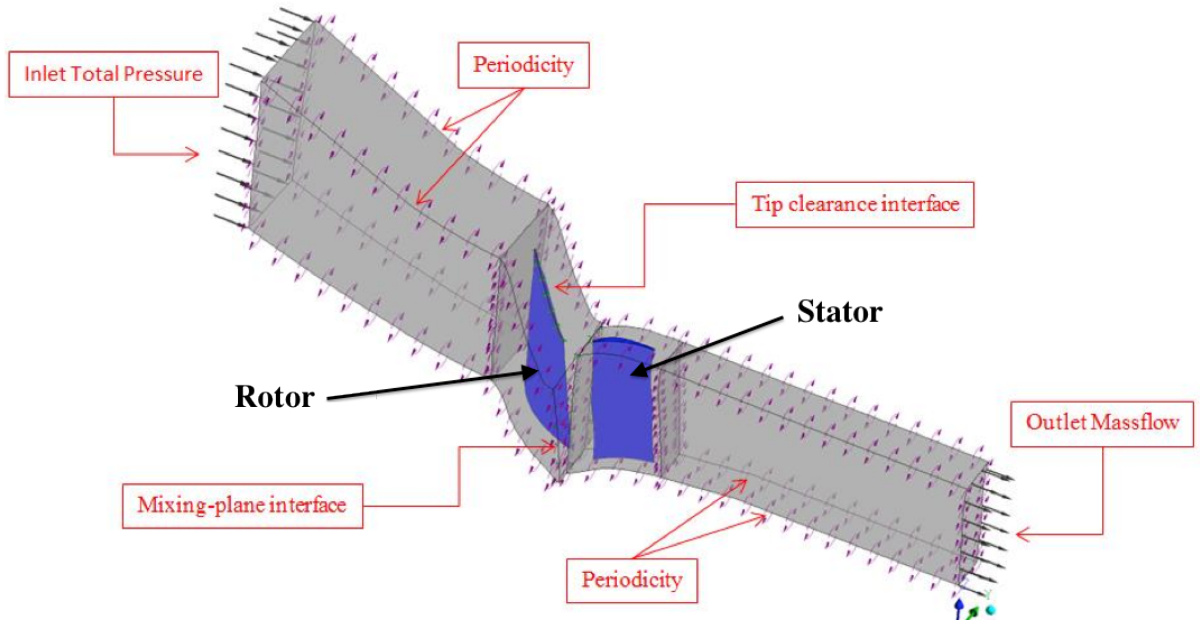

Figure 3.58: Numerical domain of the rotor and stator model used to derive the low-speed and zero-speed lines [20]

Numerical model

Geometry - The geometry consists of the first rotor and stator rows of a HPC of a high-bypass ratio turbofan engine. The domain was extended by one and a half chords upstream and two chords downstream, with the purpose of ensuring a good convergence as well as allowing reading of the results both inside and outside the expected separation bubbles. The domain was modelled following the actual annulus shape, as seen in Fig. 3.59 where part of the swan neck shaped connection which links the IPC with the HPC is clearly visible. A single blade passage for both rotor and stator was modelled to reduce computational cost through the use of periodic boundary conditions. The pitch of the rotor and stator domain are not the same, due to the different number of blades. A mixing-plane interface was used between the two domains.

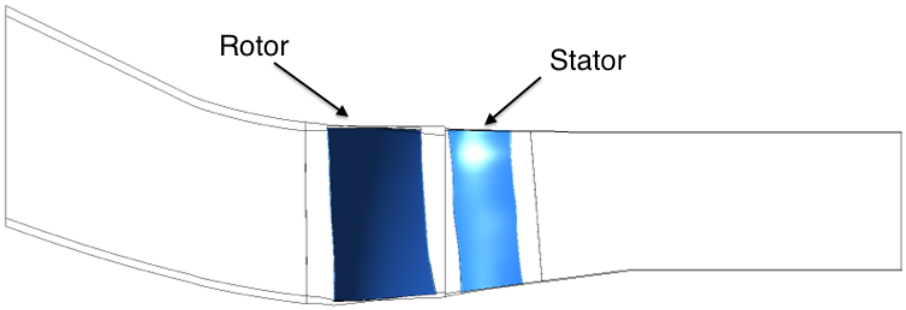

Figure 3.59: Side view of the numerical domain used to derive the low-speed and zero-speed lines [20]

Mesh - Turbogrid was used as the mesh generator to gain experience on meshing with a different software, and since it is easier than ICEM to create structured meshes for turbomachinery components. By adopting the meshing guidelines from Pengue [8] and Reulke [12], a mesh sensitivity study was not required. For the boundary layer, the enhanced wall treatment approach was followed, therefore a $y^+ < 2$ was required. This was achieved over most of the blade surface. In areas were $y^+ > 2$, ANSYS CFX allows activation of the automatic near wall treatment option. The final number of cells in the domain reached 2.2 million. A mid-span section view of the meshes is shown in Fig. 3.60. Convergence criteria were set to a minimum of RMS $1.0e^{-4}$ which was reached by all the parameters except the turbulent kinetic energy, which reached $3.0e^{-4}$.

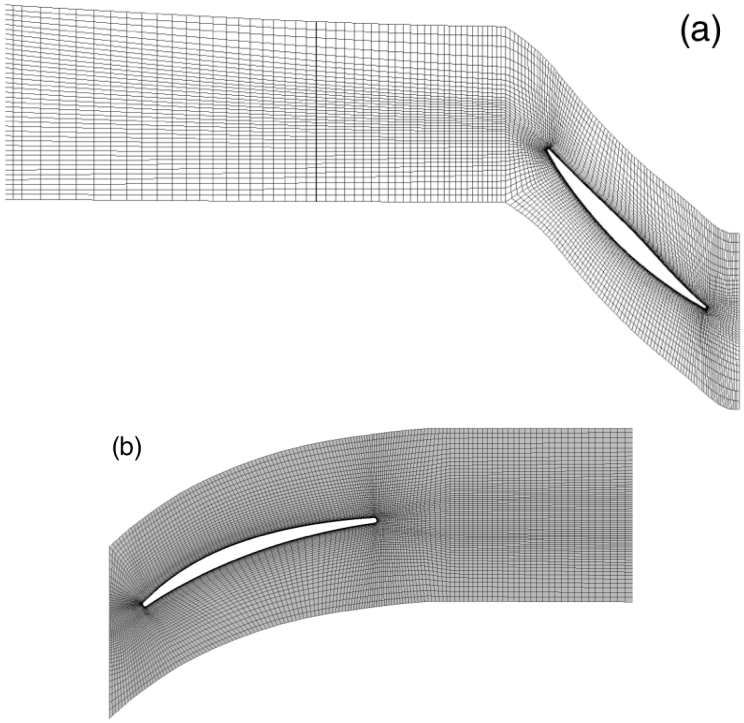

Figure 3.60: Numerical model rotor (a) and stator (b) meshes [20]

Boundary conditions - An inlet total pressure and outlet mass flow condition (classified as very robust) was used. The former was set to 0 relative to the atmospheric pressure (101325 Pa), while the latter was changed according to the simulation run. For the fluid-solid interface, a no slip condition was imposed. The rotational speed of the blade was imposed through the rotation of the whole rotor domain. In the case of the rotor, the external casing was rotating with a velocity contrary to the shaft rotation, so that the velocity of the wall with respect to a fixed reference frame was zero. The hub wall was fixed to the domain rotation.

A rotational periodic boundary condition was applied to the sides of the domain to reduce the full annulus model to a simpler single blade passage. For the rotor-stator interface domains, two methods are widely used: a) Mixing-plane b) Frozen rotor. The mixing-plane approach is usually preferred, while the frozen rotor interface is still commonly used to derive reasonable initial conditions needed for transient simulations. The use of a mixing-plane interface was selected since simulations were run steady state.

Turbulence model - Previous analysis by Pengue [8], shows that in the presence of far off-design incidence angles, where highly separated flows are expected, the $k-\omega$ SST turbulence model ensures a better capturing of the physical phenomenon. Therefore, the $k-\omega$ Shear-Stress Transport turbulence model was adopted with a pressure-based implicit solver, first order upwind and high resolution advection. Fluid was set as a real gas to allow for compressibility effects, whilst viscosity was set using Sutherland's equation with reference viscosity at 18.27μPas at a reference temperature of 291.15 K with Sutherland's constant as 120 K, as was used in 3.3.5.

Cases run - The first set of simulations aimed at establishing a number of free windmilling speeds, i.e. total torque on the shaft is zero. This was achieved by fixing the mass flow and running the model iteratively at steady state at a number of rotational speeds until the speed at which zero torque acting on the blade, was found. Once the free windmilling speeds were found, the mass flow was progressively reduced whilst keeping the rotational speed constant, as tabulated in Table 3.3. This resulted in the derivation of the low-speed lines for the half-stage model. A sample of the rotating rotor simulations is shown in Figs. 3.61 and 3.62.

Speed (rpm)	Mass flow (kg/s)							
Locked (0)	0.01	0.015	0.02	0.025	0.03	0.035	0.04	/
667	0.0094	0.02	0.013	0.017	0.018	0.019	0.022	/
1159	0.016	0.02	0.026	0.028	0.03	0.032	0.036	0.04
2012	0.028	0.034	0.04	0.05	0.06	0.07	/	/

Table 3.3: Parameter space and test matrix for single stage numerical simulations

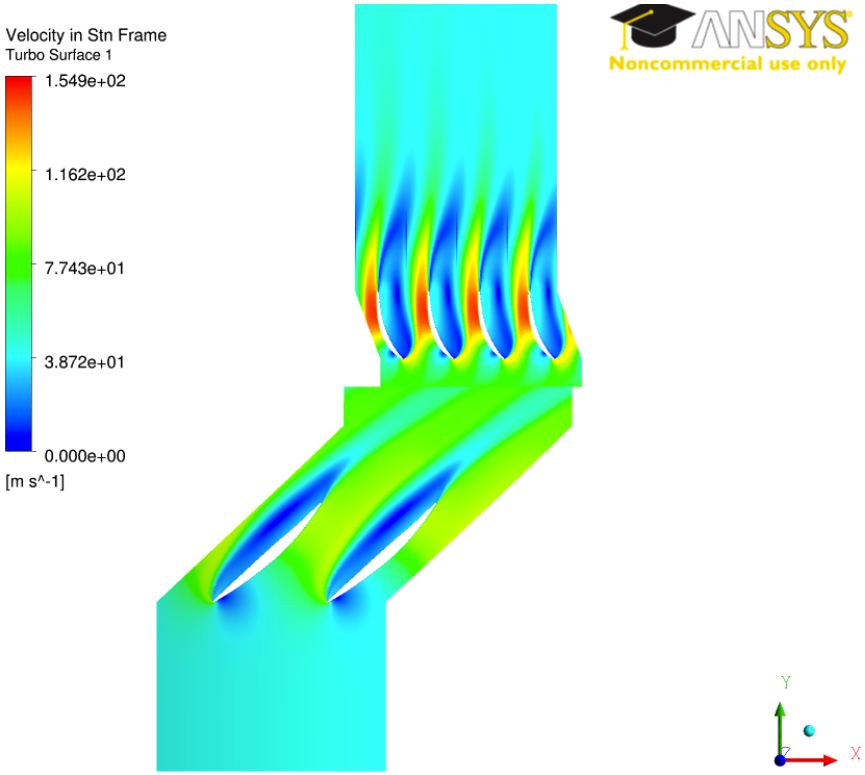

Figure 3.61: Velocity magnitude single stage model (Inlet Mach 0.12, 200 rpm) [20]

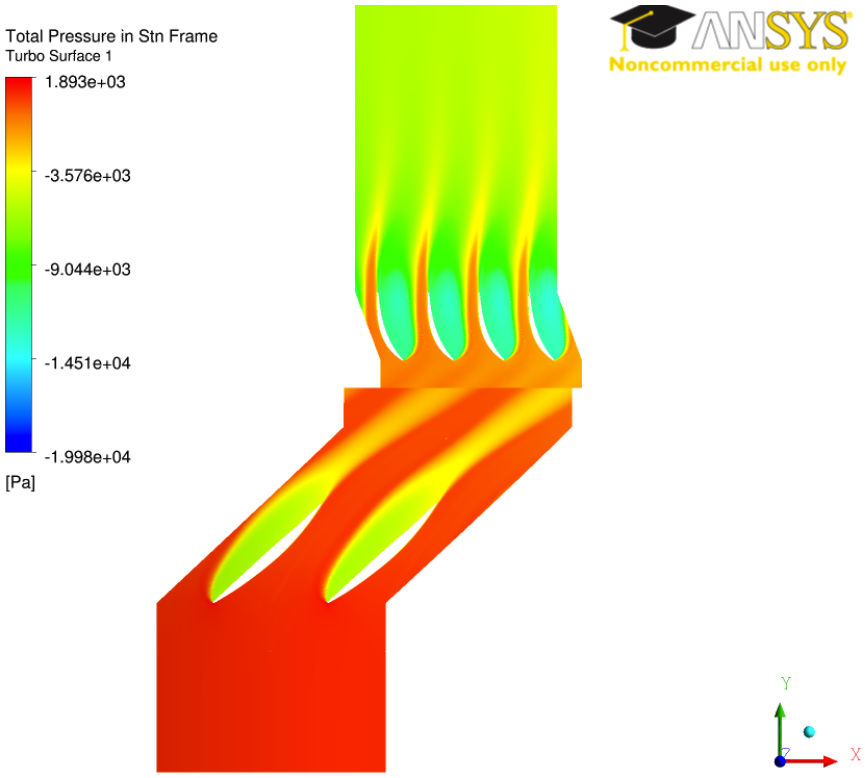

Figure 3.62: Total pressure single stage model (Inlet Mach 0.12, 200 rpm) [20]

The zero-speed and idle-speed curves extracted from the CFD were used in the map generation subroutine, bypassing the zero-speed curve generation step. The code-generated speed lines were plotted for comparison with the CFD results. As shown in Fig. 3.63, the speed curves clearly exhibit too strong a slope compared to CFD results. Surge is also predicted at a pressure ratio higher than in CFD computations, while the choking line appears at a lower pressure ratio.

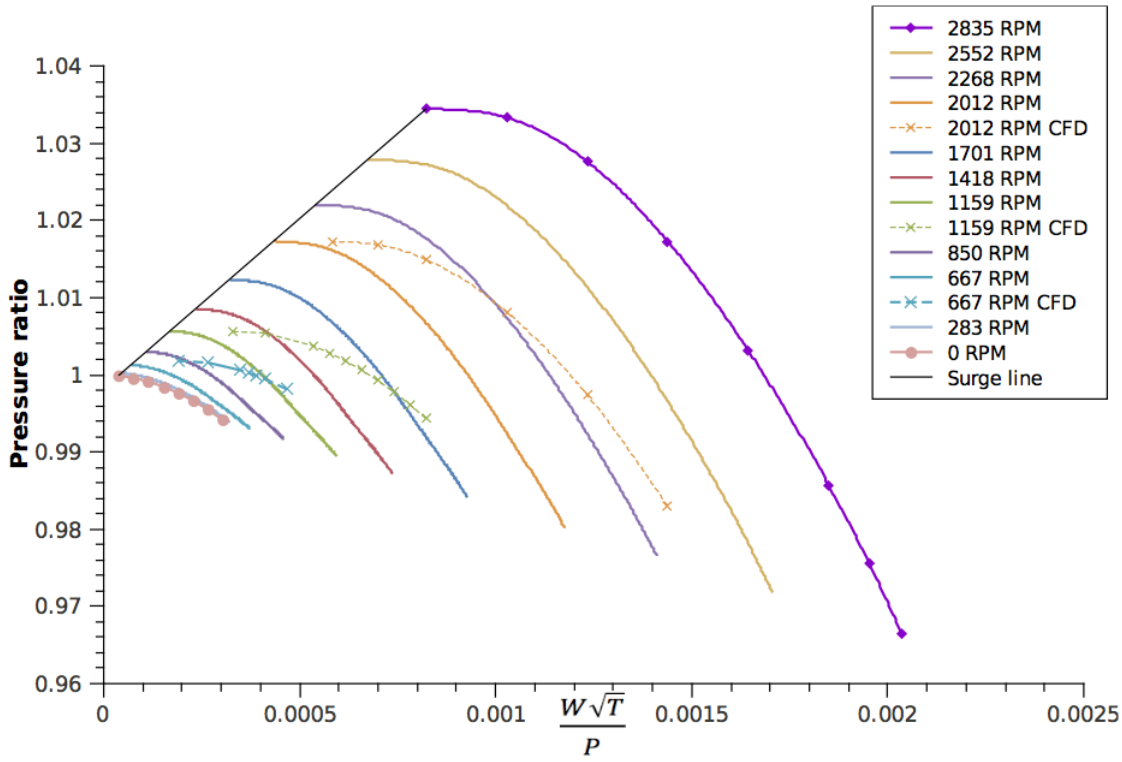

Figure 3.63: Comparison of the speed lines from the numerical simulations and the interpolated lines from the compressor code using a polynomial interpolation [15]

This behaviour is explained by the interpolation polynomial. An analysis of the numerical simulation results showed that the relationship between the rotational speed and non-dimensional mass-flow is closer to a first order (linear) type, while the relationship between speed and pressure ratio is of a second order type. Changing the code's quasi non-dimensional mass flow interpolation scheme from a 2^{nd} order polynomial to a linear function, the agreement between the interpolated lines and the CFD simulations improved considerably as shown in Fig. 3.64. The surge line also features a more parabolic shape in agreement with the CFD points.

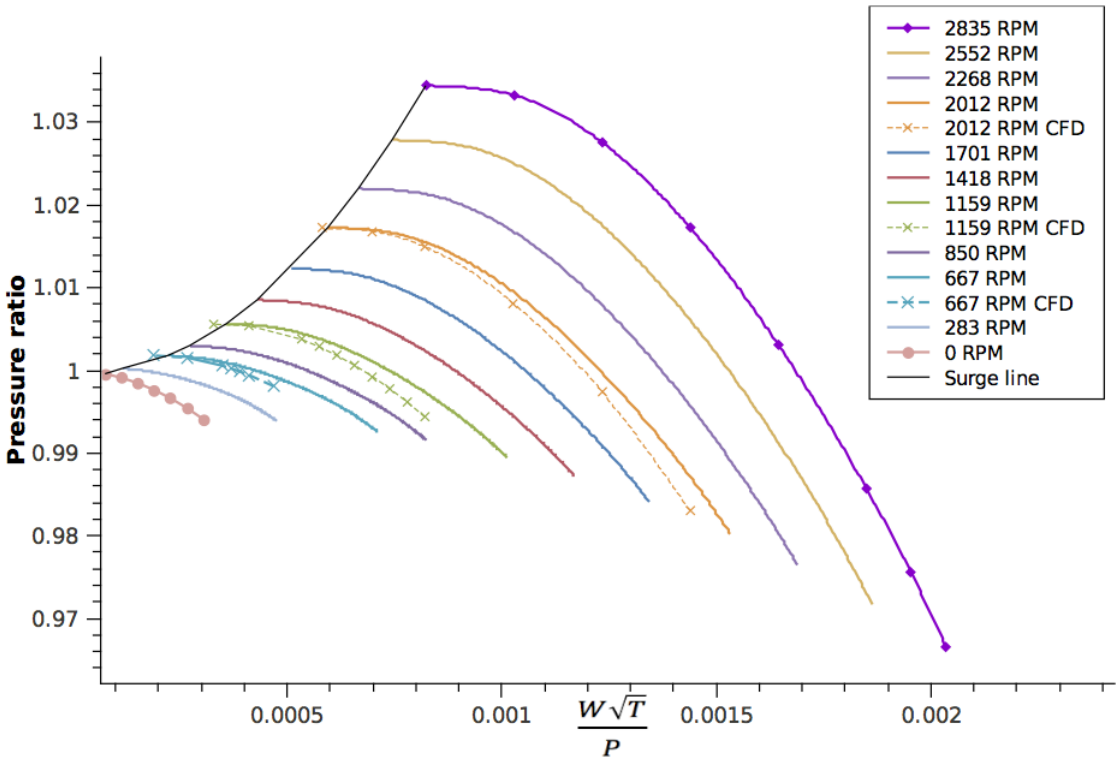

Figure 3.64: Comparison of the speed lines from the numerical simulations and the interpolated lines from the compressor code using a linear interpolation [15]

Concluding, a second order interpolation of the non-dimensional mass flow provides a more realistic compressor sub-idle map characteristic, which also aligns very well with the CFD extracted low-speed lines. In view of these results, the code was updated so that the user can choose between a 2^{nd} order polynomial or linear interpolation between the zero-speed line and the above-idle data. The implementation and comparison between the two interpolation methods is given in section 3.4.

3.3.9 Concluding remarks

The objective of the research described within this section was to understand the flow's behaviour and compressor blade aerodynamics at high negative incidence, in order to be able to predict the compressor's zero speed line more accurately through stage-stacking.

Observations from the numerical simulations indicate how the velocity profiles for high negative incidence cases are similar to those of stalled blades, which aligns with the concept described in Zachos [5] that at such far off-design conditions, the aerofoil loses most of its aerodynamic properties and behaves more similarly to a flat plate. The flow angle downstream of the blade's trailing edge was found to change with the distance downstream as a result of the separated flow region effectively changing the shape of the channel. Eventually the flow settles to a constant angle.

The distance downstream where the flow angle stabilises, was found to be highly dependent on the blade geometry and incidence angle. This has important implications in terms of both numerical and experimental measurements since the tangential force coefficient (C_f) is determined from the flow angle upstream and downstream of the blade. The study shows that the coefficient's value will change depending how far downstream it is measured, making it hard to determine which position will produce a representative value of the coefficient.

A suitable alternative method was found through measuring the axial and tangential forces acting on the blade, from which C_p and C_f were calculated. This proved to be very effective, producing a single value for each coefficient which represents the actual forces experienced by the blade. Such a method would be suitable also within an experimental facility through the use of force balances, allowing the determination of blade coefficients in highly separated flows.

The deviation of the flow from the blade outlet angle at far off-design conditions was studied to determine which model is most suitable, if any. The study shows the model proposed by Creveling and Carmody [17], predicts deviation well for high negative inci-

dence cases (down to $i = -60°$), for which it had not been validated. The model was adopted and coefficients for different stagger (ξ) angles and solidities ($\frac{s}{c}$) were extracted.

The narrowing of the blade channel due to the presence of a highly separated flow region had not been previously explored, resulting in a possible underestimation of the choking mass flow through a locked-rotor compressor. Compressible flow numerical simulations for various blade operating conditions and geometries were used to observe the relation between the geometric and effective flow area up to choking conditions. The results show how at low inlet Mach numbers, the flow is highly separated at high negative incidences, resulting in a flow effective area sometimes less than half the geometric area. However as the inlet Mach number increases, the flow starts to reattach with the blade surface, thus increasing the flow effective area.

The ratio between effective and geometric area can increase from 0.55 to 0.725 between low and high Mach number cases for the same geometrical setup. The data gathered from the study is significant in altitude relight cases since it can be used to estimate more accurately the core mass flow in a locked-rotor case, which is then used to predict the bypass ratio, the fan speed and therefore the engine drag. The blade coefficients under high inlet Mach number and compressible flow conditions were also derived.

The conclusion from previous researchers that Blade Element Theory could be applied to high negative incidence cases, was tested by running a full sweep of negative incidence angles. The analysis of the results suggests that BET is not particularly suitable for such cases, with the numerically averaged characteristics of the 2D elements not aligning very well with the full 3D blade ones. This is expected since radial flows at such conditions are very significant. Blade Element Theory ignores such radial flows, and therefore cannot represent well the flow properties of a 3D blade.

Numerical simulations of a single-stage rotating rotor model were used to analyse the relationship of specific torque and quasi non-dimensional mass flow with quasi non-dimensional speed. In the extrapolation method, a 2nd order polynomial was used to

extrapolate these values. The data extracted from the numerical simulations however indicates a more linear relationship between quasi non-dimensional flow and quasi non-dimensional speed. The interpolation process was shown to give better results when this linear relationship was used, aligning well the interpolated map with the numerically derived speed lines, especially in terms of the stall line.

The fundamental knowledge and models resulting from the numerical studies were then implemented within a new version of the compressor sub-idle map generation code. A description of this implementation and the validation work against engine test data is described in the next section.

3.4 Updated sub-idle compressor characteristics generation code

In order to utilise all the knowledge gained from the numerical simulations described in section 3.3, it was decided that rather than updating or modifying the code written by Aslanidou [13] and Zachos [5], it would be more practical to write a fresh new version of the sub-idle compressor map generation code. Though based on the same stage-stacking principle, the new code written as part of this research, is based on isentropic compressible flow equations. A description of the updates made over the previous version of the code is given in the following subsections. This is followed by a view of the resulting characteristics generated, and validation against experimental engine test data.

3.4.1 Updates to the compressor sub-idle map generation code

Blade Element Theory

To include the use of BET in the code, the compressor annulus was split into smaller annular sectors and stage-stacking run separately for each sector. Flow properties at the compressor outlet are then averaged across all the span divisions. Each span section has the same area ratio between the inlet and outlet. Otherwise, each span will have a different artificial increase in axial velocity. The code was modified to calculate the radial position where the annulus will be split using Eqn. (3.28), such that the flow's axial acceleration is equal for each span. The span divisions of the test case run as illustrated in Fig. 3.65.

$$R_{span(i,j)} = \sqrt{\frac{R^2_{tip(i)} - R^2_{root(i)}}{N_{spns}} + R^2_{root(i,j-1)}} \tag{3.28}$$

The tangential force (Y) that the flow imposes on the blade is calculated using the tangential force coefficient (C_f). The tangential force is then multiplied by the effective radius to estimate the torque. The effective radius of each span division was assumed to be at its centroid, calculated using Eqn. (3.29). Effective torque radii for the test case run are illustrated in Fig. 3.65.

$$R_{Torq(i,j)} = \frac{1}{2}\left[\frac{R_{in(i,j)} + R_{out(i,j)}}{2} + \frac{R_{in(i,j-1)} + R_{out(i,j-1)}}{2}\right] \tag{3.29}$$

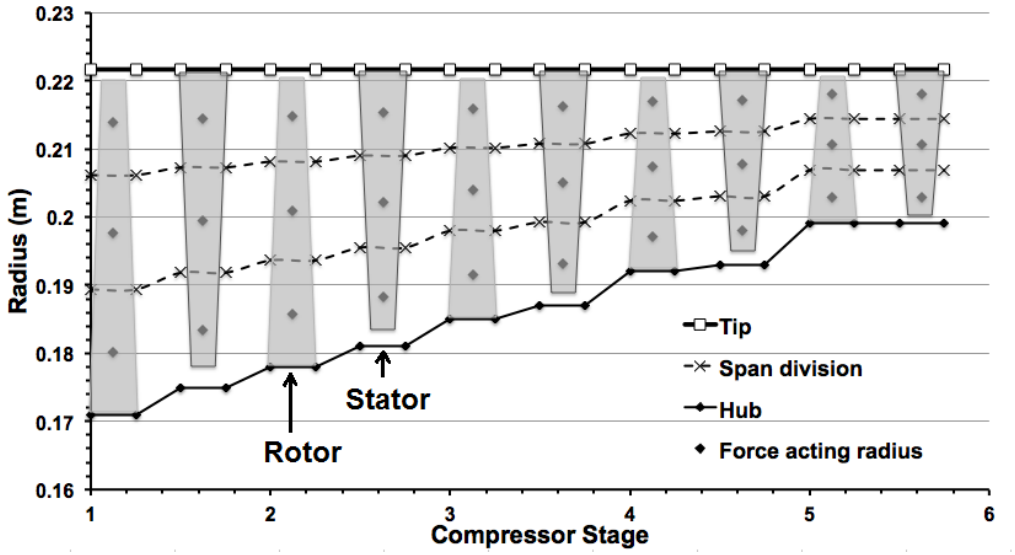

Figure 3.65: Division of spans for Blade Element Theory use - 3 span example

Flow deviation

The previous version of the code [13] relied on Carter's rule to predict flow deviation. Due to the far off-design operating condition, the assumption that Carter's rule predicts accurately the flow deviation is not valid. The flow deviation characteristics described in section 3.3.4, based on Creveling and Carmody [17] but extracted from the numerical simulations, were added to the code. The code interrogates the values of the coefficients for the two conditions closest to that required. It then linearly interpolates between these sets of values and estimates the flow deviation. Another option included is to use the blade's force coefficient (C_f) to predict the flow outlet angle through the knowledge of the inlet angle and reverse engineering Eqn. (3.8) in the form given in Eqn. (3.30). The option of using Carter's rule and modified Carter's rule were also kept. An overview of the routine for predicting flow deviation, is illustrated in Fig. 3.66, were a, b, c and d are the constants derived from the study described in section 3.3.4.

$$\alpha_2 = \tan^{-1}\left(\frac{C_f}{2} - \tan\alpha_1\right) \tag{3.30}$$

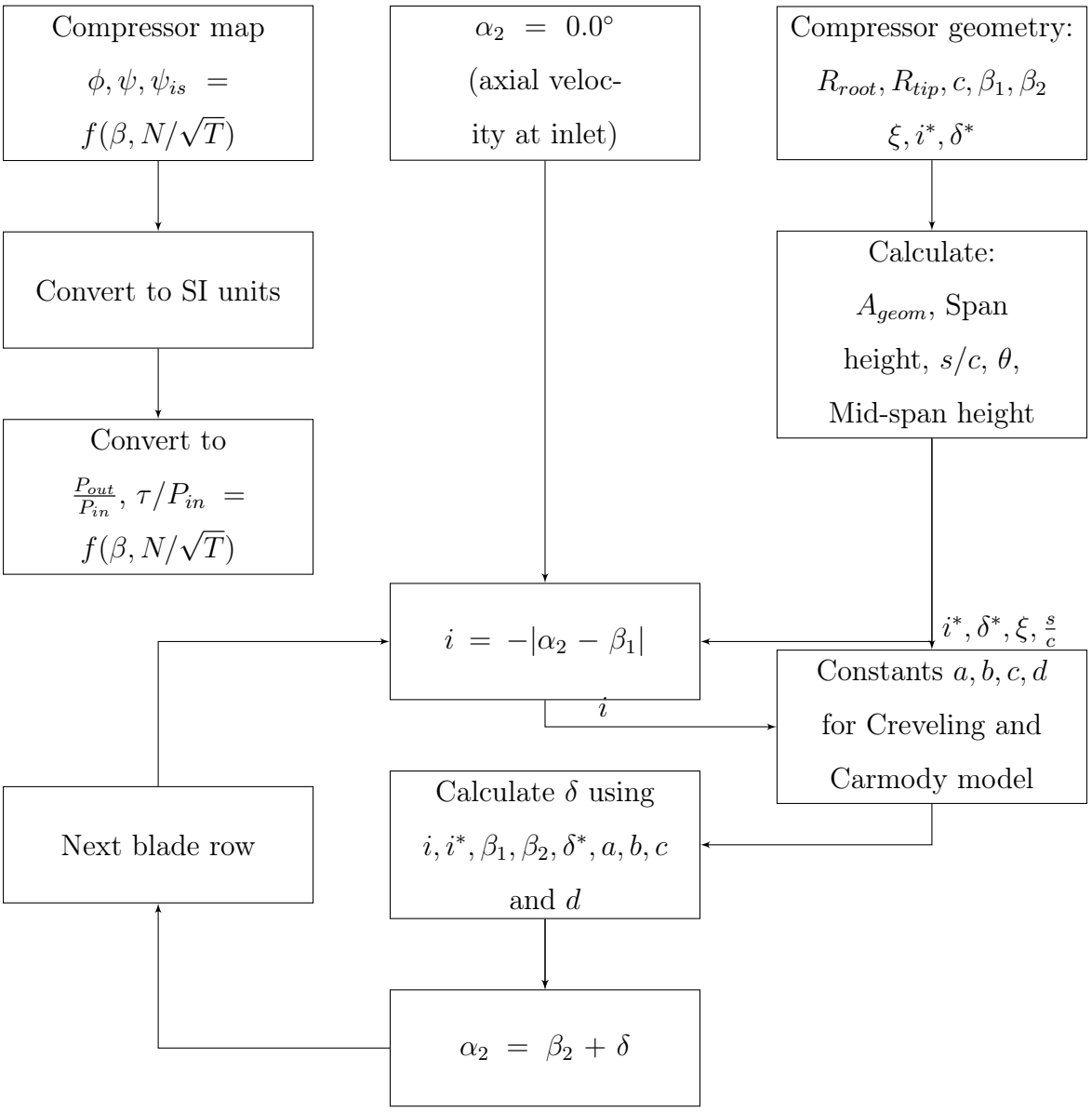

Figure 3.66: Compressor code geometry and map inputs with calculation of incidence angle for each blade row

Blockage

To account for the flow separation, the change in flow effective area with the blade's operating condition was included, where the ratio of geometric to effective area is extracted from a tabulated form of the results shown in Fig. 3.49, as a function of solidity, stagger, flow Mach number and incidence angle. The ratio is multiplied by the physical area calculated from the compressor geometry to give the flow effective area as explained in the following sections.

Compressible flow and stage-stacking

The stage-stacking calculation is viewed as a series of cascades which are fed high pressure air from an upstream reservoir. The air flows through the cascades which impose a total pressure loss. The flow then exhausts to atmosphere. The first point on the zero speed line is at a pressure ratio of unity when the quasi non-dimensional mass flow is zero. In this case, the reservoir is at ambient static pressure.

The next calculation increases the reservoir static pressure to above ambient. Within the reservoir, this also corresponds to the total pressure. The total temperature in the reservoir is assumed equal to ambient. When the air flows into the compressor, it can be assumed that there are no losses up till the leading edge of the first blade row. Therefore the first blade sees a total pressure equal to the static pressure in the reservoir.

An initial flow Mach number is guessed. The static pressure is calculated as a function of the Mach number using Eqn. (3.31). Since there is no work done on the flow, the total temperature remains constant throughout the compressor. The static temperature is also calculated from the Mach number using Eqn. (3.32). A flow chart of the code's stage-stacking process is illustrated in Fig. 3.67.

$$\frac{P}{p} = \left(1 + \frac{\gamma - 1}{2} M^2\right)^{\frac{\gamma}{\gamma - 1}} \tag{3.31}$$

$$\frac{T}{t} = \left(1 + \frac{\gamma - 1}{2} M^2\right) \tag{3.32}$$

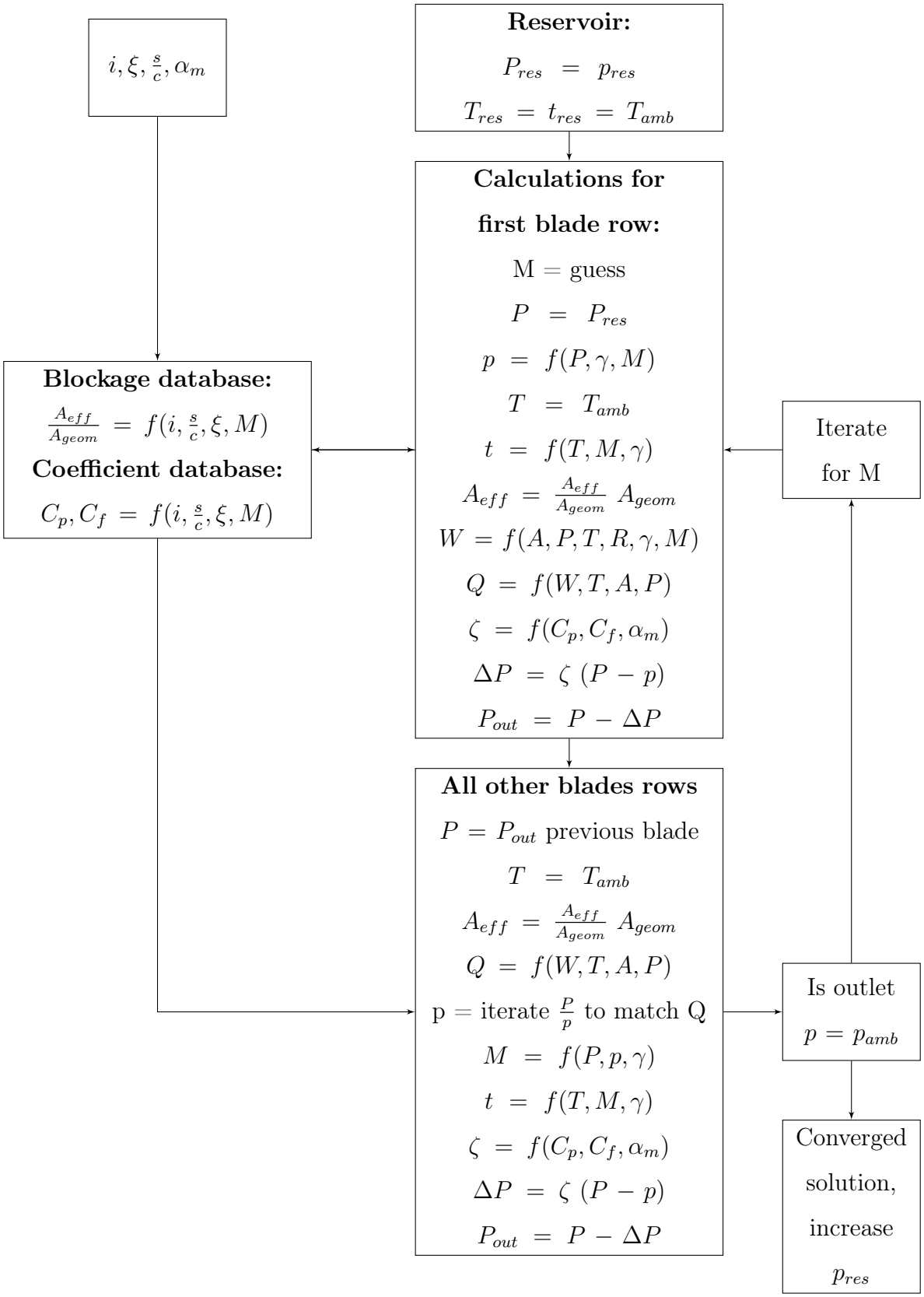

Figure 3.67: Compressor code stage-stacking routine

The flow effective area is calculated from the blockage ratio, derived as a function of stagger, incidence, solidity and flow Mach number, from the database. The mass flow is established using the compressible mass flow equation given in Eqn. (3.33). Mass flow is calculated using the inlet area (A), whereas the flow effective area (A_{eff}) is used to calculate the Mach number in the channel throat and check whether it is choked. At this point, the Q parameter can be calculated using Eqn. (3.34). The blade coefficients C_p and C_f are extracted from the database as a function of incidence, stagger, solidity and flow Mach number. The total pressure loss coefficient (ζ) is estimated from the blade coefficients using Eqn. (3.35).

$$W = \frac{A\ P}{\sqrt{T}}\sqrt{\frac{\gamma}{R}}M\left(1+\frac{\gamma-1}{2}M^2\right)^{-\frac{\gamma+1}{2(\gamma-1)}} \tag{3.33}$$

$$Q = \frac{W\sqrt{T}}{A\ P} \tag{3.34}$$

$$C_p = C_f\ \tan\alpha_m - \zeta \tag{3.35}$$

The total pressure loss (ΔP) can be estimated from ζ using Eqn. (3.36).

$$\zeta = \Delta P/(P-p) \tag{3.36}$$

This however is not the ideal case since Eqn. (3.35) is derived from incompressible flow. A more accurate method is to derive the drag coefficient (C_d) and estimate the total pressure loss using the blade frontal area as the characteristic area. It is suggested that further work on the compressor code addresses this issue.

For the second blade row, the mass flow (W), total pressure (P), total temperature (T) and area (A) are known, and therefore the Q can be calculated. From known Q, the P/p is found by iterating for the static pressure (p) using Eqn. (3.37). The Mach number and static temperature can therefore also be derived once Q is known. Similarly to the first blade row, the flow effective area is calculated from the database and the Mach number for that area calculated to ensure the blade row is not choked. This process is repeated for each blade row. Finally at the compressor outlet, the static pressure must match the ambient static pressure. The compressor's guessed inlet Mach number is changed iteratively until this condition is achieved.

$$Q = 1000 * \sqrt{\frac{2\gamma}{(\gamma-1)R}\left(\frac{P}{p}\right)^{-2/\gamma}\left(1-\frac{P}{p}\right)^{\frac{1-\gamma}{\gamma}}} \tag{3.37}$$

The process is repeated with increasing static pressures in the reservoir until a total pressure ratio against quasi non-dimensional mass flow profile is achieved and eventually the compressor chokes. An example of the flow pressures and Mach number for a converged solution having an inlet total pressure of 119,000 Pa is shown in Fig. 3.68.

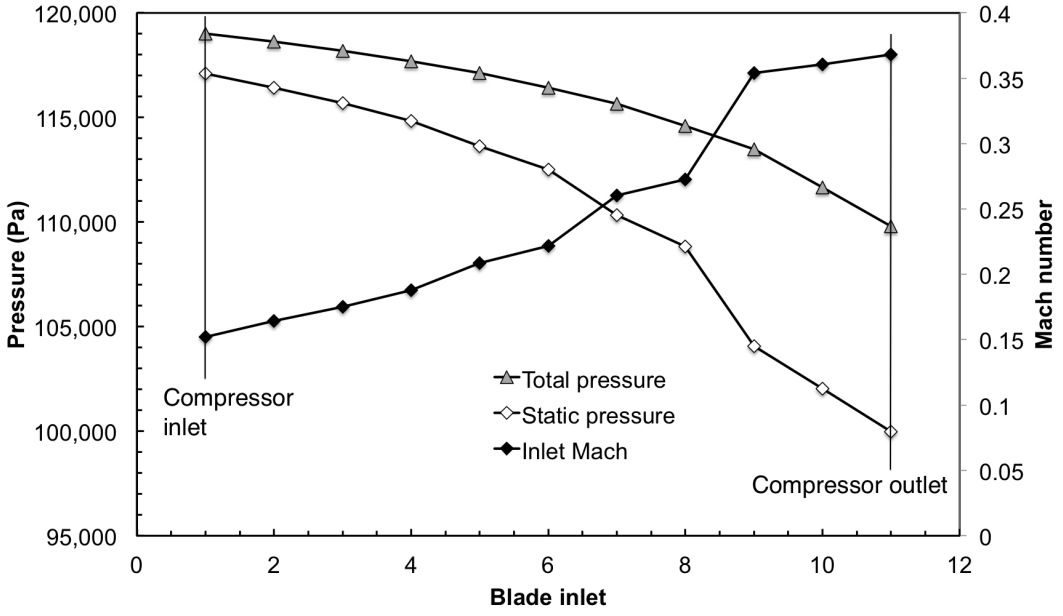

Figure 3.68: Total pressure (P), static pressure (p) and Mach number for a converged case with inlet total pressure of 119,000 Pa

Interpolation method

The validity of using a second order polynomial interpolation was investigated in section 3.3.8. Comparison against numerically obtained rotating single stage characteristics against interpolated values indicate that a linear interpolation for the quasi non-dimensional mass flow against quasi non-dimensional speed, produces speed lines that align better with the numerical results.

This option was added into the code, allowing the user to choose between polynomial and linear interpolation. Results from a test case are shown in Fig. 3.69 where the interpolated map using both methods is shown. The comparison indicates clearly that the linear interpolation produces a curved stall line, continuing with the above-idle original map. The polynomial interpolation produces a straight stall line, which is not what one would expect. The linear interpolation also pushes the speed line choking points towards higher quasi non-dimensional mass flows. This was also observed in the analysis carried out in section 3.3.8.

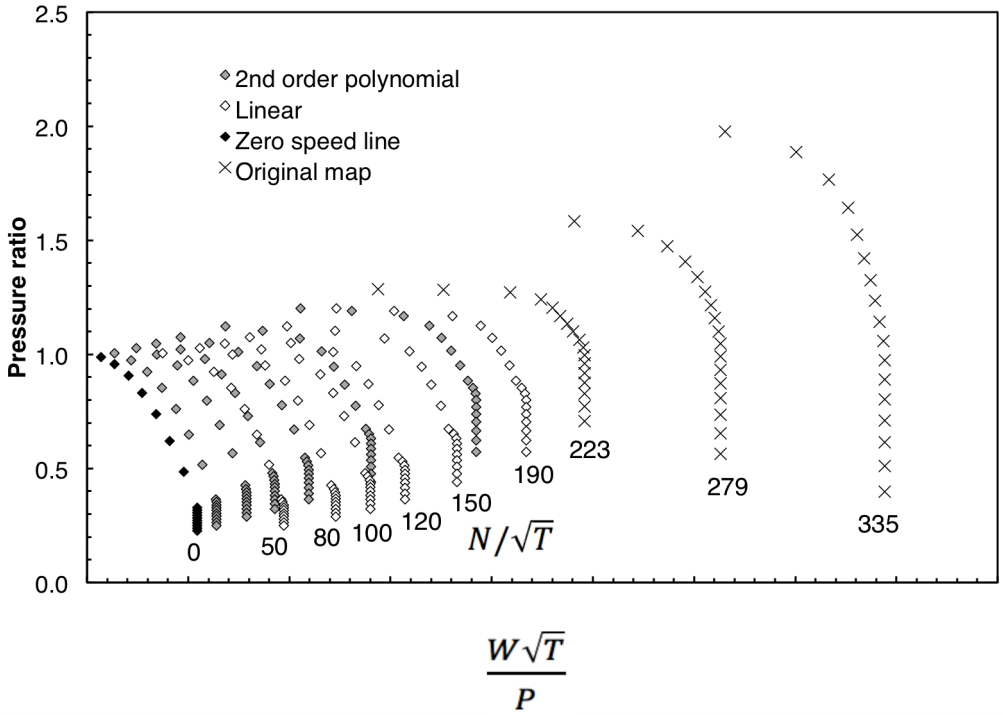

Figure 3.69: Comparison of linear and second order polynomial interpolation methods between the zero-speed and idle-speed lines

3.4.2 Results

The high-pressure compressor was used as a test case. The compressor geometry and above-idle characteristics derived from rig tests, were provided by the sponsor. The resulting zero-speed line and interpolated sub-idle maps are shown in Figs. 3.70 and 3.71.

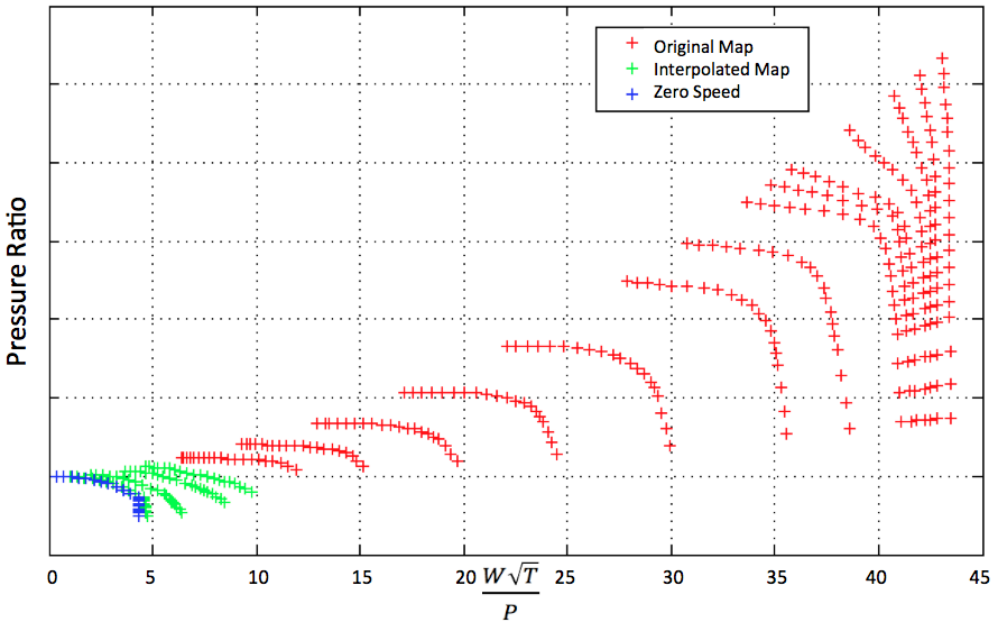

Figure 3.70: HPC pressure ratio characteristics (τ/P) ; above and sub-idle conditions

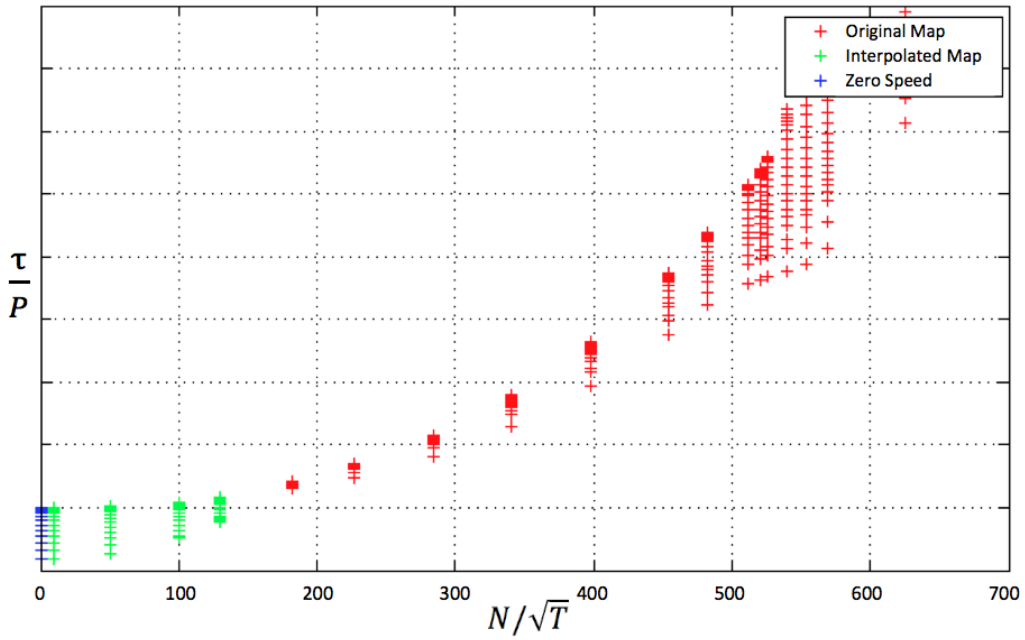

Figure 3.71: HPC specific torque characteristics (τ/P); above and sub-idle conditions

3.4.3 Validation

Sub-idle engine performance solver

It is very difficult to validate the accuracy of the results generated by the code since there is very little data on locked and low-speed compressor characteristics. Any data available is also susceptible to large instrumentation errors. As part of the verification process, the code with accompanying report and user guide [74], was presented to the sponsoring company for evaluation. A number of suggestions and improvements were made following this first evaluation, reported in Jenkins [75].

The sub-idle compressor characteristics generated by the code were subsequently supplied to Maini [76] [21]. The objective of this collaboration was to use the generated data within an in-house performance solver and compare it with a limited number of available groundstart data. Test data from an engine hot start, a cold start and a rundown were used, however the validation was focused mostly on the hot start condition due to the higher amount of engine test data available.

This transient test data used for the validation process, is illustrated in Fig. 3.72 which shows IP shaft speed (NI), HP shaft speed (NH), HPC inlet (P_{26}) and exit (P_{30}) total pressure, and HPC inlet mass flow (W_{26}) against time as the engine accelerates. Cranking (marked by the red dashed line) starts at $t = 20$ s. The high pressure spool starts rotating at $t = 24$ s, highlighted by the blue dashed line. Engine light-up is at $t = 40$ s, noticeable by the step-change in P_{30}, shown in the middle plot. From the lowest plot one can observe that the core mass flow measurements are very unsteady in sub-idle region. This is due to the pressure probe picking ambient noise, as explained in Elysee [77]. A five-point moving average smoothing was carried out on the measured mass flow, as shown in Figure 3.72.

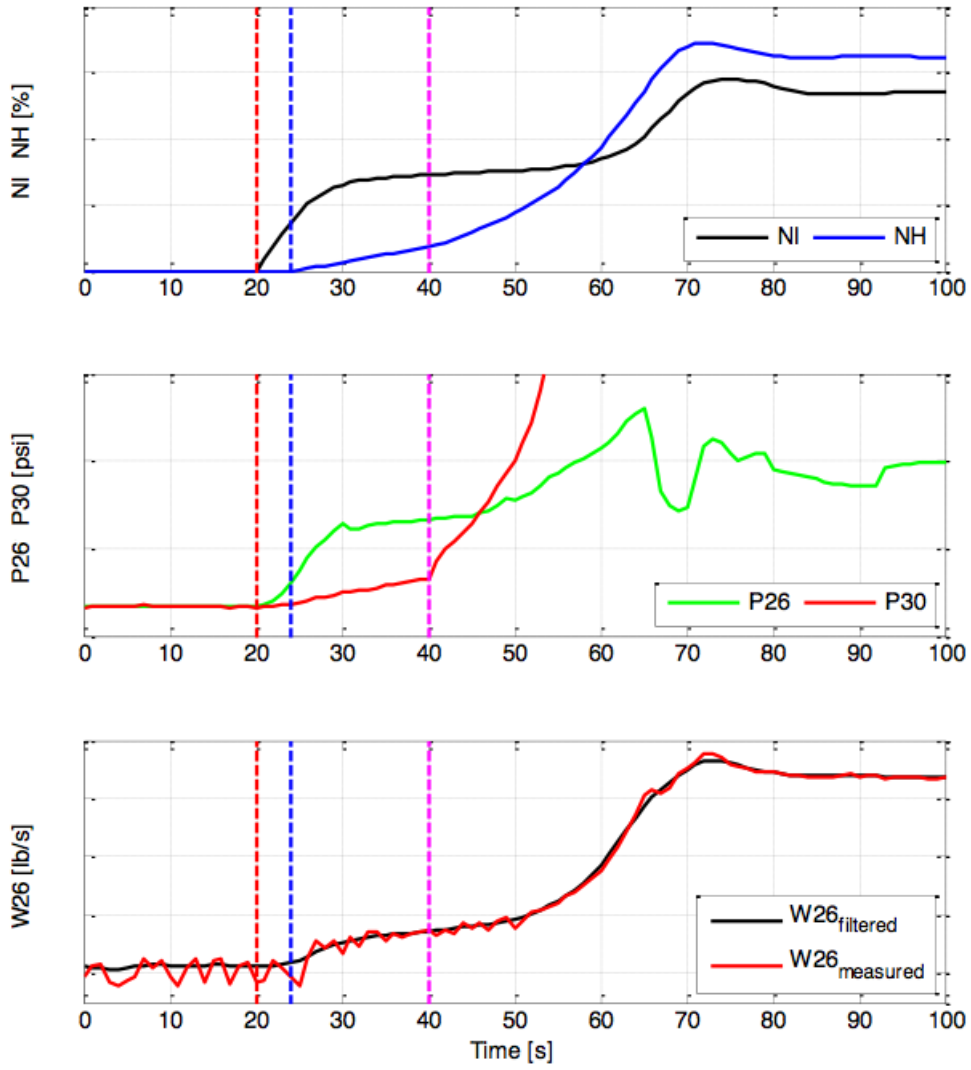

Figure 3.72: Experimental data - IP shaft speed (NI), HP shaft speed (NH), HPC inlet (P_{26}) and exit (P_{30}) total pressure, and HPC inlet mass flow (W_{26}) - used for validation of the generated HP sub-idle compressor map [21]

Figure 3.73 shows the percentage HP speed and core mass flows. This plot highlights the capability limits of the new solver by Maini [76] [21] using the sub-idle compressor characteristics generated in the current study, relative to the previous tools available. These previous tools often fail to converge for engine power settings lower than 50% NH speed. The blue dashed line in Fig 3.73 represents the minimum limit attainable with the above-idle characteristics extracted from compressor test rig data (180 $N/\sqrt{T}$ corresponding to 24% HP speed). The sub-idle engine performance tool designed by Maini [21] combined with the sub-idle compressor map generated as a result of this research, can pick up engine powers down to 2% NH speed.

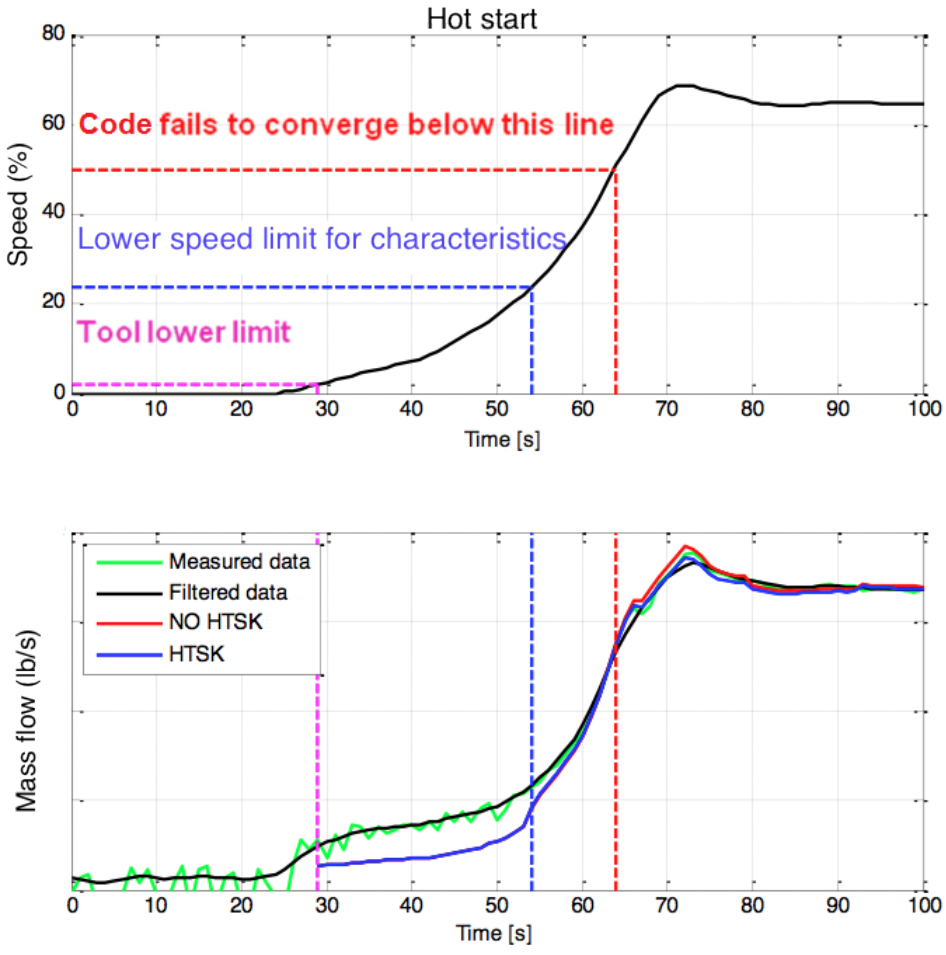

Figure 3.73: Operating limits of the previous performance solvers and the new solver using the generated sub-idle compressor characteristics [21]

The lower plot in Fig. 3.73 shows the measured mass flow, the smoothed mass flow and two results from the sub-idle performance tool. Both simulations with heat soakage (HTSK) and without were run. Although heat soakage seems to have no effect on the sub-idle part, it affects the idle region. When starting the engine, the core flow rates are so low that heat exchange does not seem to be significant. However this could be related to the fact that heat soakage calculation computes the heat transfer coefficient by means of an empirical correlation valid for turbulent flows [21]. Even if sensible, this issue doesn't seem to be responsible for inaccuracy in the sub-idle region. From this point all the calculations were carried out with heat soakage activated as it avoids overshooting T_{26} during transients, resulting in a closer match between calculated W_{26} and measured data.

Simulation results against test data

The simulation results indicate that there is some error in predicting the core mass flow, as shown in Fig. 3.74. The error is quite high at low-speeds, as much as 40% relative to the engine data. However one must point out that the level of error at the point where the simulation starts using the original compressor map, is also significant; almost 10%. This may indicate that the idle-speed line used to interpolate the sub-idle map may not be accurate, and that a higher speed line may have to be selected. The agreement for total pressure between the engine data and the solver is very close, as shown in Fig. 3.75, with the maximum error in the low-speed part not exceeding 1%. This is very encouraging, and shows that whilst there is still some work to be done to align the mass flow better, the characteristics generated are realistic.

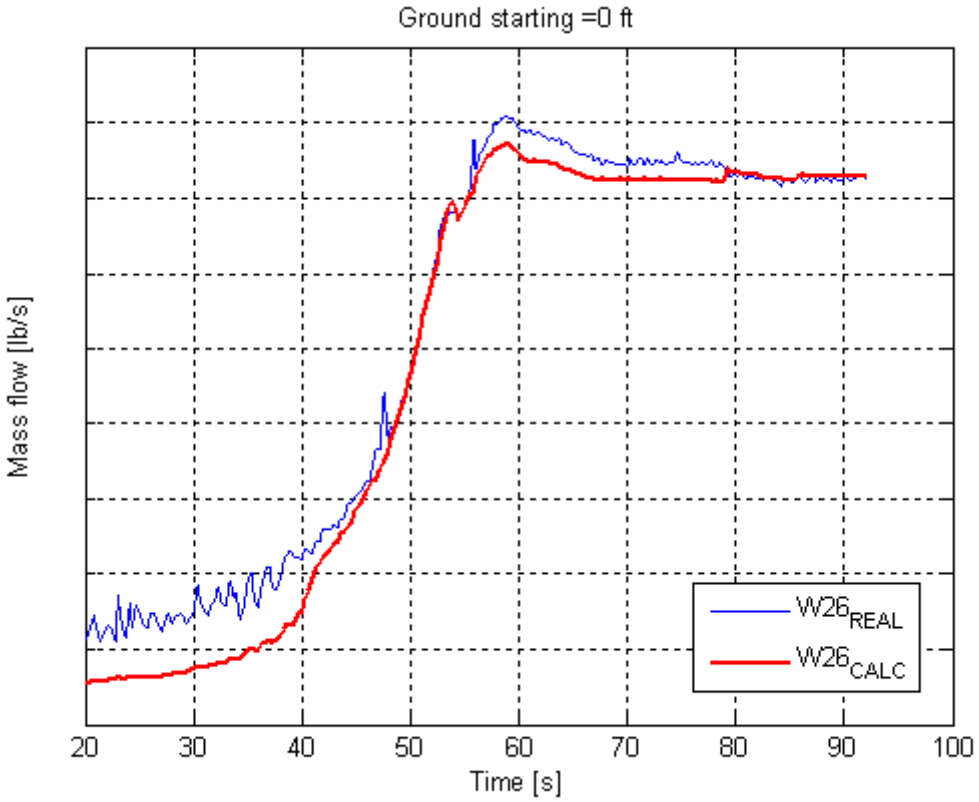

Figure 3.74: Core mass flow comparison between engine test data and results from the performance solver using the generated sub-idle compressor characteristics [21]

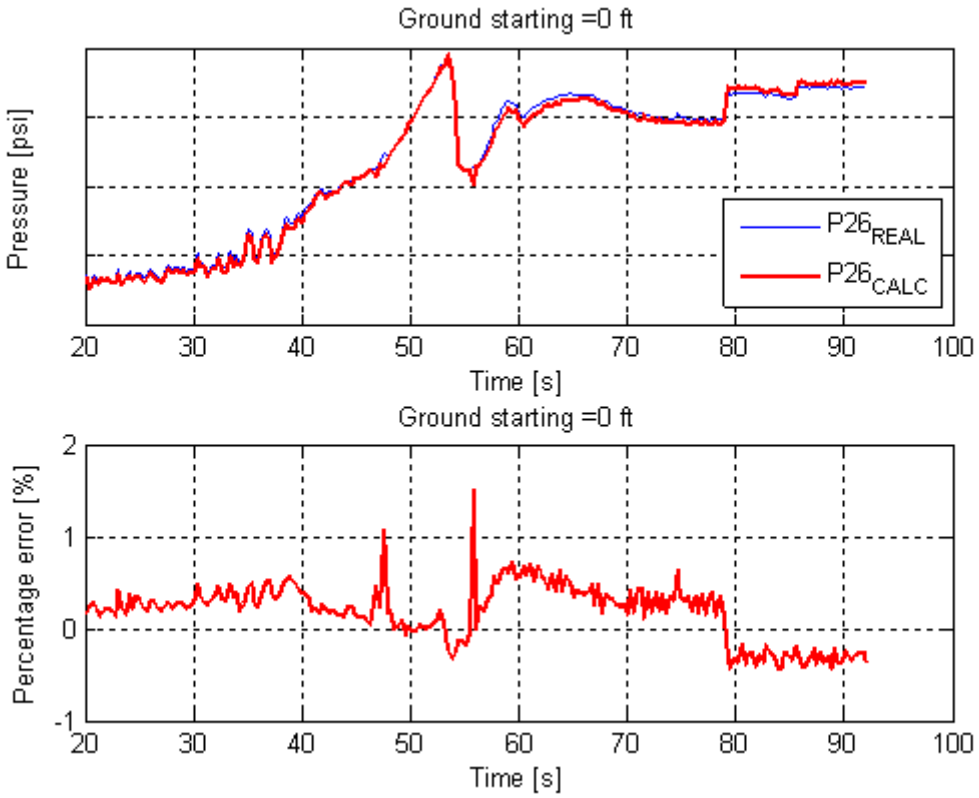

Figure 3.75: Core total pressure comparison between engine test data and results from the performance solver using the generated sub-idle compressor characteristics [21]

This validation process was conducted to understand how close or far the predictions by the sub-idle map generating code were from the actual compressor characteristics. Given that there is no compressor experimental data to which the characteristics can be compared to, the results shown above indicate that the characteristics generated are close to the real compressor.

However, it is still fundamental that a set of sub-idle compressor characteristics is obtained experimentally, which should serve as the benchmark with which the map generation code's capability is properly assessed.

Comparison with extrapolation method

A quick comparison of the maps generated by the interpolation methodology against the extrapolation results (Fig. 3.76) indicate that the new methodology is more realistic, with the lowest speed line showing a pressure loss and not choking at a pressure ratio of unity. Additionally, comparing map generation results between Figs. 3.77 and 3.78 it is noticeable how ϕ increases exponentially as the compressor speed approaches zero for the interpolation case, which is what is expected when the rotational speed is very low but there is still a significant flow due to ram air. For extrapolation however, the value of ϕ has a finite value even at the lowest speed, which is not possible.

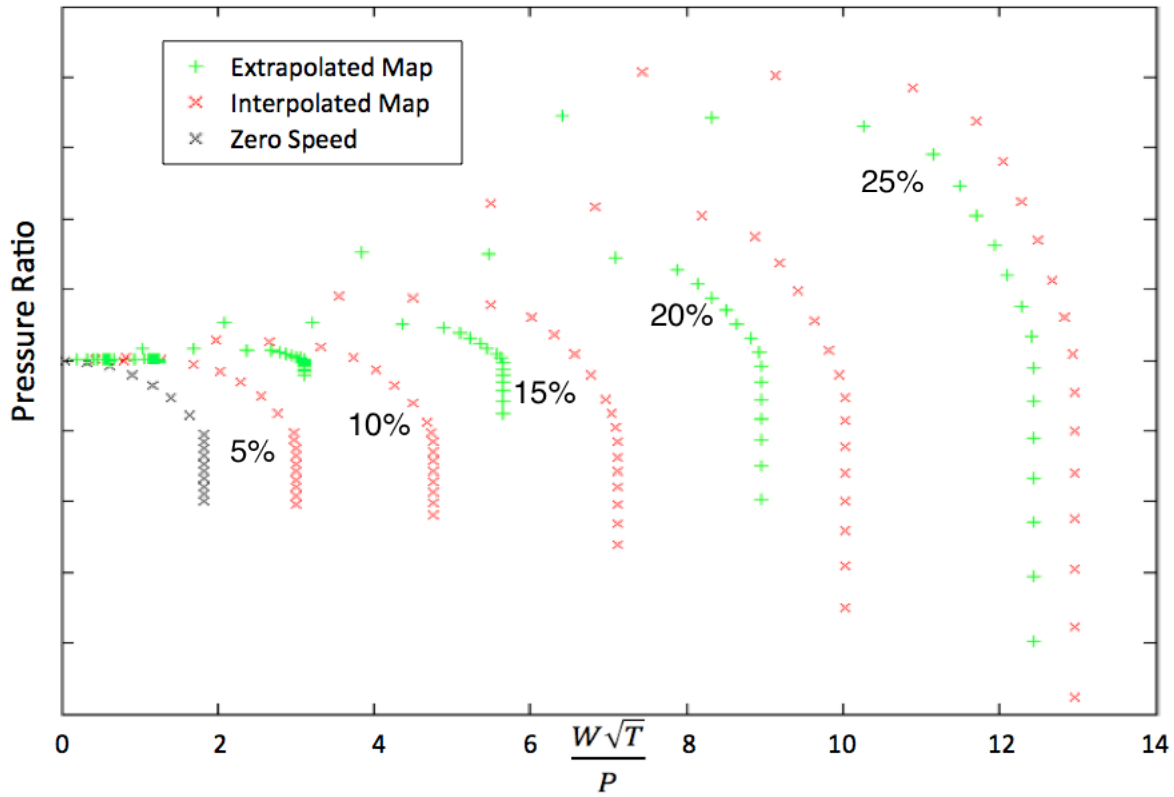

Figure 3.76: Comparison of a typical sub-idle compressor map generated with interpolation and extrapolation methodologies - speed lines shown as percentage of design speed

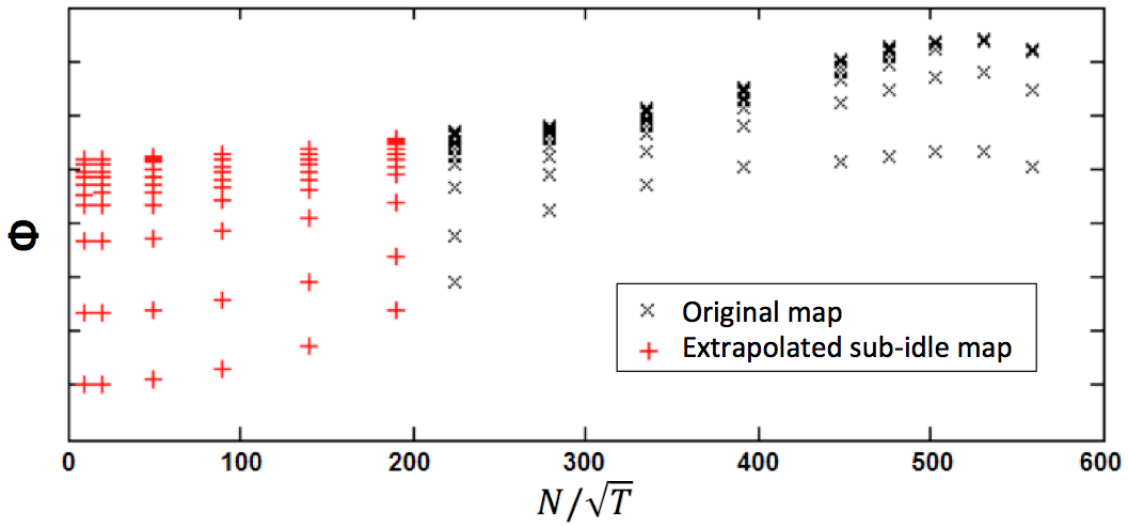

Figure 3.77: Compressor linearised flow parameter (ϕ) against $N/\sqrt{T}$ characteristics using extrapolation by Leitges [6]

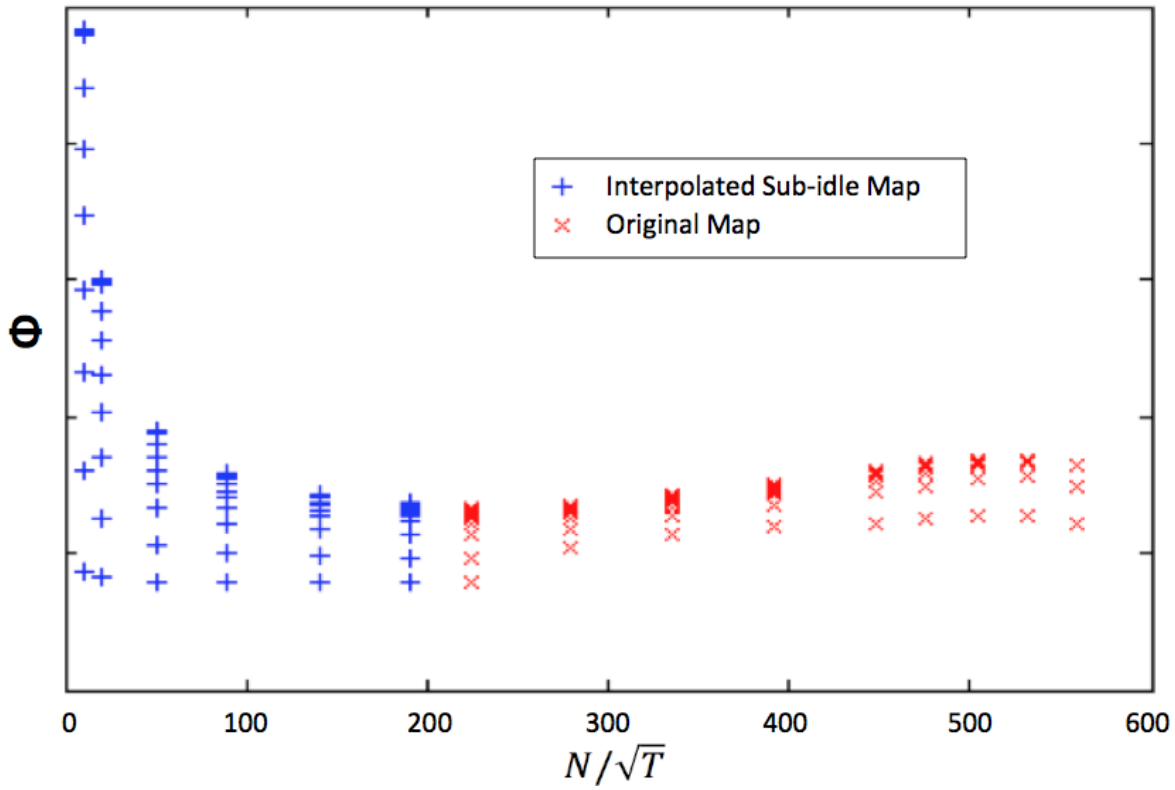

Figure 3.78: Compressor linearised flow parameter (ϕ) against $N/\sqrt{T}$ characteristics using zero-speed line prediction and interpolation

3.5 Concluding remarks

The numerical studies described within this chapter, were all aimed at understanding better the flow characteristics of a locked-rotor axial compressor blade in order to educate the stage-stacking compressor sub-idle map prediction code. Conclusions from the numerical work are highlighted in section 3.3.9. A new version of the compressor sub-idle map generating code was written to include the numerical results. To allow compressible flow calculations, the stage-stacking routine is based on isentropic flow equations, relying on Q functions and flow Mach number to calculate the properties at each stage. The flow deviation routine was updated to include Creveling and Carmody's [17] correlation, which was found to remain valid at high negative incidences. The code also uses a new database of blade coefficients, including values for high flow Mach numbers, as a function of the incidence, stagger and solidity of the blade. The reduction of flow effective area due to flow separation is factored in to predict more accurately the choking point, relying on the database extracted from compressible flow numerical simulations.

The maps generated were used within a whole engine performance solver, with results compared against engine test data. The results match very well for total pressure, but the mass flow is underestimated. There are a number of reasons for this discrepancy:

- The error is also significant when the solver starts using the original map. This indicates that the lowest speed lines on the original map are also inaccurate, which will create further errors in the interpolated sub-idle map.
- The code is based on half-stage numerical studies. Therefore the stage-stacking technique is very simplistic relative to the full compressor and is therefore not very accurate in modelling such complex flow.
- Blade-to-blade interaction was not studied. The code assumes that the flow mixes out before reaching the next blade row. This is of course not true as the numerical studies clearly indicate strong wakes at more that two chords downstream. The flow within the interstage gap therefore needs to be looked further into.

Chapter 4

Torque Based Whole Engine Sub-Idle Synthesis Solver

4.1 Introduction

In Chapter 3, the implications representing the compressor characteristics at low-speed due to it acting as a stirrer or turbine, were outlined. As described in [1], since it is not possible to use the standard definition of efficiency, sub-idle performance solvers use ϕ, ψ and ψ_{is} as defined in Eqns. (3.2), (3.3) and (3.4) to define turbomachinery characteristics. This however creates problems when the speed approaches zero since the values of ϕ, ψ and ψ_{is} asymptote up to infinity. Previous studies [49], [45], [5] concluded that the specific torque parameter (τ/P) is more suited for transient accelerating from zero-speed up through the engine's low-speed regime. The whole engine sub-idle performance synthesis solver therefore had to be converted to using engine parameters based on torque.

A description of the performance solver's overall structure, functionality and matching scheme is first given. This is followed by an overview of the current compressor and turbine sub-routines and a description of the conversion work carried out in converting them from linearised parameter-based, to torque based. The conversion of the compressor and turbine characteristics required by the new version of the solver is also given. The chapter concludes with a comparison of a performance simulation run with the original and torque-based solver, demonstrating that the functionality, which was validated

against engine test data by Moxon [23] and Monticelli [78], was not altered. Thus the new solver retains the original functionality whilst using parameters that are more suitable for low-power conditions.

4.2 Overview of engine sub-idle performance solver

Each engine manufacturer will have its own set of performance solvers, including a version for sub-idle simulations. These differ significantly between one another due to the different design philosophies and level of expertise. The solver used within this project is designed and used by the sponsoring company. Further details on its functionality can be found in [79] [80] [81]. The engine sub-idle performance solver is divided into various sub-routines. Most sub-routines are responsible for the performance calculations of the individual components, of which thermodynamic processes are calculated in the compressor, combustion, turbine and nozzle sub-routines. Figure 4.1 shows the main engine components with designated station numbering. Others routines resolve the engine matching scheme, steady state and transient calculations. Additional modules include duct losses, bleed flows, and intake characteristics amongst others. The solver has one main routine that links all the other various sub-routines. The engine is viewed as a set of interconnected gas flow passages and a major part of the definition of the engine performance is obtained from knowledge of the conditions pertaining at a number of stations in the gas flow (station data). These stations are usually at the beginning and the end of some definite physical feature of the engine, such as an intake, compressor, combustion chamber, turbine or nozzle. Each station stores the values for:

1. Fuel/Air ratio
2. Mass Flow
3. Pressure
4. Temperature
5. Velocity
6. Cross-sectional Area

Two further items $W\sqrt{T}/P$ and enthalpy are calculated and displayed only at output. These parameters are all stored in a common block so that they are easily accessible by each sub-routine. Each sub-routine requires inlet parameters to work out those at the outlet. Some of these are read from the component entry station, i.e. station data (e.g. total pressure at the compressor inlet). Other parameters that are specific to the component are provided through the engine matching routine and are called 'brick data', (e.g. power required from the turbine is provided through the matching brick after the compressor power is calculated). To build the engine model, the solver requires three main files: Cycle Definition File (CDF), Model Changes and Case Set as explained in the following sections.

4.2.1 Inputs and Outputs

The main input data required by the solver consists of the component characteristics, stored in the Cycle Definition File (CDF). A basic cycle definition file will include:

- Compressor map: $\phi, \psi, \psi_{is} = f(N/\sqrt{T}, \beta)$
- Turbine map: $\phi, \psi_{is} = f(N/\sqrt{T}, \psi)$
- Duct losses: $\Delta P/q = f(M)$
- Nozzle characteristics: Cv and $Cd = f(P/p)$
- Combustion efficiency characteristic: $\eta = f(\theta, W\sqrt{T}/P)$
- Starter characteristics: Torque $= f(N_{starter}, \text{Electrical power or } \Delta P/P)$

The CDF file should also contain initial guesses for the engine matching routine. A Model Changes file stores temporary changes in the engine characteristics in a similar manner as the CDF. By entering a different fuel schedule in the Model Changes file, a different start can be simulated without modifying the original baseline characteristics and settings. This is also useful when testing different powered starts or different scaling factors for the turbomachinery. The Case Set sets the engine operating condition by declaring the environmental (altitude, flight Mach number) settings, and engine settings (e.g. power setting, gear ratios, cut-out speeds). Once converged, the engine component parameters

such as rotational speed, mass flow, and total pressure at each station number can be plotted to analyse the engine's performance. Typical plots are shown in section 4.7 and chapter 9.

4.2.2 Engine matching algorithm

The engine matching routine enables the solution of a set of non-linear simultaneous equations. It uses a damped Quasi-Newton method to solve the iteration with numerical differencing to calculate partial derivatives for the variables listed in Table 4.1, and is called at the end of the iterative loop. An iterative loop can be set up for several variables and requirements (called matching quantities as listed in Table 4.2) but all of these parameters need not be used in a particular match.

The initial guesses for the connected variables are set in an array before the start of the matching loop, either from the Cycle Definition File or by direct calculation within the engine routine. Some of the matching quantities in a matching calculation will be used to ensure flow continuity or some other form of gas dynamics consistency, for example: mass flow at exit for low-pressure (LP) compressor is equal to mass flow at entry to HP Compressor, calculated effective nozzle area is equal to the geometric area multiplied by the discharge coefficient. The model matches by balancing spool torque and pressures, as opposed to the typical non-dimensional mass flow in other performance models. The calculation of required and available torque is illustrated in Fig. 4.2.

Pressure matching is used to minimise the case where if the flow matching was used, a negative pressure at the nozzle could be achieved at windmilling, which would invalidate the pressure momentum of flow passing through the engine. This case would not occur in above idle cases, where the nozzle exit total pressures and velocities will be higher than the ambient and assist in producing thrust.

Figure 4.1: Main engine station numbers

For transient simulations, a time-based input parameter is required - generally fuel flow. Modelling of non-steady state processes such as heat soakage and volume packing is introduced through dedicated sub-routines. Modelling of shaft inertia is also required for determining acceleration rates. The shaft inertia is also used within the starter motor sub-routine, which is not described here but further details can be found in [79].

Description	Units
LP shaft speed ^{2}	rpm^2
IP shaft speed ^{2}	rpm^2
HP shaft speed ^{2}	rpm^2
ESS inlet axial velocity ^{2}	$(ft/s)^2$
OGV inlet axial velocity ^{2}	$(ft/s)^2$
Fan Beta	
IPC Beta	
HPC Beta	
HPT Δ H / HP speed ^{2}	$CHU/lb/rpm^2$
IPT ΔH / IP speed ^{2}	$CHU/lb/rpm^2$
LPT ΔH / LP speed ^{2}	$CHU/lb/rpm^2$
Fuel flow	lbs/hr

Table 4.1: List of variables used by sub-idle performance solver for engine matching

Description	Units
IPC inlet total pressure	psia
HPC inlet total pressure	psia
HPT inlet total pressure	psia
IPT inlet total pressure	psia
LPT inlet total pressure	psia
Hot nozzle inlet total pressure	psia
Fan OGV inlet total pressure	psia
Cold nozzle inlet total pressure	psia
HP shaft torque	lb ft
IP shaft torque	lb ft
LP shaft torque	lb ft

Table 4.2: List of matching quantities used by sub-idle performance solver for engine matching

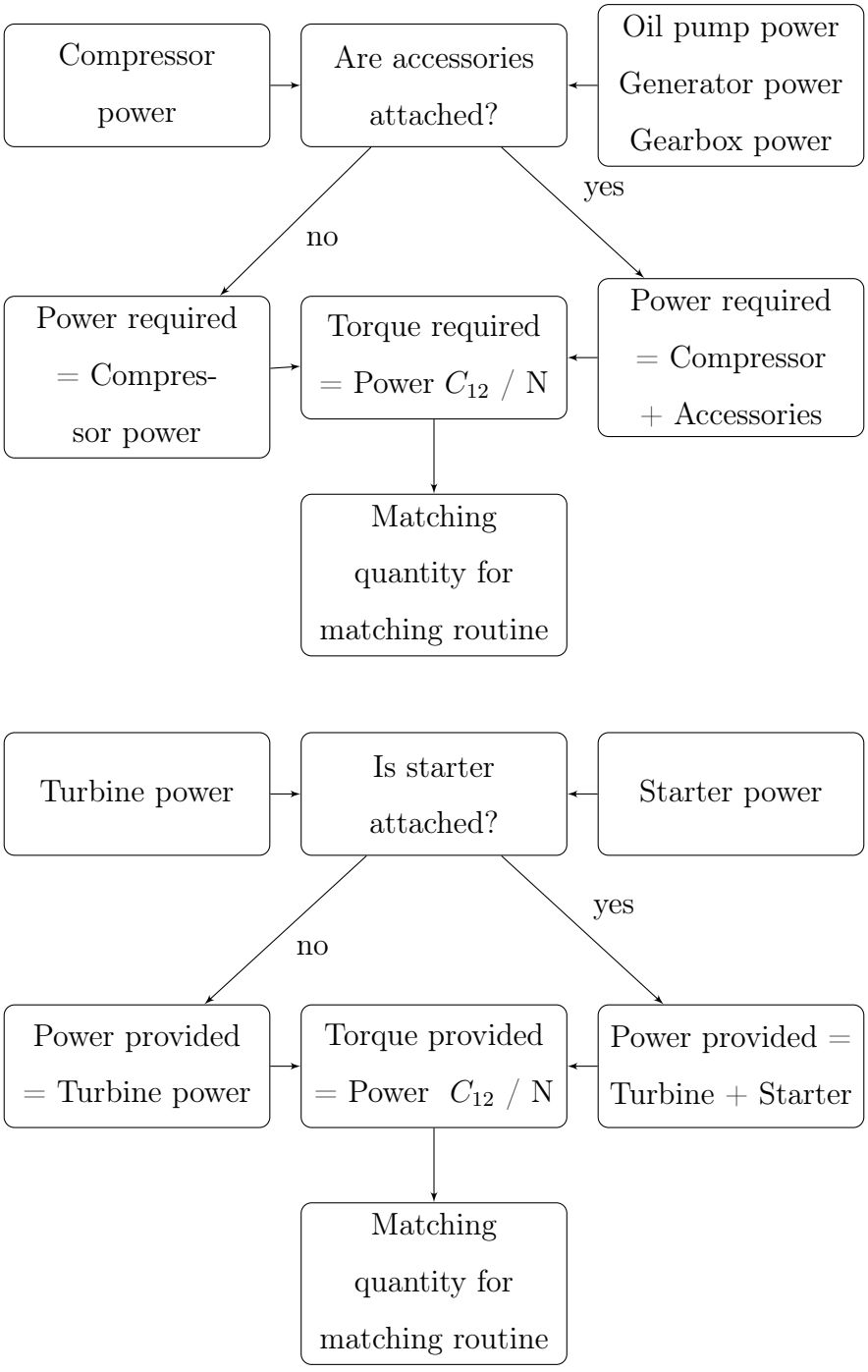

Figure 4.2: Calculation of torque parameters for engine matching routine

4.2.3 Conversion work

The original performance solver's engine matching brick uses torque and power to balance the compressor and turbine parameters. This brick therefore did not need any major modification. The work was more focused on the compressor and turbine bricks, since the equations and calculations within these bricks are based on linearised parameters. Apart from the modification of the bricks, the compressor and turbine characteristics were converted from linearised parameter based, to specific torque (τ/P), pressure ratio and speed ($N/\sqrt{T}$). The following sections describe the work undertaken, the methodology followed, and the results achieved starting from a description of how the original bricks worked.

A brief description of how the sub-routines work is given, emphasising on the parts that eventually were modified as part of the conversion to torque-based parameters. A number of sub-functions within the routines are considered confidential intellectual property of the sponsoring company. Consequently, some of them were not available to analyse, whilst others cannot be published. However, such parts of the sub-routines do not influence the work undertaken, and therefore their analysis is considered beyond the scope of this study.

4.3 Compressor

The compressor characteristics are provided to the performance solver in terms of ϕ, ψ and ψ_{is} as a function of beta lines (β) and non-dimensional speed ($N/\sqrt{T}$). The aim was to convert these to maps of quasi non-dimensional mass flow ($W\sqrt{T}/P$), pressure ratio and specific torque (τ/P) as a function of the beta parameter and non-dimensional speed. To operate, the compressor brick uses both station (see section 4.2) and brick data, which is tabulated in Table. 4.3. The station data is extracted from the common block.

Input No	**Parameter**	**Comments**
1.	$N/\sqrt{T}$	Can input 0.0
2.	β	Can input 0.0
3.	Not used	Can input 0.0
4.	Graph number for $W\sqrt{T}/NP$	–
5.	Graph number for $\Delta H/(N^2)$	–
6.	Graph number for $\eta\Delta H/(N^2)$	–
7.	Array position for factors and deltas	–
8.	Flow area for static pressure calculations	In sq inches

Table 4.3: Original compressor input brick data

A simplified flowchart of the linearised parameter-based compressor sub-routine is illustrated in Fig. 4.3. Initially starting from guessed values of $N/\sqrt{T_1}$ and β for the compressor, the routine extracts the values of ϕ, ψ and from the compressor characteristics provided in the Cycle Definition File. If the map is from a different compressor, scaling is done accordingly. The routine then proceeds to calculate Q, p_1, W_1 and ΔH from the characteristics. The compressor mass flow (W_1) is calculated through the flow parameter (ϕ) extracted from the characteristics, and the non-dimensional speed ($N/\sqrt{T}$) as shown in Eqn. (4.1).

$$W\sqrt{T}/P = \frac{W\sqrt{T}/P}{N/\sqrt{T}}\ N/\sqrt{T} = \phi\ N/\sqrt{T} \tag{4.1}$$

Pressure ratio is calculated as a function of inlet temperature and effective enthalpy rise $\eta\Delta H$. Gas composition in terms of the fuel-to-air ratio (FAR) is considered since this sub-function is used also for turbine calculations. However it has no effect on the compressor calculations. Efficiency is calculated as the ratio between ideal and effective enthalpy rise. Enthalpy at inlet is calculated as a function of inlet total temperature, whilst outlet total temperature is calculated from the enthalpy at outlet. Power is calculated from the mass flow rate and enthalpy rise using Eqn. (4.2). It is converted from CHU/s to horsepower using C_{15}. Station output data (P_2, T_2, W_2 and H_2) is subsequently stored in an array and act as inputs for the component downstream. After using the initial guesses, the solver iterates values of $N/\sqrt{T_1}$ and β until the power between the compressor and the respective turbine, is balanced. Table. 4.4 gives a list of the output brick data. Not all the values are required by the engine matching scheme. Outputs 3, 8, 9 and 10 are used merely for diagnostic purposes.

Output No	**Parameter**	**Units used**
1.	Compressor power	h.p.
2.	Compressor pressure ratio	
3.	Compressor efficiency	(as a fraction)
4.	Compressor $\Delta H/T$	$C.H.U/lbK$
5.	Compressor speed	$r.p.m.$
6.	Compressor inlet $N/\sqrt{T}$	$r.p.m./\sqrt{K}$
7.	Compressor beta (β)	$-$
8.	Compressor WT/NP	$(lbs/sec)K/(r.p.m. * p.s.i.a.)$
9.	Compressor $\Delta H/N^2$	$C.H.U./lbr.p.m^2$
10.	Compressor $\eta\Delta H/N^2$	$C.H.U./lbr.p.m^2$

Table 4.4: Original compressor output brick data

$$\text{Power} = W\ \Delta H\ C_{15} \tag{4.2}$$

where C_{15} is a constant to convert power from CHU/s to horse power

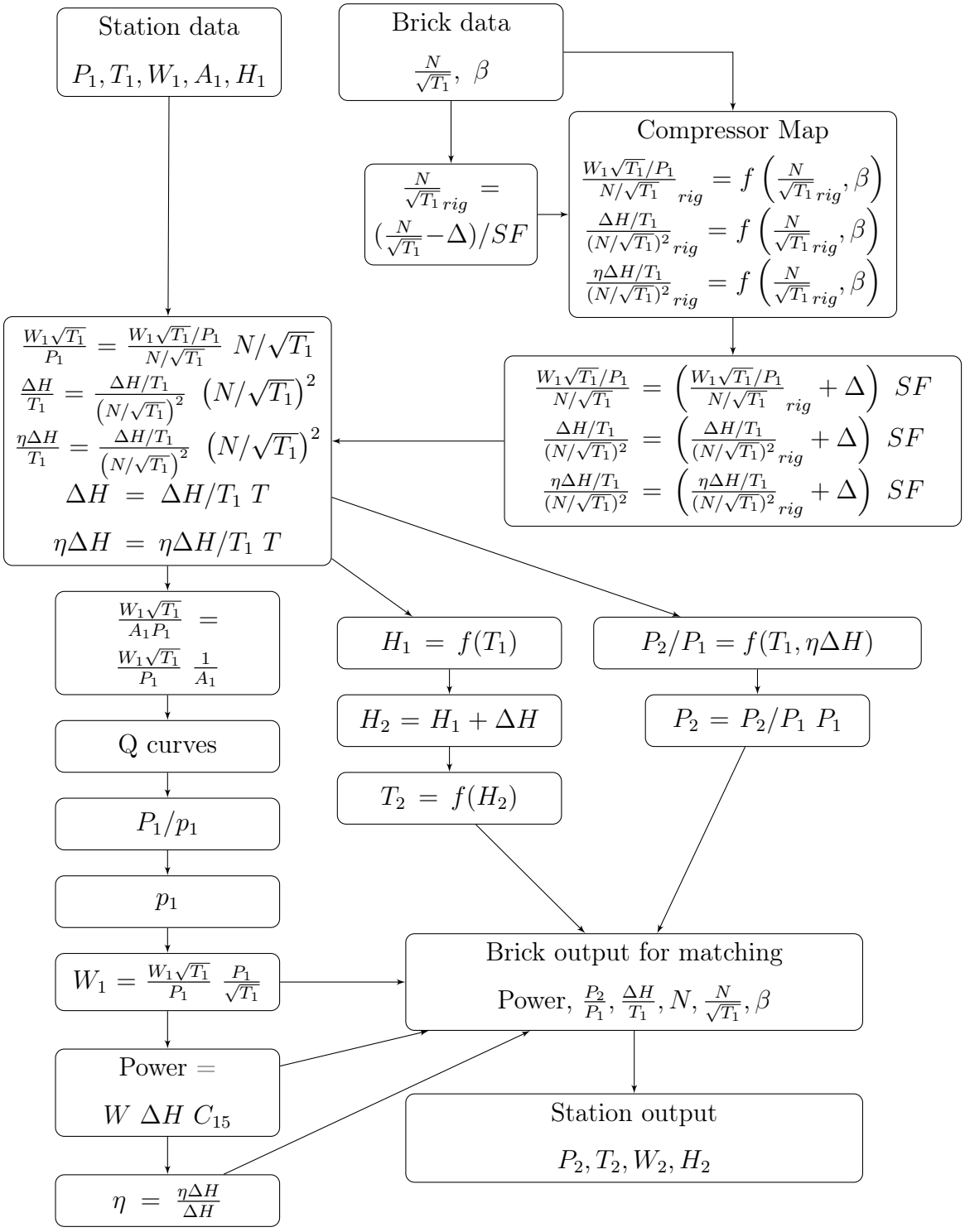

Figure 4.3: Simplified overview of linearised parameter-based compressor sub-routine

4.3.1 Modification of Compressor Brick

The solver was modified so that the brick reads directly values of non-dimensional mass flow ($W\sqrt{T}/P$), pressure ratio and specific torque (τ/P) from characteristics based on non-dimensional speed ($N/\sqrt{T}$) and the beta parameter (β) as illustrated in Fig. 4.4. This required that the characteristics be converted as well, which is explained in section 4.3.2. The enthalpy rise is also extracted from specific torque, and then used to calculate the inlet total temperature. Compressor power is calculated through the specific torque using Eqn. (4.3). This was done to eliminate the need for calculating the enthalpy change and to rely more on the torque parameter.

The total pressure rise across the compressor is not provided directly from the characteristics. Using compressor inlet to outlet total pressure ratio directly instead of calculating it from isentropic efficiency, enthalpy rise, and the fuel-to-ratio (which considers the gas composition and hence the changes in specific heat capacity (c_p) and ratio of specific heats (γ)) did not introduce any errors since there is no fuel present in the compressor and the power range considered is too low for the specific heats to change significantly. However this assumption is no longer valid for above-idle simulations, as calculated in Maini [76].

$$\text{Power} = \frac{\tau}{P}\ \frac{N}{\sqrt{T}}\ P\ \sqrt{T}\ \frac{\pi}{30}\ C_{15} \tag{4.3}$$

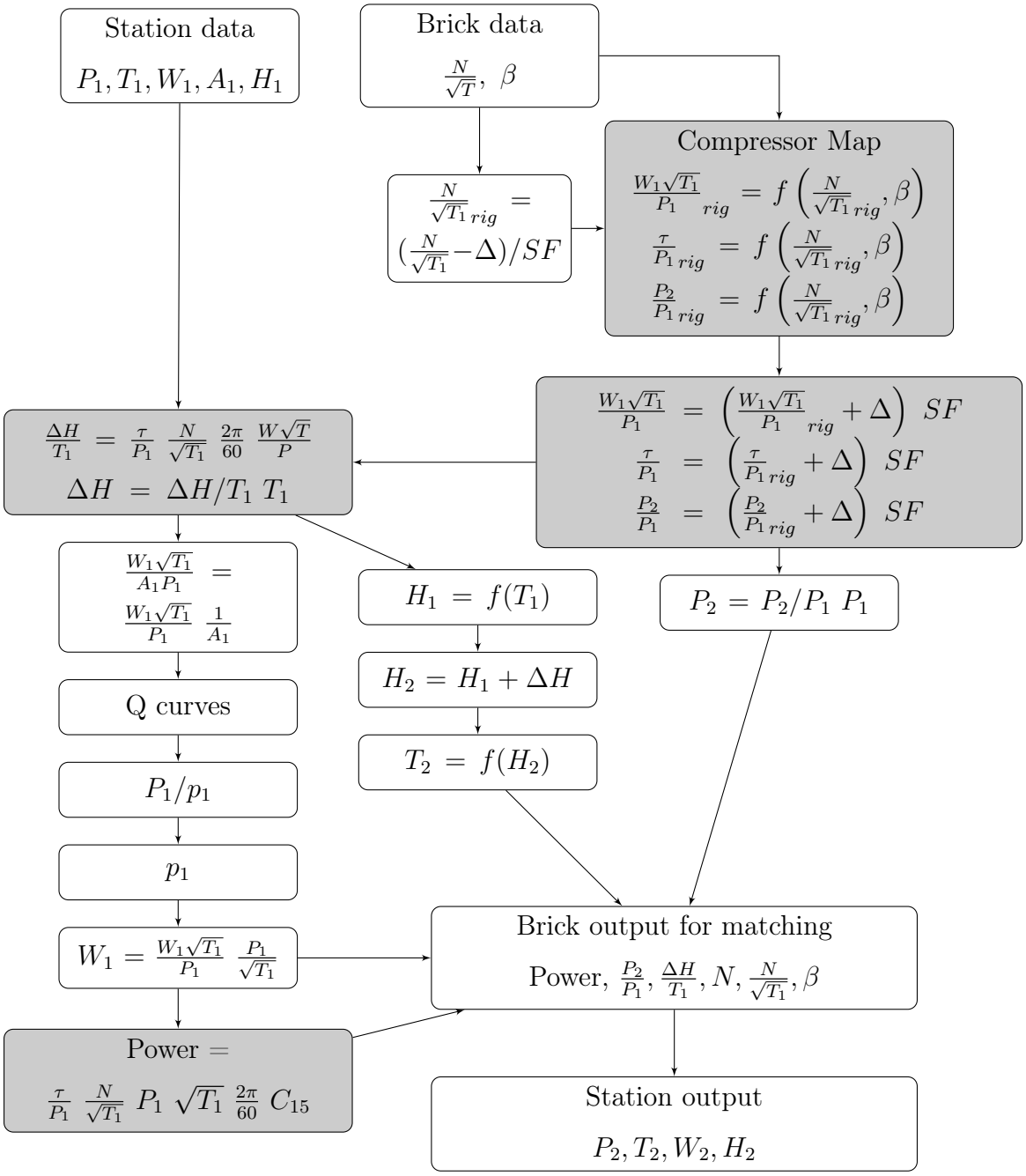

Figure 4.4: Simplified overview of new torque-based compressor sub-routine (changes to original solver in grey boxes)

4.3.2 Conversion of Compressor Characteristics

Conversion of the compressor characteristics is facilitated by the fact that the graphs are based on the β parameter. The conversion from linearised to conventional parameters is explained below.

Specific Torque

Specific torque can be calculated using Eqn. (3.6).

Non-Dimensional Mass Flow

As given in Eqn. (4.1)

Pressure Ratio

Starting from the definition of isentropic efficiency for a compressor:

$$\eta_{is} = \frac{\left(\frac{P_2}{P_1}\right)^{\frac{\gamma}{\gamma-1}} - 1}{\frac{T_2}{T_1} - 1} \quad \text{or} \quad \left[\eta_{is}\left(\frac{T_2}{T_1} - 1\right) + 1\right]^{\frac{\gamma}{\gamma-1}} = \frac{P_2}{P_1} \tag{4.4}$$

$$\Delta H = C_p\left(T_2 - T_1\right) \quad \text{or} \quad \frac{\Delta H}{T_1 C_p} = \frac{T_2}{T_1} - 1 \tag{4.5}$$

For compressors:

$$\eta_{is} = \frac{\psi_{is}}{\psi} \tag{4.6}$$

Also:

$$\frac{\Delta H}{T_1} = \frac{\Delta H/T_1}{\left(N/\sqrt{T_1}\right)^2} \ \left(N/\sqrt{T_1}\right)^2 = \psi \ \left(N/\sqrt{T_1}\right)^2 \tag{4.7}$$

and therefore, pressure ratio expressed as a function of linearised parameters:

$$\frac{P_2}{P_1} = \left[\frac{\psi_{is}\ (N/\sqrt{T})^2}{C_p} + 1\right]^{\frac{\gamma}{\gamma-1}} \tag{4.8}$$

An example conversion for a high-pressure compressor is given in Fig. 4.5.

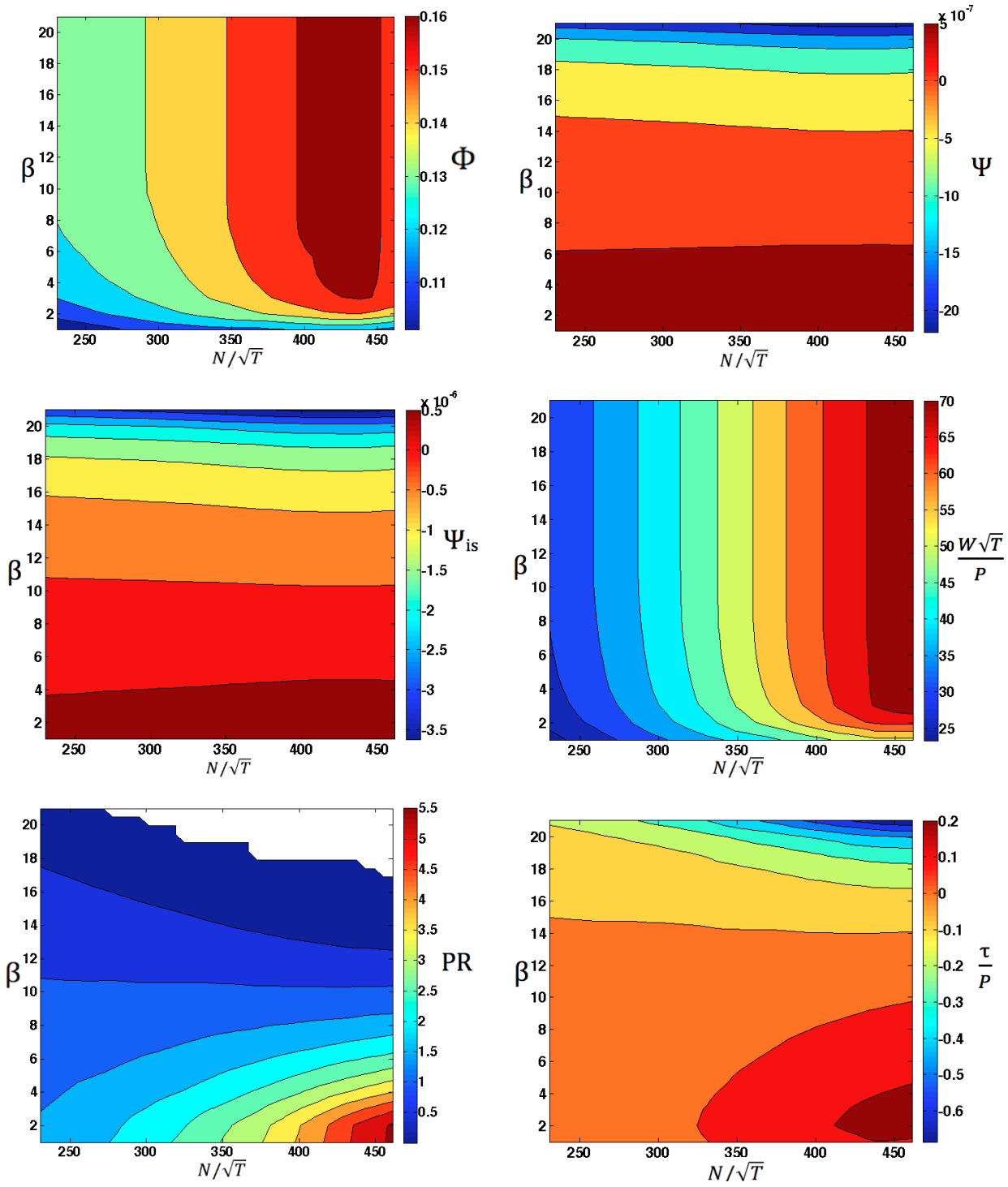

Figure 4.5: Compressor characteristics in linearised format (ϕ, ψ and ψ_{is}), and converted to conventional format (non-dimensional mass flow, pressure ratio and specific torque)

4.4 Turbine

The turbine characteristics are provided to the performance solver in terms of ϕ and ψ_{is} as a function of ψ and non-dimensional speed ($N/\sqrt{T}$). The aim was to convert these to maps of non-dimensional mass flow ($W\sqrt{T}/P$) and pressure ratio as a function of specific torque and non-dimensional speed. To operate, the turbine brick uses both station and brick data, which is tabulated in Table 4.5. The station data is extracted from the common block (as explained in section 4.2). The following is a list and explanation of the brick data used:

Input No	**Parameter**	**Comments**
1.	Turbine power in h.p	Usually not used
2.	Turbine $\Delta H/N^2$	Can input 0.0
3.	Turbine $N/\sqrt{T}$	Can input 0.0
4.	Graph number for WT/NP	–
5.	Graph number for $\Delta H/(\eta N^2)$	–
6.	Graph number for swirl	–
7.	Array position for factors and deltas	–
8.	Flow area for static pressure calculations	In sq inches

Table 4.5: Original turbine input brick data

Calculations were based on the turbine enthalpy change ($\Delta H/N^2$) provided by the matching brick. The turbine brick has the option of specifying either a turbine power or a ($\Delta H/N^2$). Item 2 picks up a value from the matching brick input, overwriting any turbine input for item 2 in the deck. Therefore a zero value can be inserted. If a non-zero value is input as item 1 then the turbine brick will calculate a value of $\Delta H/N^2$ from this power. Item 3 picks up a value calculated from the matching brick and inlet temperature, overwriting any turbine input that exists for item 3 in the deck, and so a zero value can be inserted. The required graph numbers for items 4, 5 and 6 are the graph number that the solver refers to for reading turbine characteristics. Factors and deltas, as for the compressor, are used to scale the map characteristics.

An overview of the linearised parameter-based turbine subroutine is illustrated in Fig. 4.6 where after following any scaling (if required), the brick input data ψ and $N/\sqrt{T}$ are used to extract ψ_{is} and ϕ from the turbine characteristics provided in the Cycle Definition File. The non-dimensional mass flow and enthalpy change is calculated using Eqns. (4.9) and (4.10) respectively.

$$\frac{W\sqrt{T}}{P} = \frac{W\sqrt{T}/P}{N/\sqrt{T}} \frac{N}{\sqrt{T}} = \phi \frac{N}{\sqrt{T}} \tag{4.9}$$

$$\frac{\Delta H/T}{\eta} = \left(\frac{\Delta H/T}{\eta(N/\sqrt{T})^2}\right) \left(\frac{N}{\sqrt{T}}\right)^2 T = \psi_{is} \left(\frac{N}{\sqrt{T}}\right)^2 T \tag{4.10}$$

The turbine pressure ratio (or expansion ratio) is calculated as a function of fuel-to-air ratio, total inlet temperature and $\Delta H/\eta$ through a separate sub-routine. Turbine efficiency and power are calculated using Eqns. (4.11) and (4.12) respectively. Table 4.6 shows the sub-routine's brick output data.

$$\eta = \frac{\Delta H/\eta T}{(\Delta H/T)} = \frac{\psi}{\psi_{is}} \tag{4.11}$$

$$\text{Power} = W\ \Delta H\ C_{15} \tag{4.12}$$

Output No	**Parameter**	**Units used**
1.	Turbine power	h.p.
2.	Turbine pressure ratio	
3.	Turbine efficiency	(as a fraction)
4.	Turbine $\Delta H/T$	$C.H.U/lbK$
5.	Turbine speed	$r.p.m.$
6.	Turbine inlet $N/\sqrt{T}$	$r.p.m./\sqrt{K}$
7.	Turbine exit swirl angle	in degrees
8.	Turbine WT/NP	$(lbs/sec)K/(r.p.m. * p.s.i.a.)$
9.	Turbine $\Delta H/N^2$	$C.H.U./lbr.p.m^2$
10.	Turbine $\Delta H/\eta N^2$	$C.H.U./lbr.p.m^2$

Table 4.6: Original turbine output brick data

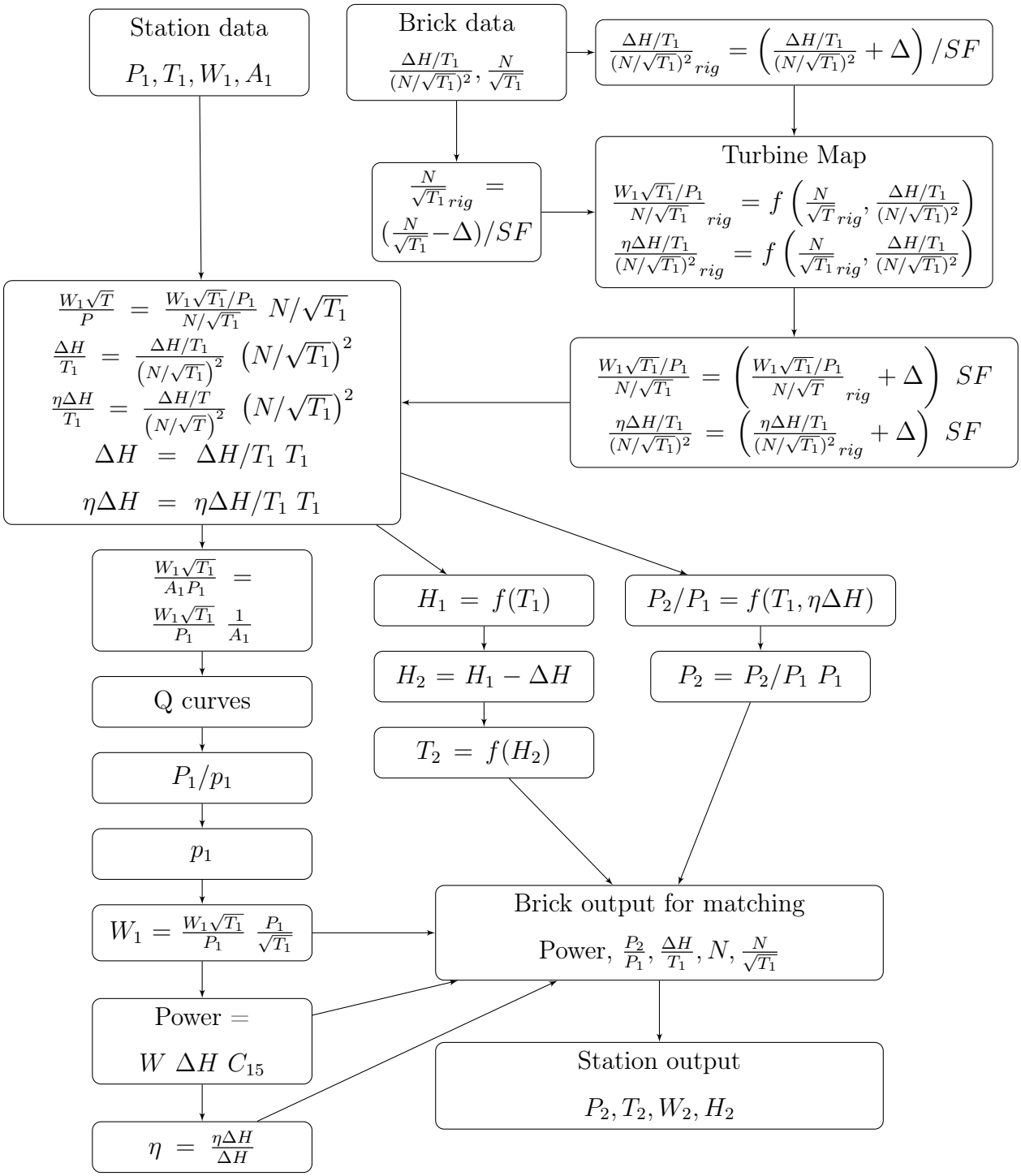

Figure 4.6: Simplified overview of linearised parameter-based turbine sub-routine

4.4.1 Modification of Turbine Brick

Specific Torque and Power

If the turbine brick uses power provided from the matching brick (input item 1), then the torque can be directly derived from the power using Eqn. (4.13). This is the ideal method since it would eliminate the need of the input enthalpy term ($\Delta H/N^2$) which would create problems at very low speeds due to the speed term in the denominator.

$$\frac{\tau}{P} = \frac{\text{Power } C_{12}}{P\ N} \tag{4.13}$$

where C_{12} is used to convert torque to power (33,000 ft.lbf/min)/(2π rad/rev)

It is possible to calculate torque through the enthalpy term ($\Delta H/N^2$) using Eqn. (4.14). This option was however not introduced, leaving torque to be calculated from power.

$$\frac{\tau}{P} = W\ \frac{\Delta H}{T}\ C_{12}\ C_{15}\ \frac{1}{P}\ \frac{1}{N}\ T \tag{4.14}$$

Specific torque is used to look up the turbine expansion ratio and non-dimensional mass flow characteristics, eliminating the use of ϕ and ψ_{is}, as illustrated in Fig. 4.7 where an overview of the new torque-based routine is given. This requires the characteristics to be converted from ϕ and ψ_{is} as a function of non-dimensional speed and ψ, to $W\sqrt{T}/P$ and pressure ratio as a function of specific torque and non-dimensional speed, as explained in section 4.4.2. Specific torque was used to calculate the turbine output power using Eqn. (4.15), substituting the original enthalpy based calculation (Eqn. (4.12)).

$$\text{Power} = \frac{\tau}{P}\ P\ N\ \frac{1}{C_{12}} \tag{4.15}$$

Calculating the wrong torque could result in the correct turbine power since Eqn. (4.15) is a re-arrangement of Eqn. (4.13). To check for errors, Eqn. (4.12) was used temporarily to ensure that the torque was correctly estimated, since otherwise the ΔH would be incorrect and would show in the simulation results.

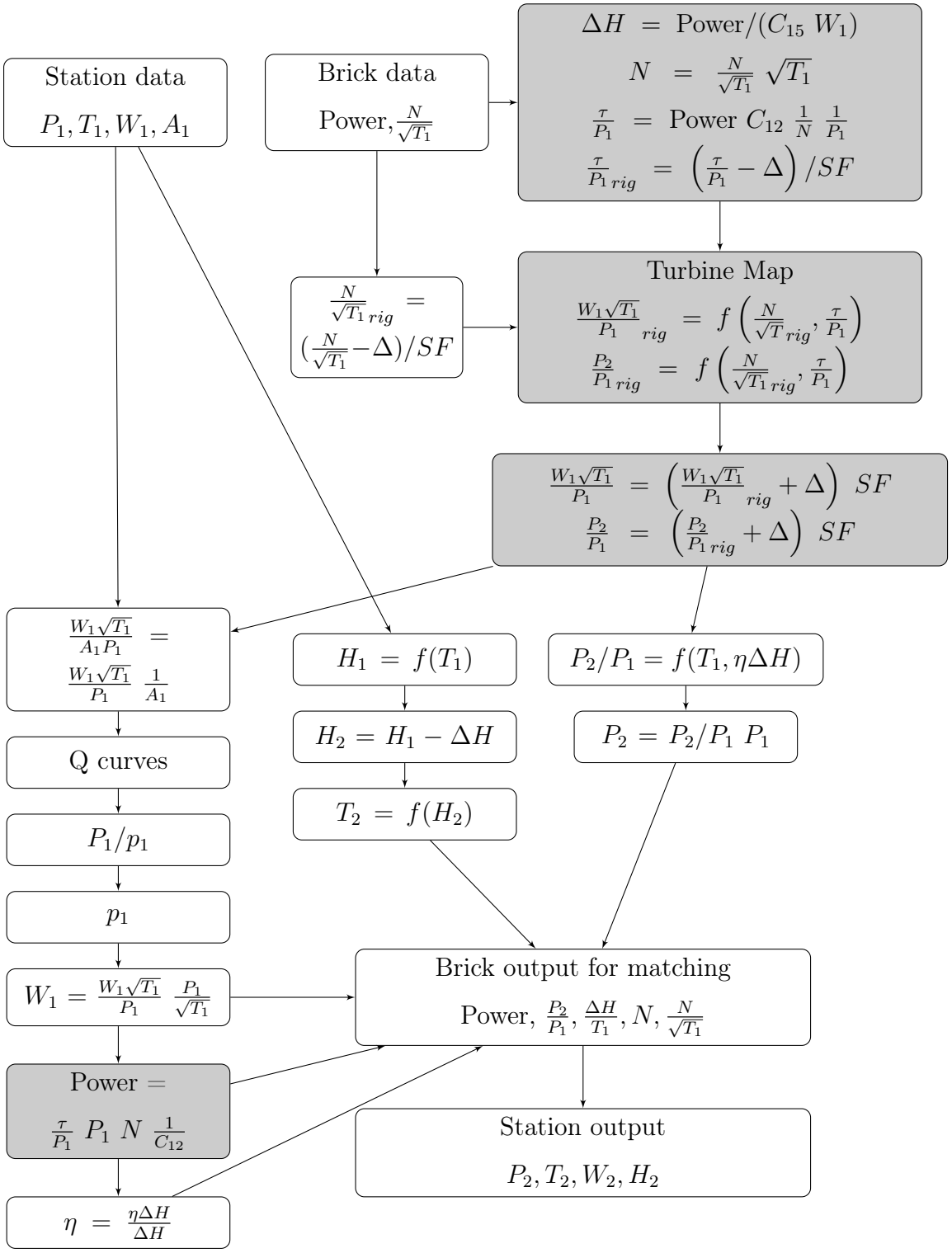

Figure 4.7: Simplified overview of new torque-based turbine sub-routine (changes to original solver in grey boxes)

Introducing pressure ratio directly

The original turbine brick calculated expansion ratio as a function of the turbine efficiency and air-to-fuel ratio, taking into account the gas composition within a separate sub-routine. To introduce pressure ratio as an input parameter from turbine characteristics, the pressure ratio has to be calculated directly from the original linearised parameters. Whilst this process is straight forward, Eqn. (4.22) includes the gas properties: specific heat capacity (c_p) and the ratio of specific heats (γ). These properties are not constant in the turbine, since the temperature and gas composition will vary as the engine accelerates. It was necessary to estimate how much error is introduced, assuming constant gas properties. Removing the brick that calculates turbine expansion ratio and replacing it by the simpler Eqns. (4.21) and (4.22), turbine work (ψ) and efficiency (ψ_{is}) parameters were used directly. Results in Fig. 4.8 illustrate that there is no error at low speeds, whilst the effect of maintaining constant gas properties becomes more evident as the engine accelerates to idle. The error is relatively low and the effect on the engine transient in terms of expansion ratio and shaft speeds is acceptable (1.5% for high pressure turbine (HPT) expansion ratio and 0.4% for HPT shaft speed). Further improvements of the turbine sub-routine could address this issue by factoring the expansion ratio as a function of the gas properties, and reduce the error.

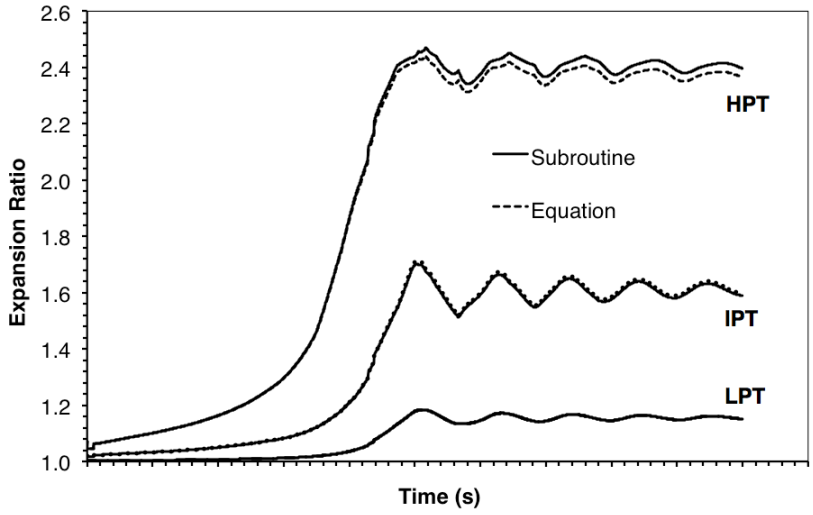

Figure 4.8: Comparison of turbine expansion ratios calculated through the original subroutine and the simple equation - engine groundstart simulation to idle speed

4.4.2 Conversion of Turbine Characteristics

In order to accommodate the new torque-based brick, the turbine characteristics had to be converted to remove the dependency on the rotational speed as shown in Fig. 4.9. Specific torque, pressure ratio and non-dimensional mass flow were extracted from the original maps using the following process:

Specific Torque

Similar to the compressor, Eqn. (3.6) is used to derive specific torque from the linearised parameters.

Non-Dimensional Mass Flow

Similar to the compressor, Eqn. (4.1) is used to calculate the turbine non-dimensional mass flow.

Pressure Ratio

$$T_4 - T_5 = T_4\ \eta\ \left[1 - \left(\frac{P_5}{P_4}\right)^{\frac{\gamma-1}{\gamma}}\right] \quad \text{or} \quad 1 - \frac{T_5}{T_4} = \eta\ \left[1 - \left(\frac{P_5}{P_4}\right)^{\frac{\gamma-1}{\gamma}}\right] \tag{4.16}$$

$$\Delta H = C_p\,(T_4 - T_5) \quad \text{or} \quad \frac{\Delta H}{T_4 C_p} = 1 - \frac{T_5}{T_4} \tag{4.17}$$

Therefore, pressure ratio can be expressed as:

$$\frac{P_5}{P_4} = \left(1 - \frac{\Delta H/T_4}{\eta C_p}\right)^{\frac{\gamma}{\gamma-1}} \tag{4.18}$$

For turbines:

$$\eta = \frac{\psi}{\psi_{is}} \tag{4.19}$$

Also:

$$\frac{\Delta H}{T_4} = \frac{\Delta H/T_4}{\left(N/\sqrt{T_4}\right)^2}\ \left(N/\sqrt{T_4}\right)^2 = \psi\ \left(N/\sqrt{T_4}\right)^2 \tag{4.20}$$

and therefore:

$$\frac{P_5}{P_4} = \left[1 - \frac{\psi\ \left(N/\sqrt{T_4}\right)^2}{\psi/\psi_{is}\ C_p}\right]^{\frac{\gamma}{\gamma-1}} \tag{4.21}$$

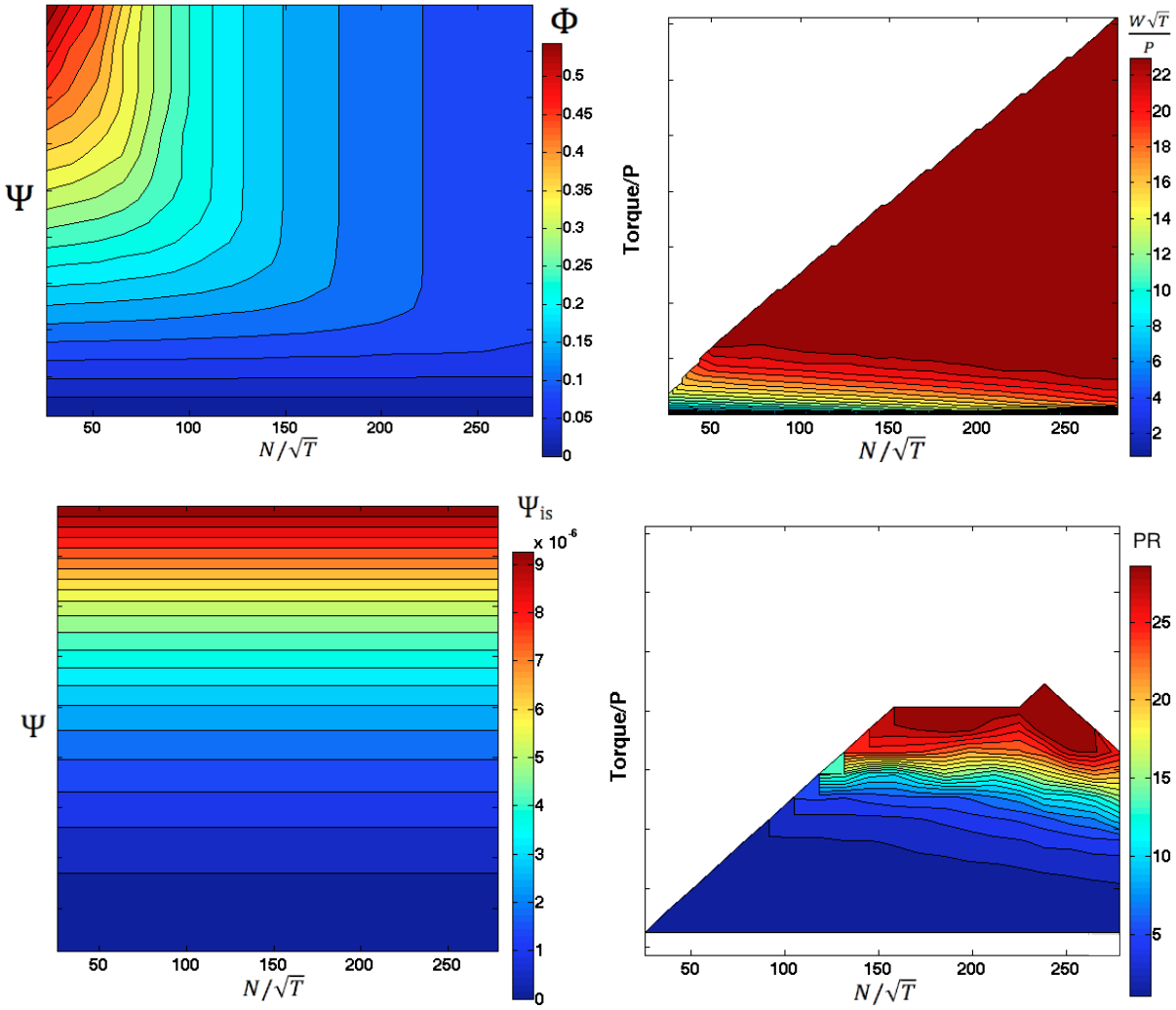

Figure 4.9: Conversion of turbine characteristics: from (left) ϕ and ψ_{is} in terms of non-dimensional speed ($N/\sqrt{T}$) and ψ to (right) quasi non-dimensional mass flow ($W\sqrt{T}/P$) and pressure ratio in terms of non-dimensional speed ($N/\sqrt{T}$) and specific torque (τ/P)

Performance solvers however use the turbine expansion ratio rather than the pressure ratio. Therefore the reciprocal of the value given in Eqn. (4.21) is used:

$$\text{Expansion Ratio} = \frac{P_4}{P_5} \tag{4.22}$$

The conversion of the compressor maps was facilitated by the characteristics being based on the independent β parameter, resulting in the original grid for the x and y axes parameters being maintained. For the turbine, this is not the case. Converting from ϕ to $W\sqrt{T}/P$ and from ψ_{is} to pressure ratio as a function of the original work parameter (ψ) and non-dimensional speed ($N/\sqrt{T}$) was successful, obtaining the same results as for the original linearised-based solver.

However, converting these characteristics to specific torque (τ/P) based distorts the original grid form of the x and y axes, as shown in Fig. 4.10. The solver requires the data in a tabular form and therefore the scattered torque-based turbine characteristics had to be manipulated into a grid form.

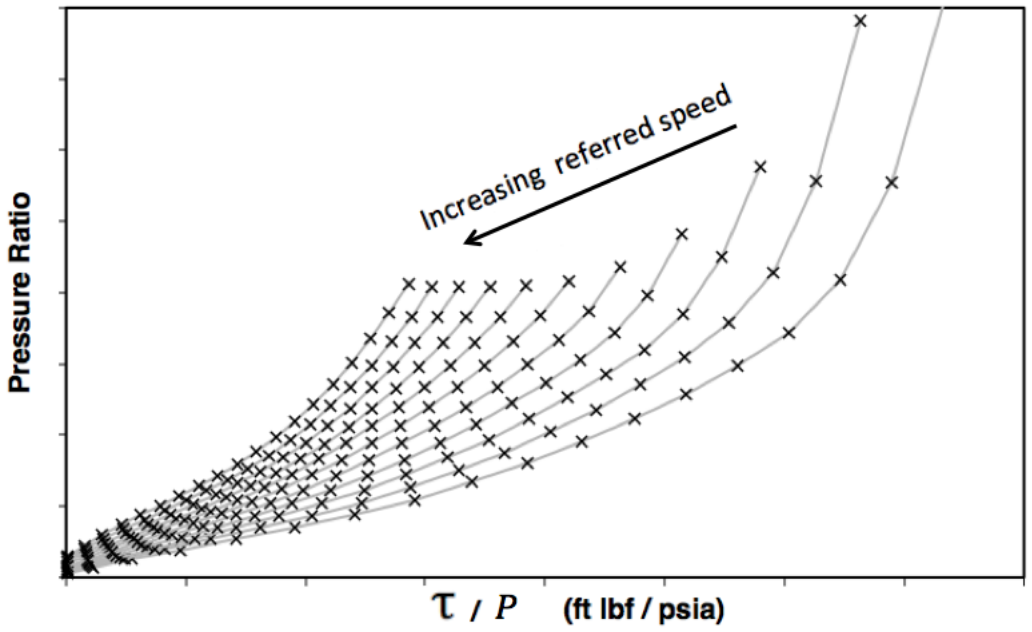

Figure 4.10: Turbine pressure ratio = f(specific torque, non-dimensional speed); map is not aligned to a uniform grid and needs to be manipulated

This was done through a Matlab script using the 'TriScatteredInterp' function [82]. TriScatteredInterp [82] is used for interpolation on a scattered dataset in a 2D or 3D space using a Delaunay triangulation. The script first determines the limits of the x and y axes, and then distributes the intermediate values equally, creating a uniformly spaced grid. The size of the grid is user-defined and was set to 50, which is the maximum limit that the performance solver can accept. The script then reads the scattered data and creates an interpolant that fits a surface of the form $V = F(X, Y)$ to the scattered data, where F is the surface function. Using the newly created grid and the surface function, the script then generates a new set of data, this time equally spaced over a uniform grid.

An example for the turbine semi non-dimensional mass flow is given in Fig. 4.11(a) where it can be observed that the original data is not distributed evenly in grid form. In this example, 150 points in grid form were generated using the TriScatteredInterp function. A 3D view of the map is given in Fig. 4.11(b) to show clearly the function fitted to the data points.

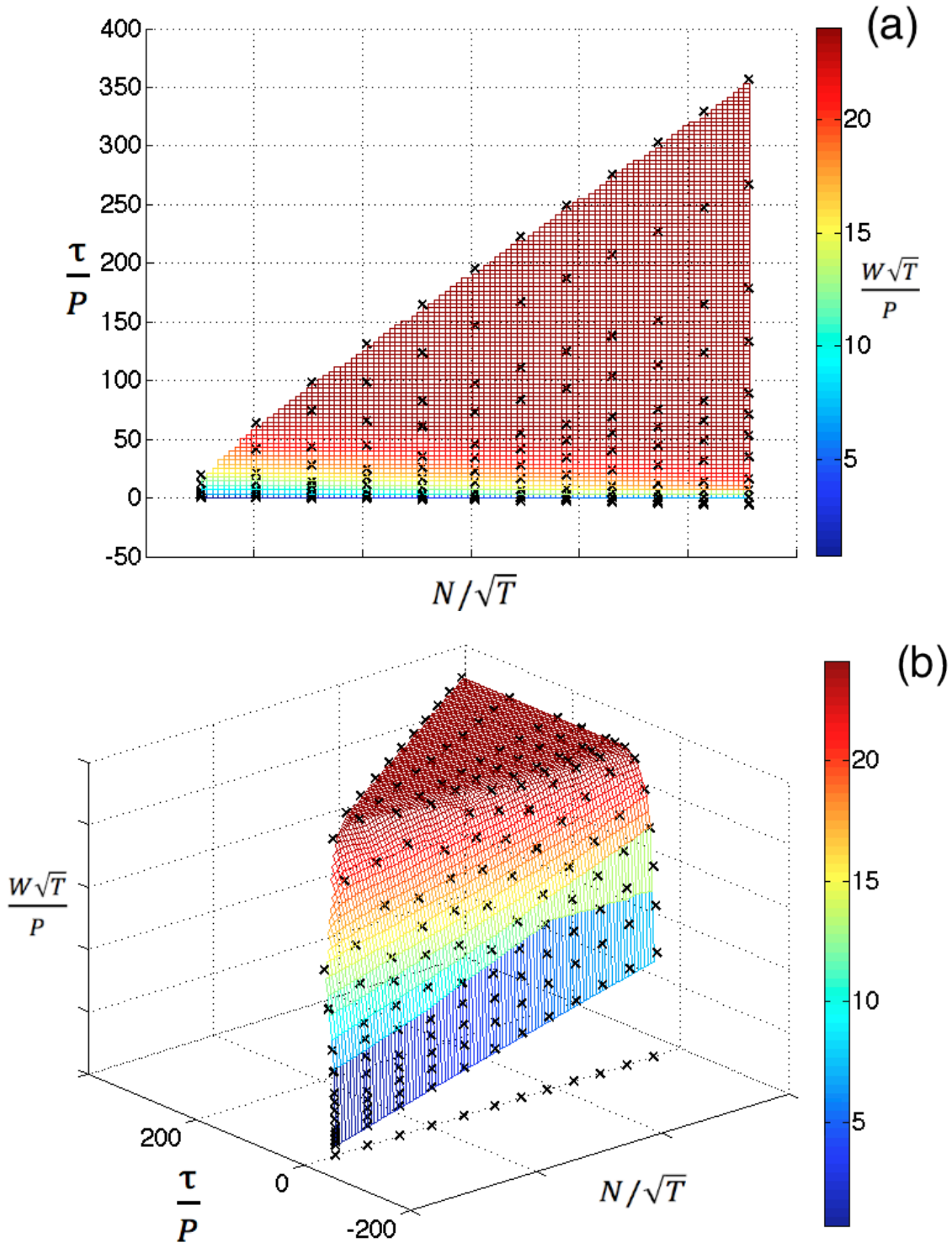

Figure 4.11: Turbine semi non-dimensional mass flow characteristic as a function of specific torque and non-dimensional speed after manipulation with the Matlab TriScatteredInterp script to distribute the scattered data onto a uniformly spaced grid.

4.5 Scaling factors

Scaling factors are used when the turbomachinery characteristics introduced into the solver are not the ones of the actual component used. If the components are of the same technology level, the difference between them would generally be in capacity and pressure ratio. It is therefore acceptable to use a different component map and scale it to represent the one being simulated. Less common is the use of deltas, where the whole map is shifted by a certain value. Scaling factors are introduced for flow (ψ), non-dimensional speed ($N/\sqrt{T}$), work (ψ) and efficiency (ψ_{is}). Due to the conversion work done to the performance solver, the new scaling factors had to be calculated.

Compressor

- Speed

The non-dimensional speed did not require modification since it is common for both the linearised and the conventional parameter systems. Therefore the original non-dimensional speed scaling factor (CN) is maintained.

- Flow

The compressor flow scaling factor (CW) is calculated by simply multiplying it with the speed scaling factor, as shown below.

$$CW_{WrTP} = CW_{\phi}\ CN \tag{4.23}$$

- Pressure ratio

The scaling factor for pressure ratio between the rig data compressor and the compressor being modelled should be known. Generally for similar compressors of the same manufacturer, this value is close to unity.

- Specific torque

Using the equation for calculating the specific torque (Eqn. (3.6)), the scaling factor (CT) can be calculated through the flow (CW_{ϕ}), work (CH) and speed (CN) original scaling factors through Eqn. (4.24).

$$CT = CW_{\phi}\ CH\ CN^2 \tag{4.24}$$

Turbine

- Speed

As for the compressor, the non-dimensional speed was not modified, and therefore the original non-dimensional speed scaling factor (CN) is maintained.

- Flow

As for the compressor, the new turbine flow scaling factor (CW_{WrTP}) is calculated by simply multiplying it with the speed scaling factor (CN), as shown in Eqn. (4.23).

- Pressure ratio

As for the compressor, the scaling factor for pressure ratio between the rig data turbine and the turbine being modelled should be known and generally this value is close to unity for turbines of similar design and technology level.

- Specific torque

The specific torque substituted the work parameter (ψ), however these are essentially representing the same entity, and thus the same scaling factor as for the work parameter (CH) is used.

4.6 House keeping modifications

Since the solver is used within the sponsoring company, it was vital that the modifications done were in line with the company coding standards.

- Parameter switch

The sponsoring company's performance solver is standardised, with each brick named specifically for a particular function. Following a discussion with the industrial supervisors, it was decided that the modifications should not be implemented as completely new bricks. Rather, the current bricks should be updated to accommodate the new capability. This would avoid creating new non-standard brick names.

To do so, a switch (named SWCPAR) was inserted in the main routine and the compressor and turbine sub-routines which allows the user to switch between using linearised parameter version (SWCPAR = 1.0), or the torque-based parameter version (SWCPAR = 2.0). The user can change the value of the switch in the Case Set file.

- Torque value output

Even though provision for swirl calculations is included in the original turbine brick, this is not normally used. Following the modification of the brick, it was felt that the value of the torque calculated is more important, and therefore item 7 in the output brick data was set to give the specific torque calculated.

- Scaling factors

Once the solver was converted to torque, the scaling factors for work (CH) and pressure (CHI) coefficients were no longer required. The solver was written in such a way that when the parameter switch is set to conventional (SWCPAR = 2.0), these scaling factors are interpreted as the specific torque (CT) and pressure ratio (CP) scaling factors respectively. The user therefore has to make sure that the values are accordingly changed when switching from linearised to torque mode.

4.7 Validation of the torque-based performance solver

The criterion used to validate the modifications and upgrades made to the solver was that the results should be identical to those produced by the original linearised parameter-based version. The original version was already successfully validated against engine experimental data by Moxon [23]. To ease troubleshooting, the compressor and turbine bricks were tested separately. The modification of the compressor brick and the conversion of the characteristics resulted in the solver giving identical results to the original version. During the validation process for the turbine, it was found that the quality of the original turbine map influenced the results. Certain combinations of the values read from the original map would result an undefined number when converted with the Matlab tool. This happens mostly in the low-speed side of the map. Whilst Matlab ignores this value (giving it a NaN designation), the performance solver reads this as a zero value with the result that at low-speeds, it interpolates between a real value and zero. This gives an artificially low value of pressure ratio or non-dimensional mass flow.

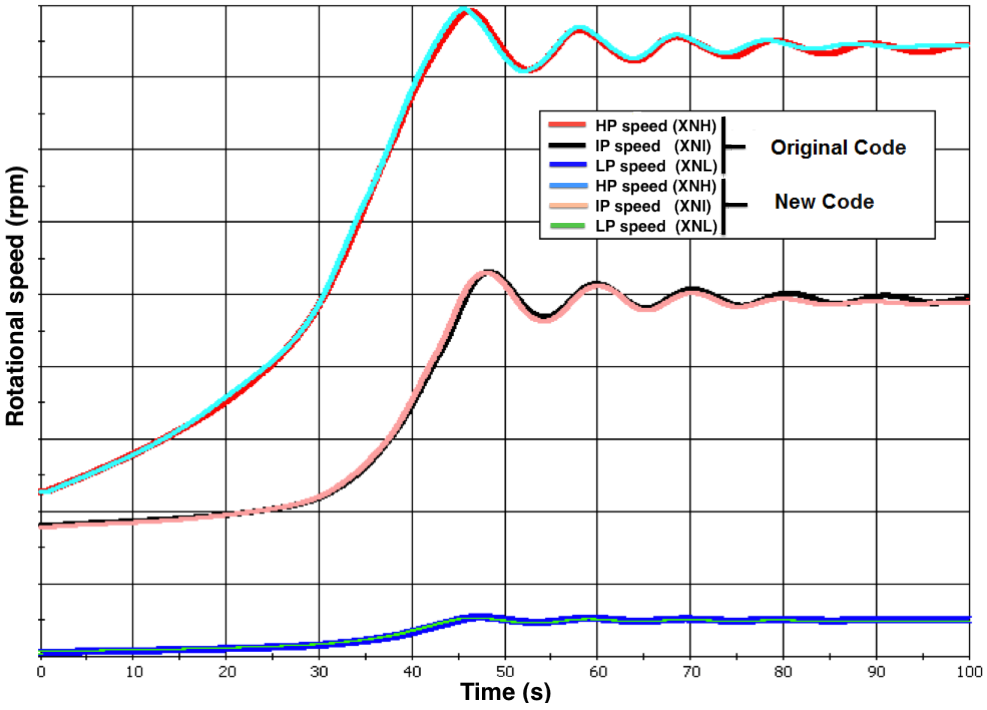

Figure 4.12: Comparison of an engine groundstart transient simulation: original sub-idle solver and new torque-based version - all compressors and intermediate pressure turbine

To prevent this, the missing data is removed and the performance solver's built-in function automatically extrapolates values from the remaining rows. When the map was of good quality and well defined for low-speeds, this problem doesn't occur. For the validation case, the intermediate pressure turbine (IPT) map was of very good quality. Using the new version of the performance solver for the compressors and the IPT only, the results as shown in Fig. 4.12 match those from the original solver. On the other hand, the low-pressure turbine (LPT) and HPT maps were not defined well enough at low-speeds. Using the aforementioned fix, results align with the original solver's results within a difference of 3 seconds, as shown in Fig. 4.13. The problem is not encountered in the compressor because the compressor characteristics are based on the beta parameter which facilitates the conversion of the characteristics. Overall, it can be concluded that the new torque-based engine performance solver produces the same results as the original solver, with the addition that it uses parameters that are better suited for low-speed performance simulations. Whilst the conversion method for the compressor map is satisfactory, conversion of the turbine map requires further work.

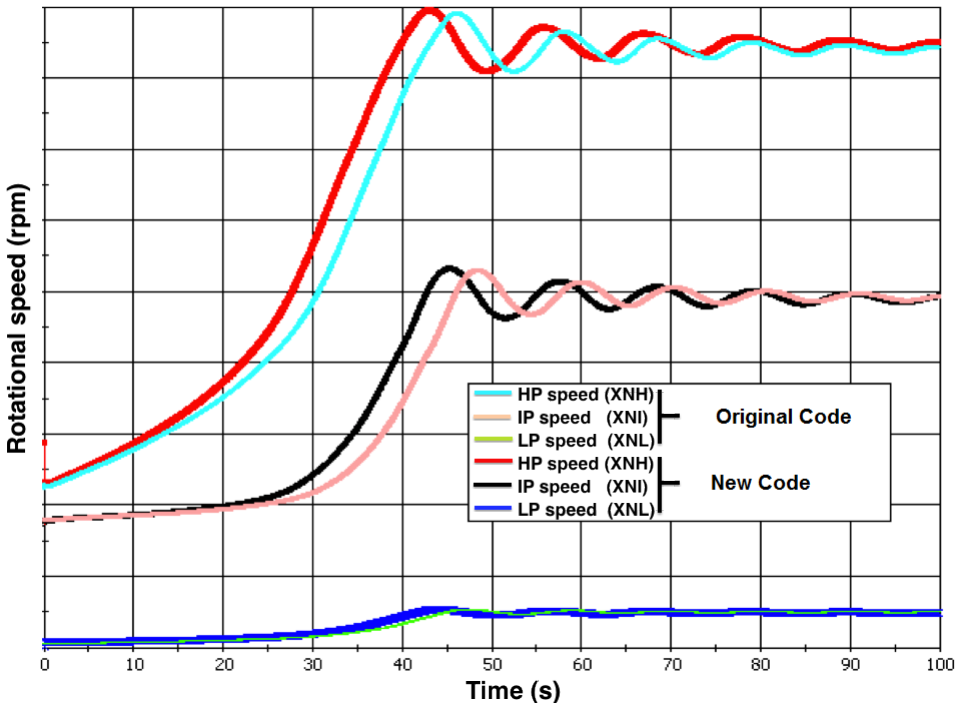

Figure 4.13: Comparison of an engine groundstart transient simulation: original sub-idle solver and new torque-based version - all compressors and all turbines

4.8 Concluding remarks

The basis of the research work described above is the inability of linearised parameters (ϕ, ψ and ψ_{is}) in representing compressor characteristics down to zero speed. This prevents the performance simulation of a gas turbine engine from static conditions. Previous research indicated the use of specific torque as more suitable to represent low-speed compressor characteristics. The linearised parameter-based whole engine performance synthesis solver used by the sponsor, was modified to run compressor and turbine calculations from torque based characteristics. Conversion of the compressor and turbine maps was also required, to be used with the new version of the performance solver.

The modified compressor and turbine sub-routines were successfully implemented into the main performance solver. Using the converted torque-based maps, whole engine performance simulation results using the torque-based performance solver, matched the original solver's simulation results. This demonstrates that the functionality and validation against engine test data that the original solver had, was maintained whilst the capability was improved by basing the calculations on torque, which is better suited for low-speed performance modelling. This brings the solver a step closer to being able to simulate engine starts from a static condition, which should be the next major solver modification to be made by future researchers. Conversion of the turbine map also requires further work to ensure all the characteristics are converted properly and without areas of undefined values.

The result has significant industrial relevance since accurate simulations of groundstarts and altitude relights from low and zero speeds are desirable. Converting and validating the performance solver for torque-based calculations is a major milestone towards achieving such goal. From a scientific point of view, it demonstrates a practical and validated use of torque-based solvers. It also offers the possibility of testing the results from the compressor sub-idle map generating code described in chapter 3 to run more accurate sub-idle performance simulations from zero-speed and maximising its potential.

Chapter 5

Sub-Idle Combustion Efficiency Model

The following chapter describes the research work undertaken on combustion efficiency at sub-idle conditions. The goal was to create an analytical / empirical model in the form of a sub-routine that can predict the sub-idle combustion efficiency depending on the combustor's operating condition. This can subsequently be coded into the whole engine performance solver. The combustion efficiency sub-routine developed is based on the model proposed by Lefebvre [22], chosen because of its good validation against experimental results. Values predicted by the model agree well with the experimental data. The study also indicated that current empirical equations for spray Sauter Mean Diameter (SMD), tend to underestimate the droplet sizes at sub-idle conditions, thus overestimating the overall combustion efficiency.

Numerical studies were undertaken to support the model development by providing a better insight into the flow and spray phenomena characteristics within the combustor at sub-idle, and verify whether fuel spray and flow correlations are valid at relight conditions. The numerical work, explained in much further detail in Chapter 6 includes an analysis of the swirler flowfield, overall combustor aerodynamics and atomizer performance at windmilling and groundstart conditions.

5.1 Introduction

Gas turbine combustion has always been a difficult and highly empirical area of research. Most of the development work is based on previous experience and data from combustor rig tests. A correlation between combustion efficiency (defined as the percentage energy released relative to the energy available in the fuel) and the combustor operating conditions was eventually identified. Childs [83] observed a good correlation between efficiency and the combustor inlet static pressure and temperature, and the reference inlet velocity. Over time, this evolved into the 'theta' (θ) parameter which is still used as the standard correlating parameter for efficiency (Eqn. (5.1)).

Efficiency increases with θ, although the definition of θ may vary from one manufacturer to another. At nominal operating conditions, combustion efficiency is close to 100%, whereas at sub-idle it can be as low as 10-30%. Predicting the combustion efficiency at low power is important since it determines the fuel flow, the shaft acceleration rates and the overall engine re/starting performance. However the aero-thermal dynamics within the combustor at low power are very poorly understood, making the development of predictive models a very difficult task.

$$\theta = \frac{{P_3}^{1.3} V_c \exp\left(T_c/400\right)}{W_a} \tag{5.1}$$

5.2 Combustion at sub-idle conditions

Combustion is a complex process depending on a number of phenomena. Various researchers [22] [83] have tried to investigate and simplify these phenomena in order to derive a series of correlations which could help predict the combustion performance. The most well known combustion model is the one proposed by Lefebvre [22] [28] [84] which, as shown in Eqns. (5.2)-(5.5), suggest that combustion efficiency is dependant on the rate of fuel droplet evaporation, mixing and reaction.

$$\eta_c = (\text{air flow rate})^{-1} \left(\frac{1}{\text{evaporation rate}} + \frac{1}{\text{mixing rate}} + \frac{1}{\text{reaction rate}} \right)^{-1} \tag{5.2}$$

$$\eta = \eta_{c_\theta} \eta_{c_e} \tag{5.3}$$

$$\eta_{c_\theta} = 1 - \exp\left[\frac{-0.022 {P_3}^{1.3} V_c \exp\left(T_c/400\right)}{f_c W_a}\right] \tag{5.4}$$

$$\eta_{c_e} = 1 - \exp\left[\frac{-36 \times 10^{-6} P_3 V_c \lambda_{eff}}{T_c {D_o}^2 f_c W_A}\right] \tag{5.5}$$

The model proposed by Lefebvre [22] was validated extensively against experimental test data. The predicted values align well with the experimental data, as shown in Fig. 5.1, where combustion efficiency is well predicted down to a value of approximately 60%. Similarly, Su and Zhou [85] [86] obtained a good agreement with Lefebvre [22]. The model proposed by Lefebvre [22] therefore seems to be reliable and capable of predicting with sufficient accuracy, combustion efficiency at conditions when the atomization process is the rate-limiting step.

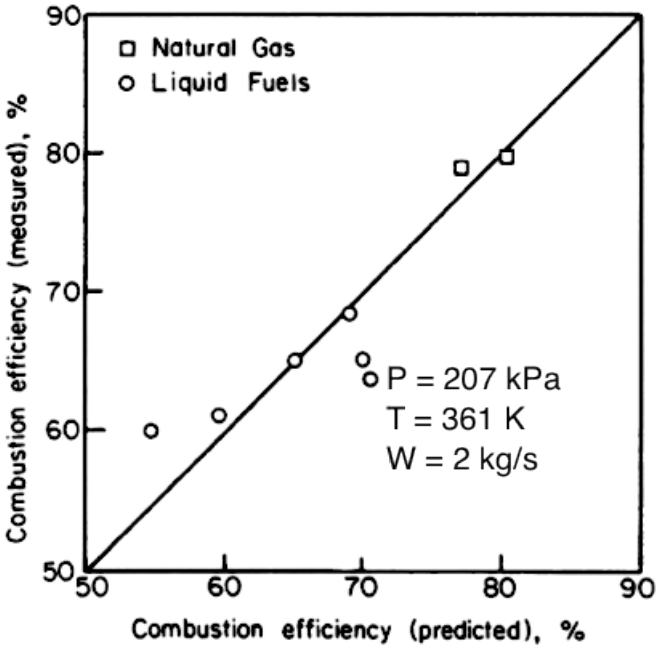

Figure 5.1: Comparison of predicted and experimental data for combustion efficiency [22]

Current sub-idle combustion efficiency prediction methods

Most sub-idle combustion efficiency codes rely on characteristics based on the θ parameter. Generally however such characteristics do not capture well the efficiency at low power. An additional parameter is introduced as a factor to reduce the θ-based efficiency. This factor, known as the 'inefficiency factor', effectively represents the evaporation rate-limited efficiency. It is generally reverse engineered from test data, in an attempt to align the solver predictions with the engine data. This methodology is described by Moxon [23], and the characteristics used are show in Figs. 5.2 and 5.3.

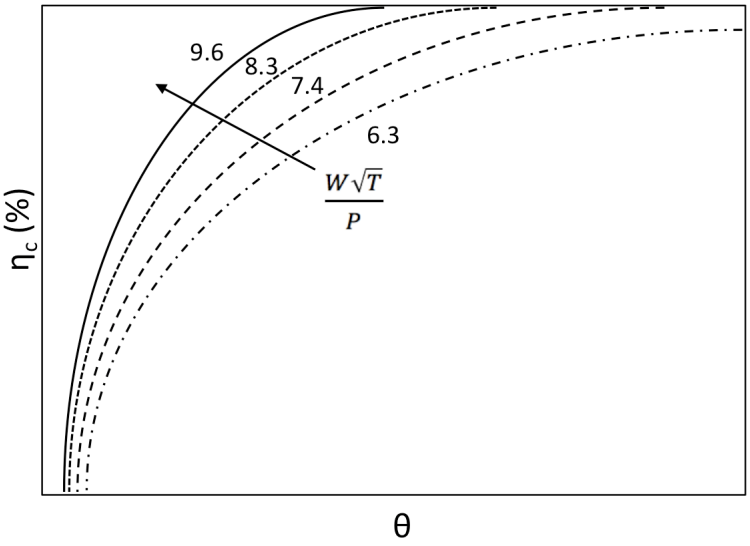

Figure 5.2: θ based combustion efficiency characteristics for different non-dimensional mass flows ($W\sqrt{T}/P$)[23]

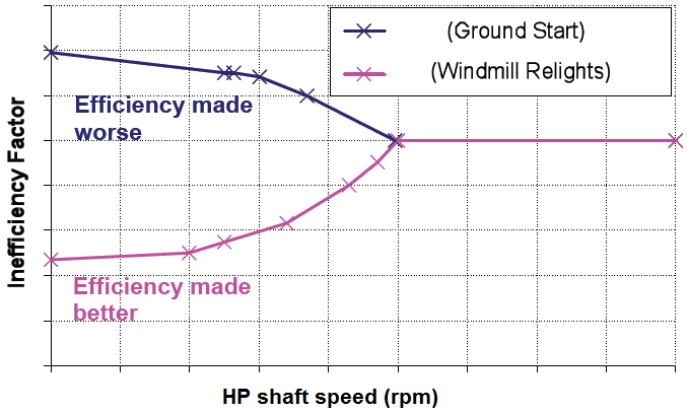

Figure 5.3: Combustion 'inefficiency' factor used to align solver predictions with engine test data for sub-idle combustion efficiency [23]

5.3 Combustion efficiency estimation model

The sub-idle combustion efficiency sub-routine built, is designed to be plugged into the current performance solver to substitute the current efficiency estimation. It is based on Lefebvre's [22] theory that sub-idle combustion is limited mainly by the evaporation rate of the fuel droplets. The low atomization quality at low power, hinders the evaporation rate of the large fuel droplets, limiting the combustion rate. The model therefore computes both the reaction and evaporation rate-limited efficiency. The reaction rate is straight forward, based on the commonly used θ parameter (Eqn. (5.1)). The evaporation-rate limited efficiency is however more complex to estimate since it depends on a number of parameters which are difficult to estimate analytically. Whilst further details are given further on in this chapter, an overview of the process is shown in Fig. 5.4.

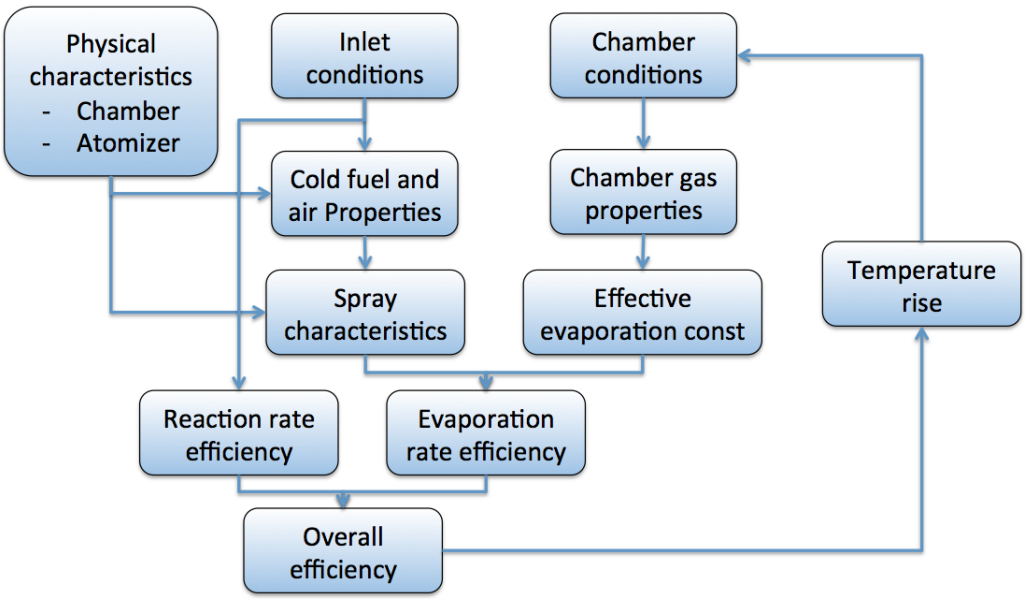

Figure 5.4: Overview of how the sub-idle combustion efficiency sub-routine works.

The model requires a number of geometrical parameters such as the atomizer pre-filming (D_p) and hydraulic (D_h) diameter, the size of the primary zone (V_c), and the fraction of air used in combustion (f_c). The inlet conditions for each time-step (pressure, temperature, air flow rate and fuel flow rate) are supplied to the sub-routine by the solver during the engine matching process. From the inlet conditions, the combustor inlet air and fuel properties (see section 5.3.1) are estimated.

The spray characteristics are predicted using the current empirical correlations [25] [26] for airblast atomization. These however were found to underestimate the size of SMD. A factor was introduced depending on the operating pressure (based on studies by Caines et al [30], Beck et al [31], and the numerical studies explained in section 6.3) to correct the equations for sub-idle operating conditions.

At this point, there is enough information to estimate the overall combustion efficiency by calculating the reaction and evaporation rate-based values using Eqns. (5.4) and (5.5) respectively. Any increase in combustion temperature is then calculated using the value of combustion efficiency estimated, the fuel calorific value, and the temperature rise charts given in Walsh and Fletcher [1] as shown in Fig. 5.5.

Once the temperature rise is known, the new gas properties inside the chamber are re-calculated based on the new chamber temperature. The model moves on to the next time-step, introducing the new inlet conditions to the combustor. Under steady-state, these values would be constant and the temperature rise would be zero. During a transient however, each time-step would introduce the new values.

The equations described in the following sections were all derived from Lefebvre [87] [28] and Cranfield University Gas Turbine Combustion Notes [88], unless otherwise stated.

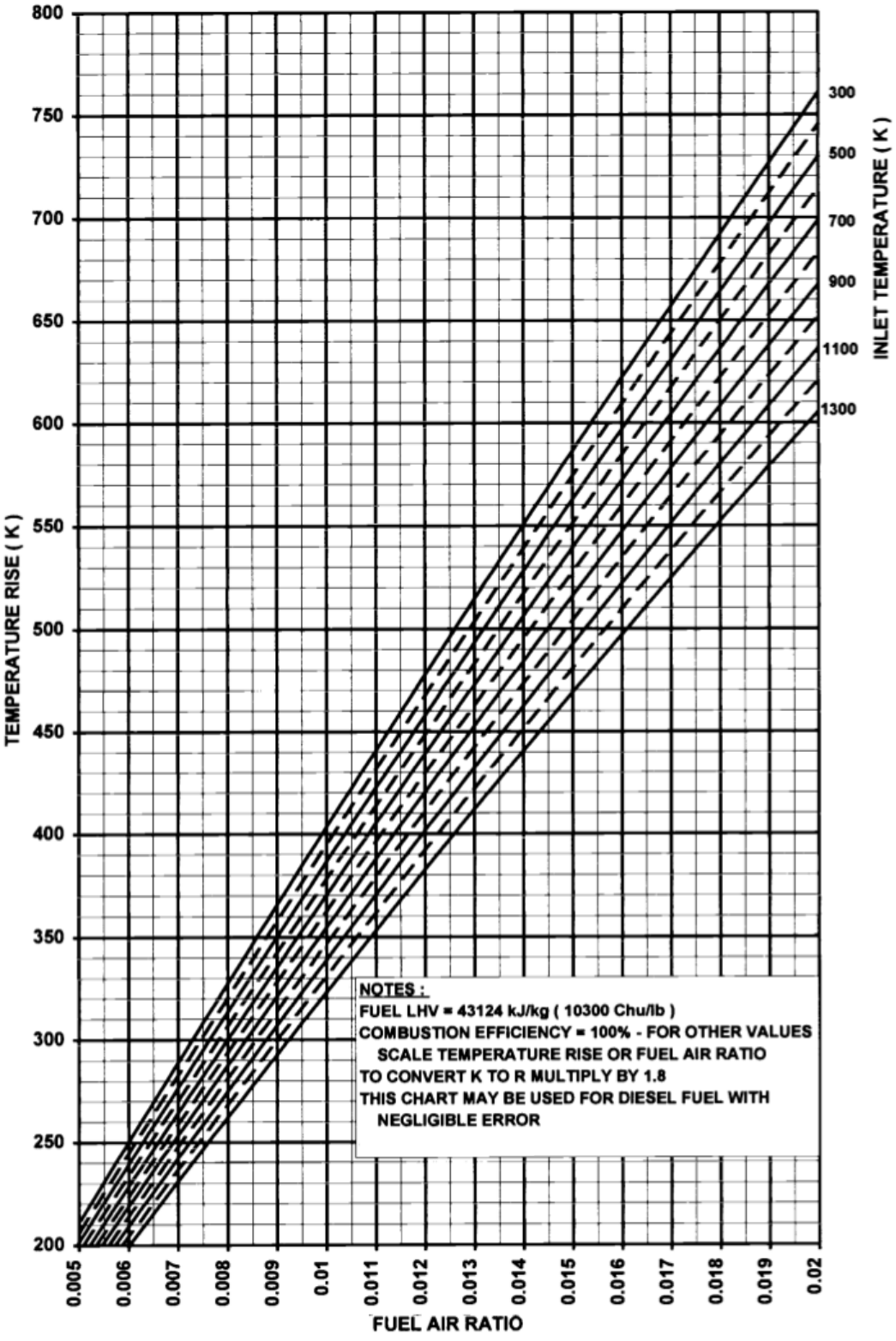

Figure 5.5: Temperature rise charts [1]

5.3.1 Estimation of thermodynamic and physical properties

Air properties

The air specific heat capacity (C_p), thermal conductivity (k), and dynamic viscosity (μ) are defined as a polynomial function of temperature as shown in Fig. 5.6. Gas properties for the inlet air were calculated using the compressor delivery air temperature, whilst for the combustion chamber gases, properties were calculated using the reference temperature as explained further on.

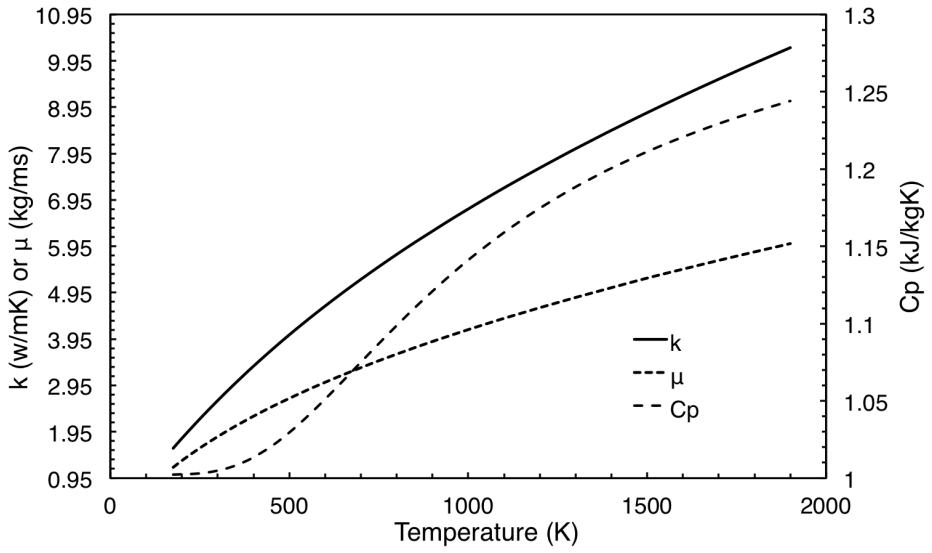

Figure 5.6: Air properties used in the model as a function of temperature

The ideal gas equation was used for estimation of the air density (kg/m^3):

$$\rho_a = \frac{P_{30}}{T_{30}R} \tag{5.6}$$

Fuel properties

All the fuel properties are temperature dependent. The equations were obtained from a report provided by the sponsor [89]. For cold fuel (from the fuel tank), the same temperature as that of the HPC outlet air was assumed (T_{30}). For hot fuel, the temperature was assumed equal to that of the hot gases inside the chamber (T_{31}).

Fuel density (kg/m^3):

$$\rho_f = 1021 - (0.73528T_f) \tag{5.7}$$

Fuel dynamic viscosity (kg/ms):

$$\mu_f = 59734\ e^{-0.03727T_f}\rho_f/100000 \qquad T_f \leq 273 \tag{5.8}$$

$$\mu_f = 72.215\ e^{-0.0128T_f}\rho_f/100000 \qquad T_f > 273 \tag{5.9}$$

Fuel surface tension (kg/s^2):

$$\sigma_f = [46.126 - (0.07786T_f)]\,/1000 \tag{5.10}$$

Gas properties inside combustion chamber

The gas properties within the chamber are required to calculate the effective evaporation constant of the fuel droplet. The equations used to estimate the gas properties inside the chamber were derived from Lefebvre [87]. A constant droplet surface fuel mass fraction (Y_{Fs}) of 0.5 was assumed. The first step is to estimate the fuel and air mass fractions for both reference and droplet surface.

Reference fuel mass fraction:

$$Y_{Fr} = Y_{Fs} + \frac{Y_{F\infty} - Y_{Fs}}{3} \tag{5.11}$$

however to simplify, if it is assumed that the fuel concentration at an infinite distance from the drop is zero, Eqn. (5.11) becomes:

$$Y_{F_r} = \frac{2}{3}Y_{F_s} \tag{5.12}$$

Reference air mass fraction:

$$Y_{A_r} = 1 - Y_{F_r} = 1 - \frac{2}{3}Y_{F_s} \tag{5.13}$$

Next, the reference (T_{ref}) and droplet surface temperatures (T_{surf}) have to be estimated, using Eqns. (5.14) and (5.15). The droplet surface temperature needs to be iterated until the values of the heat (B_T) and mass (B_M) transfer numbers coincide, as explained in [87] and shown further on.

$$T_{surf} = 0.3(T_{30}) + 0.7(T_{31}) \tag{5.14}$$

$$T_{ref} = T_{surf} + \left[\left(T_{31} - T_{surf}\right)/3\right] \tag{5.15}$$

The reference specific heat capacity (c_{pg}) and thermal conductivity (k_g) of the chamber gas also need to be estimated to calculate the droplet's evaporation as given in Eqn. (5.24). These are defined as a function of the reference air and fuel mass fraction, and the properties of the constituent gases i.e. air and fuel vapour as shown below:

$$c_{pg} = Y_{Ar}(c_{pa} \text{ at } T_{ref}) + Y_{Fr}(c_{pv} \text{ at } T_{ref}) \tag{5.16}$$

$$k_g = Y_{Ar}(k_A \text{ at } T_{ref}) + Y_{Fr}(k_v \text{ at } T_{ref}) \tag{5.17}$$

For fuel vapor:

$$c_{pv} = (363 + 0.467T_{ref})(5 - 0.001\rho_{Fo}) \tag{5.18}$$

where ρ_{Fo} is the fuel density at 288.6 K (taken as 724 kg/m^3).

$$k_v = 0.01[13.2 - 0.0313(T_{bn} - 273)]\left(\frac{T_{ref}}{273}\right)^n \tag{5.19}$$

where

$$n = 2 - 0.0372\left(\frac{T_{ref}}{T_{bn}}\right)^2 \tag{5.20}$$

and T_{bn} is the boiling temperature at normal atmospheric pressure (K), taken as 333 K for kerosene.

Mass transfer number:

$$B_M = Y_{Fs}/(1 - Y_{Fs}) \tag{5.21}$$

Heat transfer number:

$$B_T = \frac{c_{pg}(T_\infty - T_{surf})}{L_{eff}} \tag{5.22}$$

The transfer number (B) is evaluated by iterating the values of B_M and B_T by changing the assumed surface temperature (Eqn. (5.14)) until both values coincide. Generally it can be assumed that for kerosene, this has a value of 3.4. However the model was designed to calculate B for each time step. The droplet's Reynolds number is defined by Eqn. (5.23)

$$Re_{droplet} = u'D/v_g \tag{5.23}$$

where u' is the fluctuating velocity. The droplet Reynolds number was difficult to calculate, but it is known that it should vary between 5 and 20, 20 being for high turbulence combustion [87]. It was therefore introduced as a function of the air mass flow rate, assuming that the turbulence increases with higher air flow rates.

Once the transfer number (B), the gas properties (k_g and c_{pg}), fuel density (ρ_f), and the droplet's Reynolds number are estimated, the effective evaporation constant can be calculated using Eqn. (5.24).

$$\lambda_{eff} = \frac{8\left(k/c_p\right)_g \ln\left(1+B\right)\left(1+0.22\mathrm{Re}_{D_o}{}^{0.5}\right)}{\rho_f} \tag{5.24}$$

Spray SMD

To estimate a representative size of the fuel droplets for this model, Lefebvre [22] uses the Sauter Mean Diameter (SMD) which represents better the spray properties than the droplet diameter parameter (D_0) in Eqn. (5.5). Lefebvre [22] suggests using the correlation by El-Shanawany and Lefebvre [26], given in Eqn. (5.25).

$$\mathrm{SMD} = D_h\left[1+\frac{W_f}{W_a}\right]\left[0.33\left(\frac{\sigma_f}{\rho_a {U_a}^2 D_p}\right)^{0.6}\left(\frac{\rho_f}{\rho_a}\right)^{0.1} + 0.068\left(\frac{{\mu_f}^2}{\rho_f \sigma_f D_p}\right)^{0.5}\right] \tag{5.25}$$

A similar correlation is derived by Rizkalla and Lefebvre [25], given in Eqn. (5.26). This was added to the model so the user can choose which to adopt. To estimate which model captures best the atomization process at sub-idle, a numerical study (section 6.3) was undertaken, showing that the correlation by El-Shanawany [26] is more reliable. However the numerical results, shown in Fig. 6.35, show both correlations underestimate the spray SMD, resulting in a high value of combustion efficiency.

$$\mathrm{SMD} = 3.33\times10^{-3}\left(\frac{\sigma\rho_f D_p}{\rho_a U_a^2}\right)^{0.5}\left(1+\frac{W_f}{W_a}\right) + 13.0\times10^{-3}\left(\frac{\mu_f^2}{\sigma_f\rho_f}\right)^{0.425} D_p^{0.575}\left(1+\frac{W_f}{W_a}\right)^2 \tag{5.26}$$

5.4 Sub-idle combustion efficiency model validation

The combustion efficiency model was validated against experimental data given in Schmeltz [24]. Values of combustion efficiency for a range of AFRs (25 - 60), combustor loading (θ) (0.6 - 2.2) and combustion non-dimensional mass flows (0 - 2.5), were available from recent rig tests. Tests at such low equivalence ratios were until recently not possible to run due to the environmental issues caused by the large amount of unburnt fuel in the exhaust. New experimental facilities have permitted testing of richer mixtures and low loading, which are typical of groundstart and altitude relight conditions.

Though the data is scattered, a curve fitting correlation was provided as a function of θ, AFR and non-dimensional mass flow [24] as shown in Figs. 5.7 and 5.8. Due to the confidential nature of such data, some of the values had to be removed. This correlation was used with the combustion efficiency model to validate the predicted values. Data from an engine groundstart transient was used to analyse the model's prediction.

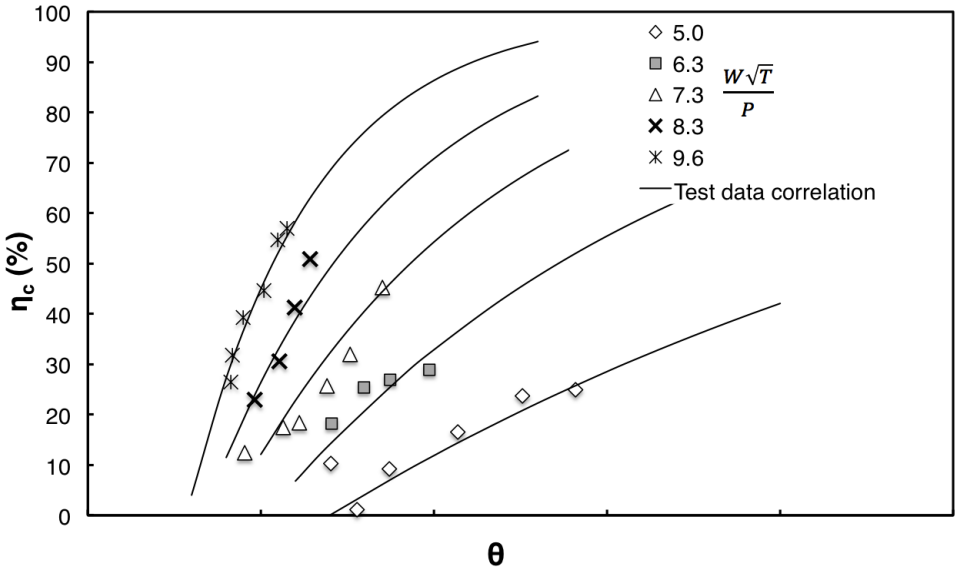

Figure 5.7: Fitting for low-power combustion ($\theta < 3$) efficiency for AFR of 60 [24]

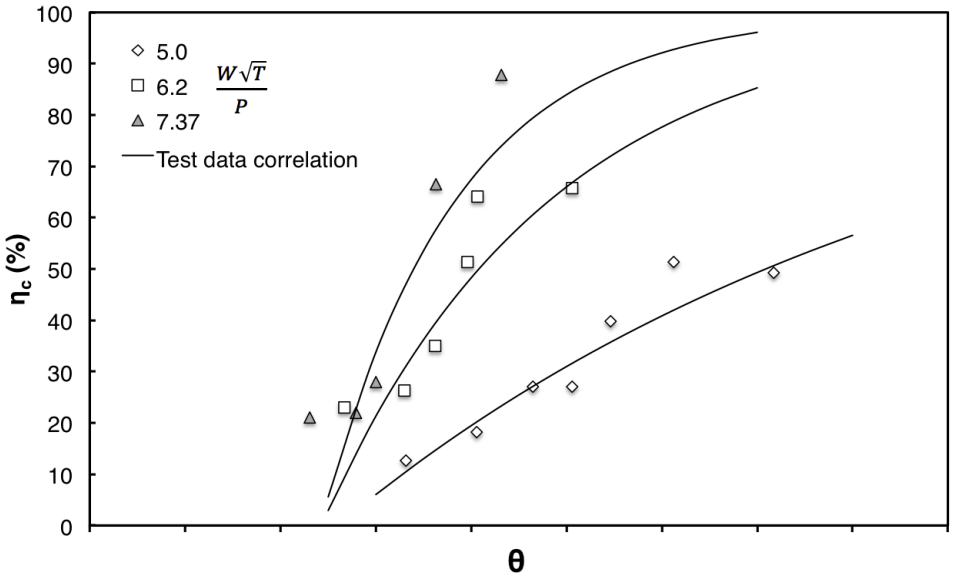

Figure 5.8: Fitting for low-power combustion efficiency ($\theta < 3$) for AFR of 25 [24]

The transient data is illustrated in Figs. 5.9 and 5.10, where the combustor inlet total pressure, air mass flow rate, inlet total temperature and fuel flow rate are plotted against time. The oscillations observed as the engine reaches idle, are due to the fuel control algorithm which tries to converge the HPC speed towards the specified idle speed. Similarly the HP spool speed is plotted in Fig. 5.11. This value is important since previous sub-idle combustion efficiency models used the spool speed as a parameter to which the efficiency was mapped. Using all the data mentioned, the combustor loading (θ) and non-dimensional mass flow were calculated (Fig. 5.12).

With all the data available, the air and fuel properties were calculated as explained in section 5.3.1. One of the most important parameters is the fuel effective evaporation constant, shown in Fig. 5.13 as it increases when the engine accelerates up to idle speed. This is expected since at higher pressures and temperatures facilitate evaporation from the fuel droplet surface.

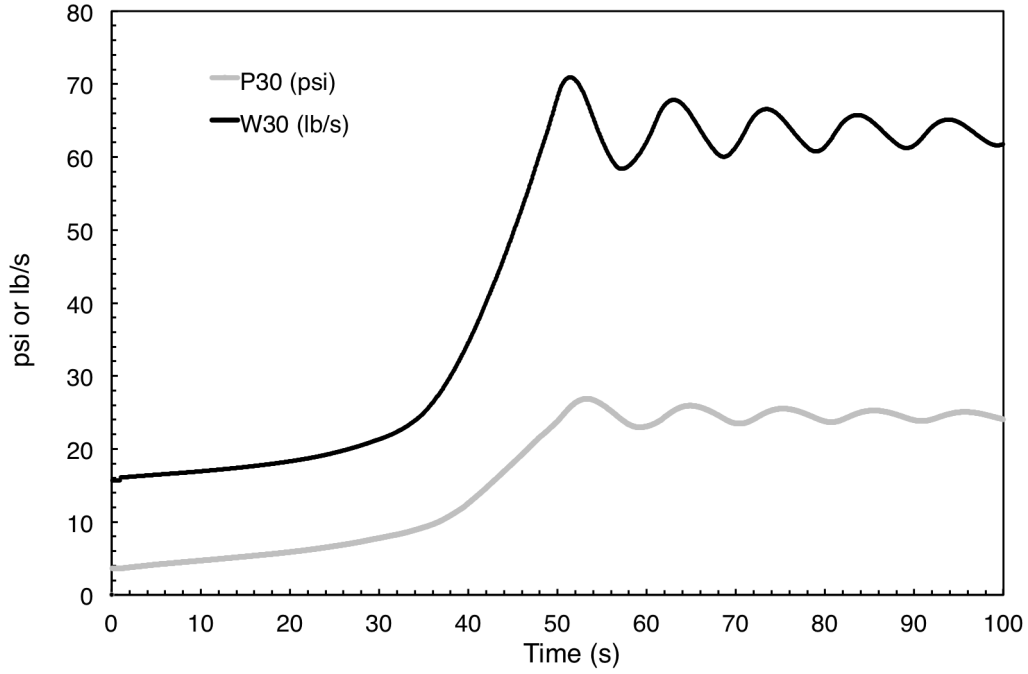

Figure 5.9: Combustor inlet total pressure and air mass flow rate of the groundstart transient test case

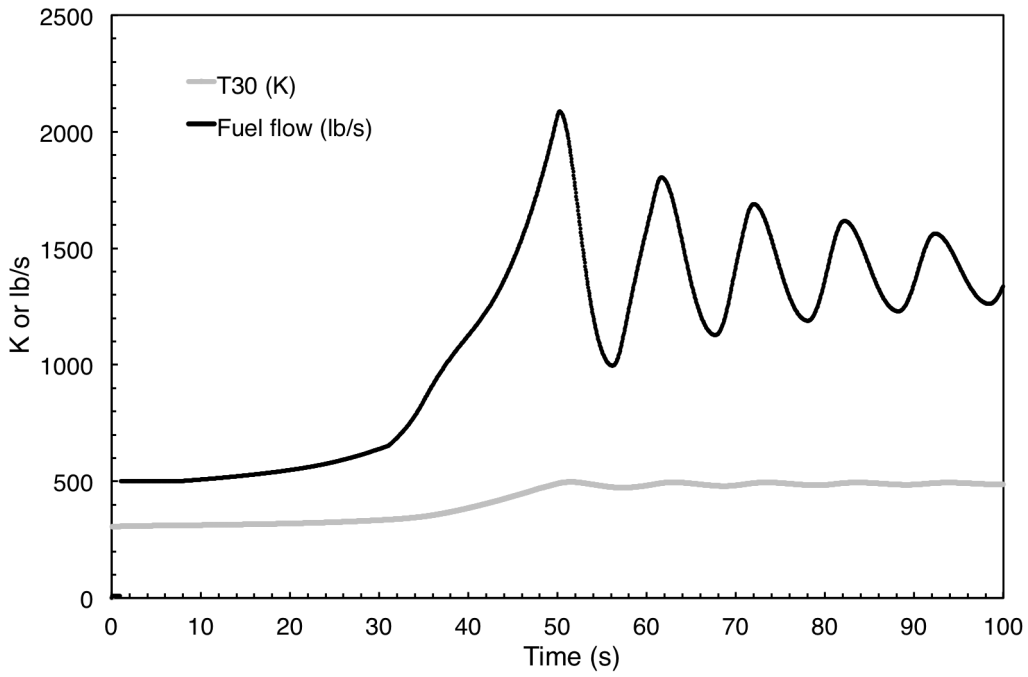

Figure 5.10: Combustor inlet total temperature and fuel flow rate of the groundstart transient test case

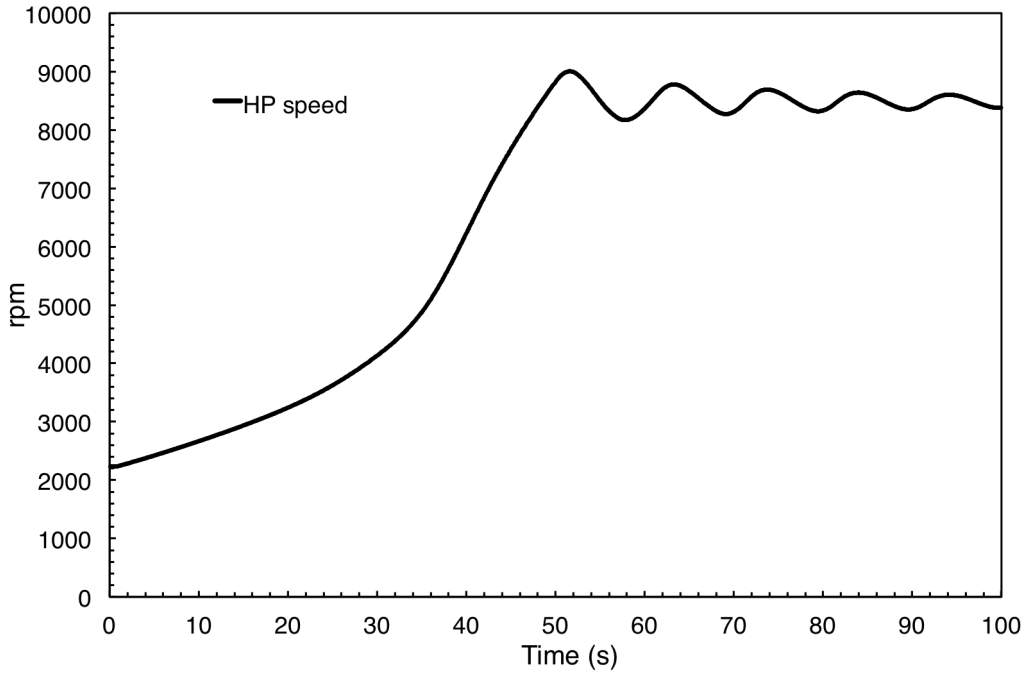

Figure 5.11: HP spool speed of the groundstart transient test case

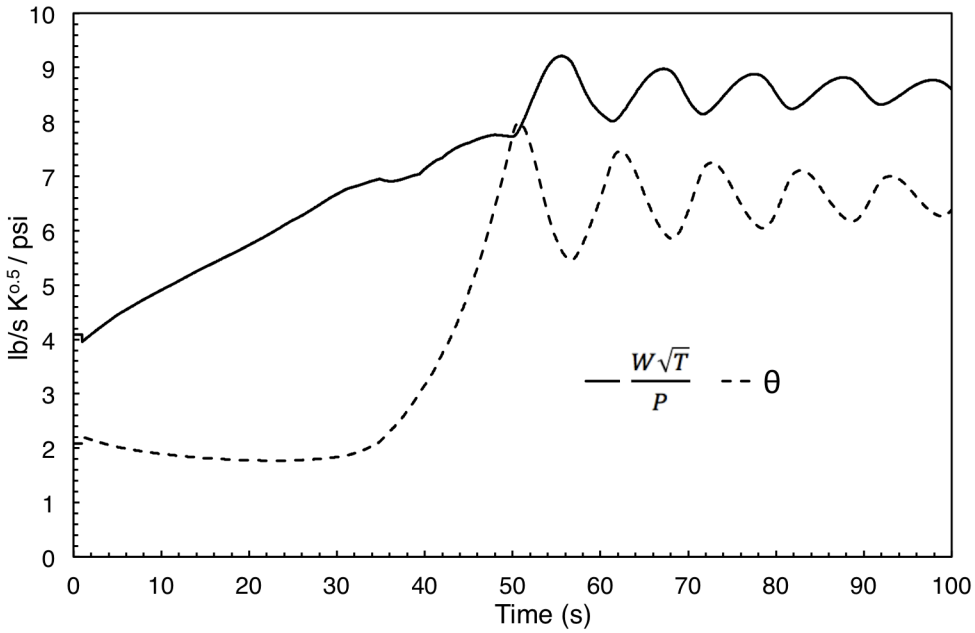

Figure 5.12: Calculated combustor loading parameter (θ) and quasi non-dimensional mass flow ($W\sqrt{T}/P$)

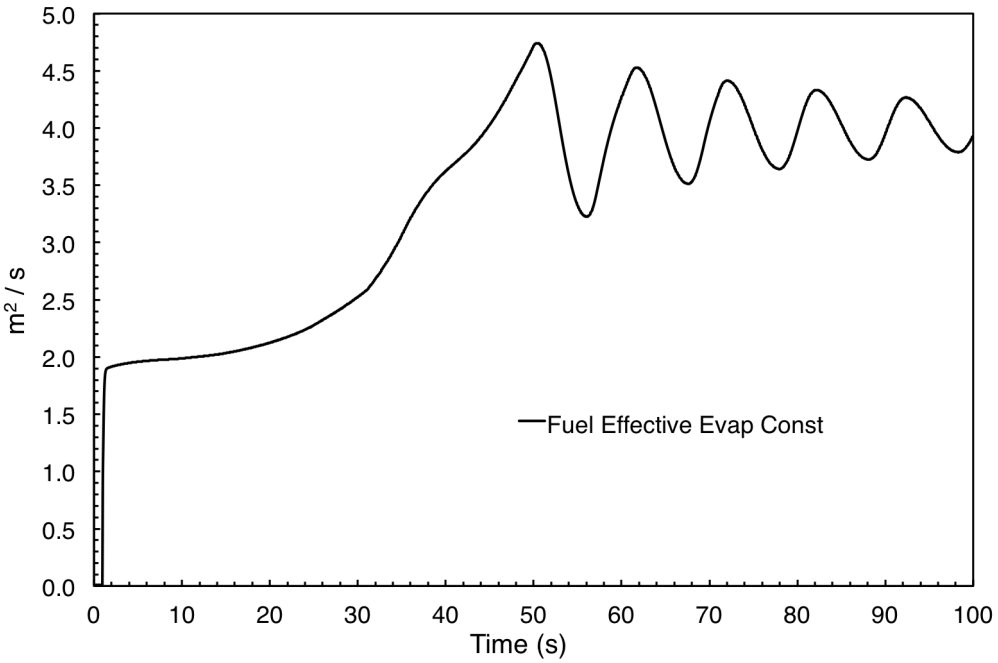

Figure 5.13: Fuel effective evaporation constant calculated for the groundstart transient

The evaporation-rate based efficiency depends heavily on the SMD, which within the model is based on empirical correlations. The estimates from these correlations are illustrated in Fig. 5.14. Here it becomes evident that the correlation by Rizkalla [25] is very optimistic. Using this value, the combustion efficiency was overestimated. The correlation by El-Shanawany [26] gave better results.

The SMD is noticed to start from a very high value due to the low pressure, low air mass flow rate through the combustor during the initial phase of the groundstart. However as the engine accelerates, the conditions become more favourable for atomization, especially due to the increase in air mass flow. This results in a decrease in spray SMD, which when coupled with the increase in the effective evaporation constant, improves the evaporation-rate based combustion efficiency, as shown in Fig. 5.15.

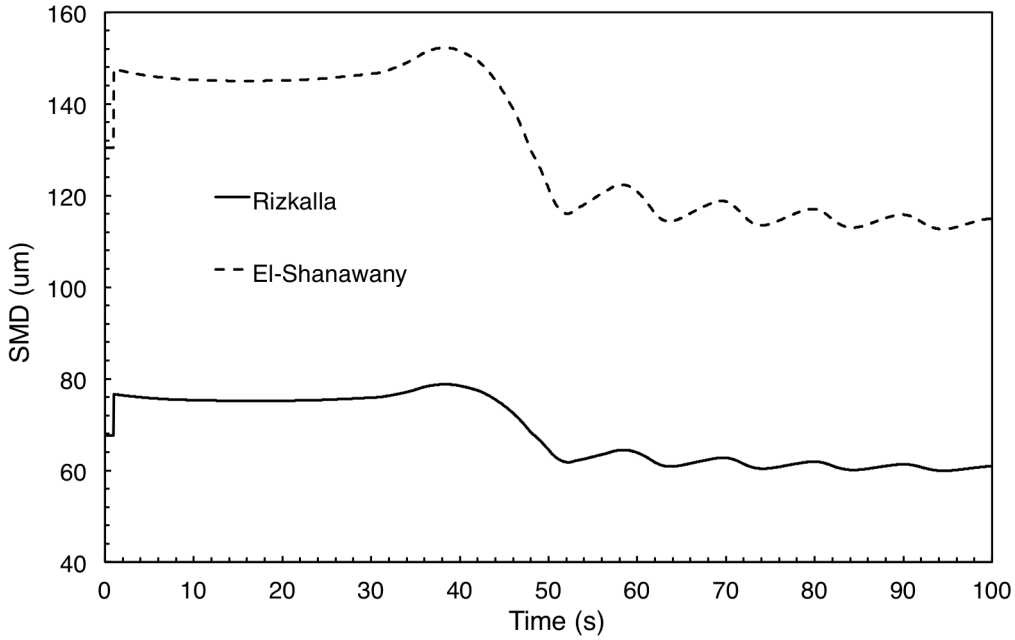

Figure 5.14: Evolution of spray SMD as engine accelerates through the groundstart - calculated using two empirical correlations: Rizkalla [25] and El-Shanawany [26]

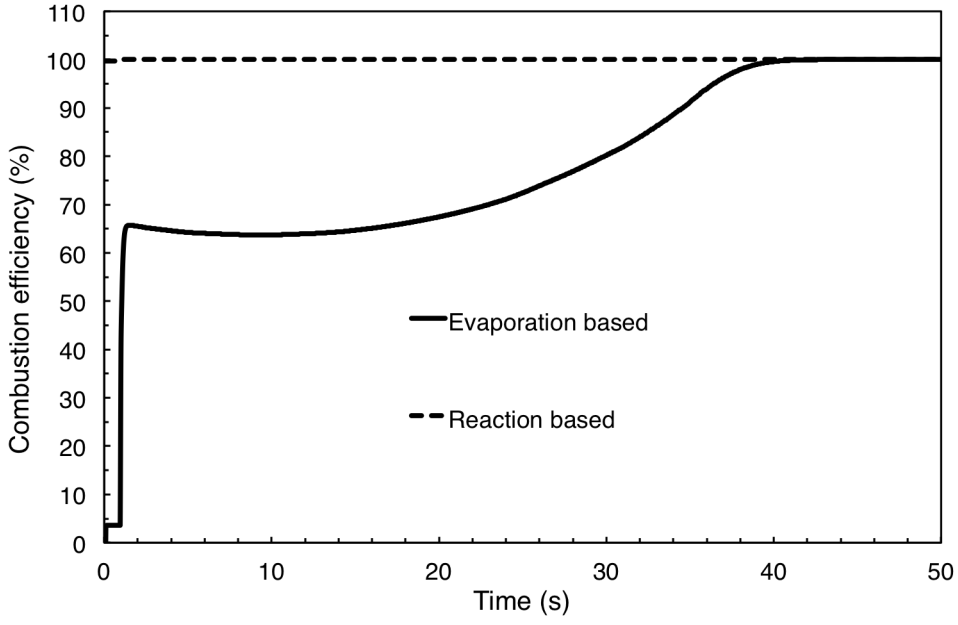

Figure 5.15: Calculated evaporation-rate and reaction-rate based combustion efficiency for the groundstart transient simulated

The overall efficiency was compared against that estimated from the test rig correlation derived by Schmeltz [24] and that predicted by the current performance solver. The results, shown in Fig. 5.16, indicate that the new model developed captures quite well the values of sub-idle combustion efficiency for this groundstart. It follows the test rig data much more closely than the current solver model, especially at the lowest power conditions. However it seems that the model is not as reliable in the first 10 second region. Though the error cannot be calculated since the test-rig data is out of range, one can presume that the efficiency is overestimated by the model.

Overall the work presented is a good starting point in developing a model that predicts the sub-idle combustion efficiency. Considering the difficulty in capturing all the phenomena taking place and the complexity associated with combustion, the results are very encouraging.

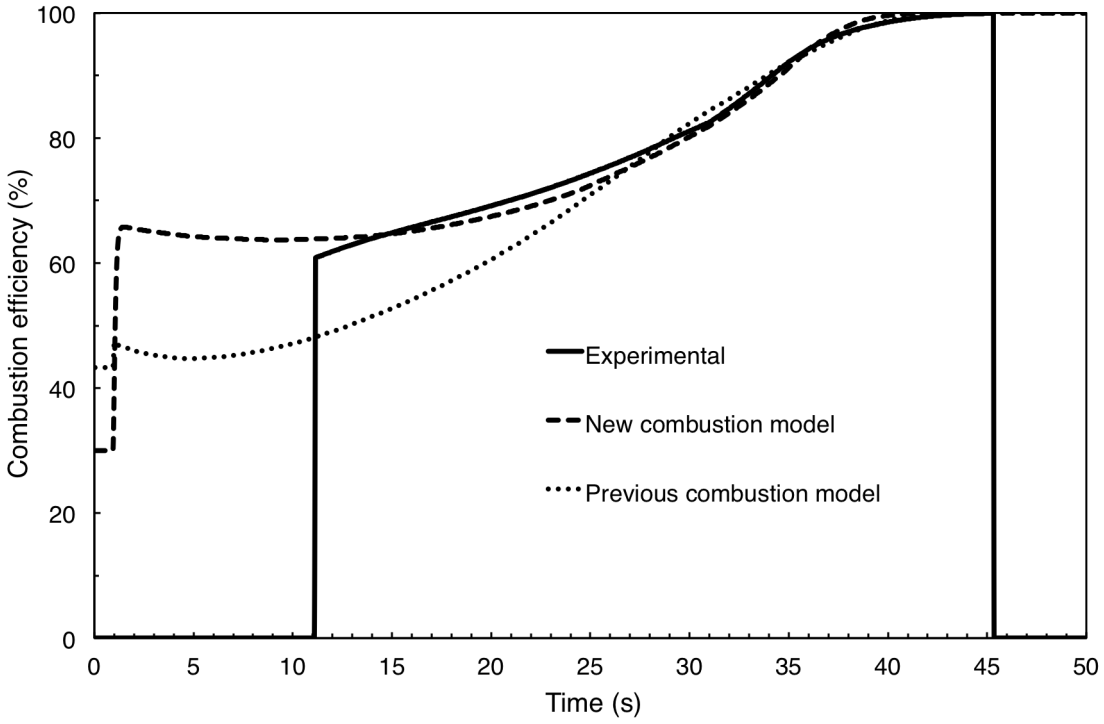

Figure 5.16: Comparison of sub-idle combustion efficiency models: the test-rig data correlation, current performance solver prediciton, and the model based on Lefebvre's combustion efficiency correlations [22]

5.5 Concluding remarks

Current combustion efficiency models within performance solvers rely heavily on empirically derived factors that scale combustion efficiency characteristics for sub-idle operation. The objective of the current research was to build a predictive model that can estimate combustion efficiency, depending on the geometrical parameters, fluid properties and operating condition. The model, developed as a sub-routine that can be implemented within the whole engine sub-idle performance solver, uses existing correlations for reaction and evaporation rate-based efficiency to estimate the overall combustion efficiency at very low power conditions. The main challenge was to code the model such that the correlations matched well with one another, especially those predicting fuel, air and mixture characteristics, and the modelling of droplet evaporation. The results match very well when compared against combustor rig test data.

The study has highlighted that current correlations for spray characteristics tend to underestimate the spray SMD, resulting in overestimating the combustion efficiency. In terms of performance modelling, this results in a lower fuel burn and faster acceleration rates relative to the real engine performance. The sub-routine itself is an important industrial deliverable since it is predictive and dependant only on the physical dimensions of the combustor and injector, and the operating condition, without the need to add empirically derived factors.

Future work on the topic is highly encouraged in the direction of estimating more accurately the gas properties inside the chamber, and a full implementation of the sub-routine within the whole engine sub-idle performance solver. This would permit transient simulations, of which results can be compared to engine data to determine the reliability of the combustion model. Numerical studies on atomizer and combustor performance at relight presented in the next chapters, provide more knowledge on a number of phenomena that influence combustion performance at low-power conditions. These results provide a better insight into what areas of the analytical model can be further enhanced.

Chapter 6

Atomizer Sub-Idle Performance

6.1 Introduction

In Chapter 5, it was noticeable that the value of combustion efficiency predicted is highly dependent on the spray characteristics. The study indicated that the correlations by El-Shanawany and Lefebvre [26] may underpredict the value of spray SMD for sub-idle conditions, due to the combustion efficiency model giving too high values of the combustion efficiency. A deeper understanding of the spray characteristics at sub-idle is therefore required to educate the combustion efficiency model. This can be done through numerical simulations, by observing the changes in spray characteristics when operating at low power, and accordingly modify the correlations currently used. The work presented in this chapter focuses on this particular aspect of sub-idle performance modelling. The study is based on previous work published in Kozaily et al [90], Mehdi et al [91] and Grech et al [92], but the level of detail of the numerical simulations was increased to capture any significant phenomena.

The areas of study are: the flow field characteristics of axial swirlers under low-power conditions, the spray characteristics of an airblast atomizer under altitude relight conditions, and the influence of compressor wakes on the combustor performance at relight. First, a brief explanation of the atomization process, as well as a description of the main parameters being investigated: flow swirl number, Sauter Mean Diameter (SMD), Rosin-Rammler distribution and minimum ignition energy is given.

6.1.1 The atomization process

Atomization is the process by which bulk fuel is converted into smaller droplets. This is done by some internal or external force which disrupts the influence of surface tension. If no such force exists, surface tension tends to keep the liquid together in a spherical form, which has minimum surface area. Whilst liquid viscosity increases the force by which the droplet tends to stay whole, external aerodynamic forces will tend to disrupt this condition. When the external disruptive forces exceed the surface tension force, the drop breaks up. The ratio between the disruptive and consolidating forces acting on the drop is called the Weber number (We). Calculated using Eqn. (6.1) the higher the Weber number, the larger the deforming forces relative to the restorative surface tension force and the greater the chance of a fuel atomization. Further details on the atomization process can be found in Lefebvre [28] [87].

$$\mathrm{We} = \frac{\rho_a U_a^2 D_{droplet}}{\sigma_f} \tag{6.1}$$

Atomization takes place in two phases: primary and secondary breakup. Primary atomization is when the fuel is broken into shreds and ligaments as illustrated in Fig. 6.1. Secondary atomization is when the larger drops are further broken down into smaller droplets. As mentioned in [28], these processes determine the characteristics of the fuel spray in terms of droplet velocity and size.

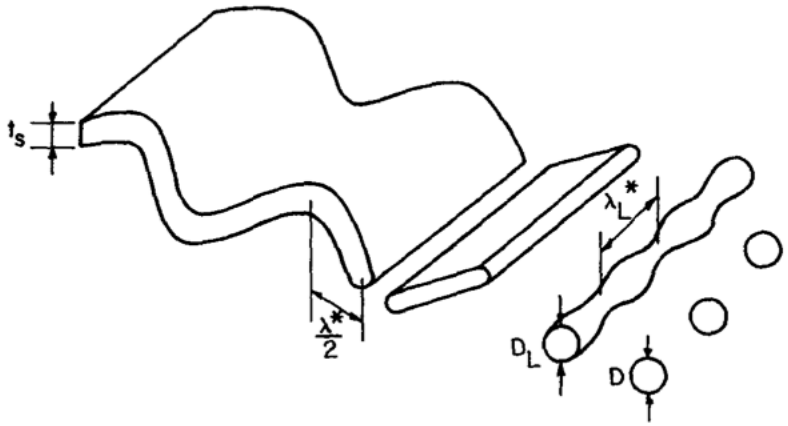

Figure 6.1: Stages of breakup of a fuel sheet [27]

6.1.2 Swirl number

The swirl number (S_N) is a non-dimensional criterion that characterises the amount of rotation imparted to the flow by the swirler. It indicates the intensity of the swirl which in turn creates a toroidal recirculation zone. The recirculating flow improves the flame stability and reduces the flame length, as shown in Fig. 6.3, thereby minimizing the combustor volume. Though the swirl number depends on the swirler's geometrical design, Sheen et al [93] have shown that, in the case of radial swirlers, conditions of low flow reduce the swirl number. This will influence the flow field, reducing the swirl intensity and changing the nature of the recirculation zone, as shown by Chatterjee et al [94]. The swirl number can be calculated as follows:

$$S_N = \frac{2G_\varphi}{G_x D_{sw}} \tag{6.2}$$

where D_{sw} is the tip-to-tip swirler diameter, and G_φ and G_x are respectively the axial flux of swirl and axial momentum (Fig. 6.2), as defined in the following equations:

$$G_\varphi = \int_0^{R_{sw}} \left(\rho UW + \rho\overline{U'W'}\right) r^2 dr \tag{6.3}$$

$$G_x = \int_0^{R_{sw}} \left(\rho U^2 + \rho\overline{U'^2} + (p - p_{atm})\right) r dr \tag{6.4}$$

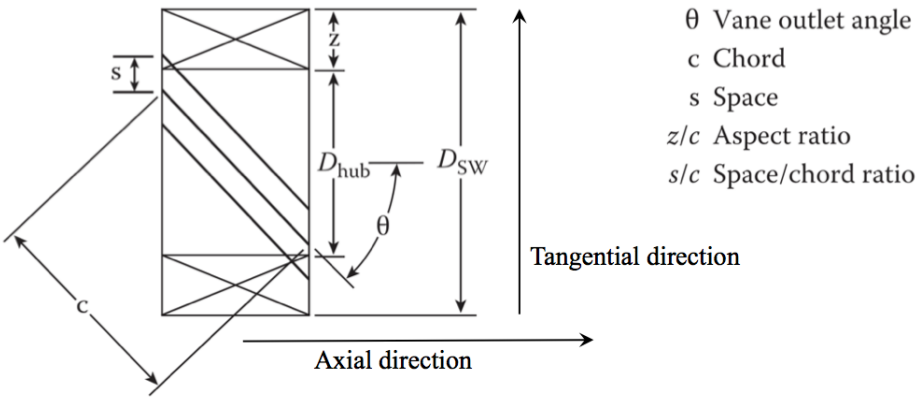

Figure 6.2: Typical flat vane axial swirler [28]

Omitting the turbulent shear stresses $\rho\overline{U'W'}$ in Eqn. (6.3) and $\rho\overline{U'^2}$ in Eqn. (6.4), the derivation by Rose [95], and Chigier and Chervinsky [96], described in detail by Beer and Chigier [97], and Sloan et al [98], gives:

$$G_\varphi = \int_0^{R_{sw}} UW\rho 2\pi r^2 \mathrm{d}r \tag{6.5}$$

$$G_x = \int_0^{R_{sw}} \left(\rho U^2 + (p - p_{atm})\right) r dr \tag{6.6}$$

For vanes mounted on a central hub, the integrals of the equations change, as shown in Eqn. (6.7).

$$G_\varphi = \int_{R_h}^{R_{sw}} UW\rho 2\pi r^2 \mathrm{d}r \tag{6.7}$$

The integral limits in Eqn. (6.7) and the definition of the swirl number were found to vary, as highlighted by Sloan et al [98]. Generally it is more common for the swirl number to be predicted using correlations based on the swirler's geometrical parameters. For an axial swirler, Eqn. (6.14) is most commonly used, of which derivation is outlined in Beer and Chigier [97].

$$S_N = \frac{2}{3}\left[\frac{1 - (D_h/D_{sw})^3}{1 - (D_h/D_{sw})^2}\right] \tan\alpha \tag{6.8}$$

One should note that all the geometric correlations used to estimate the swirl number (S_N) are usually based on assumptions and simplifications, such as inviscid flow, uniform

axial velocity distribution, negligible swirl momentum losses, and even omission of the pressure term in Eqn. (6.6). Additionally, the velocity profiles created by various swirlers can lead to very different flow patterns, but with the same swirl strengths (i.e. S_N). When uncoupled from its velocity distribution, S_N is therefore no more than an indication of the relative swirl intensity for a particular swirler [98].

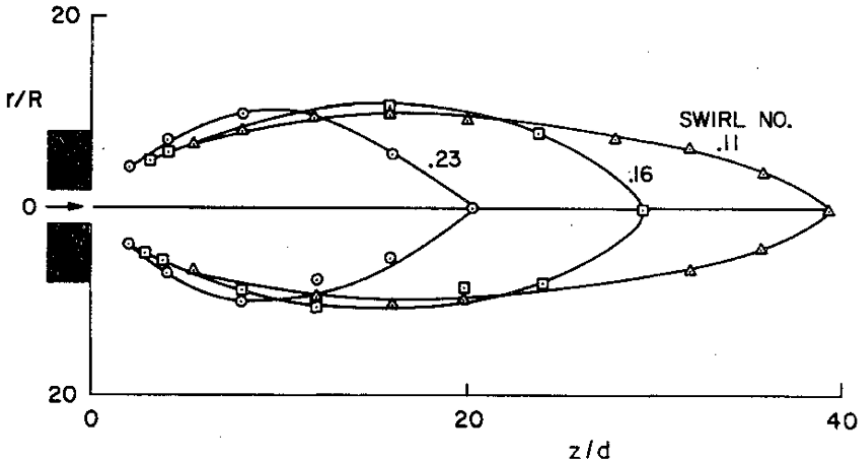

Figure 6.3: Effect of increasing swirl number on the flame front [29]

Experimental work by Sheen et al [93] shows that the degree of swirl is dependent on the flow's Reynolds number. However when $Re > 3000$, the swirl number was found to be independent of it. This is important for the current study since under windmilling conditions, the swirler Reynolds number is likely to be very small.

6.1.3 Spray characteristics

Sauter Mean Diameter

Due to the nature of the atomization process, the threads and ligaments formed by the various mechanisms of jet and sheet disintegration vary widely in diameter, resulting in main drops and satellite drops that vary in size. To carry out calculations involving sprays, it is convenient to work with mean or averaged diameters instead of complete drop size distributions. Definitions for various representative diameters for the spray droplets, and their relative application, is given in Lefebvre [87]. The Sauter Mean Diameter (D_{32}) is mostly used for mass transfer and reaction problems, and is defined as:

$$D_{32} = \frac{\sum N_i D_i^3}{\sum N_i D_i^2} \tag{6.9}$$

where i denotes the size range considered, N_i is the number of drops in size range i, and D_i is the middle diameter of size range i. Thus the SMD is the diameter of the drop whose ratio of volume to surface area is the same as that of the entire spray.

Rosin-Rammler distribution

In addition to the mean drop size, an important definition of a spray is the distribution of drop sizes it contains. Numerous methods of quantifying the distribution are explained in Lefebvre [87]. The Rosin-Rammler [33] is the most widely used expression for drop size distribution, expressed in the form:

$$1 - Q = \exp - (D/X)^q \tag{6.10}$$

where Q is the fraction of the total volume contained in drops of diameter less than D, and X and q are constants. Applying the Rosin-Rammler distribution to sprays, it is possible to describe the drop size distribution in terms of the two parameters X and q. The exponent q provides a measure of spread of the drop size, with a high value signifying a more uniform spray. An infinite value for q means the spray is perfectly homogeneous.

Minimum ignition energy

Ignition is easier in cases of high pressure, temperature and spark energy, whereas it is impeded by increases in velocity and turbulence intensity. Studies [99] emphasize that ignition performance is affected by fuel properties through the concentration of fuel vapour in the vicinity of the igniter. Much of the ignition energy is absorbed in the evaporation of the fuel droplets, depending on the distribution of the fuel and the atomization quality.

The first phase of ignition is the formation of a small spark kernel. If the rate of heat release by combustion exceeds the rate of heat loss at the surface of the inflamed volume, the spark kernel will grow in size to fill the entire combustion volume. If however the rate of heat release is less than the rate of heat loss, the temperature within the spark kernel will fall steadily until fuel evaporation ceases altogether. This leads to the definition of 'quenching distance' as the critical size that the inflamed volume must attain in order to propagate unaided, while the amount of energy required from an external source to achieve this critical size is termed the 'minimum ignition energy'. Equations for these two parameters were derived by Ballal and Lefebvre [99] for quiescent or slow-moving monodisperse mists (Eqns. (6.11) and (6.12)), providing a simple relationship with the key spray properties.

$$d_q = \left[\frac{\rho_f D_o^2}{\rho_a \phi \ln(1 + B_{st})}\right]^{0.5} \tag{6.11}$$

$$E_{min} = c_{pa}\rho_a \Delta T_{st}(\pi/6)d_q^3 \tag{6.12}$$

Assuming all the properties remain constant, it becomes evident from Eqn. (6.11) that the quenching distance is linearly proportional to fuel drop diameter. Using this relationship within Eqn. (6.12), the minimum ignition energy becomes proportional to the fuel droplet diameter cubed, as in Eqn. (6.13). Therefore, if conditions are identical, the following expression for minimum ignition energy can be used.

$$E_{min} \; \alpha \; D_o^3 \tag{6.13}$$

This becomes very significant for altitude relight conditions where it has been demonstrated [31] [30] that the spray SMD can be twice as high as nominal operating conditions, requiring therefore an eight-fold amount of ignition energy. Further details on ignition energy requirement can be found in Rao and Lefebvre [100], Ballal and Lefebvre [101] and Lefebvre [87] [28] [22].

6.2 Sub-idle flowfield characteristics of axial swirlers

Numerical methods are becoming increasingly common to understand the phenomena that dominate the combustor's performance under such far off-design conditions. This is due to their impact on the fuel spray's characteristics (as demonstrated by Caines et al [30], Beck et al [31] and Kozaily et al [90] and therefore on the relight capability. To reduce the complexity of the combustor model, swirler geometry is often omitted. The flowfield is created using an inlet velocity profile boundary condition, scaled according to the operating condition. Scaling of velocity profiles may introduce errors at conditions of very low air flow rate and low density - typical of altitude relight - due to low Reynolds number effects. It is useful to determine at which conditions velocity profile scaling is valid, due to the influence on the flame dynamics and stability, and the direct effect on assessing the engine's relight capability. Therefore to understand how much swirler flow fields change under sub-idle conditions, this study investigated the flow field characteristics of an axial swirler operating within a windmilling engine environment, as compared to nominal operating conditions.

6.2.1 Numerical modelling of swirling flows

Numerous studies, using a variety of turbulence models, have attempted to capture the swirling flow field as accurately as possible with respect to experimental data. Widmann *et al* [102] studied the isothermal airflow through a radial 12-vane-cascade swirl generator, comparing the k-ϵ standard and RNG models of which the former proved inadequate in predicting the outlet velocity profile. The swirl number from the numerical simulation underpredicts by 50% the value estimated by the geometry based correlations [97]. The standard k-ϵ model gave inaccurate predictions in the work of Brum and Samuelsen [103], with large underestimations of the axial velocity on the centre line and poor prediction of the central recirculation zone (CTRZ) length and turbulence intensity. Radial profiles of axial velocity, match well with the experimental, except in regions close to the swirler exit. The tangential velocity is well predicted in terms of profile shape, but overpredicted by $\simeq$20 to 45%. Davoudzadeh *et al* [104], using a RANS k-ϵ *Shih* model [105] found that the axial velocity profile on the centre line is well predicted, but the CTRZ length is

overpredicted by $\simeq +60\%$. The maximum CFD overestimation of a velocity peak magnitude is $\simeq \times 2.1$ relative to experimental data. Escue and Cui [106], in an attempt to reproduce the experimental results by Rocklage-Marliani *et al* [107], use both k-ϵ RNG and Reynolds Stress Model (RSM). Radial profiles of axial and tangential velocity are better captured by the k-ϵ RNG model. However RSM provides better results as the swirl number increases as the flow is more anisotropic. Weber *et al* [108] also show better agreement of the RSM model with experimental data. Turbulence kinetic energy decays unrealistically for both the k-ϵ RNG and RSM models [106].

Concluding, using RANS modelling, over/understimation of peak values by 20-45% in the velocity profiles is common, and turbulence levels (intensity and kinetic energy) are very poorly predicted. The k-ϵ Realizable turbulence model is rarely used, even though Mongia [109], found it to match the experimental results best, amongst the k-ϵ variants, k-ω and RSM turbulence models. Results from LES and DNS models are in better agreement with the experimental measurements relative to RANS [110] [111] [112], even though unsteady RANS RSM results gave good agreement with LES and experimental data [113].

6.2.2 Swirler numerical model

Validation of Numerical Solver

Validation of the numerical solver was carried out by replicating the experimental setup described in Kilik [39], to determine the level of uncertainty of the CFD results. The swirler (designated S9) consists of 16 curved vanes, with an aspect ratio of 0.4, 24.3 mm vane chord length and swirler outer diameter (D_{sw}) of 76.2 mm. A flat-vaned swirler was also tested (designated S6), having an aspect ratio of 0.4, 25.4 mm vane chord length, and outer diameter similar to S9. The vanes were set with an inlet angle of 0° and outlet angle of 50° for S9 and 60° for S6, relative to the axis of the swirler. Vane thickness was set at 1 mm. The vanes' edge profiles (both inlet and outlet) and sharpness, were not available, whilst differences due to manufacturing tolerances for the experimental work, may also impact the results. Figure 6.4 shows the swirler part of the numerical domain. The swirl number, estimated from swirler geometry, is given as 1.04 for S9 and 1.51 for S6 [39].

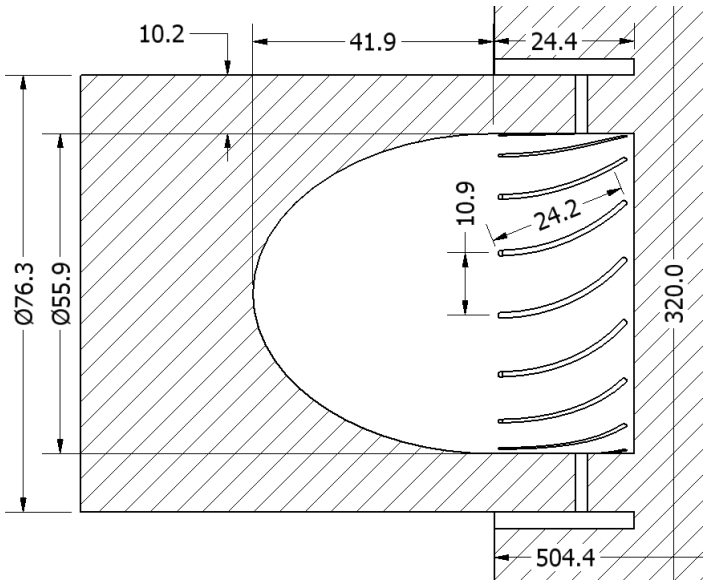

Figure 6.4: Swirler dimensions (mm)

The swirler exhausts into a cylindrical domain which, for the validation work, was set as a 'pressure outlet' since the experimental data was taken from an unconfined swirler setup. A 'pressure outlet' boundary condition was found to give better results than 'outflow' (used at the outlet of open channel flows to model flow exits, where the details of the flow velocity and pressure are not known prior to solving the flow problem [9]) relative to the experimental measurements. A full annular domain was used. Steady, 2^{nd} order and incompressible pressure-based simulations were run with ANSYS Fluent, with Quadratic Upwind Interpolation (QUICK) discretization, SIMPLE pressure-velocity coupling and Least-Squares Cell-Based Approach.

For the validation case, the operating condition was set to atmospheric pressure, with a mass flow inlet of 0.06169 kg/s (0.136 lb/s) resulting in an axial velocity of 23.77 m/s at the swirler face, this also being the value specified for the experimental setup [39]. Temperature was set at 300 K. The total pressure drop (ΔP) across the swirler was measured and defined by Kilik [39] as the difference between swirler inlet total pressure (P_i) and atmospheric pressure (P_{atm}). The static pressure drop (Δp) was measured along the swirler central axis.

Mesh

A hex-core (tetrahedral cells on the walls, hexahedral cells in the remaining volume) unstructured mesh was used, as illustrated in Fig. 6.5. Wall functions were used instead of resolving the boundary layer, thus a y^+ of 30 - 45 was used on the vane surfaces, as suggested in [9]. This value of y^+ was maintained for all the models run. A number of different meshes with increasing density were run until a finer mesh resulted in no significant change in the velocity profiles. The selected mesh has 1.96 million elements with the finer 2.5 millions elements showing no change in the velocity profiles, as shown in Fig. 6.6. A further 4.3 million element mesh was also run without any changes observed.

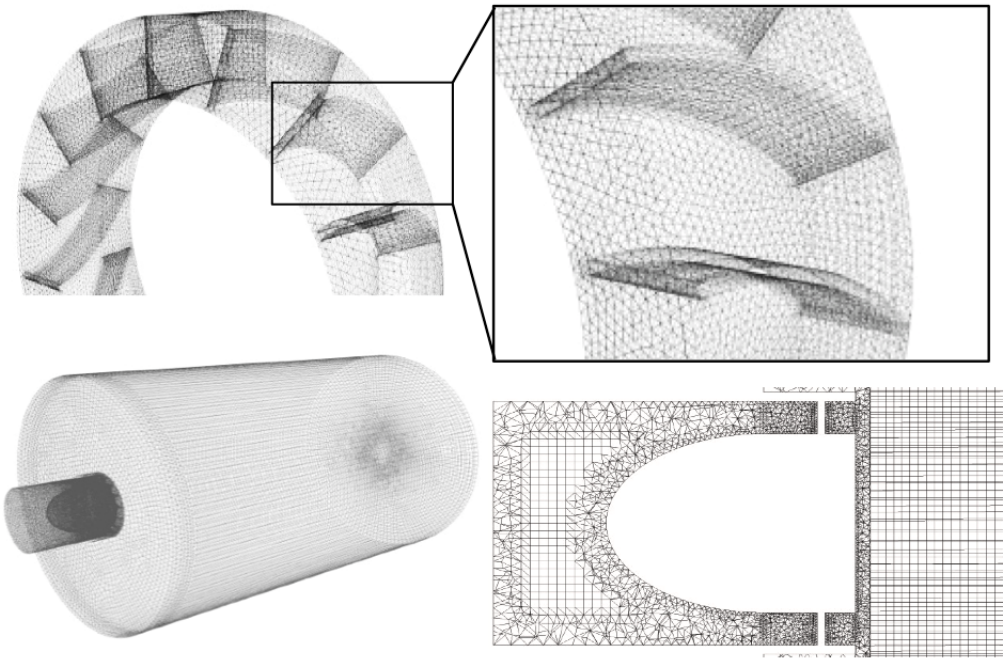

Figure 6.5: Hex-core unstructured mesh

Selection of turbulence model

Since it is difficult to determine beforehand which turbulence model will produce the best agreement with the experimental results, a number of RANS turbulence models were tested, namely: k-ϵ RNG and Realizable, standard k-ω and RSM. The standard k-ϵ model was not considered since it is known to predict swirling flowfields poorly, mainly because it neglects the anisotropic viscosity, and the generation of additional turbulence due to the effect of streamline curvature, as mentioned in Chatterjee *et al* [94] and reported in

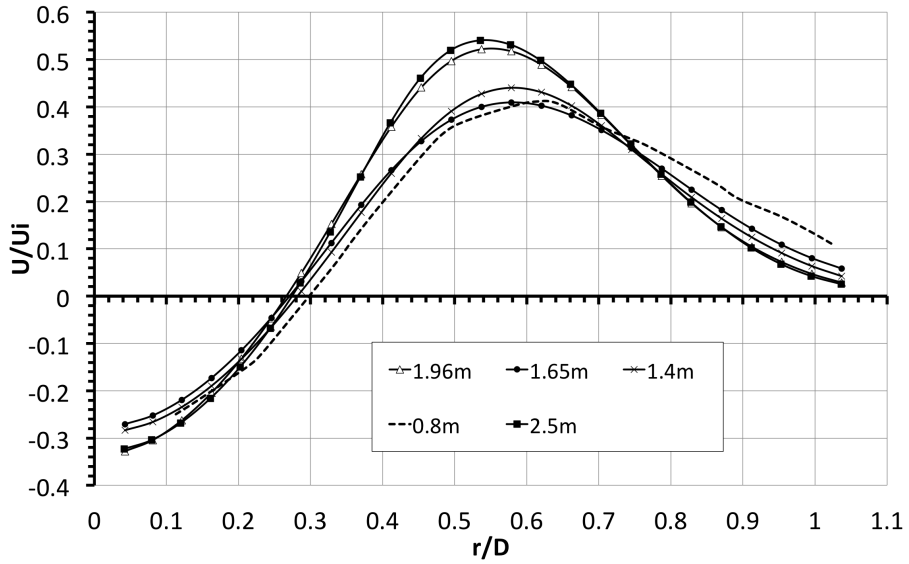

Figure 6.6: Grid independency study

Widmann *et al* [102]. The two-equation k-ϵ models all suffer from limitations due to the isotropic eddy viscosity assumption (Boussinesq hypothesis), whereas swirling flows are anisotropic. The validation is based on the agreement with experimental measurements of: axial and tangential velocity profiles, total and static pressure drop across the swirler, and the size and shape of the CTRZ.

Despite repeated efforts, a fully converged 2^{nd} order solution using RSM could not be obtained, even after starting from a converged 1^{st} order solution, and thus any RSM results shown are from the converged 1^{st} order RSM solution only. The turbulence intensity was varied between 2-10% with no change in the circumferentially averaged velocity profiles, agreeing with Wang *et al* [110] where it is demonstrated that up to 25% turbulence intensity, there is no effect on the swirling flow pattern.

Recirculation Zone Boundary

In terms of the reverse flow zone boundary (defined as the locations where $U = 0$), the k-ϵ Realizable model results agree very well with the experimental points as shown in Fig. 6.7, having a maximum error of around 2%, for both zx and zy planes. The k-ω model also predicts the boundary quite well, but overpredicts its length. The k-ϵ RNG is also unsuitable.

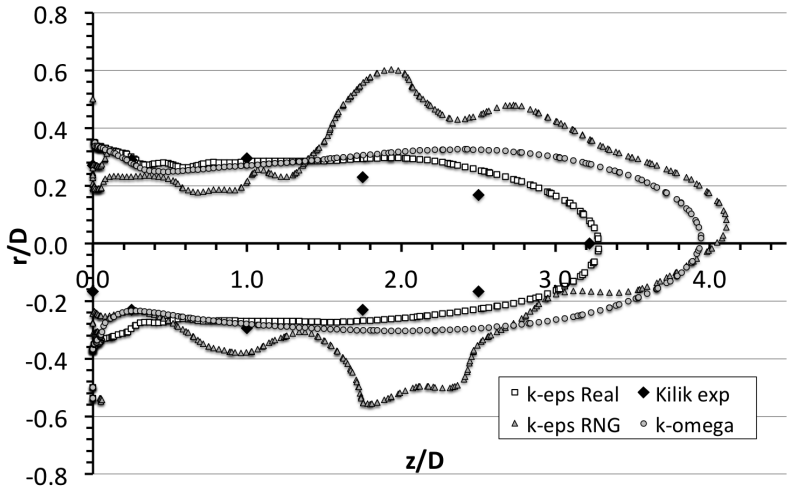

Figure 6.7: Predicted recirculation zone boundary

Pressure drop, mass flow and velocity profiles

As shown in Fig. 6.8, all the models provide a good estimate of both static and total pressure loss, with most errors being below 4% relative to experimental. Only the k-ω model overestimates significantly the static pressure drop. In terms of the mass flow prediction, Table. 6.1 shows that the percentage errors are very small for both k-ϵ Realizable and RNG models.

The circumferentially averaged and normalised velocity profiles, shown in Fig. 6.9, again indicate that the k-ϵ Realizable model produces results which align best with the experimental data. The axial velocity profiles are well captured by the numerical solver, even at far downstream positions. The tangential velocity is predicted relatively well close to the swirler, but far downstream, the magnitude is underpredicted.

Swirl Number

The swirl number characterises the swirl intensity. Generally, values above 0.6 indicate a strongly swirling flow. Theoretically, the swirl number can be estimated from the flow parameters as explained in section 6.1.2. However it is more common for the swirl number to be predicted using correlations based on the swirler's geometrical parameters. For an axial swirler, Eqn. (6.14) is most commonly used, of which derivation is outlined in Beer and Chigier [97].

	CTRZ length (mm)	Mass Flow (kg/s)
Kilik [39]	244	0.06168
k-ϵ Realizable	248 (+1.6%)	0.06167 (-0.1%)
k-ϵ RNG	306 (+25.4%)	0.06061 (-1.7%)
k-ω	301 (+23.4%)	0.0592 (-4.0%)
RSM	358 (+46.7%)	0.0586 (-5.0%)

Table 6.1: Numerical vs experimental [39] results

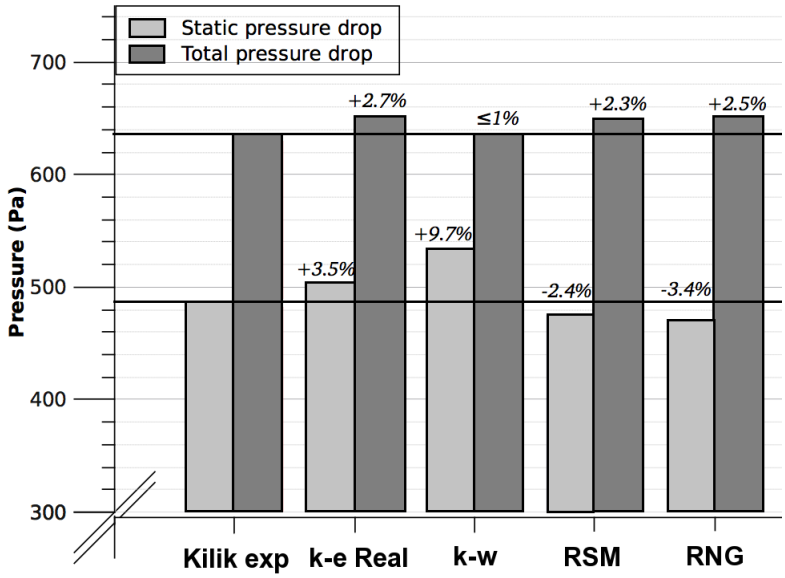

Figure 6.8: Total and static pressure losses

One should note that all the geometric correlations used to estimate the swirl number (S_N) are usually based on assumptions and simplifications, such as inviscid flow, uniform axial velocity distribution, negligible swirl momentum losses, and even omission of the pressure term in Eqn. (6.6). Additionally, the velocity profiles created by various swirlers can lead to very different flow patterns, but with the same swirl strengths (i.e. S_N).

$$S_N = \frac{2}{3}\left[\frac{1-(D_h/D_{sw})^3}{1-(D_h/D_{sw})^2}\right]\tan\alpha \tag{6.14}$$

When uncoupled from its velocity distributions S_N is therefore no more than an indication of the relative swirl intensity for a particular swirler [98]. Experimental work on radial-type swirlers by Sheen *et al* [93], shows that the degree of swirl is dependent on the flow's Reynolds number (defined using the volumetric mean axial velocity and the diameter of the circular bluff body).

For the same vane geometry, the swirl number was found to increase with Reynolds number whilst for $Re > 3000$, the swirl number was found to be independent of it. This is of significant importance for the current study since under windmilling conditions, the swirler Reynolds number is likely to be very small due to the low air flow rates and pressure. The swirl number, calculated using Eqn. (6.2) at several positions along the swirler axis, starts from a value of approximately 0.7, as illustrated in Fig. 6.10. Therefore the geometrical correlation (which in [39] gives a value of 1.04) tends to over-predict the swirl number, as mentioned and explained in Widmann *et al* [102]. The swirl number decays with the distance downstream, and this decay is also similar to the one reported in [102].

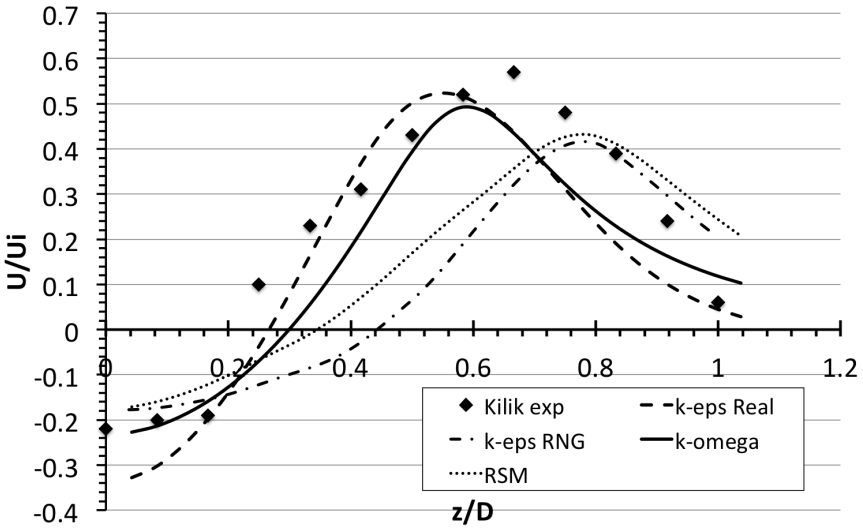

Figure 6.9: Normalised velocity profiles

On the basis of the above validation exercise, the k-ϵ Realizable turbulence model was selected and used for the rest of the study. It is important to mention that the experimental velocity profiles are based on measurements taken from a single point at each radial position, and have a 15% repeatability error [39].

It is therefore likely, that the experimental measurements were taken in regions of local maxima or minima, and thus do not represent the overall averaged velocity profile. The numerical data from the CFD is circumferentially averaged, and therefore for better comparison, Figs. 6.11 and 6.12 show both the repeatablity error for the experimental work, and the maximum, minimum and circumferentially averaged velocities found at each radial position. Convergence criteria for all simulations, including momentum and continuity, were set to $1.0e^{-5}$ and met. Turbulent kinetic energy was set for $1.0e^{-4}$ but reached a minimum of $6.0e^{-5}$.

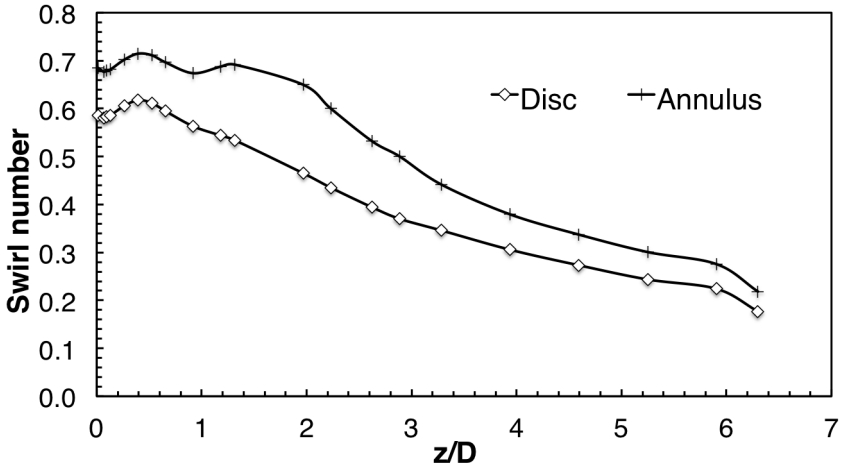

Figure 6.10: Swirl number deterioration

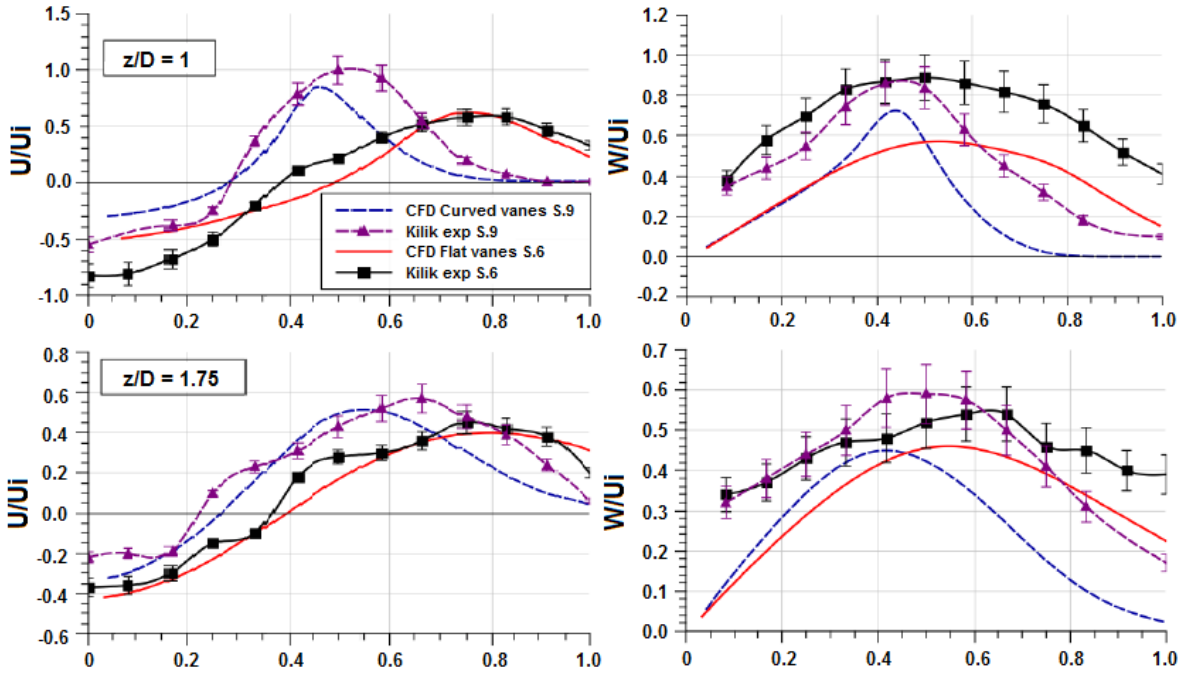

Figure 6.11: Numerical vs experimental profiles for normalised axial (U) and tangential (W) velocities with axial position downstream (z/D): flat (S6) and curved (S9) vanes

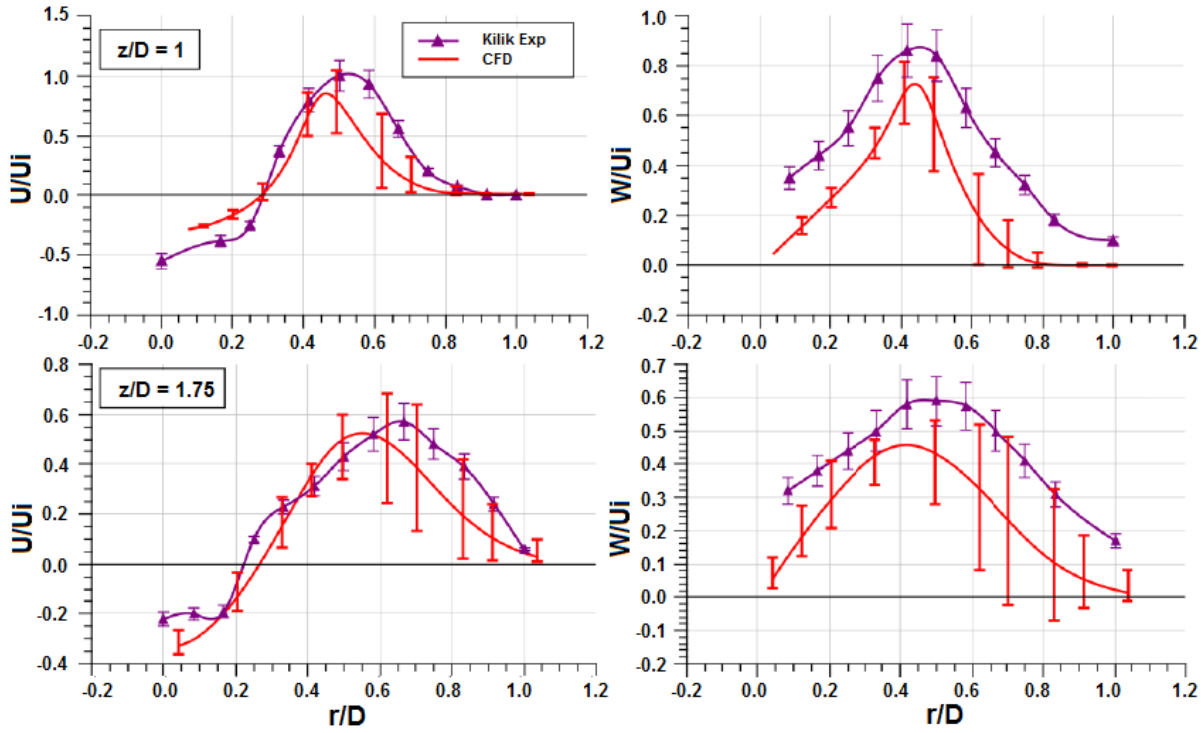

Figure 6.12: Numerical vs experimental profiles for normalised axial (U) and tangential (W) flow velocities for curved vane (S9) swirler

6.2.3 Simulations at windmilling conditions

The domain was converted to a confined configuration (representing the swirler within a combustor volume with walls) and run at sub-idle windmilling conditions. Experimental data in terms of total pressure tappings from various stations inside a turbojet engine, are presented by Vincent et al [40]. These were derived from windmilling conditions simulated inside an altitude test facility.

To estimate the combustor's boundary conditions under windmilling conditions, Read [114] assumes that half of the engine inlet dynamic head is lost in the compressor. Results from this method were compared with the experimental measurements and are illustrated in Fig. 6.13.

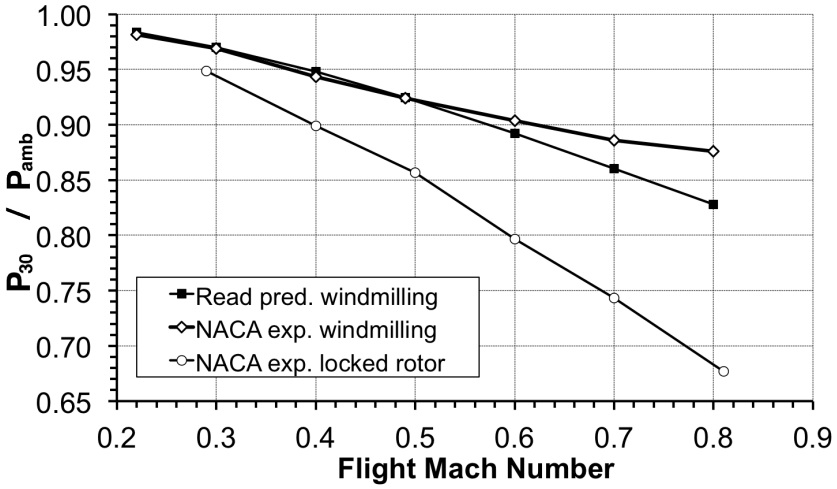

Figure 6.13: Windmilling boundary conditions

It can be observed that the assumption made by Read [114], is valid up to a flight Mach number of 0.5, above which the results diverge from the experimental measurements. One must mention that these characteristics depend also on the performance and torque requirement of the accessories that are attached to the high-pressure compressor. For this study, the experimental measurements at windmilling conditions were used as tabulated in Table 6.2.

	Groundstart	Windmilling Alt. 9144m				
	(exp. data)	M0.8	M0.7	M0.6	M0.49	M0.4
$P_{30}(kPa)$	394.9	40.1	36.9	34.7	32.8	31.8
$P_{40}(kPa)$	375.2	36	35	33.1	32	31.3
$T_{30}(K)$	473	287	273	262	251	243
$U_i(m/s)$	87.1	108.8	71.6	63.1	43.4	36.3

Table 6.2: Sub-idle boundary conditions extracted from test data [40]

Groundstart simulations

The boundary conditions used for the groundstart simulations were taken from experimental pressure readings from a modern civil high-bypass turbofan start just before ignition. This is done by taking the reading just before a step increase in the combustion chamber pressure is noticed, which indicates that ignition has occurred.

6.2.4 Results

Velocity profiles and scalability

The swirler's axial (U) and tangential (W) velocity profiles, shown in Fig. 6.14 indicate how the flow intensity diminishes with decreasing windmilling flight Mach number. This results in the decay of the central recirculation zone strength, as observed from the axial velocity distribution shown in Fig. 6.15, where the axial velocity goes from -45 m/s at a flight Mach number of 0.8, down to -15 m/s for a flight Mach number of 0.4.

The velocity profiles were then normalised using the swirler inlet velocity (U_i). The normalised profiles, as illustrated in Fig. 6.16 and Fig. 6.17, seem to converge towards a single curve, except for the low flight Mach number cases. This suggests that the low Reynolds number in the latter conditions has a significant influence, with the fluid viscosity becoming more dominant. This seems to occur at $Re_{vane} < 11,500$, as defined below:

$$Re_{vane} = \frac{\rho V_x s}{\mu} \tag{6.15}$$

The results shown in Fig. 6.16 show that for the high flight Mach number cases, both axial and tangential profiles can be scaled with good accuracy when normalised. For low flight Mach numbers however, the velocity profiles are not scalable. Figure 6.18 shows the blades' Reynolds number for the cases run.

Swirl number

The swirl number was calculated using the parameters extracted from the numerical solution. As illustrated in Fig. 6.19, relative to the groundstart case, the value at the swirler face is very low, suggesting a swirling flow of weak intensity, corresponding to a reduction in recirculating mass flow as shown in Fig. 6.15 and experimentally verified by Kilik [39]. As previously mentioned, this reduction in swirl number will impact the flame dynamics, reducing the flame speed and increasing its length as previously illustrated in Fig. 6.3, possibly reducing the flame stability due to the low level of turbulence, recirculation and mixing with incoming air and fuel.

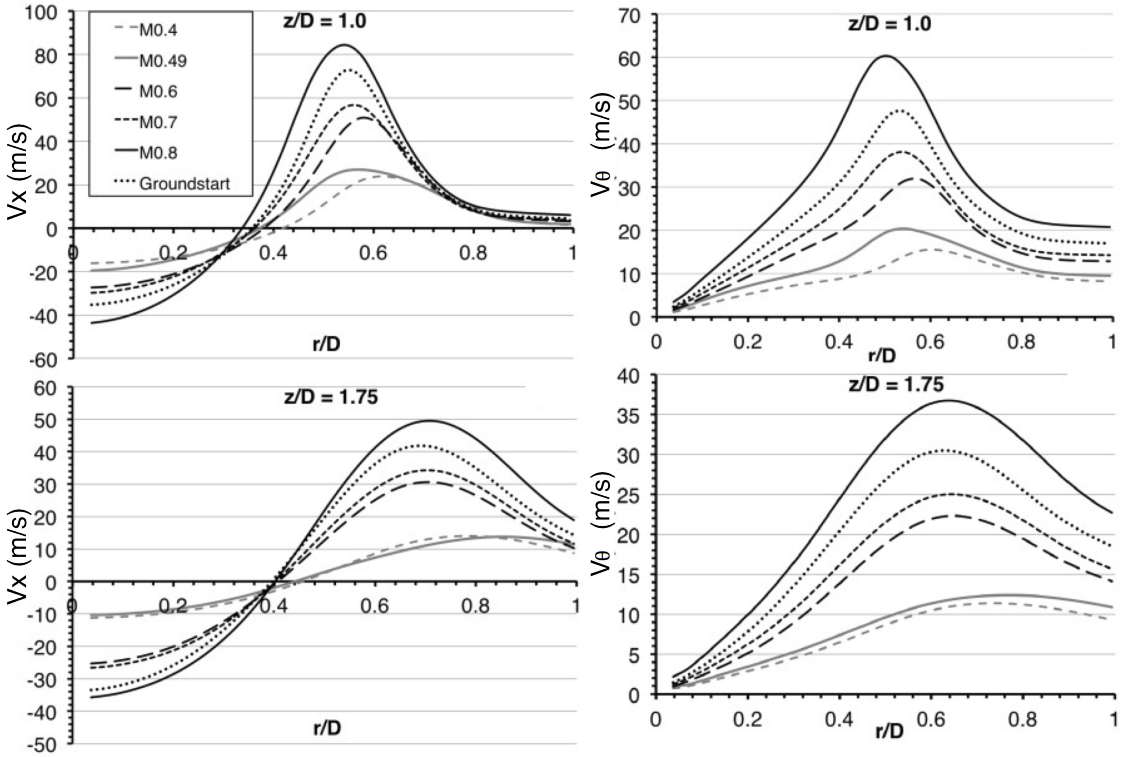

Figure 6.14: Sub-idle velocity profiles for windmilling conditions simulated

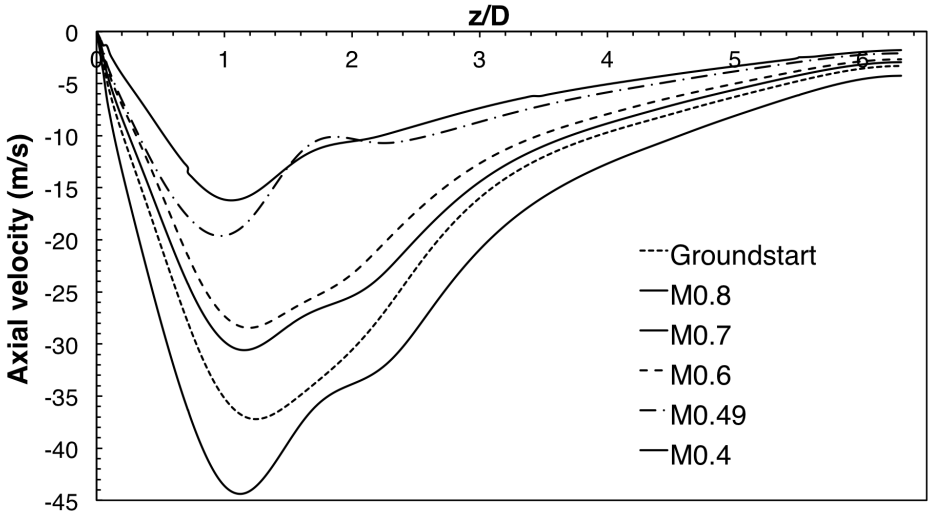

Figure 6.15: Central axial velocity profile and normalised central axial velocity

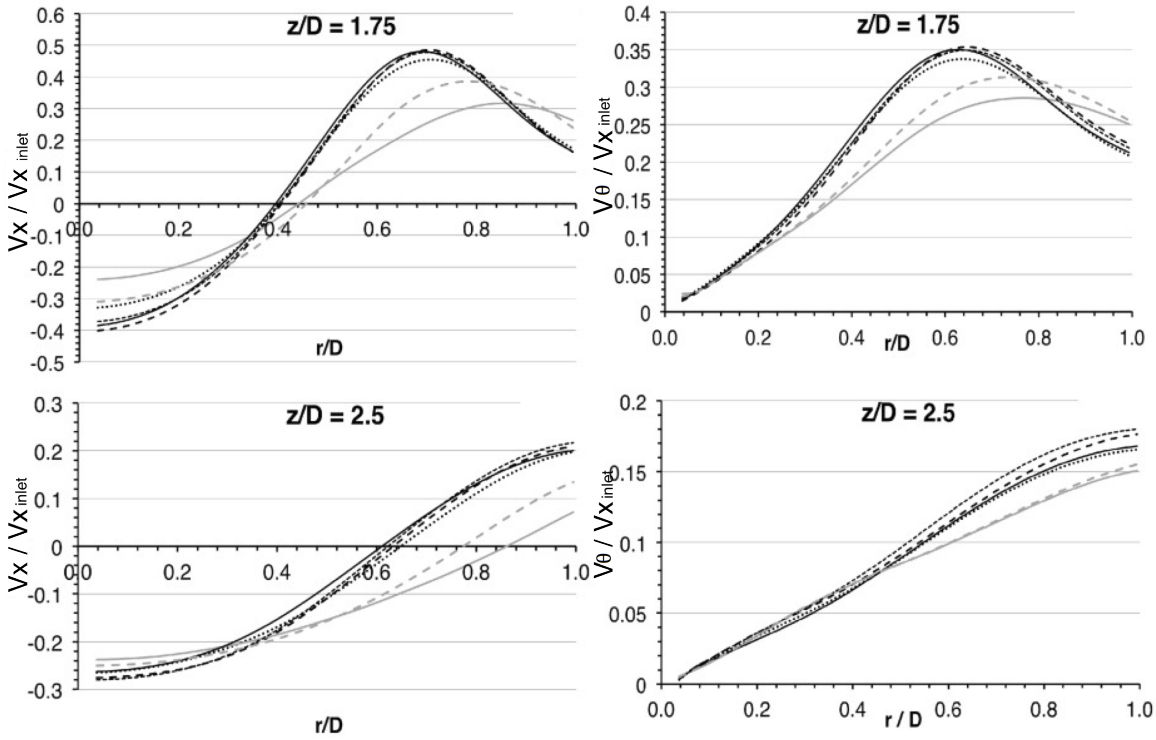

Figure 6.16: Normalised sub-idle velocity profiles

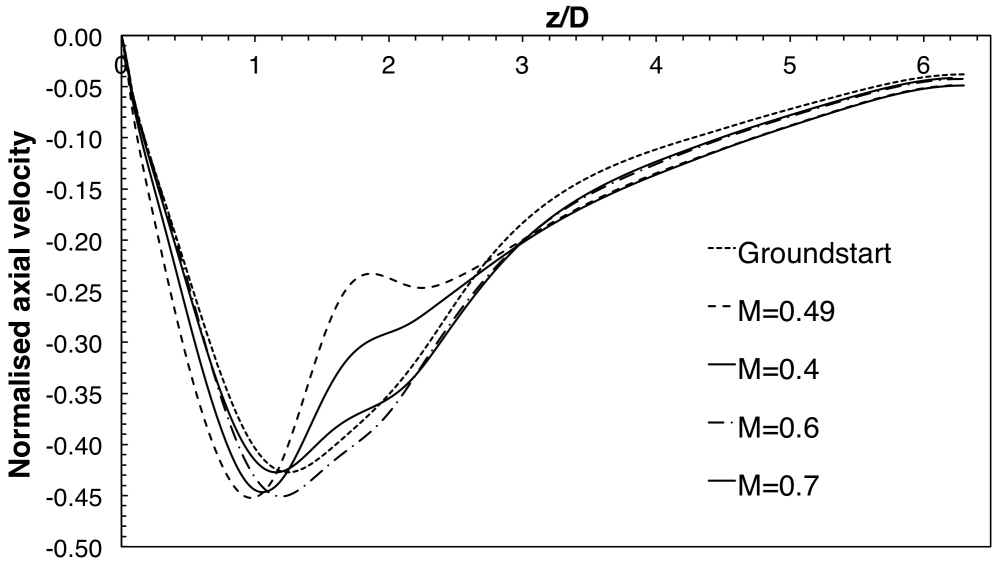

Figure 6.17: Normalised central axial velocity

The swirl number decays gradually with the distance downstream, until it attains a value similar to the groundstart condition. At first sight, no obvious link seemed to exist between the swirl number and mass flow rate. Attempts at extracting a correlation of the swirl number with dynamic head and pressure drops was tried. It was found that the swirl number can be linearly related to swirler inlet dynamic head divided by the domain inlet total pressure relative to free stream conditions. The swirl number will continue to increase with this parameter until it reaches the original design value. The correlation given in Eqn. (6.16), gives an r^2 of 0.998 and Root Mean Square Error (RMSE) of 0.0018.

$$S_N = -0.0189 + 1.2208 \left(\frac{0.5 \rho V_x^2}{P_{in} - p_{atm}} \right) \tag{6.16}$$

or in a more general form, where a and b are characteristic of the swirler:

$$S_N = a + b \left(\frac{0.5 \rho V_x^2}{P_{in} - p_{atm}} \right) \tag{6.17}$$

This relation shows that for low power conditions, the swirl intensity is not a constant value that can be simply predicted from the geometrical correlations. It is also dependent on the operating conditions. The general application of the correlation for similar swirler designs was verified by simulating the flat vaned swirler (S6) under the same windmilling conditions, as shown in Fig. 6.19. The measured swirl number shows a similar, linear relationship with the swirler inlet dynamic head. The groundstart swirl number for both swirlers also fits in this relationship demonstrating its applicability for any sub-idle condition and its use in predicting the changes in flame characteristics at sub-idle.

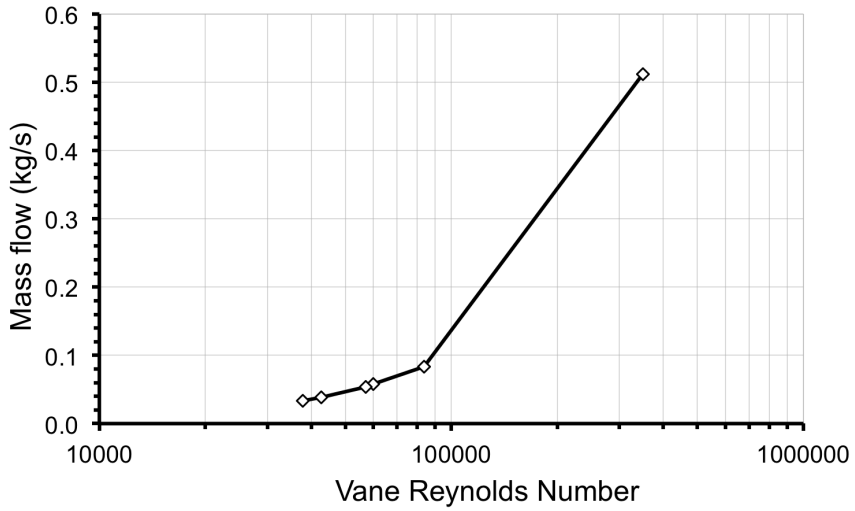

Figure 6.18: Vane Reynolds number for curved vane swirler (S9)

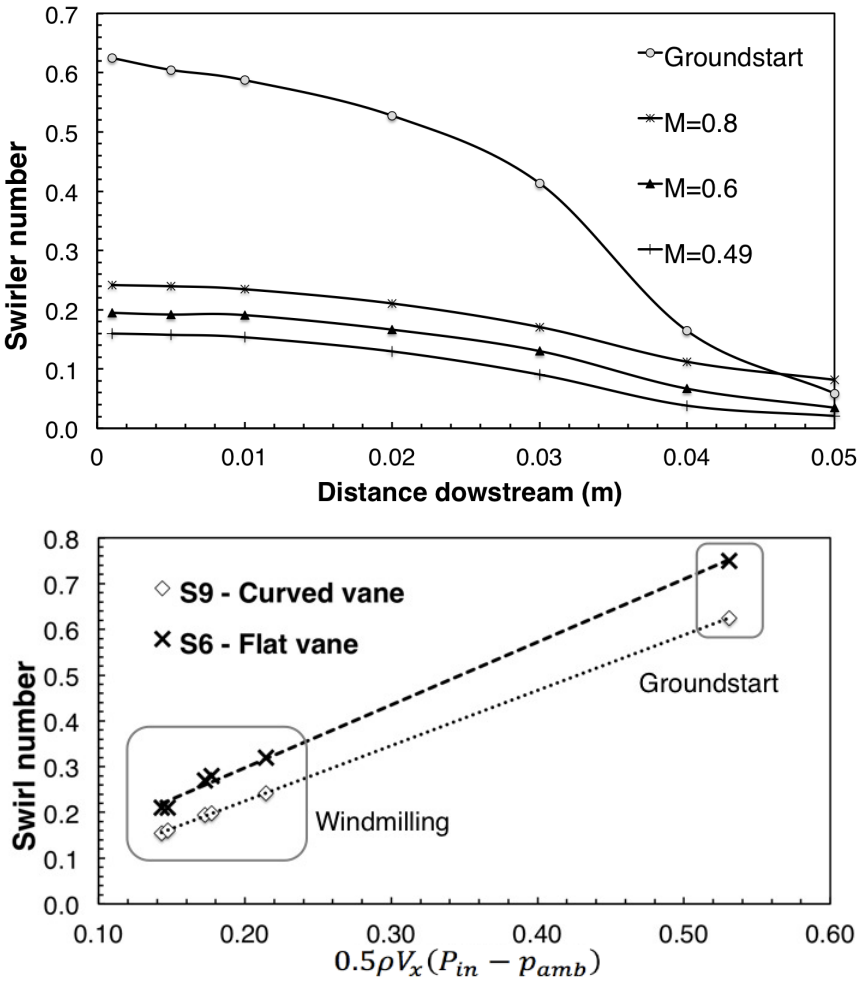

Figure 6.19: Sub-idle swirl number and swirl number correlation

The simulation results illustrated in Fig.6.19 show that under conditions of low mass flow rate and low dynamic head deduced from the reduction in windmilling flight Mach number, the rotation imparted by the swirler on the flow is reduced. This results in low tangential velocities and a weak swirl under sub-idle conditions, such as windmilling and altitude relight. In turn, this reduces the adverse pressure gradient required by the flow to create a reverse flow region. The effect is visible in Fig. 6.15, where the velocity magnitude of the reversing flow is clearly deteriorating, suggesting a recirculation zone of weaker intensity, and low reverse mass flow rate. The study also demonstrates that using scaled velocity profiles for numerical simulations where the swirler is not included, is valid except under low flight speed windmilling conditions. In such cases, it is suspected that low Reynolds number effects influence the velocity profile.

6.3 Airblast atomizer performance at sub-idle

6.3.1 Introduction

As mentioned in chapter 5, sub-idle combustion efficiency relies heavily on the prediction of the spray characteristics, mainly SMD. The combustion efficiency model described previously, uses the empirically derived correlations by El-Shanawany and Rizkalla (Eqns. (5.25) and (5.26)). These proved to under-predict the value of SMD, resulting in a relatively high value for the evaporation rate-based combustion efficiency. To overcome this, a deterioration factor had to be introduced.

Due to this shortcoming, a detailed numerical study on the atomization process at sub-idle was undertaken. The objective was to compare the spray characteristics predicted by the CFD, against those predicted by the empirical equations.

6.3.2 Methodology

Previous work carried out by Zachos [5], Kozaily [115] and Mehdi [116] on this area of study, used a relatively simple geometry for a modern airblast atomizer. The vanes were not modelled and the flow swirl was set-up by imposing a rotating inlet flow velocity. For this study a detailed geometry airblast atomizer was modelled, including the swirl vanes to capture also the influence of reduced swirl intensity and recirculation strength.

The model is described in further detail in section 6.3.4. Sub-idle conditions were simulated using total pressure boundary conditions extracted from [40], as was previously done in Chapter 6. For each sub-idle operating condition (i.e. different windmilling flight Mach numbers), the AFR was varied between 2 and 20 to represent different fuel flow rates. Observations and analyses are then made to compare the value of SMD predicted by the CFD against the empirical equations for a range of sub-idle operating conditions.

6.3.3 Literature review

Under low power conditions, spray characteristics deteriorate, as demonstrated by Caines et al [30], Jasuja [117] [118] [32], Beck et al [31] and Parsons et al [119], leading to an increase in fuel droplet diameter. An experimental investigation by Caines et al [30] shows the influence of sub-atmospheric conditions (at 31 and 41kPa) on the spray, as illustrated in Fig. 6.20. Results show a wide broadening of the droplet size distribution and SMD when compared to idle. Since most of the fuel is within the larger droplets, the evaporation rate decreases, causing a slower combustion reaction and a reduction in combustion efficiency (Datta and Som [120], Lefebvre [22], Lefebvre [87]).

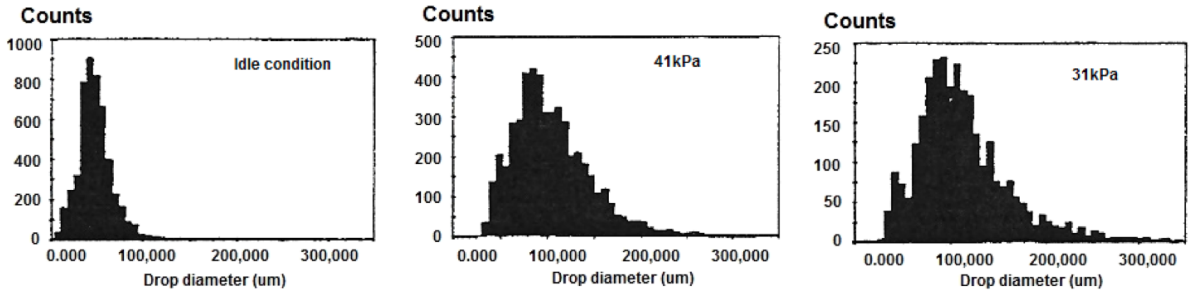

Figure 6.20: Droplet size distribution for various operating pressures [30]

Beck et al [31], as shown in Fig. 6.21, conducted similar experiments for conditions of low air velocity and different air/fuel ratios (AFR). The results indicate an increase in SMD with decreasing relative air velocity. This is attributed to the decrease in aerodynamic shear forces acting on the liquid sheet.

As the relative velocity approaches zero, the SMD continues to increase until a certain value is reached. The SMD remains constant at this value, even if the relative velocity is decreased further, indicating that a threshold exists below which the SMD does not increase further. The SMD is also sensitive to the liquid mass flow rate, with SMD increasing as the liquid mass flow increases. This is because the air/liquid mass flow ratio (basically the AFR) decreases, causing the air momentum per unit mass of liquid to decrease until it is no longer capable of fracturing the fuel efficiently.

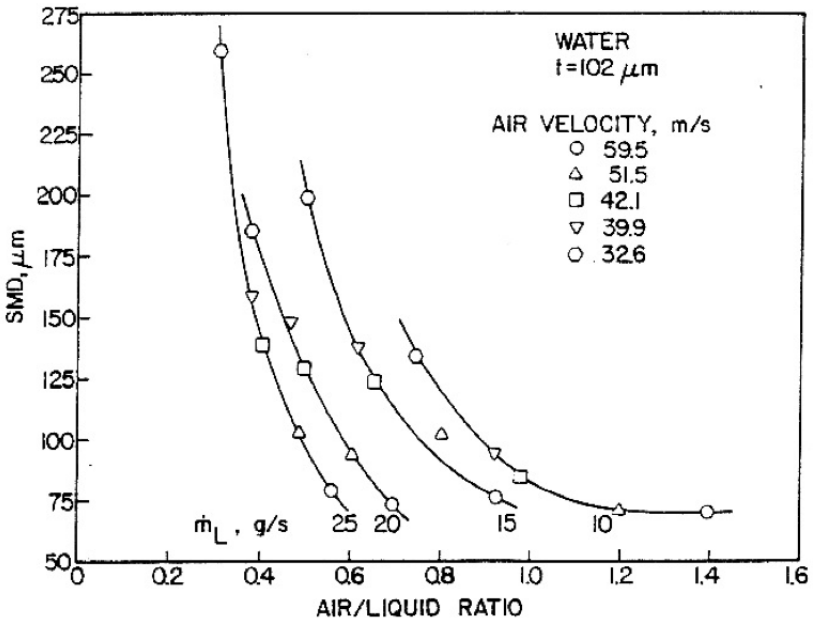

Figure 6.21: Effect of AFR and air velocity on SMD [31]

SMD was also found to deteriorate with increase in liquid surface tension and viscosity. Jasuja [117], whose experiments, as shown in Fig. 6.22, demonstrated the influence of the operating pressure on the SMD for the same AFRs, made similar observations. All these points are attributed to the Weber (We) number.

Rizkalla [121] and Rizkalla and Lefebvre [25] conducted a wide range of experimental studies on the effects of air and fuel properties on the atomization quality of an airblast atomizer, from which Eqn. (5.26) was derived. Results [25] show how for liquids of low viscosity, the dominant factors are air velocity and air density; SMD being inversely proportional to both. This again points towards having a large Weber number for better atomization. This is a very significant observation, since during an altitude relight, air density will be very low, coupled with a low velocity due to the low air mass flow passing through the wind milling engine. It was also observed that liquid viscosity has an effect, which is quite separate and independent of air velocity.

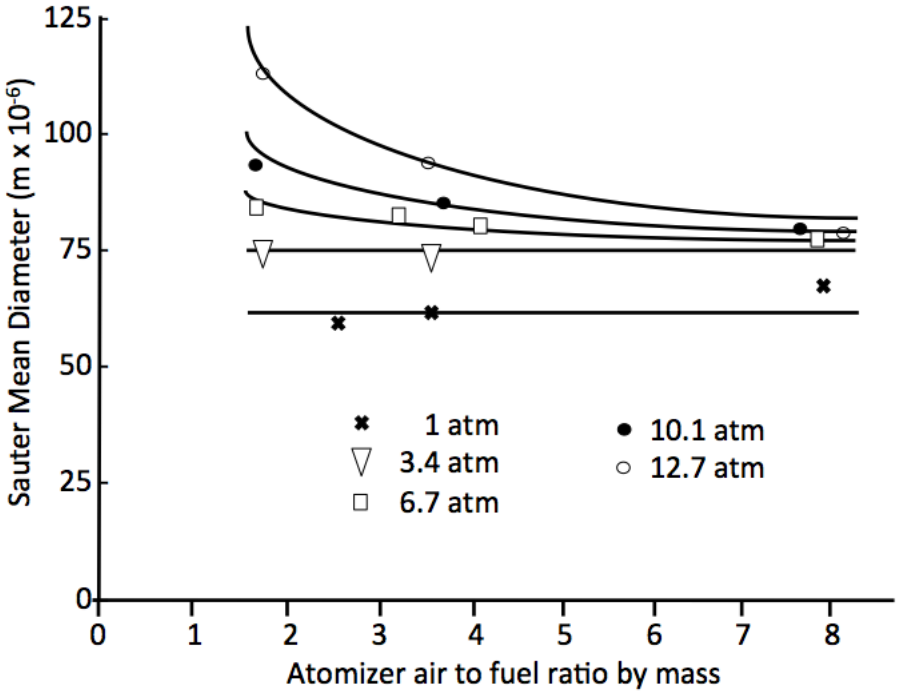

Figure 6.22: Effect of AFR and operating pressure on SMD [32]

6.3.4 Numerical model

Geometry

Due to IPR restrictions, only the diameters of the atomizer annuli were available. The number, angle and type of swirler vanes used in each annulus were guessed and subsequently changed until a good flowfield with a strong central recirculation zone formed in front of the atomizer. Generally this is achieved when the flow exits the swirler at a 45° angle relative to the atomizer axis, as shown in Fig. 6.23.

The vane angle of the outer annuli was set at 45° relative to the atomizer axis, and initially this angle was also used for the inner annulus. However, as observed in Fig. 6.23, the inner annulus has a restriction downstream of the vanes which increases the axial velocity of the central swirling flow. This results in a flow outlet angle of 30° relative to the atomizer axis, which prevents the formation of the central recirculation zone. To prevent this, the inner passage vanes were given a larger angle of 58° which results in an outlet angle of 45° at the atomizer face. Flat vanes were used for all the channels as illustrated in Fig. 6.23.

The numerical domain was extended 10 atomizer diameters downstream of the atomizer, and 2 atomizer diameters radially as shown in Fig. 6.24, to allow the flow to fully develop and avoid the recirculation reaching the exit plane.

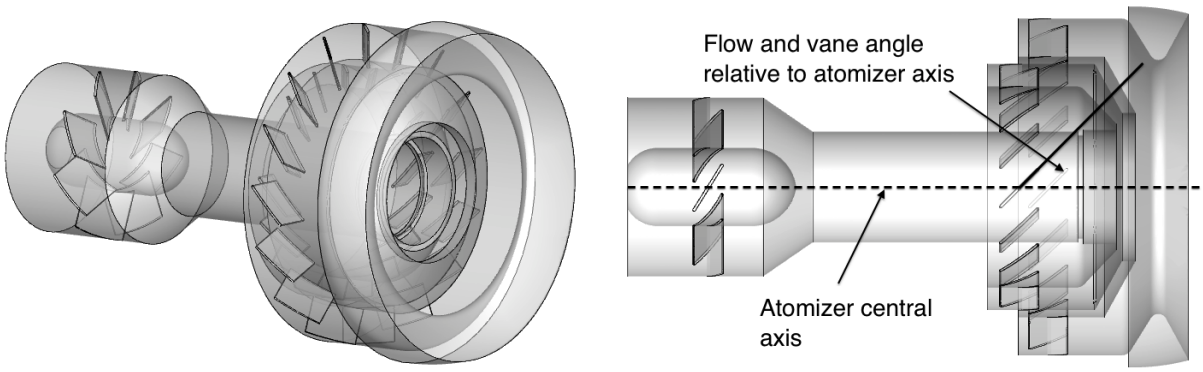

Figure 6.23: Airblast atomizer model and definition of vane and flow angle

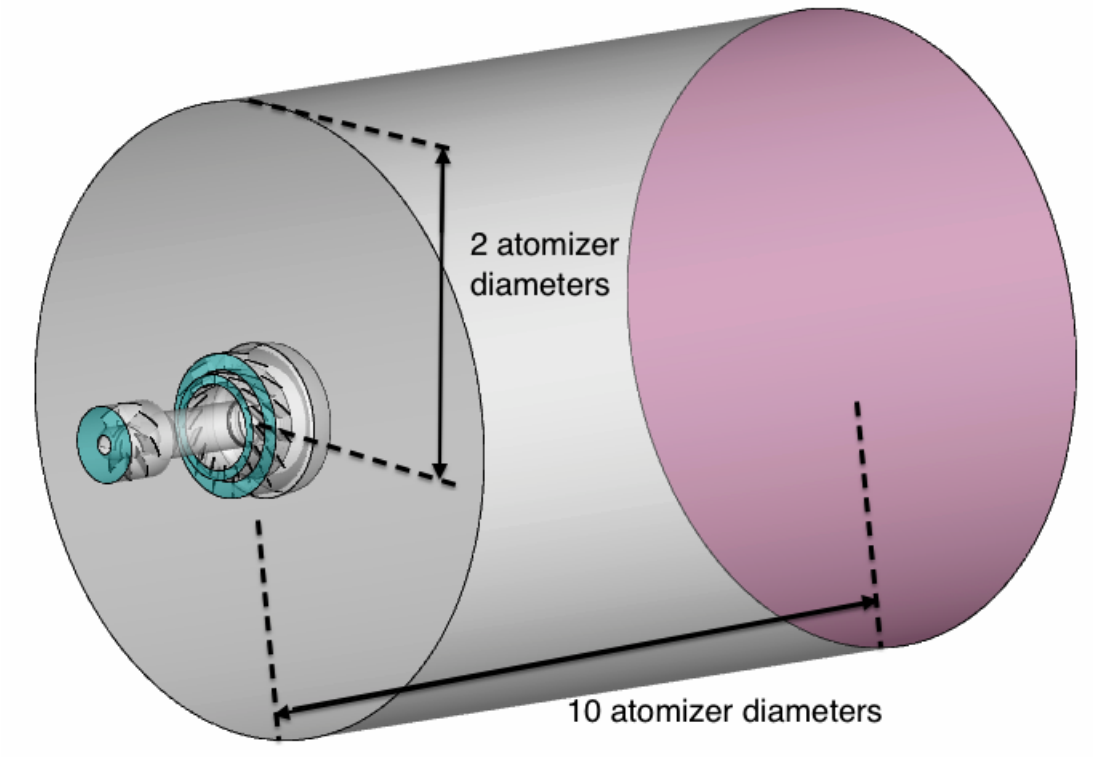

Figure 6.24: Atomizer numerical domain with: viscid wall (grey), total pressure inlet (cyan) and static pressure outlet (red)

Mesh

The model was meshed with an unstructured tetrahedral mesh using ANSYS Gambit. Prism layers were not included due to the complexity of the geometry involved. Standard wall functions were used to model the boundary layer within the solver. Figure 6.25 shows the mesh in the atomizer swirl vane regions. A mesh sensitivity study was undertaken using the axial and tangential velocity profiles of the flow field at various positions downstream of the atomizer to determine a suitable mesh density.

The variation of the flow field with mesh density at the atomizer exit plane, is illustrated in Fig. 6.26 from where a mesh of 14 million cells was chosen as the best compromise between computational power required and accuracy of the solution. Most of the cells are concentrated within the atomizer and in front of the atomizer exit plane, with coarser cells allowed further downstream to stabilise the solution.

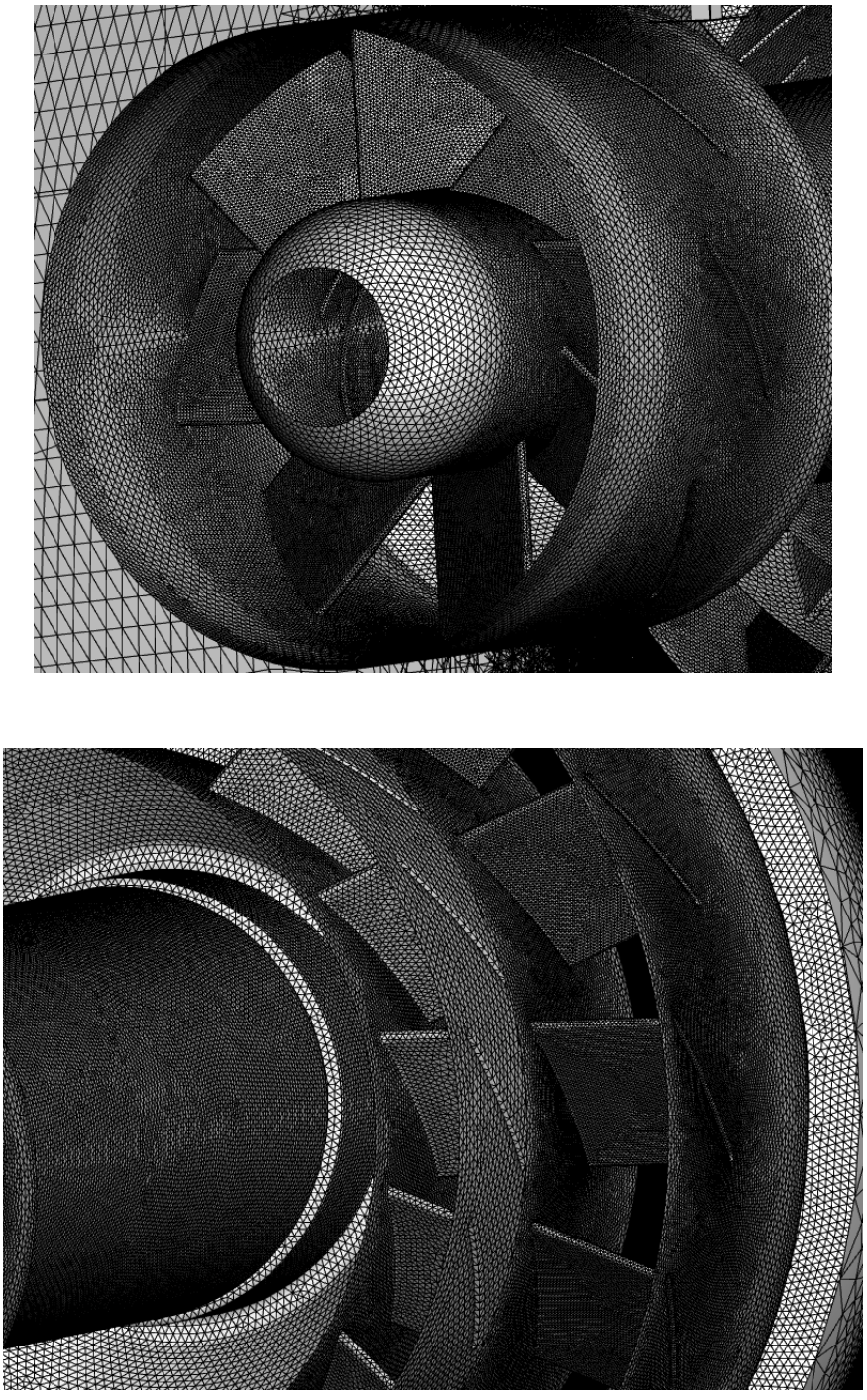

Figure 6.25: Details of the unstructured tetrahedral atomizer mesh at the inner, middle and outer vanes

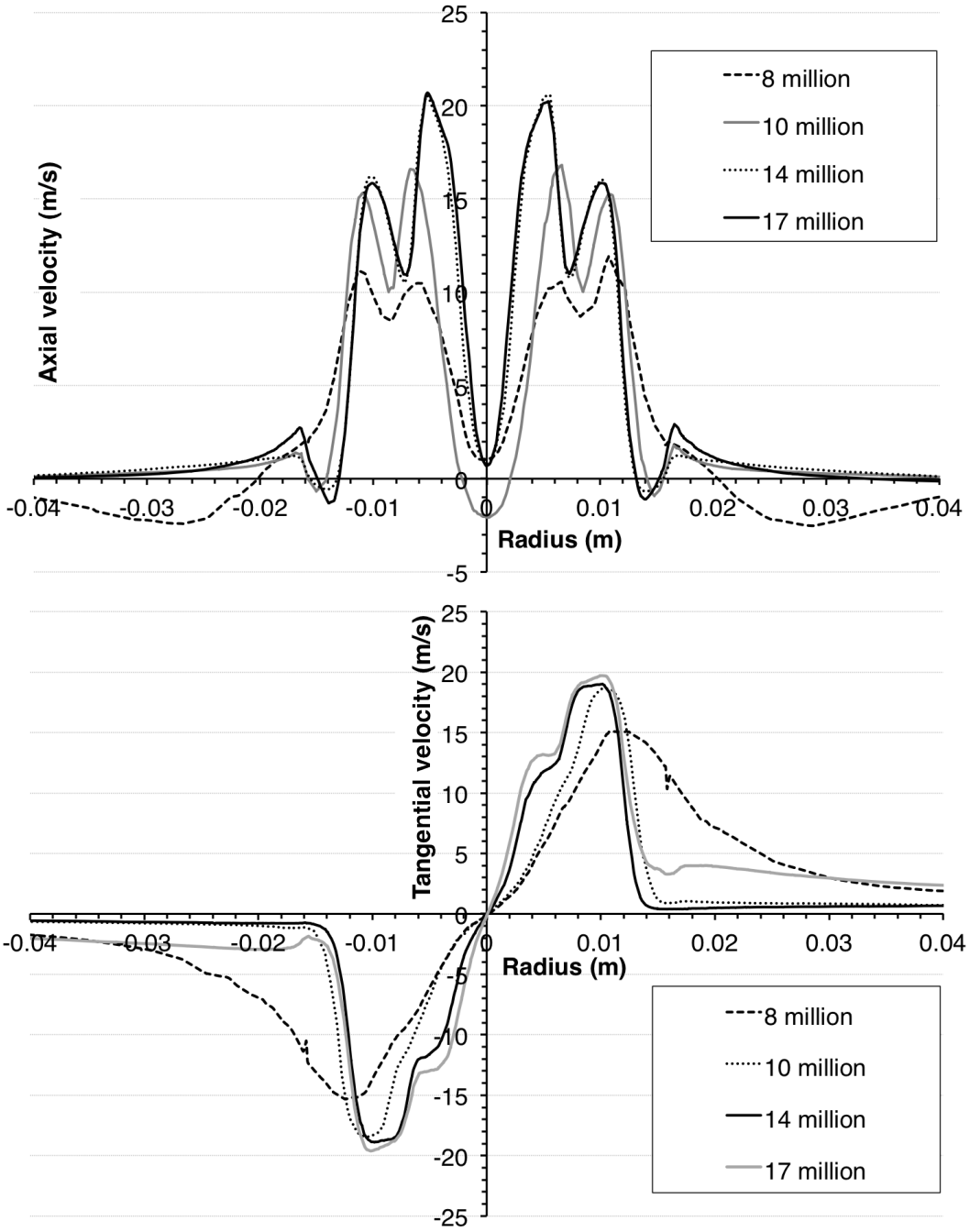

Figure 6.26: Mesh sensitivity study - axial and tangential velocity profile (m/s) at atomizer exit plane for different mesh sizes run

Solver setup

Uniform total pressure boundary conditions were used at the atomizer inlets, with static pressure at the outlet using the same conditions given in Table 6.2. The $k-\epsilon$ Realizable turbulence model was chosen based on the validation against experimental data [122], [123]. Since the flow is at low Mach number, the fluid was set as incompressible. The pressure-based simulation was run first order upwind steady for 1000 iterations, with convergence reached after 700 iterations using ANSYS Fluent. The first order upwind solution was used to initialise a second order upwind steady simulation for an additional 1000 iterations. Fuel was injected using the converged second order solution as the continuous phase. The solver's built-in airblast atomizer model was used with a relative velocity of 30m/s. The solver [9] allows the simulation of a discrete phase in a Lagrangian frame of reference. The discrete phase model (DPM) allows unsteady particle tracking within a steady continuous phase [9]. Fuel was injected with a particle time step of 0.0001 seconds, running 10 continuous phase iterations for every DPM iteration. A 10ms spray simulation was run by running 1000 iterations with the discrete phase setup. Convergence criteria for the continuous phase were all set at $1.0e^{-5}$. The solution generally converged when the turbulent kinetic energy reached this value, while other parameters such as continuity and momentum reached values close to $1.0e^{-6}$

6.3.5 Results

Flowfield

The size and intensity of the central recirculation zone in front of the atomizer has a large impact on the combustor's relight capability. To light-up, the flowfield needs to direct the fuel droplets towards the igniter. Otherwise the fuel will be out of reach from the igniter's energy, will fail to vaporise properly and ignite. Strong recirculation is desirable to stabilise and maintain the flame, preventing blow-out which can otherwise occur easily during a relight. Results were extracted along the positions illustrated in Fig. 6.27. The atomizer flowfield's central axial velocity was analysed to observe changes in recirculation size and intensity. The results, illustrated in Fig. 6.28 reflect observations made in section 6 where the size and negative axial velocity of the recirculation zone increased with flight Mach number. For this atomizer, the axial velocity goes from -2.5 m/s at Mach 0.3, down

to -32.5 m/s at Mach 0.7. This improvement in flowfield characteristics is due to the increased air mass flow, resulting in higher atomizer exit axial and tangential velocities as shown in Fig. 6.29. The formation of the vortex breakdown is observable in Fig. 6.30.

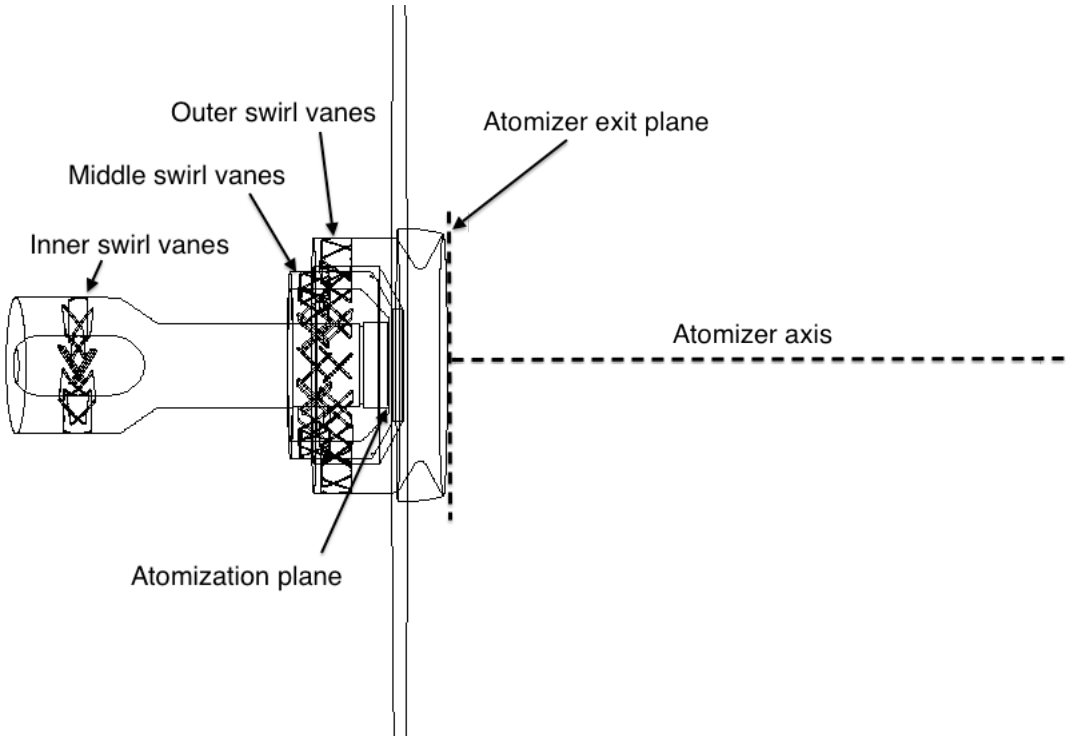

Figure 6.27: Airblast atomizer model showing position of the atomizer exit plane and the axis used for extracting flow results

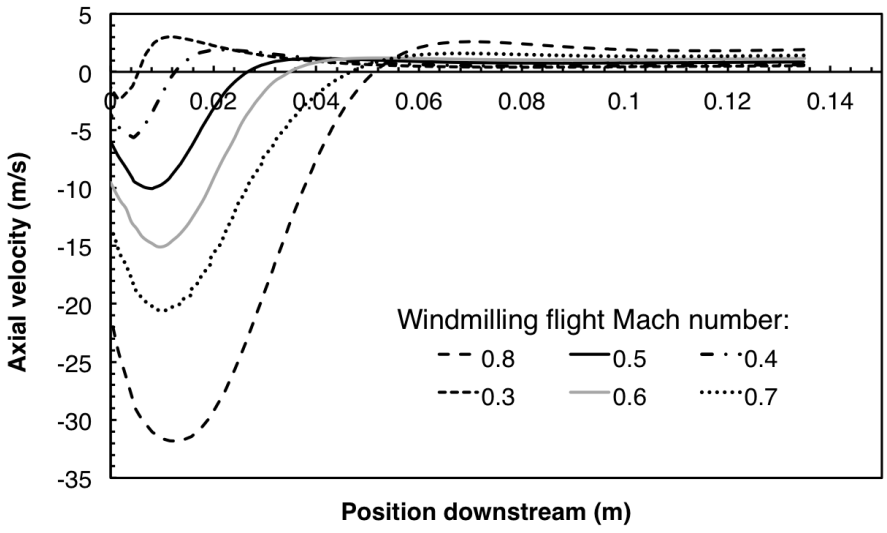

Figure 6.28: Axial velocity along atomizer central axis

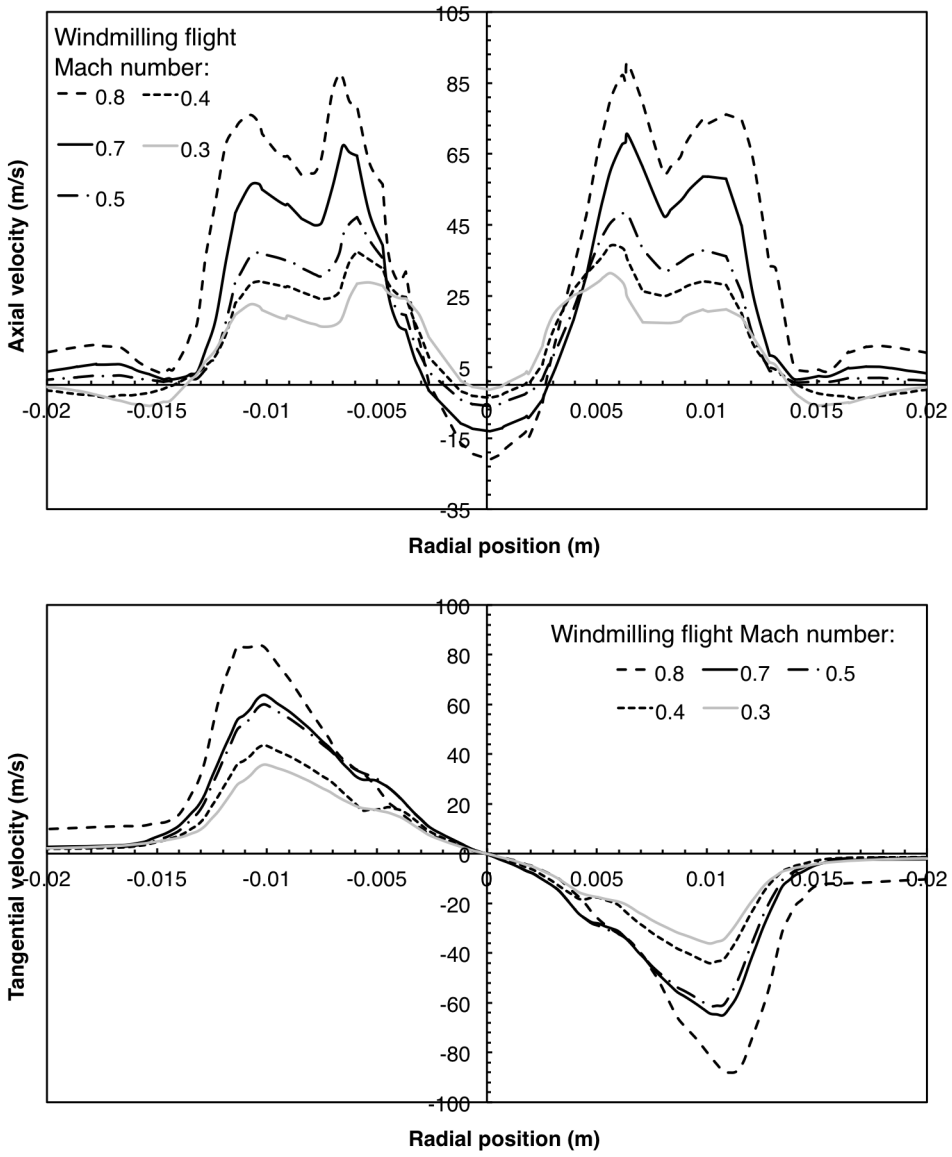

Figure 6.29: Axial and tangential velocity profiles at atomizer exit plane for the various windmilling flight Mach numbers simulations

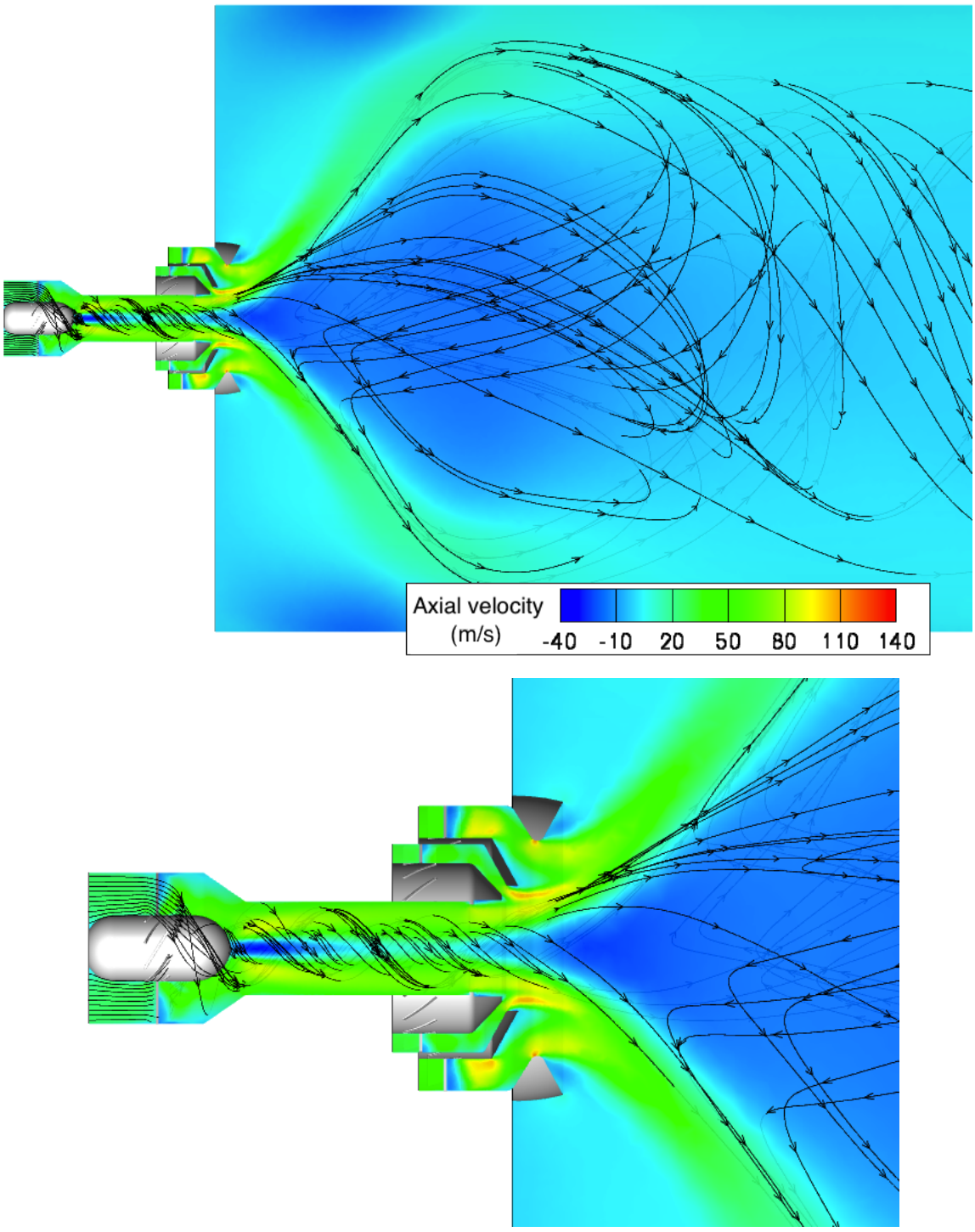

Figure 6.30: Atomizer flowfield contours of axial velocity (m/s) and streamlines for flight Mach 0.8

Spray characteristics

Each flight Mach number (0.4 - 0.8) case was run for various AFRs (2 - 20). Low AFRs are typically used during altitude relights. The results are summarised in Fig. 6.31. The SMD trends agree well with the literature ([30] [31] [117] [119]). It is expected that the SMD drops as the flight Mach number increases due to more favourable conditions at the combustor inlet, such as higher density and flow velocity through the atomizer. This trend is followed for all AFRs. The cases with the highest AFRs show the highest SMDs, which decrease as the AFR increases. Again this is expected since at low AFRs, proportional to the amount of fuel there is little air available to atomize the fuel, i.e. a low Weber number.

The Rosin-Rammler distribution of the flow was also extracted, with the results shown in Fig. 6.32. At low flight Mach number (0.4 and 0.5), the value of q remains fairly constant over the entire range of AFRs used, indicating that the low flow conditions have the dominating effect on the uniformity of the spray. At Mach 0.6 and above, there is a gradual increase in dependency on the AFR. At Mach 0.6 there is some change between AFR 2 and 5, above which the q stays fairly uniform. At Mach 0.7 and above however, the effect of AFR is more pronounced, with the spray being much more uniform at the highest AFRs for the same flight conditions. A uniform spray is desirable to control the equivalence ratio and avoid localised pockets of high temperature gases.

The minimum ignition energy (see section 6.1.3) was simplified as function of the droplet diameter in Eqn. (6.13). Assuming this relationship, it is possible to estimate the increase in minimum ignition energy required when the SMD deteriorates. The values shown in Fig. 6.33 indicate the factor increase in E_{min} relative to the smallest SMD measured from the simulations. Since E_{min} is a function of the droplet diameter cubed, the factor increase is very large, with the lowest SMD showing an increase in energy required by a factor of 55. At higher AFRs, the maximum factor increase is by 10 for the lowest flight Mach number case. An example of the spray simulation is shown in Fig. 6.34.

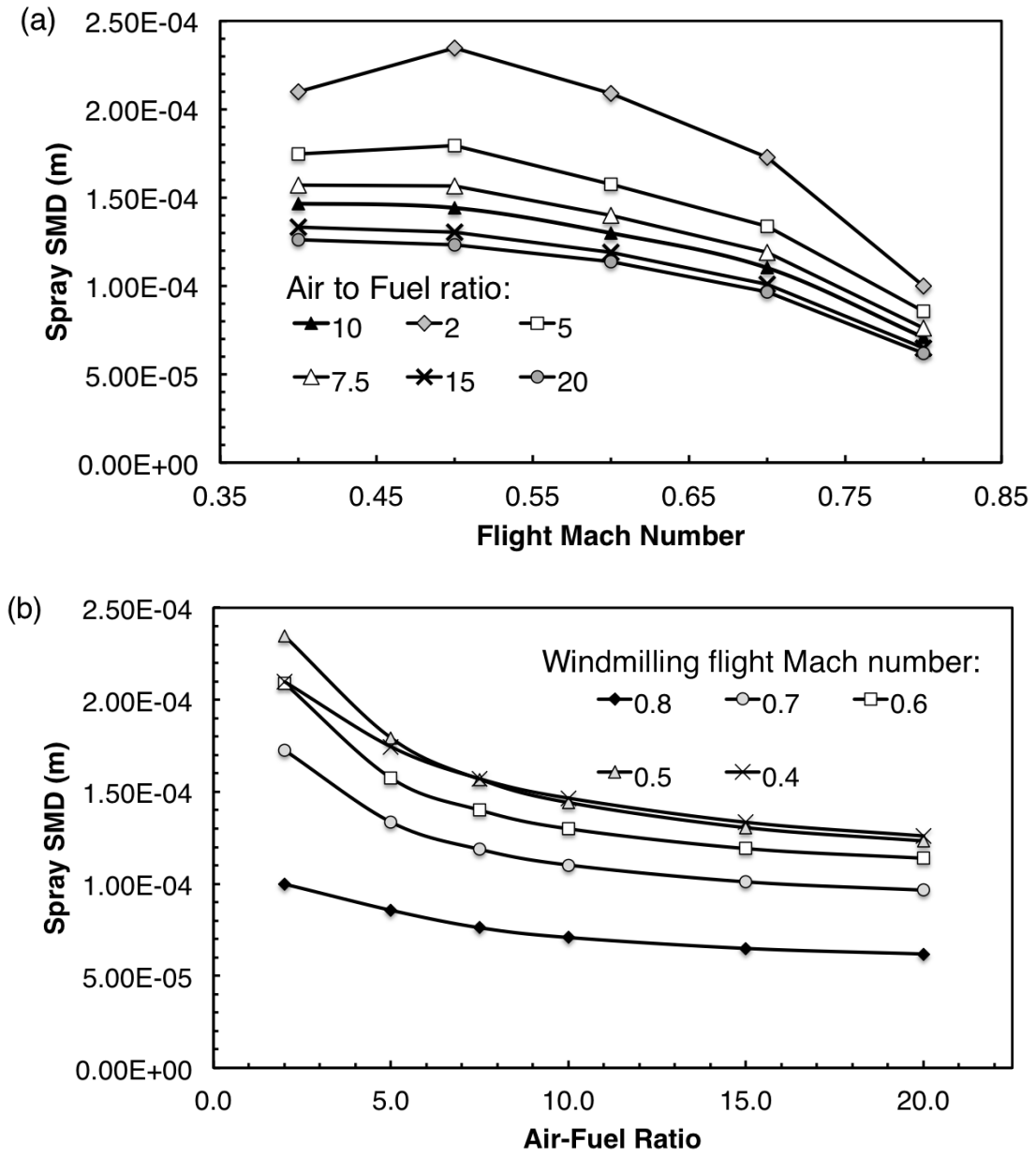

Figure 6.31: Numerical simulation SMD results in terms of (a) the flight Mach number and (b) AFR

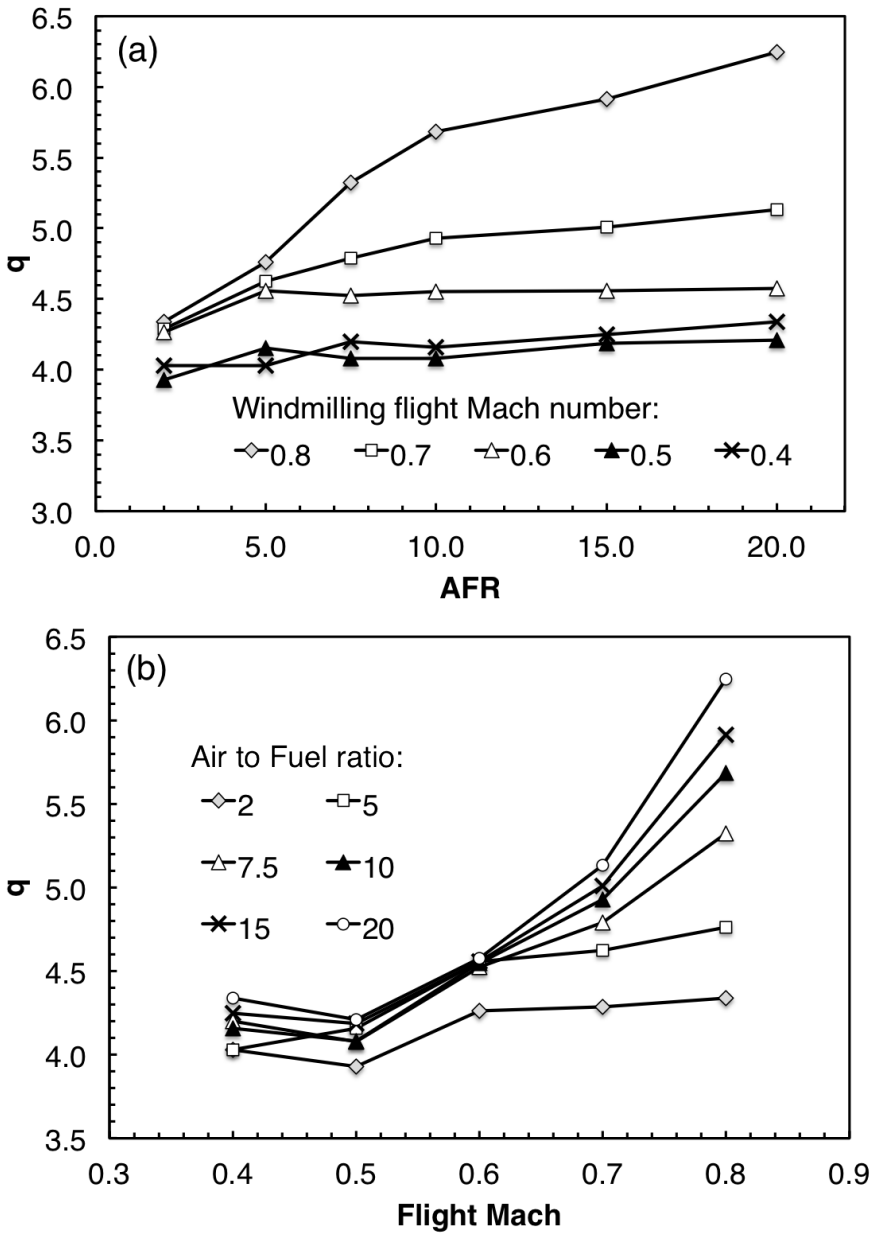

Figure 6.32: Rosin-Rammler [33] distribution of numerical simulation results in terms of the (a) flight Mach number and (b) AFR

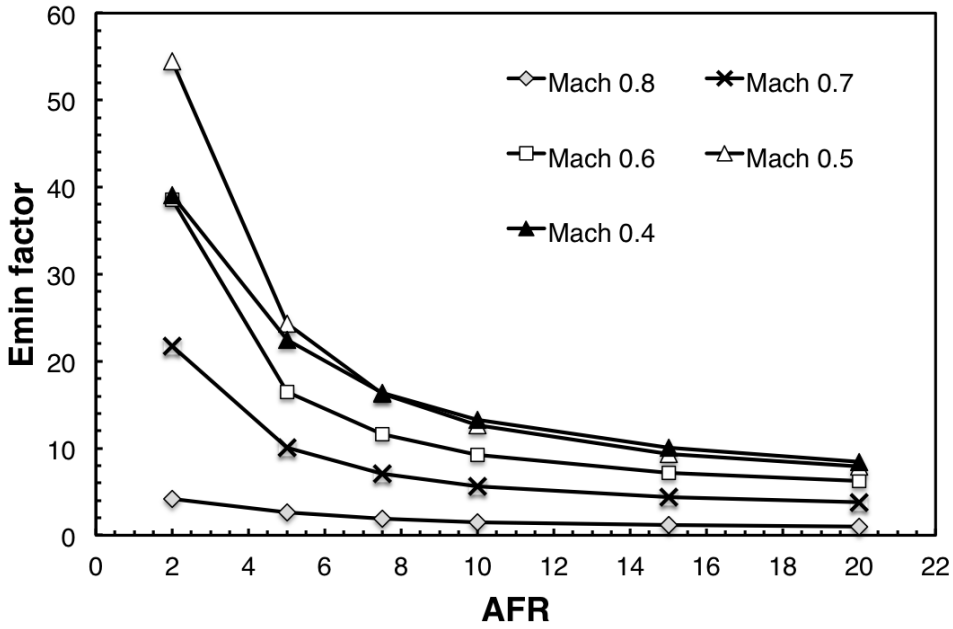

Figure 6.33: Effect of sub-idle SMD characteristics on minimum ignition energy

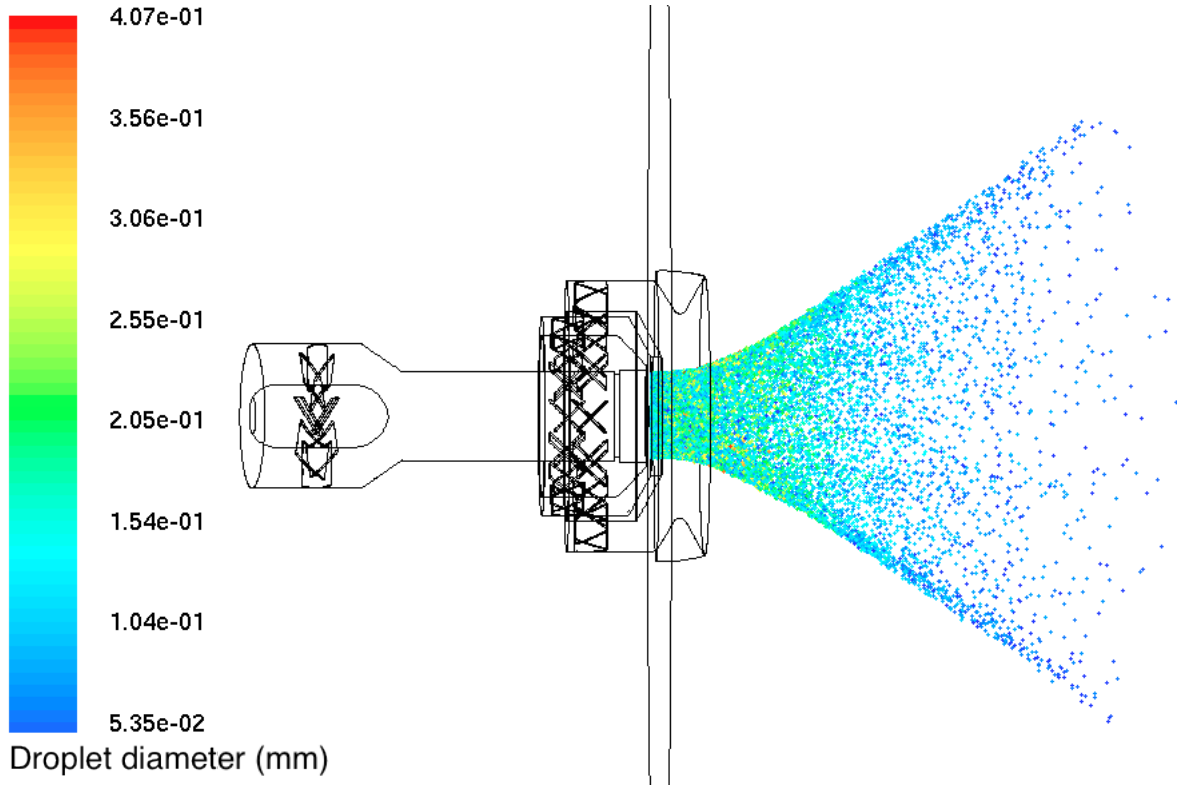

Figure 6.34: Atomizer spray simulation showing droplet diameters - flight Mach 0.4 and AFR 10

Comparison with SMD correlations

To evaluate the reliability of standard SMD correlations for airblast atomizers, the flow properties and atomizer parameters were input into the correlations and the results compared with the SMD derived from the numerical simulations. The correlations evaluated were El-Shanawany and Lefebvre [26] and Rizkalla and Lefebvre [25], as given by Eqns. (5.25) and (5.26) respectively. The results are illustrated in Fig. 6.35.

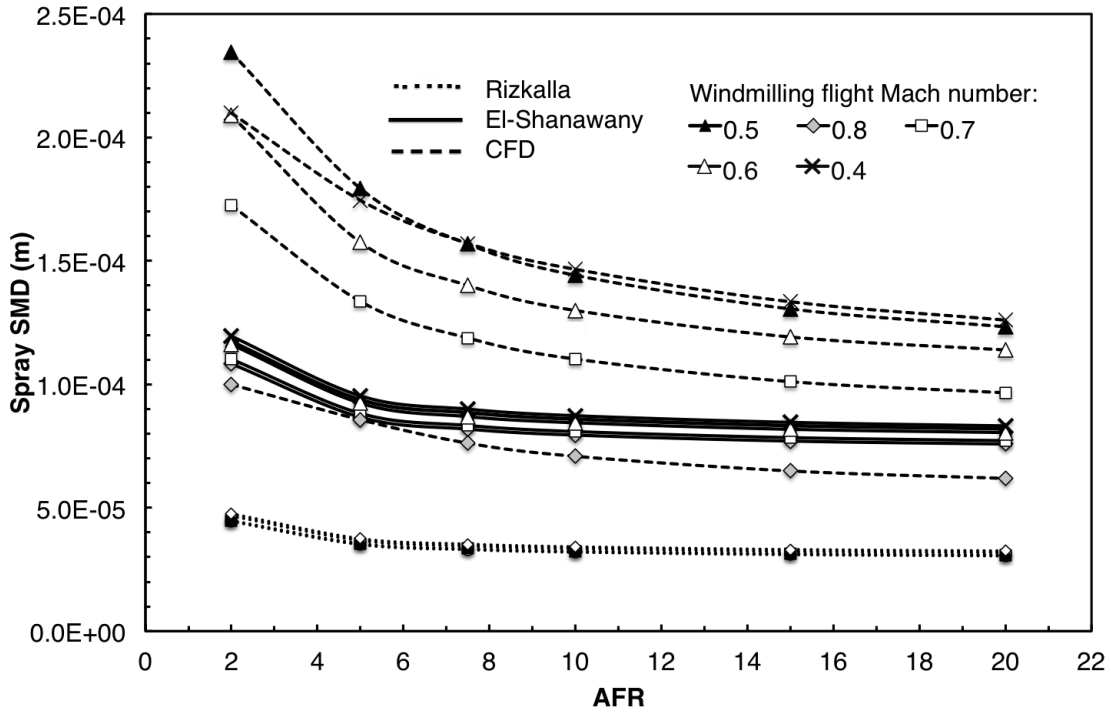

Figure 6.35: Comparison of spray SMD for different flight Mach numbers; numerical simulations (dashed line), El-Shanawany and Lefebvre (solid line), Rizkalla and Lefebvre (dotted line)

6.4 Concluding remarks

Knowledge on combustion at low power conditions is still relatively limited. As part of the work in trying to model combustion efficiency at low power, it was fundamental to understanding better which phenomena dominate the combustion process at such conditions. The flow and spray characteristics of axial swirl atomizers were the two areas studied. Previous research [92] [115] [116] used constant flow angles to represent the atomizer at various operating conditions. To verify this assumption, a simple single annulus axial swirler was numerically modelled. The numerical setup was first validated against experimental data, following which it was run at boundary conditions representative of a combustor under altitude windmilling conditions. Results clearly show a significant change in flow characteristics with the windmilling flight Mach number, where the both axial and tangential velocities, the swirl number, and the size and strength of the recirculation zone, deteriorate as the flight Mach number decreases. The results also demonstrate that the atomizer should be included in the numerical domain if realistic flow characteristics are to be modelled. A correlation between the swirl number and the swirler operating condition was also derived, and found to be valid for both flat and curve vaned swirlers.

The study was extended to a more complex multi-annular axially swirling airblast atomizer using the same validated numerical scheme. Results reflect those of the simpler model where the flow and recirculation strength deteriorate at low flight Mach numbers. With the introduction of fuel, the spray characteristics (SMD and Rosin-Rammler distribution) were found to deteriorate with decreasing flight Mach number and air-to-fuel ratio, reflecting the influence of both a weaker flow field and reduced Weber number on the fuel droplets. One must mention however that atomization models in numerical solvers are not as accurate and reliable, and therefore results should be analysed qualitatively rather than in absolute terms.

The spray numerical results were compared against spray SMD correlations [26] and [25]. The comparison indicates that such correlations tend to underestimate the spray SMD, and are quite insensitive to changes in sub-idle operating conditions.

Chapter 7

Influence of Compressor Wakes on Combustor Relight Performance

7.1 Introduction

When analysing the performance of a combustion chamber using either CFD or test rigs, the flow fed to the chamber in the pre-diffuser section generally does not include any wakes from the compressor outlet vanes [124]. At design point this is justified since such wakes are very small and mix out rapidly before reaching the atomizer, with little consequence on the fuel atomization process. During an unassisted altitude relight however, the compressor is operating at a very far off-design operating point. As already shown in previous chapters, at such conditions the blades will be subjected to a highly negative incidence, producing large wakes. These wakes can be quite strong when the flow Mach number is high.

It is not known whether such wakes mix out or reach the atomizer inlet. Their effect on combustor performance has never been analysed since relight tests are conducted in an ATF or flying test bed (FTB), where it is not possible to measure the inlet flow velocity profile. One may speculate that such wakes result in a non-uniform flow entering a pre-filming airblast atomizer, subjecting the film of fuel to a range of velocities, leading to areas having a low We number with formation of larger droplet diameters. On the other hand, the atomizer face might be subjected to a concentrated region of high velocity

air, increasing the We number and resulting in better atomization. In order to predict more accurately the value of combustion efficiency at relight, it is important to determine the nature and magnitude of this effect. To address this unexplored area of research and shed more light on the effect of these wakes, a detailed numerical simulation of a full combustor model was run, subjected to different wake intensities generated from a model of the compressor OGVs.

7.2 Literature review

There is not much work done on this particular topic since it is generally assumed that the compressor wakes tend to mix out quickly before reaching the atomizer. However a limited number of studies were carried out, albeit on design point operating conditions where the wakes are very small and the flow downstream of the compressor is not very separated.

The influence of compressor OGV blades and structural struts on a fuel injector, including the effects on the injector flow field, was studied by Barker and Carrotte [125]. Cases with steep velocity gradients, and therefore higher shear stresses, lead to rapid mixing of the wakes. However as the wakes thicken the rate of mixing decreases. Wakes observed at the pre-diffuser exit, pass through the dump cavity resulting in pressure variations being observed in the vicinity of the injectors. Local variation in total pressure presented to the injector due to wakes from OGV blades, was of the order of 20% of the pressure drop across the fuel injector. The inner annulus of the injector was the most sensitive to the wakes [125]. Overall, the presence of the wakes resulted in a velocity variation of the order of 15% in the downstream injector flow field, which can affect the mixing pattern within the flame tube. However, as pointed out in [125], these results will vary from section to section since the number of OGVs is not necessarily a multiple of the number of injectors or burner sectors.

Similar studies on the flow field variation downstream of a compressor OGV are described in Walker et al [126], and Walker and Carrotte [127]. A detailed study, even though on lean-burn combustors is described in Ford et al [34]. The geometry of lean-burn combus-

tors is significantly different from rich-burn ones (which is the type used in the current study), as illustrated in Fig. 7.1. One has to appreciate that the size of the diffuser exit relative to the injector diameter in the case of the lean-burn type, is much greater than that of the rich-burn. It is therefore more likely that in the lean-burn type, the wakes will penetrate the injector due to their relatively small size.

In the rich-burn type, the wakes are much larger than the injector diameter and therefore it is less likely that an individual wake will penetrate the combustor. It is more likely that the wakes will hit the injector and diffuse, creating a region of high static pressure at the injector face. The effect of these wakes (Fig. 7.2) results in a significant variation in the velocity profile, both radially and circumferentially, of the atomizer flow (Fig. 7.3).

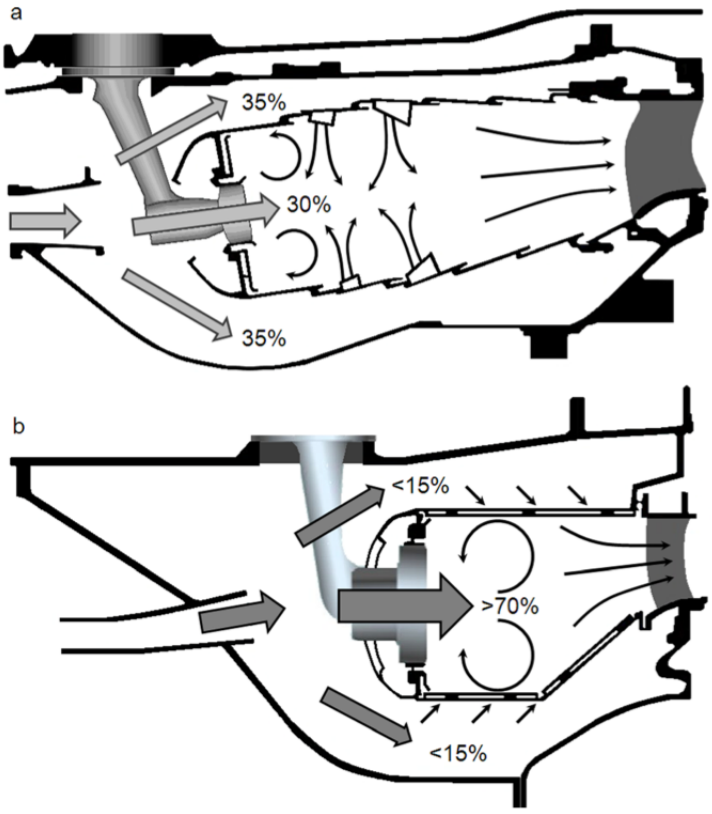

Figure 7.1: Geometrical difference: rich-burn (a) and lean-burn (b) combustor [34]

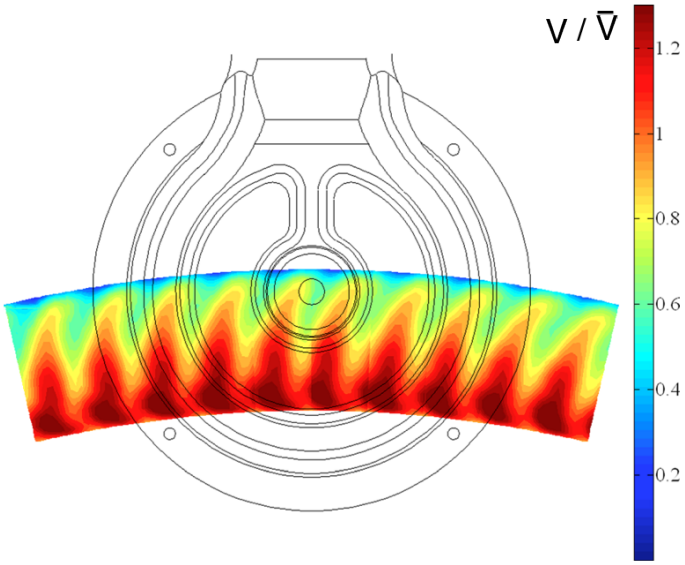

Figure 7.2: Pre-diffuser exit contour of flow velocity normal to the measurement plane relative to area weighted spatial average for a lean-burn combustor [34]

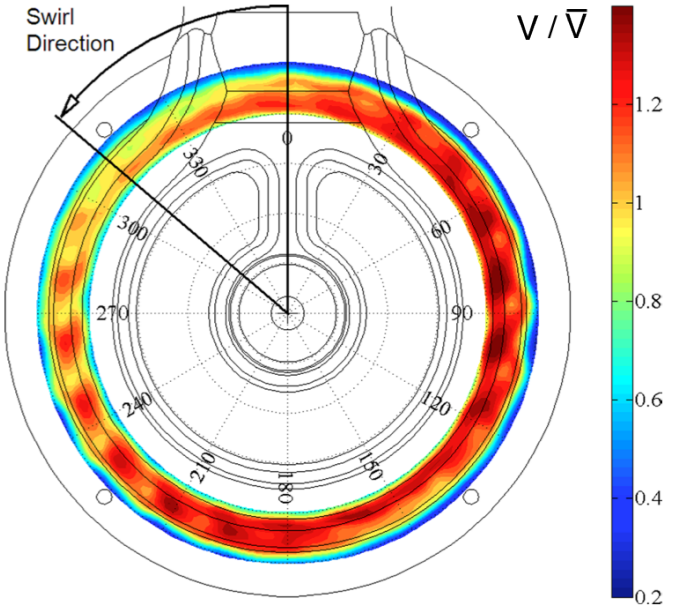

Figure 7.3: Atomizer exit contour of flow velocity normal to the measurement plane relative to area weighted spatial average for a lean-burn combustor [34]

7.3 Methodology

The combustor model used is a rich-burn type from a low-bypass military turbofan. The full combustor geometry including the compressor OGVs was provided by the sponsoring company. The altitude relight test data used to establish the boundary conditions of the model was also provided by the sponsor. The actual boundary condition values and geometries used cannot be published here due to confidentiality. To simplify the model, the combustor and OGVs were modelled separately. The velocity profile from the OGV model was then read at the plane equivalent to the combustor inlet plane, and used as the inlet boundary condition of the combustor model as illustrated in Fig. 7.4. In this manner, the same model set-up can be subjected to wake profiles of different strengths. Two relight conditions were investigated; the top left (TLC) and top right corners (TRC) of the relight envelope. For each condition the air mass flow rate, temperature and density were calculated from the altitude relight data, however the incidence angle on the OGVs was varied to create wakes of different strengths. In this manner the effect of the wake characteristics is isolated from the influence of having a variation in air mass flow rate.

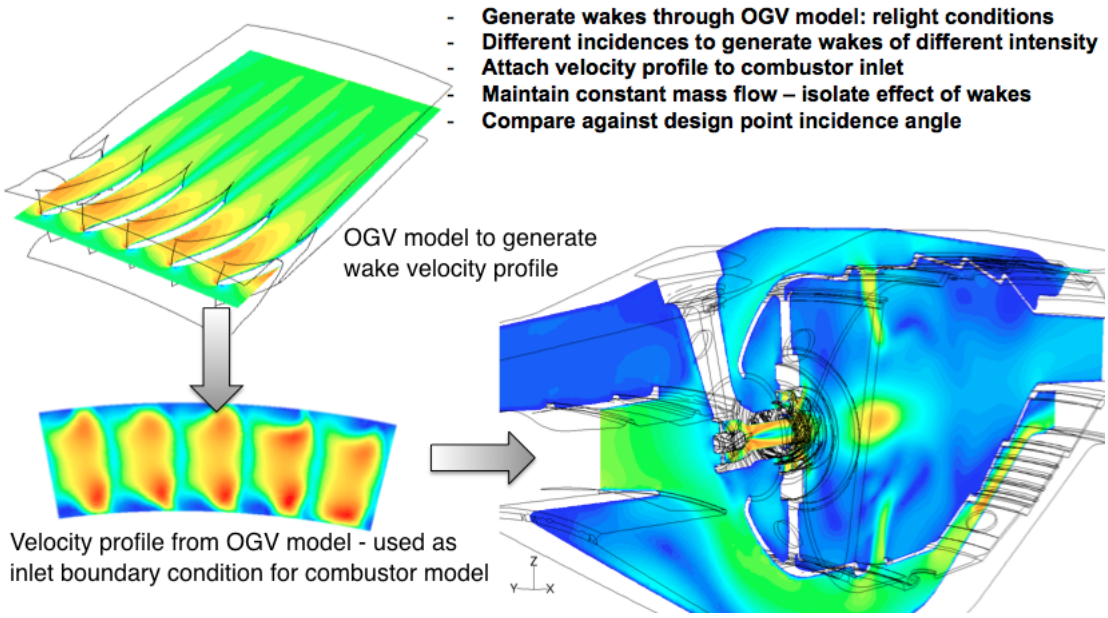

Figure 7.4: Methodology used to create altitude relight conditions for the full combustor numerical model

7.4 Combustor numerical model

A detailed combustor geometry was employed, of which features are illustrated in Fig. 7.5. The model is rotationally periodic with a domain of 20°, representing one sector of the annular combustor. Nearly all the geometrical details were included in the model, including the primary and secondary cooling holes, and the atomizer channels and vanes. Features considered too complex to model, such as the film cooling slots, the heat shield, and effusion cooling, were omitted and replaced by simpler inlet and outlet boundary conditions, as shown in Fig. 7.6.

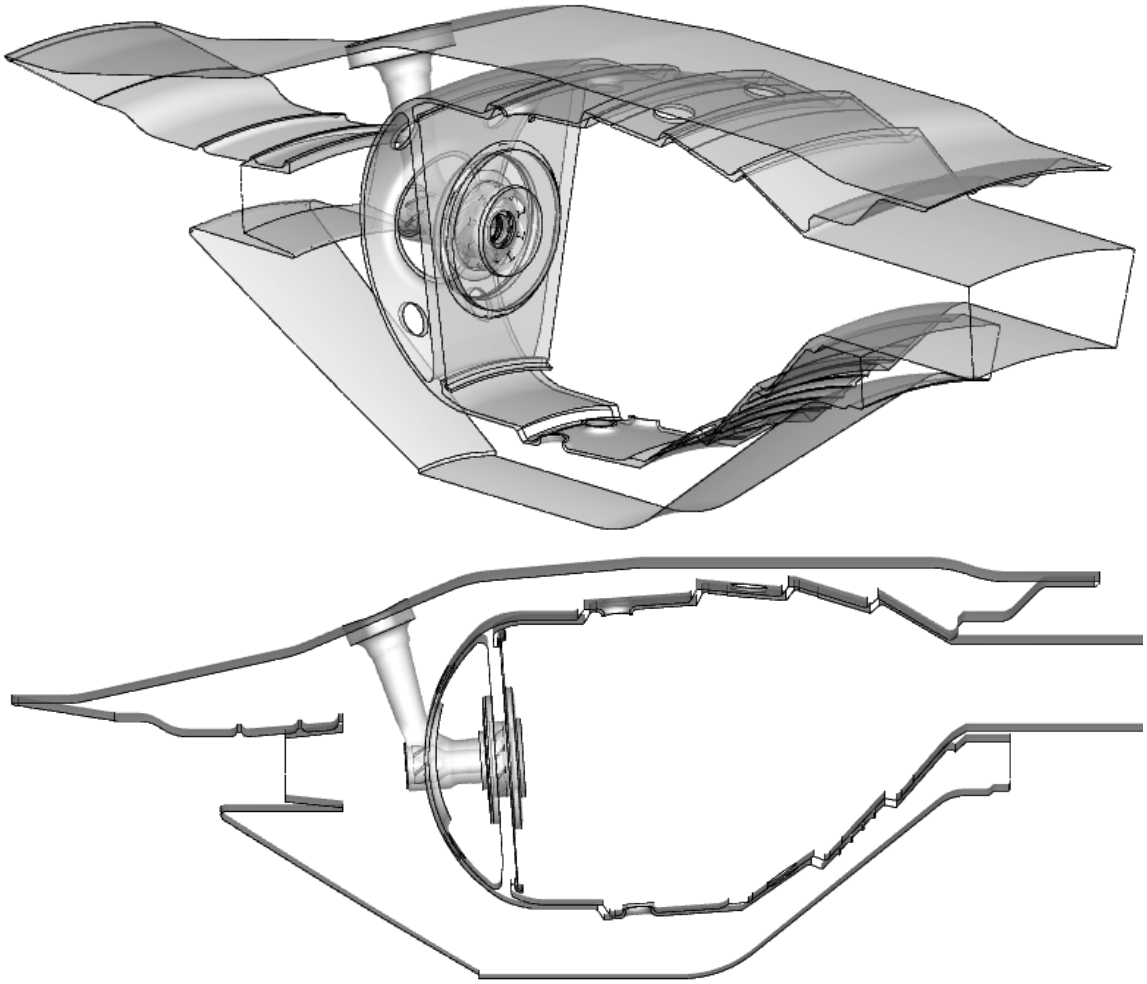

Figure 7.5: Combustor numerical model domain

The domain was split into separate volumes to control better the distribution of the mesh, and then meshed in *ANSYS* Gambit. An unstructured tetrahedral mesh was used with refinements in areas where it was predicted that the flow would change rapidly. Particular attention was given to the swirler channels, the volume in front of the swirler, and the primary and secondary cooling holes, as shown in Fig. 7.7. Due to the size of the model and the mesh, a mesh independency study was not possible.

To ascertain the reliability of the results, the mesh and flow fields were analysed and approved by the sponsor's combustion aero-thermal methods team. The finalised mesh resulted in $17e^6$ cells. The overall quality of the mesh is very high, however due to the complex geometry a few cells have a high level of skewness.

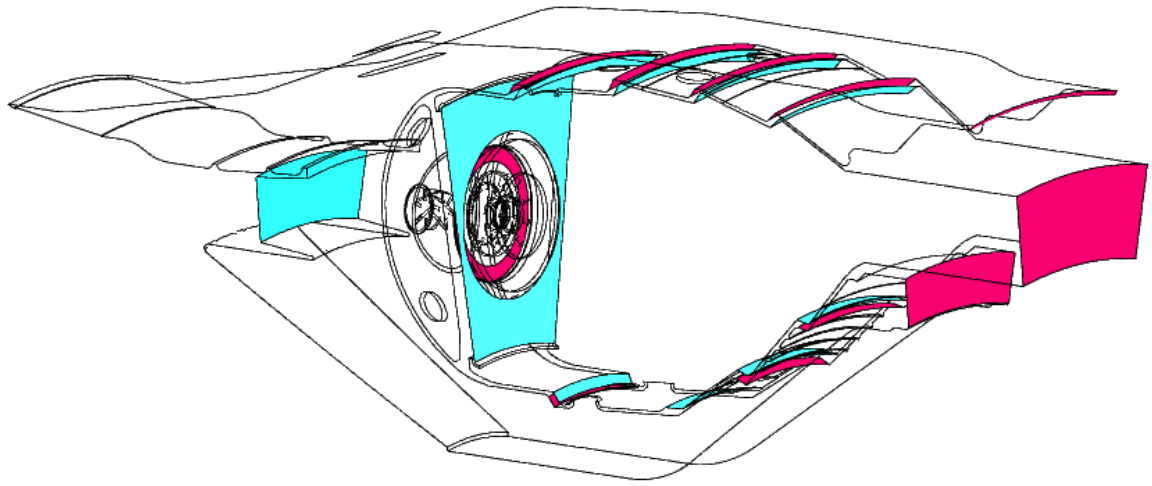

Figure 7.6: Combustor model boundaries showing how film cooling was modelled using inlet (cyan) and outlet (red) boundary conditions

The model was run in *ANSYS* Fluent using a pressure-based implicit steady-state incompressible flow setup with k-ϵ Realizable turbulence model, running an initialisation first order upwind run, followed by a second order upwind simulation. Boundaries were set as velocity inlet and static pressure outlet. Convergence was reached after 3000 iterations, with residuals reaching levels of $1.0e^{-8}$.

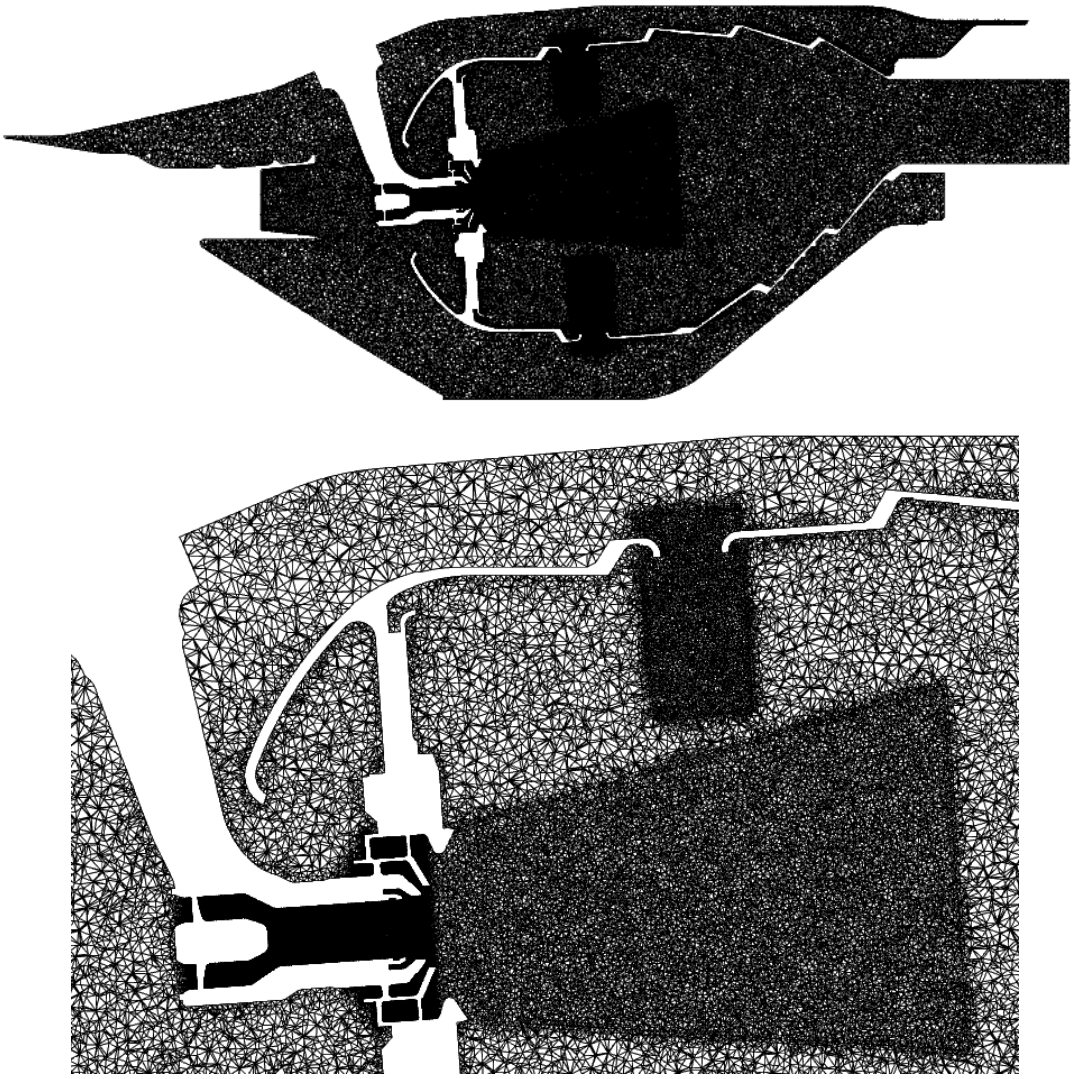

Figure 7.7: Combustor model mesh and detail of the atomizer and primary cooling hole refined mesh areas

7.5 Boundary conditions

The top left (TLC) and top right corners (TRC) of the altitude relight envelope are the limits of the engine's altitude relight capability as shown in Fig. 7.8. To calculate the numerical model's boundary conditions, the operating pressure, loading (θ), mass flow and the combustor geometrical parameters were extracted from the ATF data provided by the sponsor.

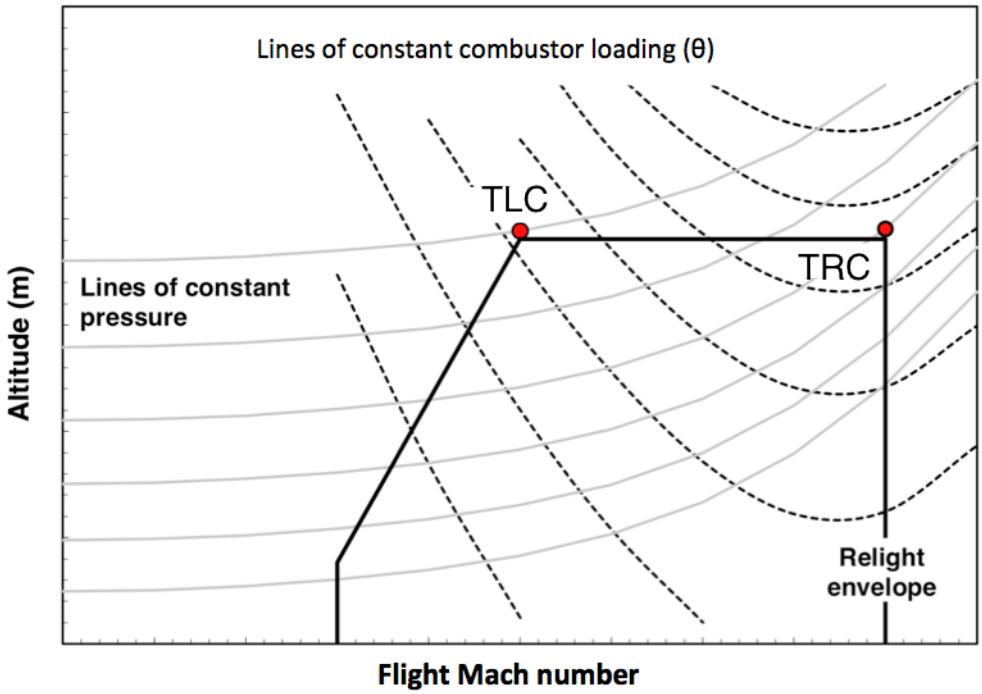

Figure 7.8: Operating points from which combustor boundary conditions were derived

The temperature and air density were extracted from the loading parameter using Eqn. (7.1). The conditions simulated therefore replicate those experienced by the combustion chamber during a real altitude relight.

$$\theta = \frac{W_{rc}\ 10^6}{P^{1.3} V_{pz} \exp\left(\frac{T_{30}}{300}\right)} \tag{7.1}$$

The axial velocity into the OGV model is calculated from the density, mass flow and inlet area. This is maintained constant throughout to isolate the effect of incidence from the increased mass flow. To change the incidence angle on the OGV blades, the tangential

velocity was varied. Since the film cooling slots were modelled as inlet and outlet boundaries, an estimate of their mass flow rate was required. This was done using a specific 1-D code used by the sponsor. Following calibration with combustor test data at high power, the code is able to predict the mass flow through the smaller channels. This allows for simpler yet accurate numerical models to be developed and used, reducing computational time and power.

However one must mention that the code is used for design point flow predictions, and not for far off-design operations. Therefore its accuracy at the latter conditions is not known and is possibly less than for design point, especially since it is expected that the flow ratios between inlet will change as far off-design condition is reached. The effect on the results for this study are not expected to be significant since they depend mostly on the flow upstream of the atomizer, which is all numerically modelled. The combustor total pressure loss ($\Delta P/P$) of the numerical model matched well with the flow test data provided by the sponsor.

7.6 Outlet guide vanes numerical model

In order to impose a realistic boundary condition at the combustor pre-diffuser inlet, the OGV model was run at various incidences to create the wake velocity characteristics. The OGV model consists of a rotationally periodic 20° section of the compressor outlet, including five OGV blades. A high density unstructured tetrahedral mesh was used in the blade area to capture well the flow separation, with a coarser mesh at the outlet to stabilise the solution. The mesh is similar to that described in section 3.3.1 since the blade is subject to similar conditions. However a $30 < y^+ < 40$ was used, relying on wall functions to calculate the boundary layer. This was done to reduce the mesh size since five blades had to be meshed, significantly increasing the computational power required.

The final mesh size was 10.5 million cells, illustrated in Fig. 7.9. A mesh dependency study could not be conducted due to the limited time available for using the sponsor's cluster computing capability. The OGV model was run using a velocity inlet and static

pressure outlet boundary condition, with a constant total temperature of 275 K. ANSYS Fluent was used with the $k-\omega$ SST turbulence model, incompressible flow. A 2^{nd} order upwind implicit pressure-based simulation was run starting from a 1^{st} order scheme converged solution. Convergence criteria was set to $1.0e^{-5}$, however turbulent kinetic energy and axial momentum residuals reached only values of $1.0e^{-4}$. It is suggested that future work can refine the mesh to try to reduce the residual level.

Whilst the mass flow was kept constant, the model was run with a number of different inlet velocity angles, effectively changing the incidence angles on the blades to create wakes of various intensities. The velocity profile at the plane corresponding to the combustor pre-diffuser inlet in the OGV model was then extracted. The flow inlet angle relative to the axial direction (α) was varied from 35° (design point) to -40° (inlet metal angle 33° relative to axial) as illustrated in Fig. 7.10 where the position of the reading plane is also shown.

The effect of the inlet angle is noticeable as illustrated in Fig. 7.11. At design point, the velocity profile at the pre-diffuser inlet is relatively uniform. Regions of corner stall form at the hub and tip of the blade as the incidence becomes more negative, shown clearly in Fig. 7.12. These regions grow, forcing flow towards mid-span. The separated and low-velocity region in the blade channel forces the flow to separate circumferentially and concentrate into smaller packets. These wakes eventually start to mix out.

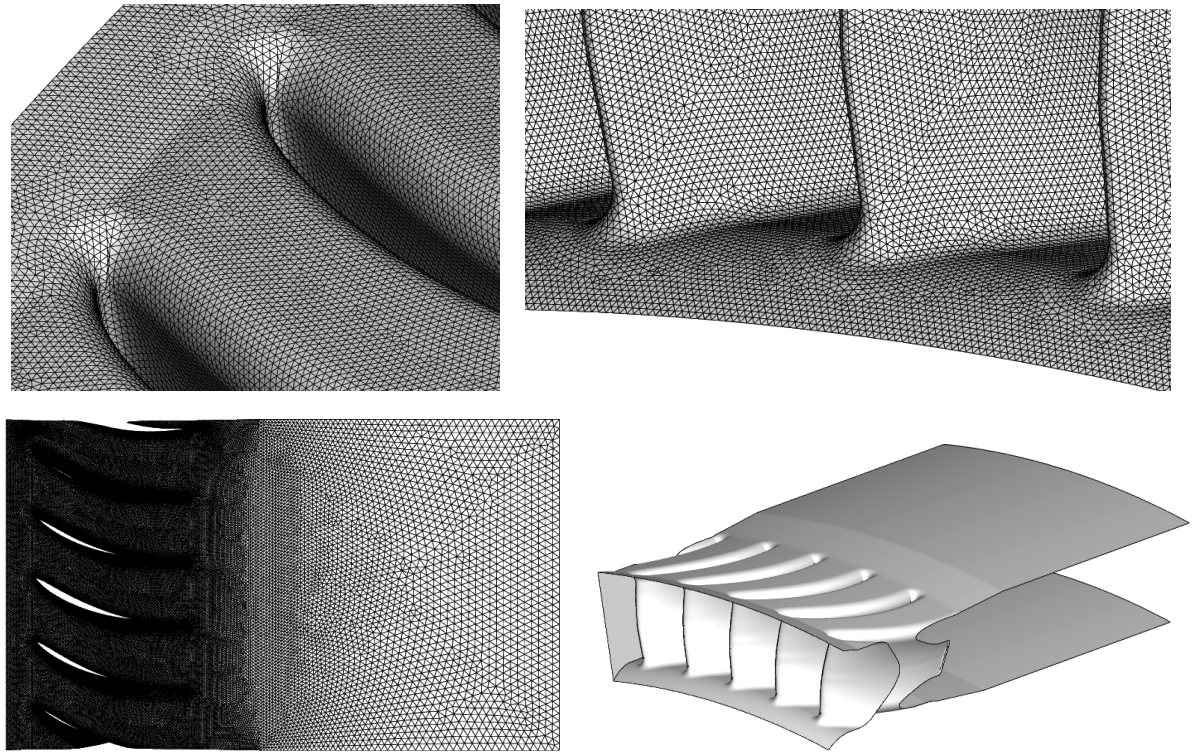

Figure 7.9: OGV domain and mesh with detailed views

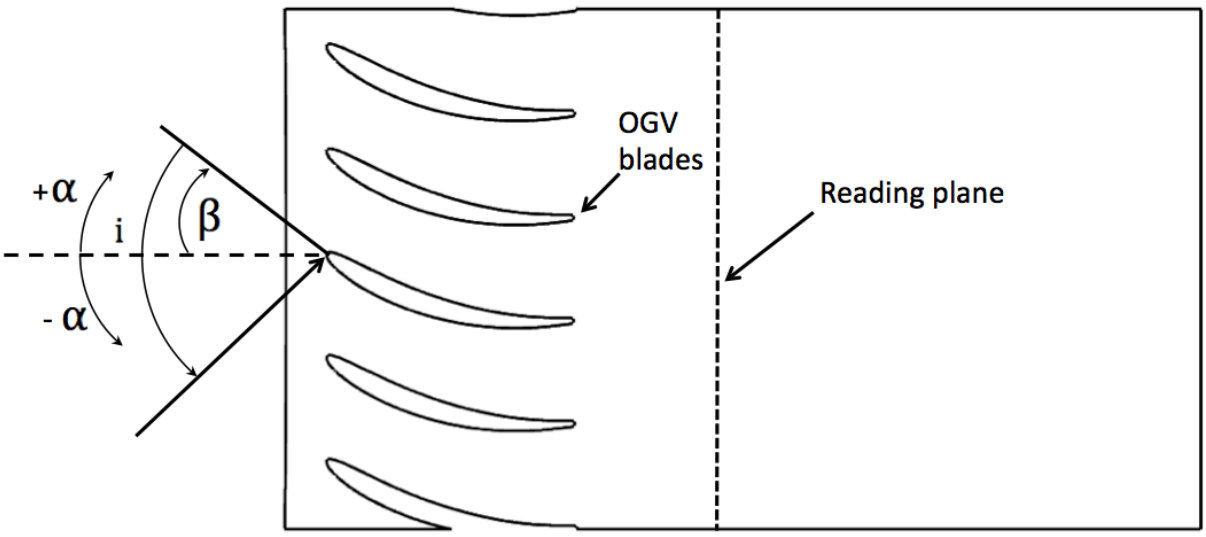

Figure 7.10: OGV inlet angles and reading plane position

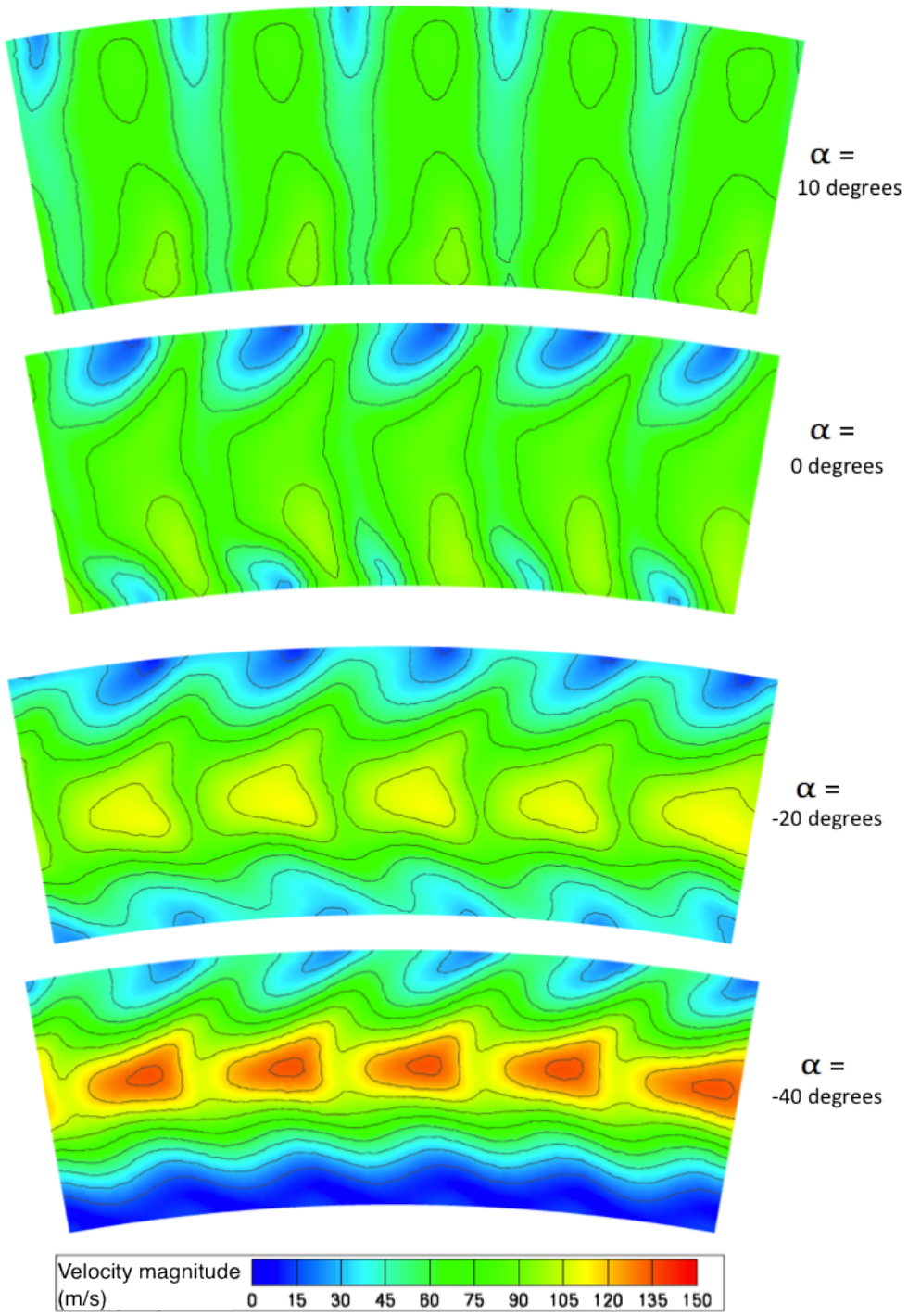

Figure 7.11: Velocity magnitude contours (m/s) at OGV domain reading plane, showing increase in wake intensity as inlet angle becomes more negative (annotated angles are relative to axial direction).

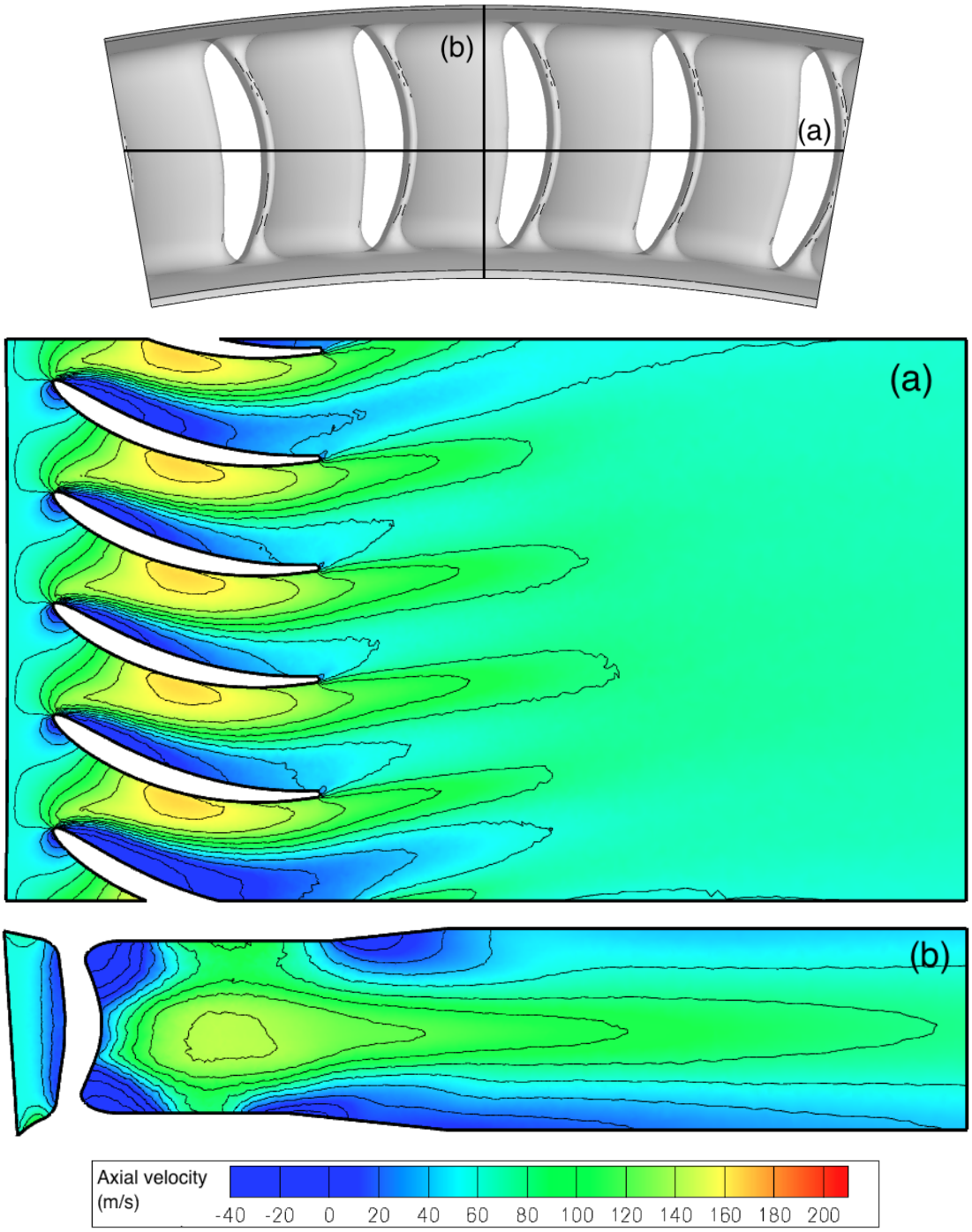

Figure 7.12: Plan (a) and side (b) sectional views of the OGV wakes - contours of axial velocity (m/s) for TRC $\alpha = -35°$

7.7 Results

The effect of the wakes on the combustor's performance can be evaluated by analysing the changes in flow characteristics in various important areas of the combustor. The positions analysed in this study are illustrated in Fig. 7.13. First the axial velocity profile at the diffuser exit is analysed to understand how different the inlet boundary condition into the combustor is when the off-design case is considered, relative to the design point case.

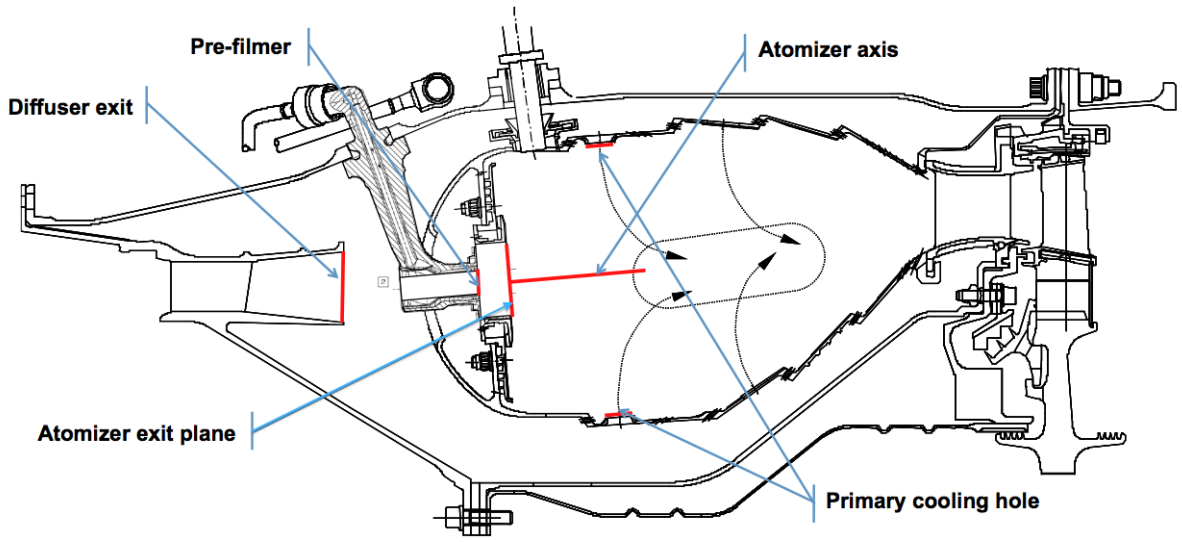

Figure 7.13: Positions where velocity profiles were measured

The effect on the atomizer is studied by observing changes in the flow velocity at the pre-filmer plane, the atomizer exit plane, and the size and magnitude of the central recirculation zone (see Fig. 7.13). The flow characteristics at the pre-filmer plane, such as the magnitude of axial and tangential velocity, give a good indication of the fuel atomization quality. A higher velocity increases the Weber number and therefore the chances of the air shattering the fuel droplet.

The atomizer flowfield gives an indication of how strong the central recirculation zone is. A large and strong recirculation increases the chances of ignition and maintains flame stability, which is desirable. Finally, there was an indication that the flow distribution around the combustor flame tube, changes when the off-design case is simulated. Therefore the flow velocity through the primary cooling holes, both on the inner and outer sides of the combustor annulus, was monitored.

7.7.1 Velocity profile at diffuser outlet

Starting from the axial velocity profile at the diffuser exit plane for the top left hand corner (TLC) of the relight envelope (see Fig. 7.14) and similarly for TRC (Fig. 7.15), it is observable that the design-point case (α = 35°) has a fairly uniform velocity distribution. For the far off-design case (α = -30°), the profile is no longer uniform. The corner stall observed in the OGV simulations, forces the flow towards mid-span, resulting in a high velocity flow at mid-span. This high velocity region is more or less aligned with the atomizer, which therefore sees a much higher inlet velocity relative to the design-point case (55 m/s at off-design relative to 30 m/s at design point). The effects of this higher velocity on the atomizer are explained in the following sections.

In the case of the top right hand corner of the relight envelope (TRC) the flow rate is expected to be higher since the flight Mach number is higher. Consequently similar behaviour is observed as for the TLC case, but the velocities are higher.

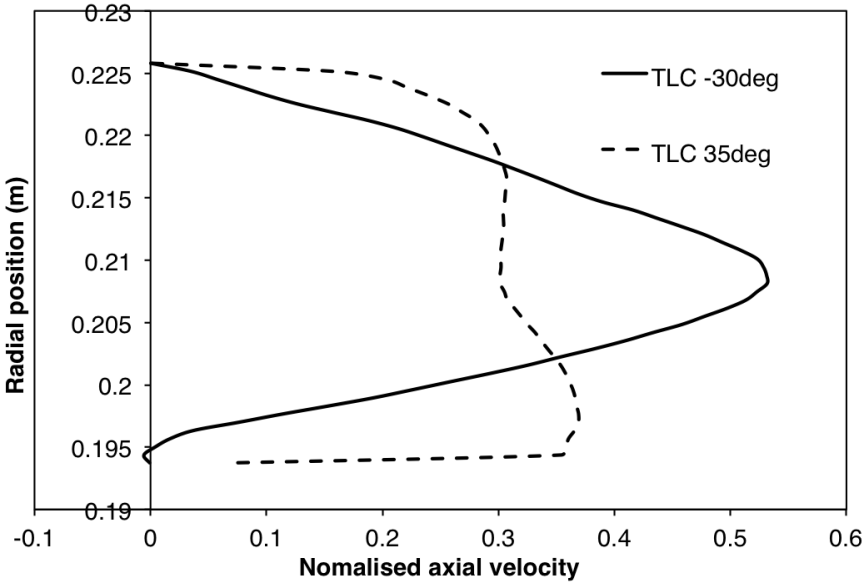

Figure 7.14: TLC case - Axial velocity profile at diffuser exit for design (α = 35°) and off-design (α = -30°) conditions

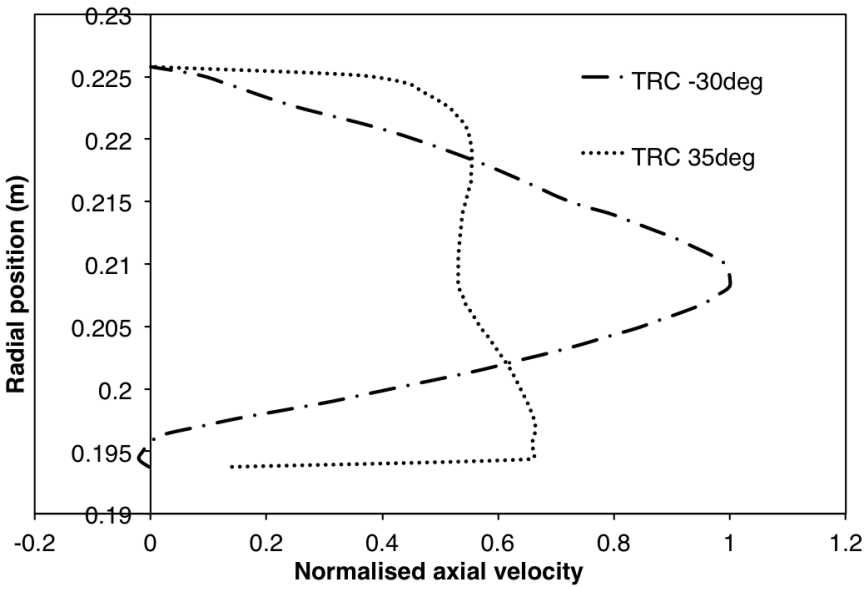

Figure 7.15: TRC case - Axial velocity profile at diffuser exit for design (α = 35°) and off-design (α = -30°) conditions

7.7.2 Velocity at pre-filmer plane

The effect of the high velocity flow at mid-span for the off-design case on the atomizer is evident in Figs. 7.16 and 7.17. The off-design cases clearly show a much higher flow velocity at the pre-filmer plane. In terms of axial velocity, it increases from 30 to 45 m/s for the TLC, and from 50 to 75 m/s for the TRC. Similar trends are observed for the tangential velocity, where the increase is from +/- 15 m/s to +/- 25 m/s for the TLC, and from +/- 40 m/s to +/- 60 m/s for the TRC.

Overall this resulted in a 46% increase of atomizer air mass flow relative to the design-point case for the TLC, and a 43% in atomizer air mass flow for the TRC. This is a significant difference which will result in a much higher Weber number for the same fuel mass flow, and therefore a finer more homogeneous spray of lower SMD and better droplet size distribution. The results also suggest that current models used in the industry, which assume a uniform inlet velocity profile, under-estimate the atomization quality, and therefore over-design the combustor.

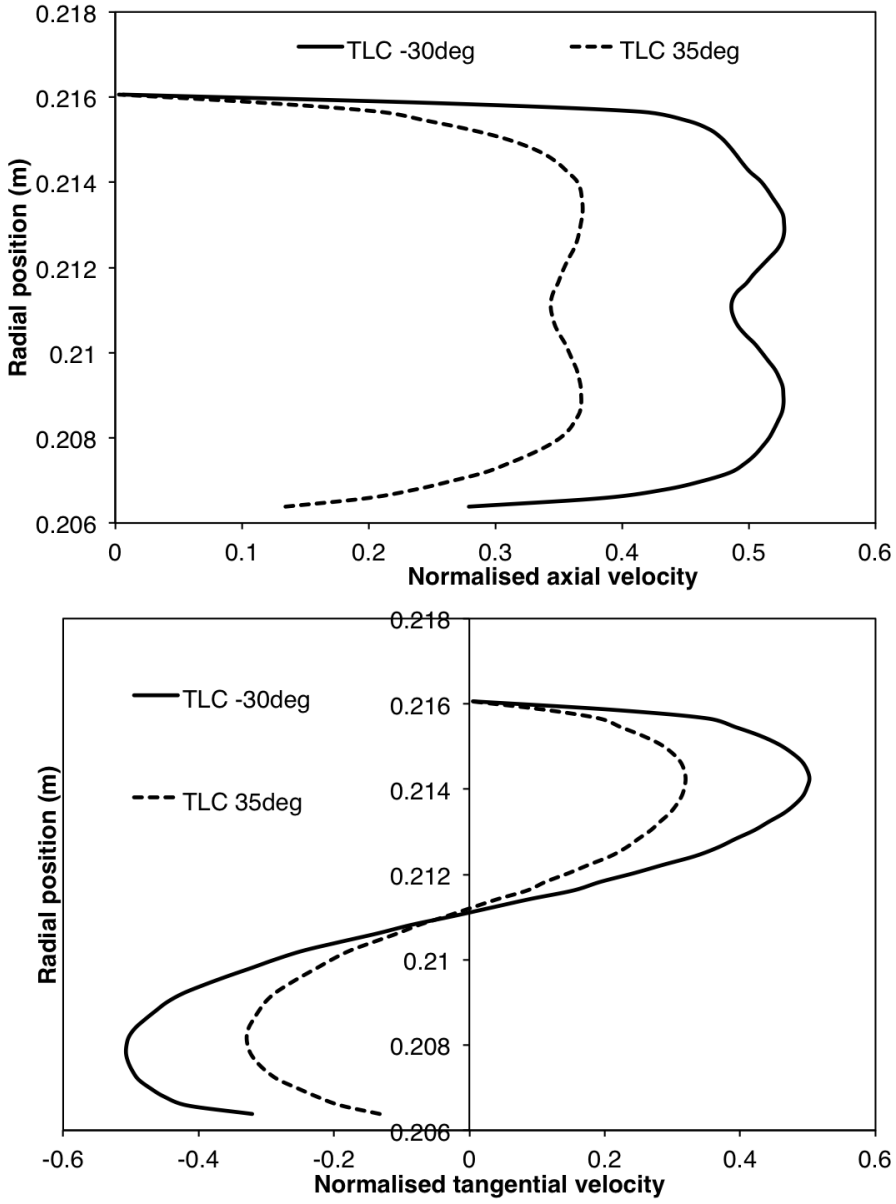

Figure 7.16: Axial and tangential normalised velocities at the pre-filmer plane for the TLC condition for design (α = 35°) and off-design (α = -30°) conditions

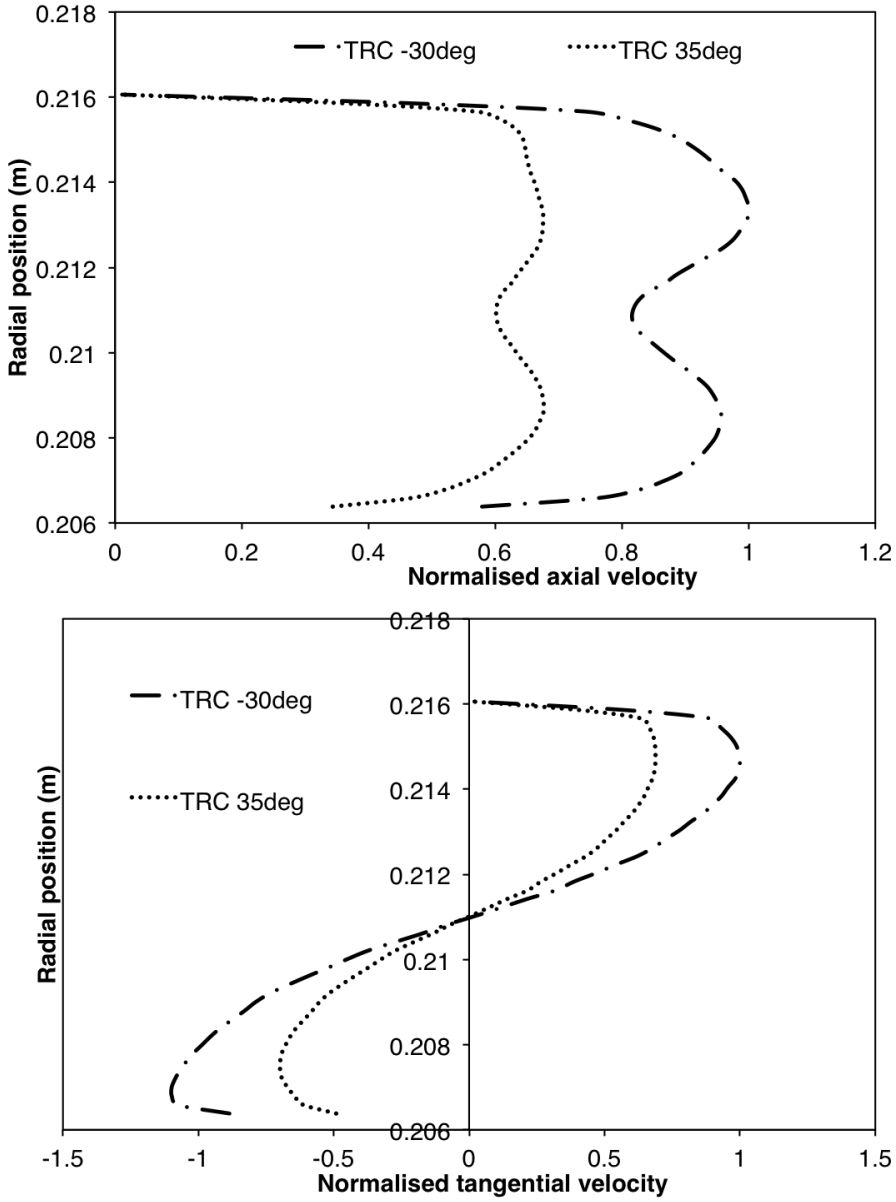

Figure 7.17: Axial and tangential normalised velocities at the pre-filmer plane for the TRC condition for design (α = 35°) and off-design (α = -30°) conditions

7.7.3 Atomizer flowfield

It is expected, from the increase in flow velocity observed at the pre-filming plane, that the atomizer flowfield will also change when the wake profile is used. Starting from the top right hand corner of relight envelope, the axial and tangential velocity profiles are illustrated in Fig. 7.18. This clearly shows a distinctive increase in both velocities when the off-design boundary conditions are applied. The result is a stronger flowfield, a larger and more intense recirculation zone as shown in Fig. 7.20. Here the off-design case shows both an increase in recirculation zone size, and a more negative reverse flow velocity. This suggests a more stable zone for the flame, increasing the probability of a successful relight.

For the top left hand corner of relight envelope, the observations are similar. However it is noticeable that the axial velocity profile in Fig. 7.19 does not have a negative region. This is confirmed by the contours in Fig. 7.22. At this point the steady simulations started showing signs of unsteadiness, and therefore it was thought that the case needs to be run unsteady for the flow to open up.

However, after running unsteady for 30 ms, the solution did not change. It would seem that there is not enough air momentum to induce the vortex breakdown phenomenon and create the torodial recirculation zone. The results are further confirmed in Fig. 7.20, where the flow has a very small negative region. Nevertheless, the impact of the off-design boundary conditions is still evident since both the axial and tangential velocities are higher than for the design-point case.

Coupled with the changes in flow velocity at the pre-filmer plane, this improvement in atomizer flow field substantiates the idea that the atomizer's performance during a relight is being underestimated because simulations run so far in the industry do not take into account the presence of large OGV wakes. One must point out that the magnitude of such wakes will not be the same, and will depend on the operating point of the compressor. It is thus possible that this effect can be less pronounced than simulated here, but will still be present and may still be worth taking into account.

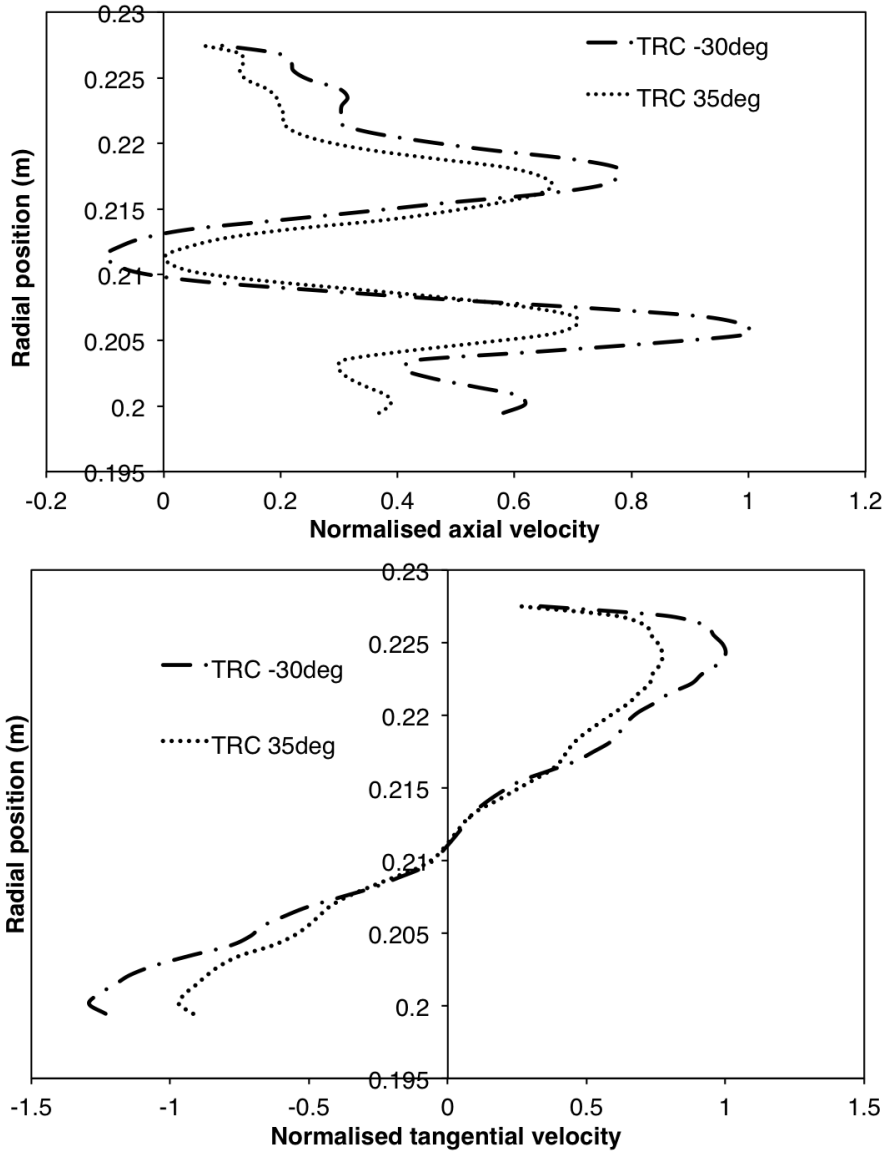

Figure 7.18: Comparison of the axial and tangential normalised velocity profiles at the atomizer exit plane for the TRC operating point at design (α = 35°) and off-design (α = -30°) conditions

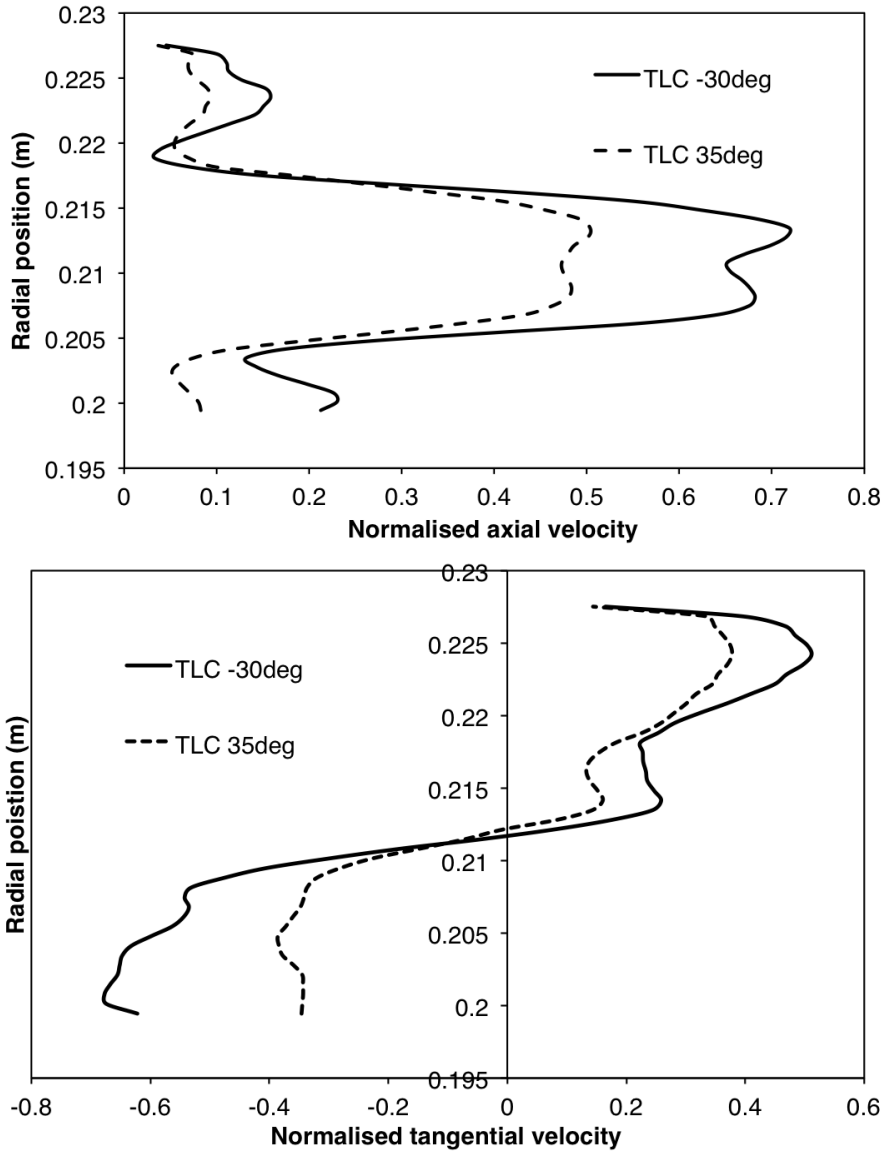

Figure 7.19: Comparison of the normalised axial and tangential velocity profiles at the atomizer exit plane for the TLC operating point at design (α = 35°) and off-design (α = -30°) conditions

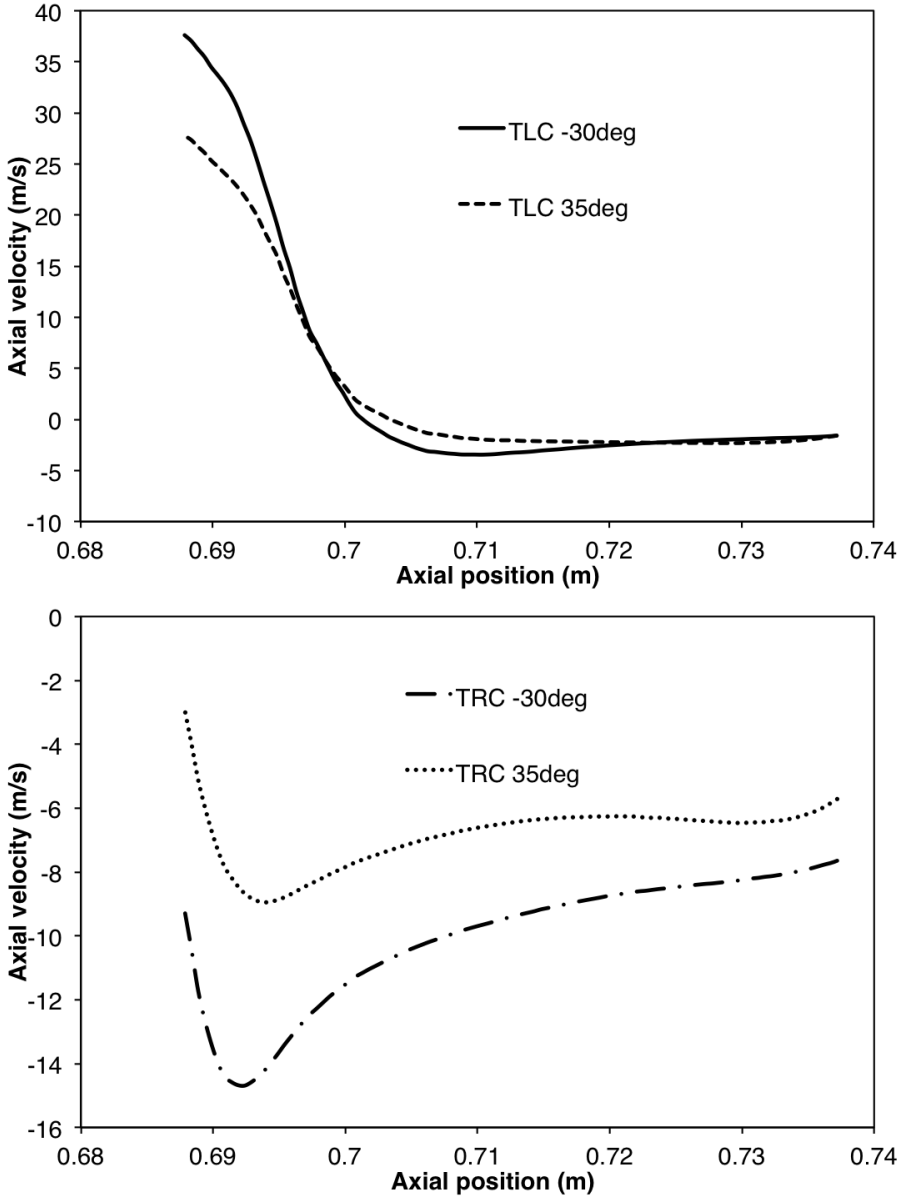

Figure 7.20: Strength and size of central recirculation zone for both corners of the relight envelope for design (α = 35°) and off-design (α = -30°) conditions

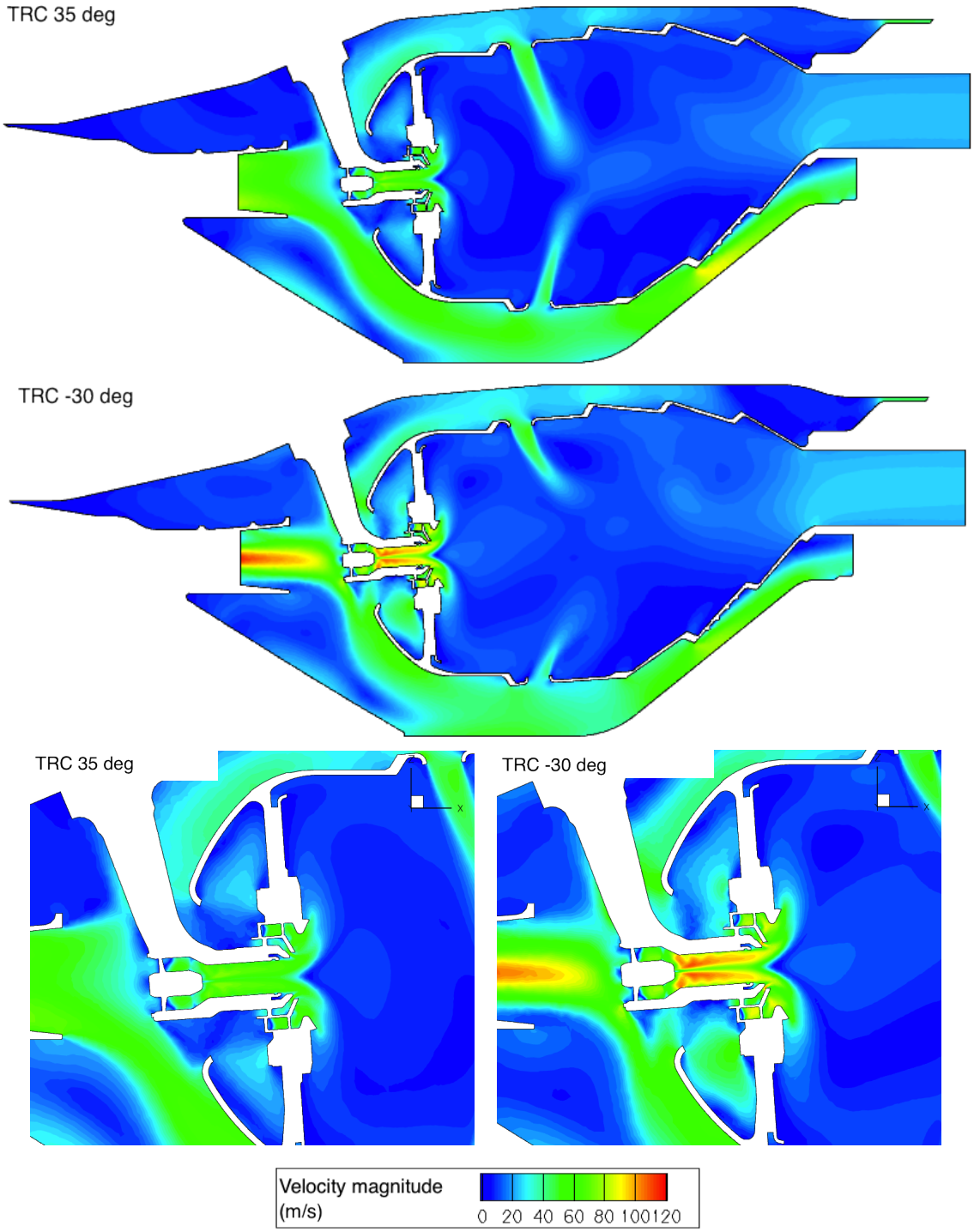

Figure 7.21: Velocity magnitude (m/s) contours for design ($\alpha = 35°$) and off-design ($\alpha = -30°$) points at the TRC operating condition with detailed views of the atomizer flow

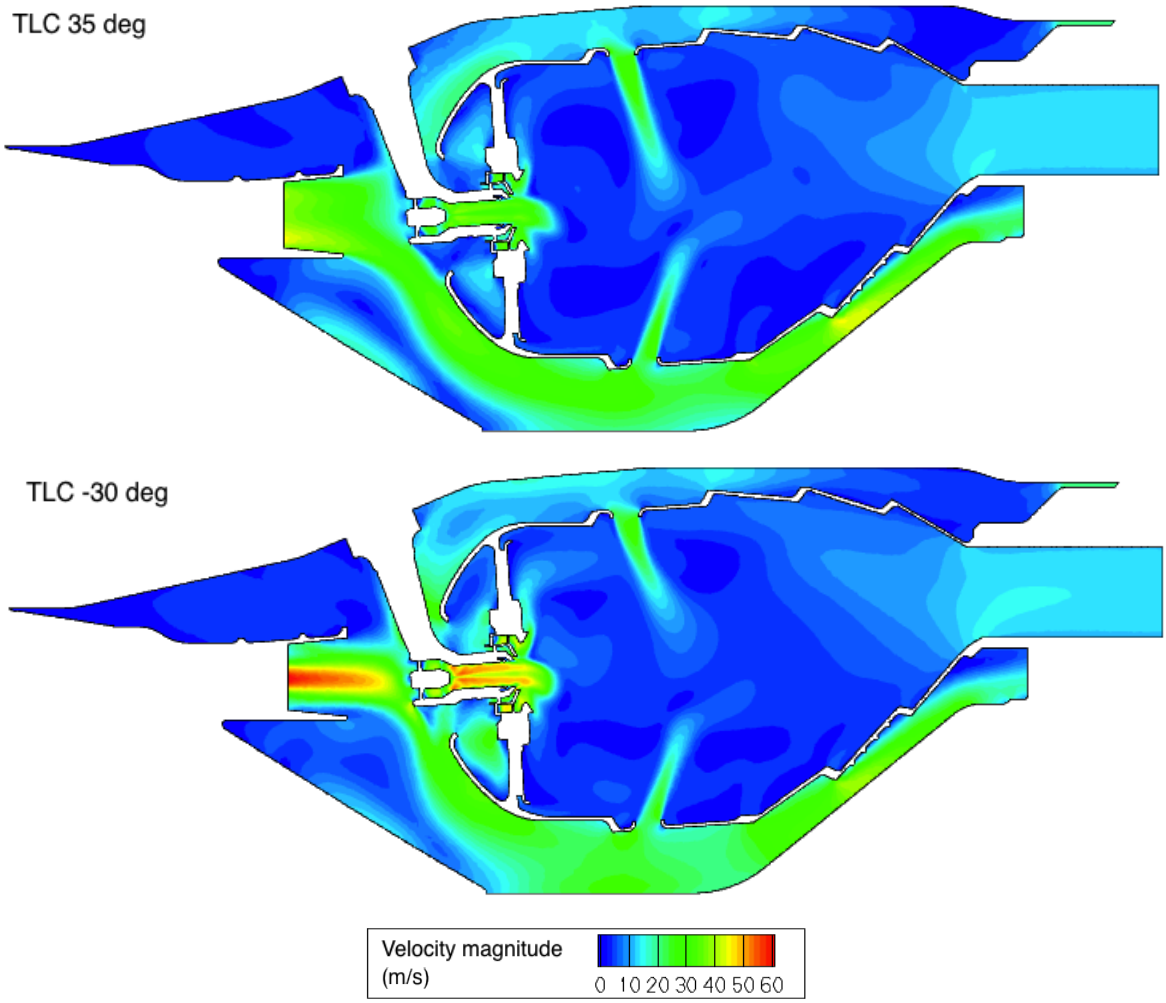

Figure 7.22: Velocity magnitude (m/s) contours for design ($\alpha = 35°$) and off-design ($\alpha =$ -30°) conditions at the TLC condition

7.7.4 Primary cooling hole flows

Since in the off-design case, there is more flow going through the atomizer, it is expected that this additional air mass flow is depleted from some other area of the combustor. By observing the velocity magnitude contours in Figs. 7.21 and 7.22, it becomes evident that the level of penetration of the air flowing through the primary port holes as illustrated in Fig. 7.23, is lower than for the off-design condition.

While the significance of this reduced penetration in terms of combustor performance is not yet clear, it is useful to analyse the magnitude of this change. The normalised radial air velocity profile for the primary holes at the inner and outer annuli are illustrated in Figs. 7.24 and 7.25.

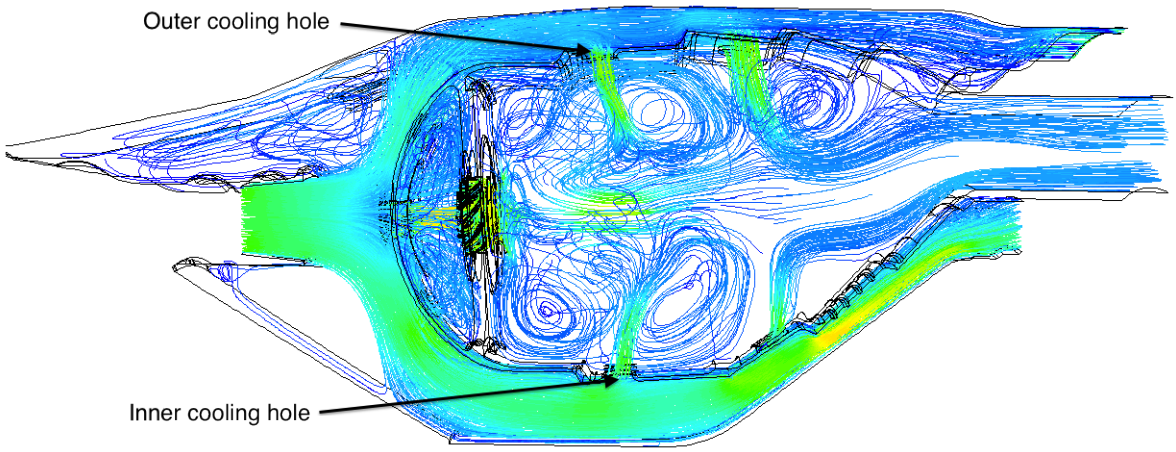

Figure 7.23: Streamlines of velocity magnitude (m/s) showing flow through primary and secondary holes in the combustor flame tube for TRC design ($\alpha = 35°$) condition

For the outer cooling hole, it would appear that there is no change in the radial velocity (and therefore air mass flow) between the off-design and design point cases, for both corners of the relight envelope simulated. On the other hand, for the inner cooling hole the radial velocity is significantly reduced in the off-design case. The non-uniform inlet velocity profile therefore increases the atomizer air mass flow at the expense of the primary hole in the inner annulus of the combustor.

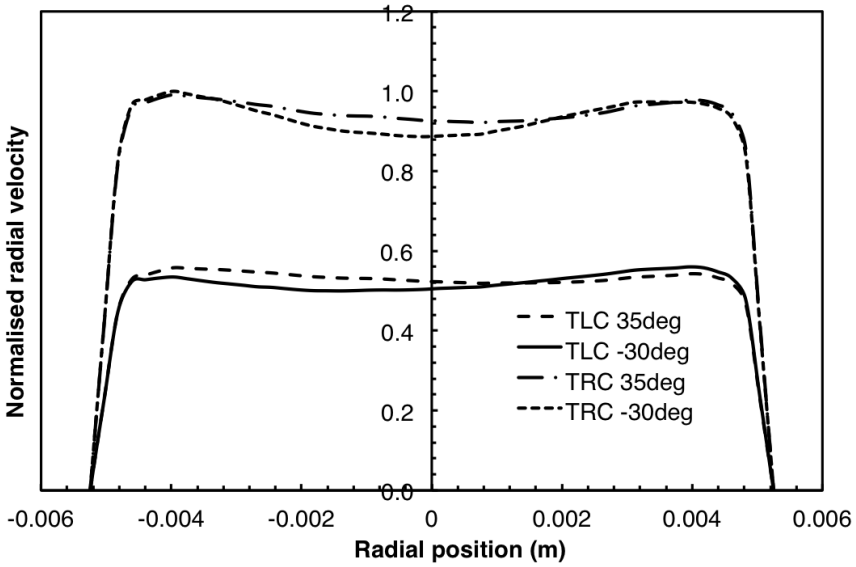

Figure 7.24: Normalised radial velocity profile of the outer primary holes of the combustor for all the cases simulated.

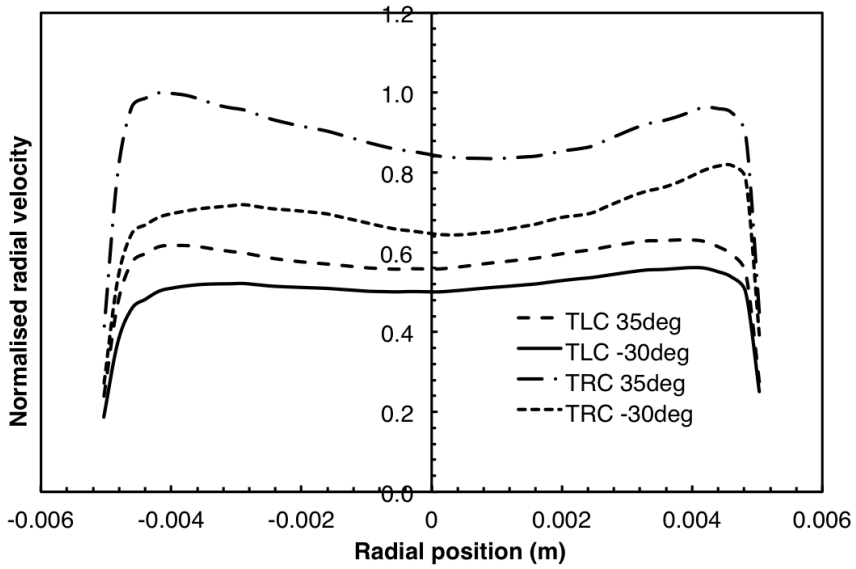

Figure 7.25: Normalised radial velocity profile of the inner primary holes of the combustor for all the cases simulated.

7.8 Concluding remarks

The study looked at how wakes, formed due to the compressor OGVs operating at far off-design conditions, could impact the combustor performance during an altitude relight manoeuvre. The conclusion is that the impact is very significant, and cannot be neglected. Numerical simulations indicate that at high negative incidences, the flow is forced towards the mid-span of the OGVs, subjecting the atomizer to a higher velocity air than the equivalent uniform inlet velocity for the same mass flow. The atomizer flowfield, air velocity at the pre-filming plane, and the size and strength of the recirculation zone, are all increased, which leads to believe that at relight there is better atomization and flow stability than previously thought. The atomizer mass flow for OGVs operating at high negative incidence, was found to be 40% higher than for those operating at design point incidence, for the same overall combustor mass flow. Current numerical and experimental studies do not include compressor wakes in altitude relight simulations. This study indicates that this is inaccurate and that both numerical simulations and experimental test rigs should include OGV wakes if realistic altitude relight conditions are to be replicated. A simple uniform flow at the pre-diffuser inlet will underestimate the atomizer flow, and consequently the fuel spray quality and atomizer flow strength.

The observations made are very significant for combustor design. Most sizing models tend to overestimate the combustor size [124], resulting in an altitude relight capability that exceeds certification requirements, but is prone to high NO_X, especially at take-off. This study gives an indication about the probable cause of this overestimation; current sizing models do not factor the effect of wakes, assuming that the velocity profile at the pre-diffuser inlet is uniform and therefore underestimating the atomization quality and recirculation zone strength. From an industrial point of view, this new knowledge can be taken advantage of by further optimising the combustor size, leading to a reduction in take-off NO_X, combustor cooling requirements and possibly a reduction in core length and weight. This study was the first within this area, and possibly has opened a new field of research on compressor / combustor interaction at relight.

The OGV numerical model was run with a uniform inlet velocity boundary condition to achieve the desired constant inlet angle and mass flow. However at low power, the compressor will be either locked or rotating at a very low speed. The blades upstream of the OGVs will also be a source of wakes and perturbations in the flow. It is not known how strong the effect of this upstream flow is on the OGV wakes and the combustor. The current study assumes that the biggest effect comes from the final blade row. However a slowly rotating compressor may impose different incidence angles on the OGV along its span, changing the inlet velocity profile. Hence, whilst the OGV wake velocity profile may not be accurate due to the omission of the compressor blades upstream of the OGVs, the study shows qualitatively that there is a significant difference between design and off-design operations, which cannot be ignored.

Further studies on this topic should move the boundaries of the numerical domain to include at least a rotor row upstream of the OGVs to create a more realistic inlet profile. Starting by assuming a locked rotor, cases should eventually include a slowly rotating compressor at various speeds and operating points. Additionally, a discrete phase representing injection of fuel should be included. Although the atomization process is not a very accurately modelled phenomena within CFD solvers, qualitative results, rather than the quantitative, would still be very useful.

Chapter 8

Sub-Idle Mixer Performance

The following chapter describes the studies undertaken to model more accurately the off-design performance of a mixed exhaust nozzle. An overview on the use and purpose of mixed exhaust systems is first given. The off-design performance is then described by analysing the characteristics and influencing parameters in mixing of highly dissimilar coaxial flows. Conclusions from previous work on off-design aero-engine mixer performance are then outlined, together with an overview of current mixer performance modelling methods. Finally the methodology followed, numerical simulations run and results are described.

8.1 Introduction

Turbofan engines can have either separate exhausts (hot and cold) or a common propelling nozzle which mixes the hot and cold streams, generally termed as a *mixed exhaust*. A mixed exhaust can improve the cycle efficiency of a turbofan engine by reducing the required fan pressure ratio. The mechanism and theory is explained in Pearson [128] and Frost [35] and will not be repeated here. The gains are not too large, and the mixer will suffer from a fundamental pressure loss, incomplete mixing, and chute pressure loss. When properly designed however, at nominal operating conditions a 2% increase in gross thrust due to a mixed exhaust configuration, results in a net thrust increase of 4% since the momentum drag remains unchanged [1]. For military turbofans travelling at Mach 2, the increase in net thrust can be up to 3% for each 1% gain in gross thrust, which is

equal to the SFC improvement since the fuel burn remains constant. Similar estimates are given by Pearson [128] and Frost [35]. The theoretical gain is a function of the bypass ratio [128], streams total pressure and temperature ratio, and nozzle pressure ratio [35]. The actual gain can be 50-60% of the theoretical gain, with a typical 1 - $1\frac{1}{2}$% gain over the separate exhausts [35].

A mixer (an example of lobed or forced mixer illustrated in Fig. 8.1) will introduce additional weight and drag due to the extended cowling at the rear of the engine, which become significant as the bypass ratio increases, reducing any gains. Lobed mixers increase the mixing perimeter by up to three times, increasing the rate of mixing. As observed by Elliot et al [129], the rapid mixing is a result of strong secondary flows associated with streamwise vortices which are shed from the lobe trailing edge. The lobe's increased area is significant in increasing this phenomenon, allowing a reduction of the mixing duct length required over annular designs, saving weight and drag.

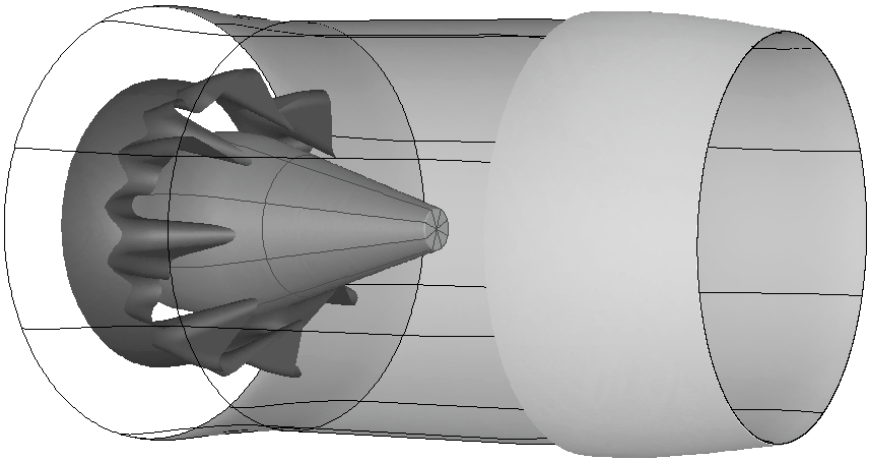

Figure 8.1: Lobed mixer

As illustrated in Fig. 8.2, gains from using a mixed system are not too large. Therefore it is important to optimise the engine for such a set-up and to minimise any losses in the mixer [128] [35] [130]. Although a fundamental pressure loss will always be present, practical optimum mixing can be achieved by maintaining total pressure and total temperature ratios of the bypass and core streams close to unity [35] [130]. Optimum mixing is described in Sanghi [130].

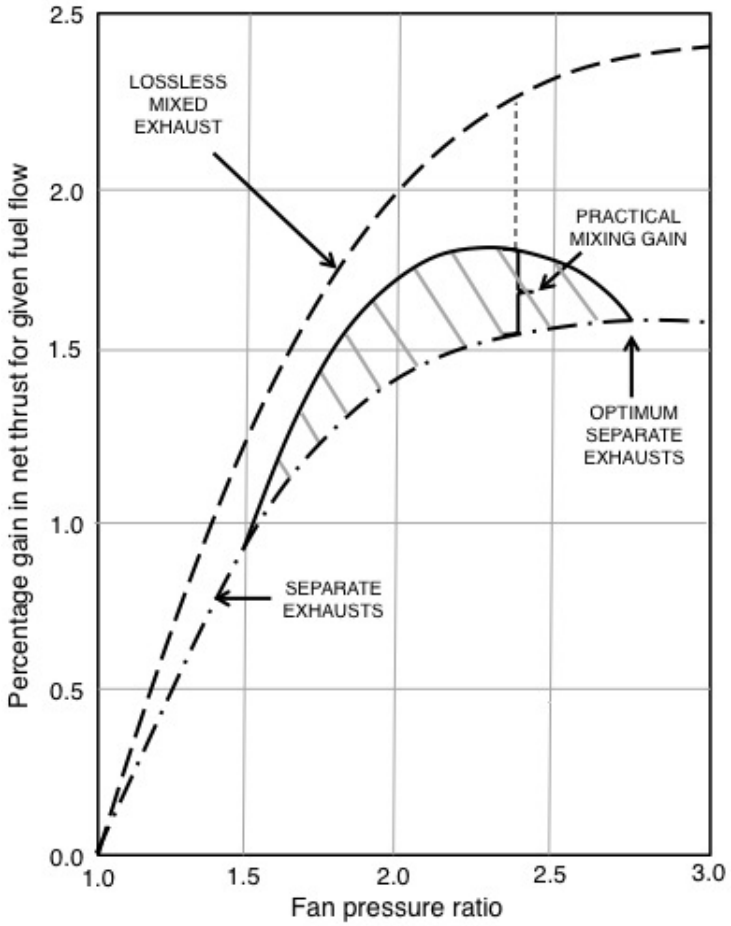

Figure 8.2: Effect of fan pressure ratio and mixing on the subsonic cruise performance [35]

8.1.1 Mixer performance at windmilling conditions

Under windmilling conditions, the blockage caused by the turbomachinery in the core will force the air through the bypass duct, drastically increasing the bypass ratio [1]. This creates a large total pressure and velocity ratio between the bypass and core streams. Additionally the nozzle pressure ratio will be very low since there is no compression from the fan or core. Frost [35] explains that any gain from a mixed exhaust system is lost as the nozzle pressure ratio falls and the total pressure ratio between the bypass and core streams departs from unity. The large total pressure ratio in the mixer leads to highly complex and turbulent mixing, as explained in section 8.2.1. Since at windmilling conditions the engine has cooled off due to the flow of cold ambient air, it is safe to assume that the total temperatures of the bypass and core streams are equal.

The mixer's design and its performance at windmilling conditions is extremely important because the nozzle pressure dictates the operating point of the turbomachinery upstream. It therefore affects the windmilling air mass flow rate, which in turn will determine whether a relight is possible and how much power off-take is available for the accessories. Alexander [131] emphasises that from a number of engines test data results, it appears that the type of mixer (chuted or annular) has a large effect on the windmilling flows through the high pressure system - engines with annular mixers having the lower flow rates. It is also reported [131] that for mixed exhaust engines the bypass ratio at design conditions will also have an effect on the core flow, with the higher bypass ratio having the lower core flows. It appears therefore that the low loss of the annular mixer results in higher jet pipe pressures, thereby reducing the flow through the core.

A good estimate of the core air mass flow rate is critical for sizing the combustion chamber. The lack of accurate predictive tools can result in either the combustor being too large resulting in both performance and weight penalties, or being too small resulting in a deterioration of the altitude relight capability. This highlights the need to properly model the mixer at far off-design conditions.

8.2 Literature review

The literature presented here is divided into three sections: the study on the behaviour of general dissimilar coaxial flows, aero-gas turbine mixer performance at off-design, and the way mixed exhausts are currently modelled in performance solvers.

8.2.1 Mixing of dissimilar coaxial flows

Whilst it is difficult to study the mixer's behaviour within the engine environment and at full scale, numerous authors have studied the underlying physical phenomena in mixing of dissimilar coaxial flows under laboratory conditions.

Gore et al [132], used flow visualisation to study the mixing of two coaxial flows (diameter ratio = 3.0) and the conditions at which this becomes turbulent. It was observed that the critical Reynolds number at which the mixing of coaxial flows becomes turbulent, is a strong function of the velocity ratio of the two flows, ranging from 1400 to 400. Similarly, Villermaux et al [133] and Rehab et al [36] (Fig. 8.3) studied coaxial flows with velocity ratios greater than unity, were the outer flow was the dominant one.

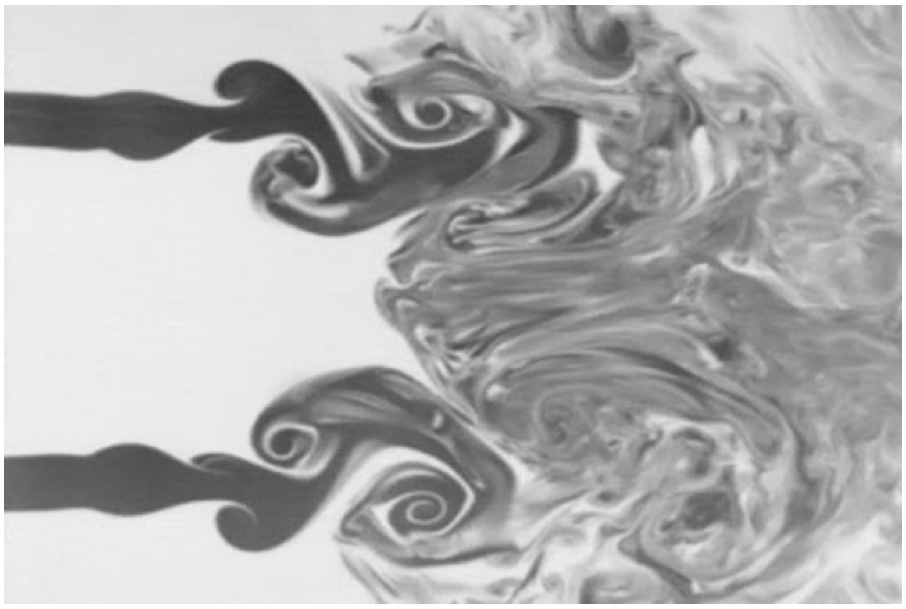

Figure 8.3: Visualisation of the mixing process, velocity ratio = 8.0 [36]

It was observed how, as mentioned in Gore et al [132], the velocity ratio plays a major role in the mixing process. Above a critical velocity ratio, the inner potential cone is truncated by a reverse flow and a wake-type flow condition is formed. This flow pattern is characterised by the existence of an unsteady recirculation bubble with the size of the recirculating bubble increasing with the velocity ratio. The mean reverse flow velocity is proportional to the outer flow's velocity. The effect of velocity ratio, and the onset of recirculation and a negative axial velocity region was also experimentally observed by Lima et al [134].

Rehab [36] and Villermaux [133] observed that recirculation will start when the velocity ratio is between 5 and 8. The physical reason being that the radial pressure jump (ΔP) between the streams is proportional to the velocity difference between the streams. When the ratio between the radial pressure jump and the dynamic pressure of the core stream reaches unity, recirculation starts. The larger the pressure jump, the higher the BPR will be for the same diameter ratio due to the higher velocity ratio.

8.2.2 Mixer performance modelling

Due to the large influence that a mixed exhaust system has on an engine's design and off-design performance, its characteristics have to be accurately modelled within the whole engine performance solver. Whilst this is relatively straight forward at design point, the turbulent mixing at off-design makes it more difficult to model its performance. At cruise design point, the downstream propelling nozzle pressure ratio at the nozzle charging plane (NCP) (P_{NCP}/p_{amb}) can be greater than 2.5:1. The nozzle charging plane is a plane which splits the bypass duct and the nozzle, and varies with engine models. It is not a physical plane, but is required to establish which pressure is used to determine the nozzle performance. Jet velocities are high enough for the mixer to be of significant benefit. Within the models, no pressure loss or a fixed value is accounted for the chutes or the mixing chamber.

Most literature on gas turbine theory pertaining to mixers [1] [135] [136] [35] indicate that the mixer static pressure ratio is unity. As Mattingley [136] discusses, this would lead to the assumption that the total pressure ratio (or total mixer pressure ratio (TMPR)) is

also almost unity at the mixer chute exit plane. Some solvers assume a maximum difference of 5% between the bypass and core total pressures. However mixer operation must be modelled at all corner points of the operational envelope to ensure satisfactory engine off-design performance [1]. The matching constraint used for a mixed engine is that the static pressure in the mixer chute must be equal for both the hot and cold chutes. Simple correlations such as the one proposed by Frost [35] are used for the mixing process to predict parameters such as the total pressure loss [1] [135]. This is however not accurate enough since the losses are a function of the mixer geometry and therefore too complex to model with simple correlations.

Howard [37] has shown that the traditional mixer modelling assumptions affect significantly the prediction of the engine performance during windmill relights. A mixer performance characteristic generated using only ATF data and interpolating among them was proposed to replace the simplistic assumption of equal static pressures. This approach works very well for engine simulations throughout the relight envelope, especially for extreme cases which was almost impossible to simulate with the traditional modeling approach. Figure 8.4 illustrates the engine's transient running line from steady-state windmilling up to idle conditions for a flight Mach of 0.9 and 25,000 ft.

This approach is the one used in this study, however ATF data is not always readily available, is often scattered, and is expensive to obtain. Therefore the mixer characteristics are extracted from numerical studies, simulating the mixer operating condition during various possible windmilling scenarios, as illustrated in Fig. 8.5.

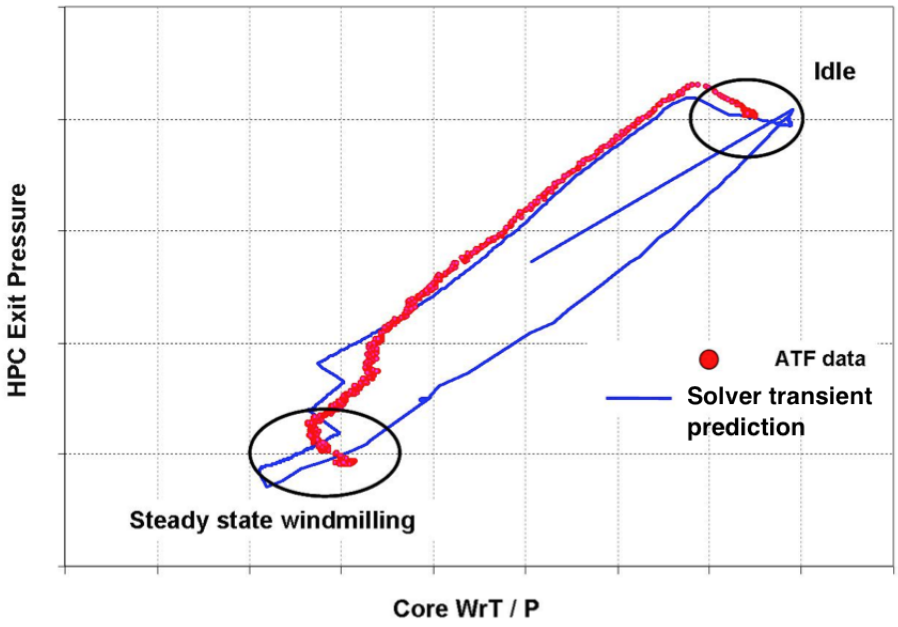

Figure 8.4: Engine measured and simulated running lines [37]

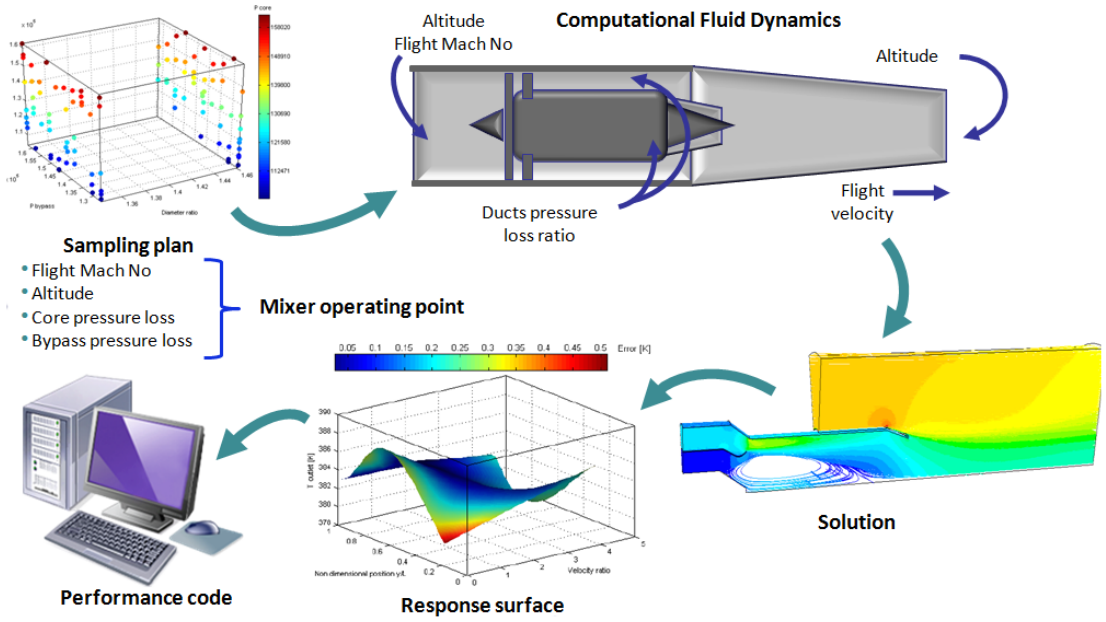

Figure 8.5: Methodology used to determine the mixer off-design characteristics

8.2.3 Numerical modelling of mixer at off-design

The extensive numerical validation of the numerical tool using experimental from Homes [137], was carried out by Russo [138]. This included a turbulence and boundary condition sensitivity study which significantly increased the trustworthiness of the tool. The study [138] showed that the effect of temperature ratio on the mixing process is very significant, and needs to be modelled. However, as previously mentioned, under windmilling conditions it is safe to assume that the streams have similar total temperatures. Russo [138] in fact maintained a constant and equal total temperature for both streams when simulating windmilling conditions. As mentioned in the literature, the velocity ratio was found to be the main driving parameter on the mixer's performance, with this ratio being proportional to the bypass ratio (see Eqn. (8.1)) since the ratio between the bypass and core densities will remain constant.

$$BPR = \frac{A_{bypass}\rho_{bypass}v_{bypass}}{A_{core}\rho_{core}v_{core}} \tag{8.1}$$

$$\text{Total Mixer Pressure Ratio } (TMPR) = \frac{P_{bypass}}{P_{core}} \tag{8.2}$$

$$\text{Nozzle Pressure Ratio } (NPR) = \frac{P_{bypass}}{P_{amb}} \tag{8.3}$$

For high TMPR, the core flow becomes less important until the TMPR becomes a function of the bypass stream Mach number only.

$$TMPR = \left(1 + \frac{\gamma - 1}{2}M_2^2\right)^{\frac{\gamma}{\gamma-1}} \tag{8.4}$$

Russo [138] observed that there is stronger interaction between BPR and TMPR at low NPRs. At these conditions the difference in total pressure between the two flows (i.e. increasing TMPR) becomes very important in determining the velocity ratio and therefore the BPR.

8.3 Engine C lobed mixer sub-idle performance

The lobed mixer used for this study is used in engine B, a low-bypass civil turbofan used on medium-sized business jets. The work was undertaken in collaboration with M. Lecoq [38] as part of his MSc project, which consisted of determining the boundary conditions and running the numerical simulations.

8.3.1 Numerical model setup

A lobed-type mixer from a small modern low-bypass turbofan was used in this study. The numerical domain starts from just downstream of the low pressure turbine and includes the lobed and bullet components, as illustrated in Fig. 8.1. The nozzle exhausts into the far field section which extends down to 80 nozzle diameters downstream and 30 nozzle diameters radially. The geometry and domain, which were provided by the company that builds this engine make, is rotationally periodic with an angle of 30°. This is enough to include two protrusions of the lobed part. Due to the complex geometry of the lobed component, an unstructured mesh was used. A dense mesh was used in the nozzle, with the cells gradually increasing in size with the distance downstream in the the far field region as illustrated in Fig. 8.6. ANSYS Gambit was used to build an unstructured tetrahedral mesh of the model. A grid independency study was carried out, focusing on the area of the mixing plane were the largest radial gradients were expected to take place.

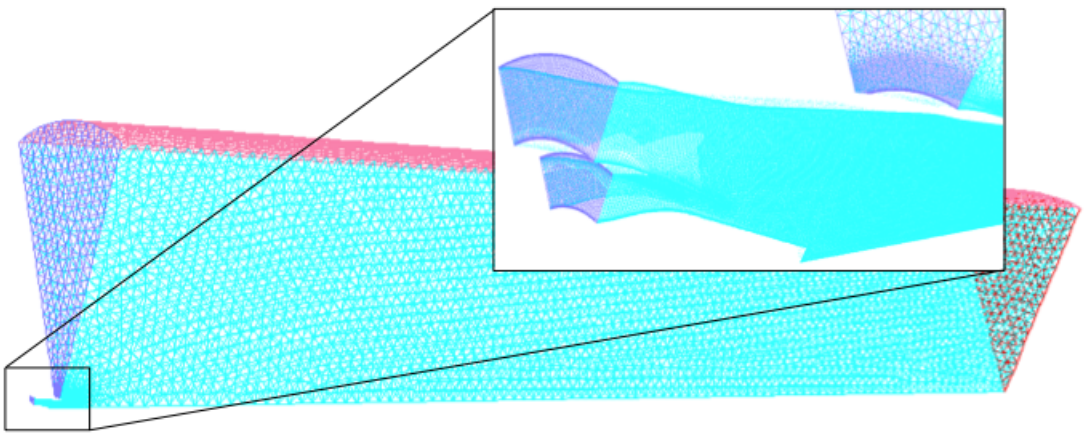

Figure 8.6: Lobed mixer mesh

Four different mesh densities, tabulated in Table. 8.1 were tried. The conditions used to perform the tests correspond to a far-off-design operating point representing windmilling conditions with the NPR and TMPR ratios set respectively at 1.5 and 1.25.

Mesh	A	B	C	D	E
Elements ($\times 10^6$ cells)	2.5	3.4	3.9	4.3	5.5

Table 8.1: Mesh sizes for grid independency study

The velocity profiles computed on a rake in the nozzle duct illustrated in Fig. 8.7, indicate that mesh D gives acceptable results using reasonable computational power and time, as shown in Fig. 8.8. Initially a fine set of prism cells was used at the mixer walls, with a $y^+ < 2$ to resolve the boundary layer as recommended in [9]. However subsequent simulations with standard wall functions produced similar results and reduced computational time and power.

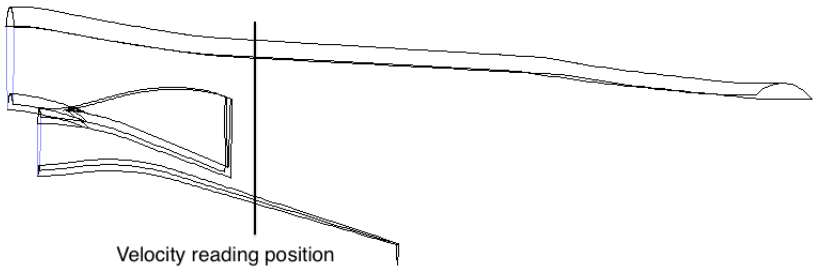

Figure 8.7: Measuring position for mesh sensitivity study

The simulations were run in ANSYS Fluent $k - \epsilon$ Realizable turbulence model using a pressure-based implicit setting, at steady state conditions and compressible flow. The fluid was treated as an ideal gas with viscosity set at a constant value of 1.789×10^{-5} kg/ms. First order upwind simulations were run with SIMPLE pressure-velocity coupling. Converged solutions were used to initialise second order upwind simulations. Boundary conditions were set as total pressure inlets for the nozzle core and bypass streams, and freestream with a flight Mach number of 0.8 for the atmosphere as tabulated in Table 8.2.

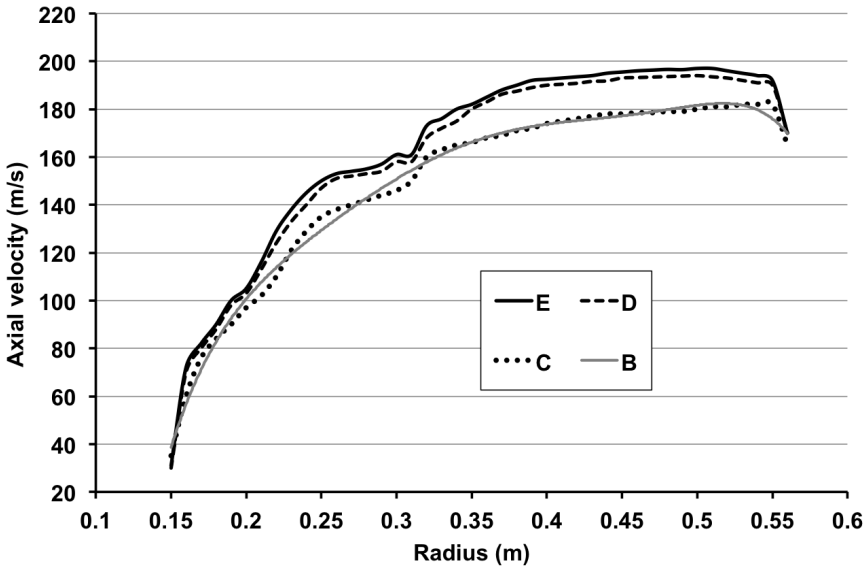

Figure 8.8: Lobed mixer mesh sensitivity study results

The total temperature was maintained constant at 217 K corresponding to an altitude of 12,500m. A sampling plan was used to identify which boundary conditions and how many simulations are required to efficiently cover the range of sub-idle operating conditions. This method was previously used by Vellutini [139] and Negro [140]. Negro [140] used four parameters to described the operating condition of the mixer: flight Mach number, flight altitude, and bypass and core percentage total pressure losses. Whilst this adequately covers the entire range of relight operating conditions, it was concluded that some conditions having different parameter values can result in the same overall condition being applied to the mixer resulting in some mixer operating conditions being duplicated.

The mixer operating condition was imposed by the Total Mixer Pressure Ratio (TMPR), and Nozzle Pressure Ratio (NPR) total pressure ratios. TMPR determines the engine's windmilling condition. At design point the TMPR is close to unity since bypass and core total pressures are almost equal. For locked-rotor conditions, the TMPR ratio is high due to the higher BPR. By running simulations with different TMPR, the mixer operating conditions for the whole engine windmilling speed range was modelled. The NPR ratio represents the flight condition. An engine running at low power will have a very low NPR. TMPR was varied between 1.0 - 2.0, whilst NPR was varied between 1.0 - 2.0. There are

combinations of TMPR and NPR which result in the core total pressure being lower than ambient. In reality this is not possible since it will result in the ambient or bypass air flowing upstream into the core. Such cases were not included in the total pressure loss response surface. The model boundary conditions were applied as illustrated in Fig. 8.9. Atmospheric static pressure (p_{atm}), and the engine face total pressure P were set according to an operating point encompassed in the studied engine relight envelope. At an altitude of 12,500 m and a flight Mach number of 0.8, p_{atm} and P_{atm} were calculated as being 17,864 Pa and 27,232 Pa respectively, setting the freestream parameters. Using values of TMPR and NPR given by the sampling plan, the bypass (P_{bypass}) and core (P_{core}) stream inlet total gauge pressures were calculated, ranging from 9,367 - 36,599 Pa (27,232 - 54,464 Pa absolute). These values were used as the total pressure inlet boundary conditions for the bypass and core streams. Convergence criteria for all monitoring parameters were set at $1.0e^{-5}$, however residual values could only reach approximately $1.0e^{-4}$, with turbulent kinetic energy reaching around $5.0e^{-4}$

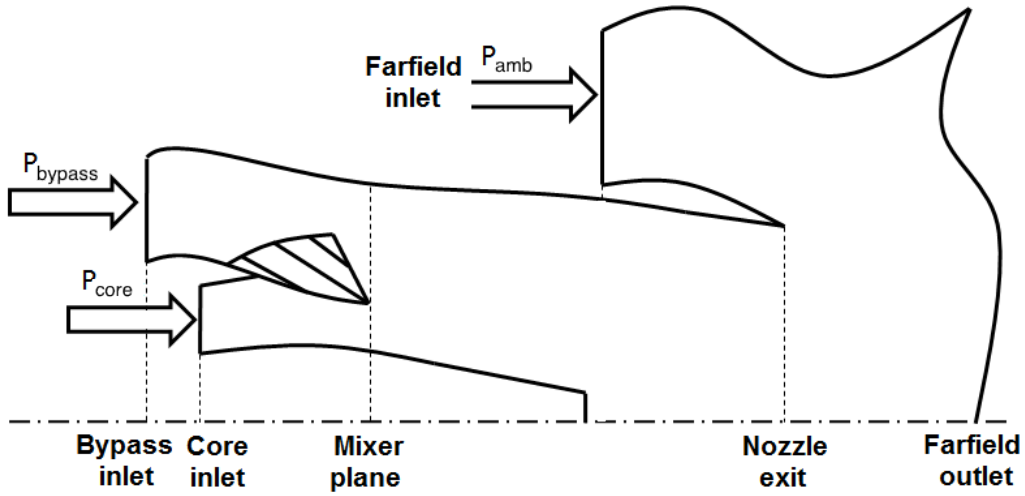

Figure 8.9: Schematic representation of the model boundary conditions [38]

8.3.2 Results and observations

Comparison of the total pressure fields between near design point (TMPR = 1.11) and far off-design operating conditions is shown in Fig. 8.10. At design point, total pressure loss is very low with a small reduction due to the blunt tip of the central exhaust cone.

NPR	1.0	1.1	1.2	1.3	1.4	1.5	1.6	1.7	1.8	1.9	2.0
P_{bypass}	27232.11	29955.32	32678.53	35401.74	38124.95	40848.16	43571.37	46294.58	49017.79	51741.00	54464.21
$TMPR$						P_{core}					
1.0	27232.11	29955.32	32678.53	35401.74	38124.95	40848.16	43571.37	46294.58	49017.79	51741.00	54464.21
1.11			29410.67	31861.56	34312.45	36763.34	39214.23	41665.12	44116.01	46566.9	49017.79
1.25				28321.39	30499.96	32678.53	34857.1	37035.66	39214.23	41392.8	43571.37
1.43						28593.71	30499.96	32406.21	34312.45	36218.7	38124.95
1.67								27776.75	29410.67	31044.6	32678.53
2.0											27232.11

Table 8.2: Absolute total pressurec (Pa) boundary conditions for mixer numerical simulations ($P_{amb} = 27232.11$ Pa)

As TMPR increases, the total pressure defect increases due to the increasingly turbulent mixing between the bypass and core streams. Two distinct flows form, one at the periphery of the mixer consisting of the bypass flow which does not participate in the mixing process, expanding rapidly into the atmosphere. The second flow is the mixture between the core flow and the rest of the bypass stream. Analysis of the flow stream lines, illustrated in Fig. 8.11, indicates clearly how at TMPR = 1.11, the flow is uniform with barely any mixing between the two streams taking place. This is due to the very low radial pressure gradient present. For the off-design conditions, the mixing is more prominent with the differential pressure gradient forcing more radial flows to take place. Recirculation forms at a critical TMPR, as visualised by the stream lines and by the contour of negative axial velocity. Recirculation grows in size and intensity as TMPR increases. Its position also changes, moving upstream as the difference in flow total pressure increases. Contours show how the bypass flow's velocity increases when it emerges into the mixer as the TMPR increases. This is due to a larger expansion ratio resulting from the overall lower pressure in the mixer. This is confirmed by comparing the turbulence intensity, illustrated in Figs. 8.12. Design condition only shows some turbulence due to the blunt tip of the central bullet, whilst there is a higher level of turbulence present throughout mixer volume for off-design conditions. As the TMPR increases beyond a critical value ($TMPR_c$), the flow starts reversing in the core duct to form a cavity. Transition from one regime to another occurs at $TMPR_c = 1.43$, irrespective of the value of NPR.

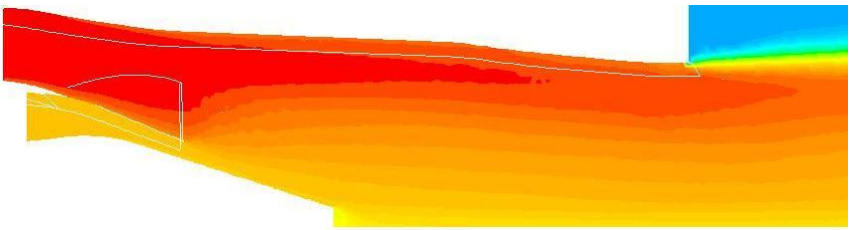

(a) $TMPR = 1.11$

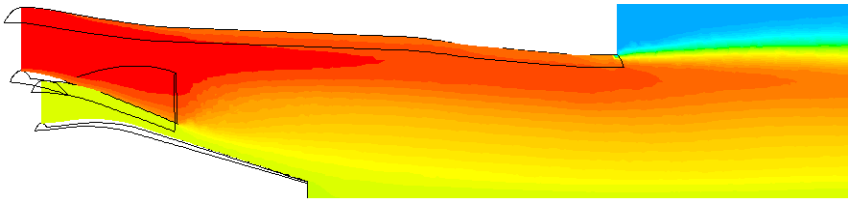

(b) $TMPR = 1.25$

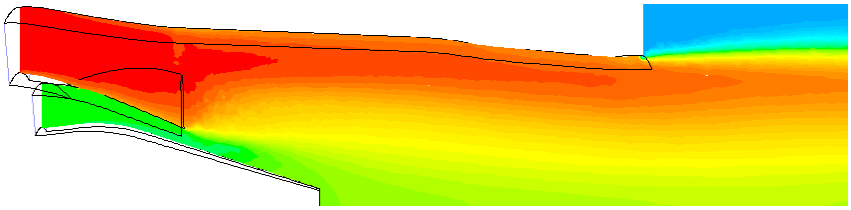

(c) $TMPR = 1.43$

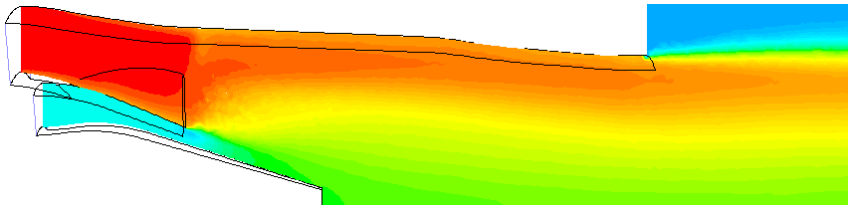

(d) $TMPR = 1.67$

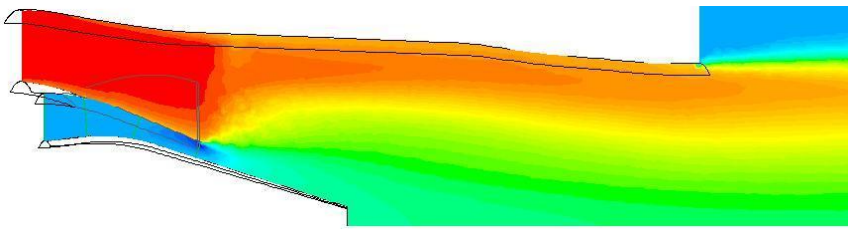

(e) $TMPR = 2.0$

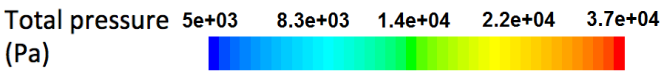

Figure 8.10: Evolution of the total pressure (Pa) field as TMPR is increased from 1.11 to 2.0 for a NPR of 2.0

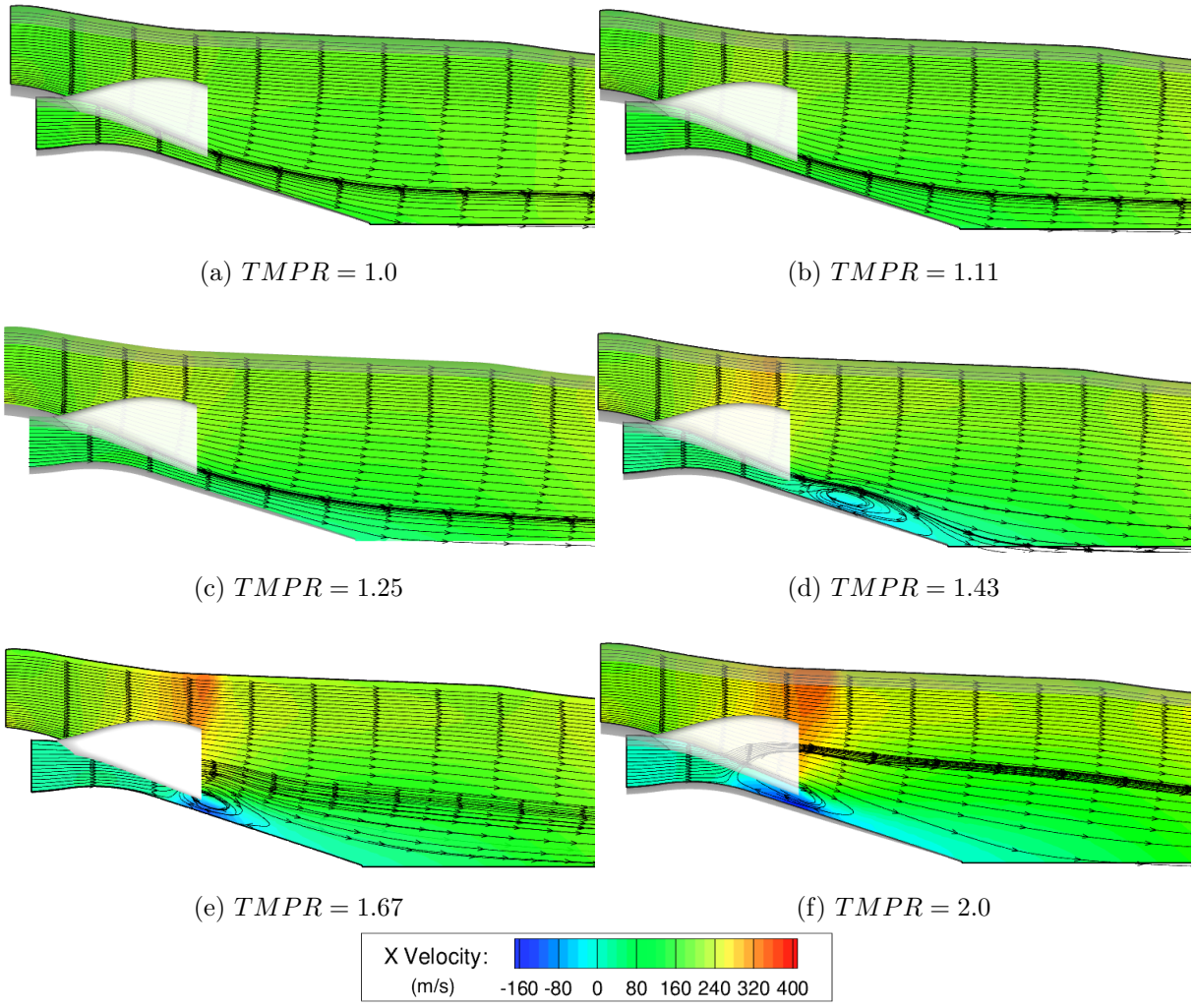

(a) $TMPR = 1.0$ (b) $TMPR = 1.11$

(c) $TMPR = 1.25$ (d) $TMPR = 1.43$

(e) $TMPR = 1.67$ (f) $TMPR = 2.0$

Figure 8.11: Flow field streams lines and axial velocity contours (m/s) as TMPR is increased from 1.11 to 2.0 for a NPR of 2.0

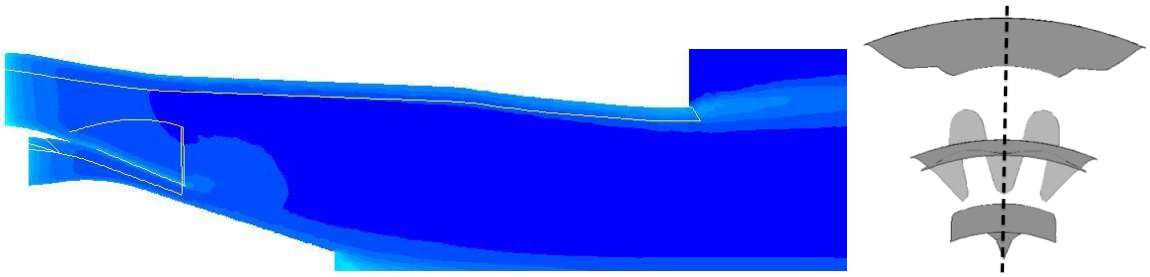

(a) $TMPR = 1.11$

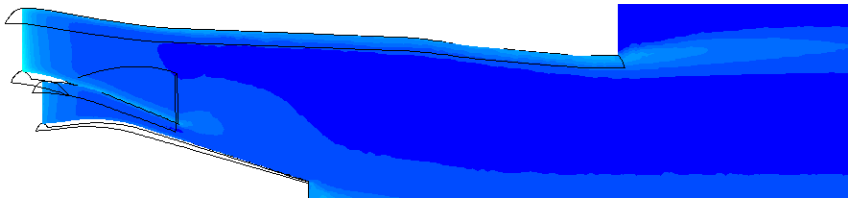

(b) $TMPR = 1.25$

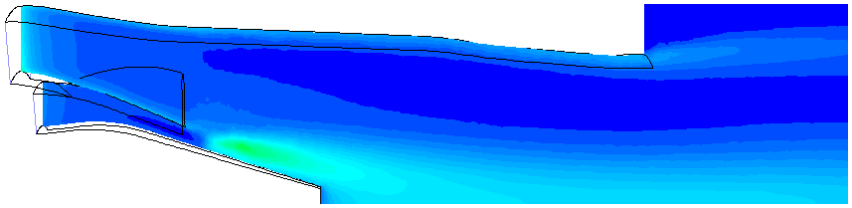

(c) $TMPR = 1.43$

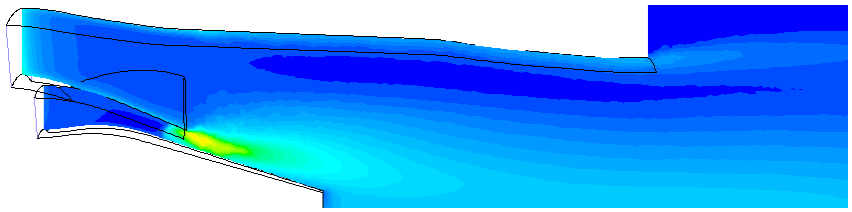

(d) $TMPR = 1.67$

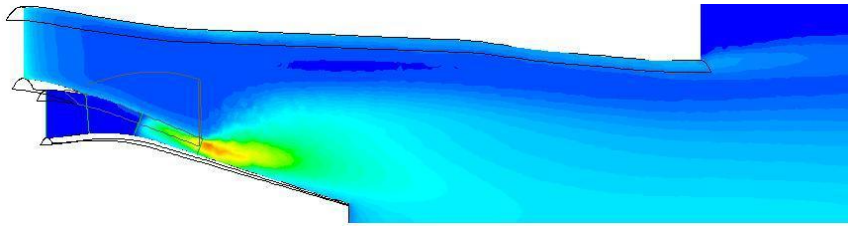

(e) $TMPR = 2.0$

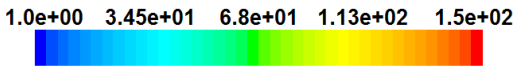

Figure 8.12: Turbulence intensity (%) as TMPR is increased from 1.11 to 2.0 for a NPR of 2.0 - inlet turbulence intensity set at 10%

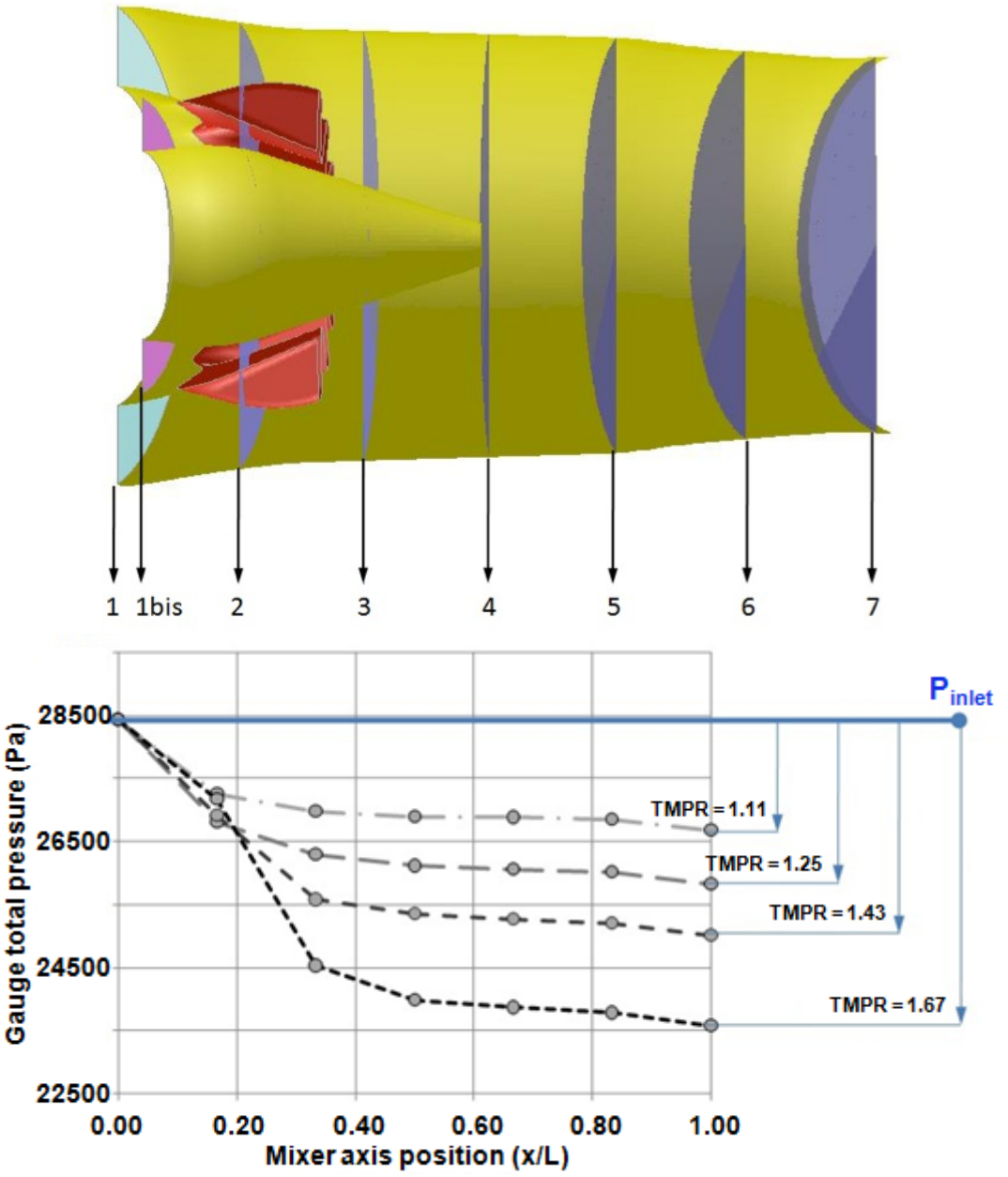

Figure 8.13: Position of measuring planes; mass-weighted average of total pressure in the mixer for a constant NPR of 1.7

At different stations along the mixer numerical model, the total pressure was measured using a mass-weighted averaging method. It is seen from Fig. 8.13 that for a given TMPR in the range $1.11 < \text{TMPR} < 1.43$ and NPR fixed at 1.7, the mean total pressure decreases gradually with distance downstream due to the mixing of bypass and core streams. The difference between the three curves is only due to the drop in core inlet total pressure as TMPR increases. However, once the recirculation flow is established (TMPR > 1.43), the presence of the cavity in the flow dissipates the energy and induces a strong reduction of the mean total pressure, shown by the steep gradients between the second and the third plane of measurements. This shows a gradual change in mixer total pressure loss with TMPR until TMPR_c is reached. The onset of recirculation at TMPR_c then creates an additional sudden increase in total pressure loss. In terms of the velocity ratio, the same trend as that of the TMPR is observed. As the TMPR increases, the velocity ratio between the two streams also increases. When the streams have similar velocities, the NPR has a minor influence on the total pressure loss, with low NPRs having the highest losses. As the velocity ratio increases, the effect of the NPR becomes more evident, as the difference in total pressure loss between NPR = 2.0 and NPR = 1.3 increases.

As shown from the results above, the mixer's off-design performance is not easy to model due to the complex flow phenomena that take place due to the mixing of highly dissimilar flows. To represent the far off-design mixer characteristics in a performance solver, a response surface that predicts the total pressure loss as a function of the mixer's operating condition can be extracted from the numerical results. The percentage total pressure loss is plotted as function of NPR and TMPR. The mixer total pressure loss is defined as:

$$\Delta P = \frac{|P_3 - P_4|}{P_3} \tag{8.5}$$

where P_4 is the mass-averaged total pressure at the nozzle exit, and P_3 the mass-averaged inlet pressure (combining the bypass and core) using the following equation:

$$P_3 = \frac{\dot{m}_{bypass}.P_{bypass} + \dot{m}_{core}.P_{core}}{\dot{m}_{bypass} + \dot{m}_{core}} \tag{8.6}$$

The response surface was produced using the triscattered interpolation method withtin Matlab using the data extracted from the numerical model, as shown in Fig. 8.14. It is clearly visible that the TMPR ratio has a very steep influence on the pressure loss, whilst the influence of the NPR is not as distinctive. The recirculation zone, experienced by the mixer operating at windmilling conditions, produces a total pressure loss between 7.17% $< \Delta P_{loss} <$ 17.34%. In comparison, the plain mixer studied in [140] had a maximum level of pressure loss of about 15% . This demonstrates how the specific geometry of the lobed mixer facilitates the formation of the recirculation, increasing the mixing losses. It is also clear that the total pressure loss map produced is specific to the geometry used. Whilst mixers of similar design will encounter similar flow phenomena, the total pressure loss map will not be the same. For mixers of a different design, the flow phenomena will also be significantly different. Further results which were commercially sensitive and could not be included in the text, can be found in [141].

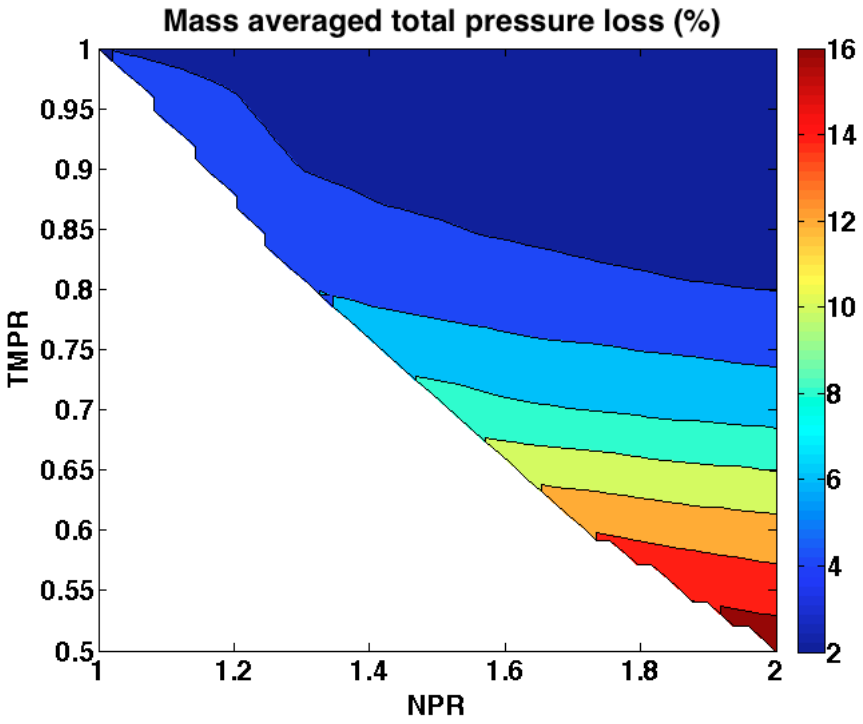

Figure 8.14: Lobed mixer total pressure response surface

8.4 Concluding remarks

The far off-design performance of a low-bypass civil turbofan mixer was studied using a numerical model. The model was run with different TMPRs and NPRs to represent a wide range of possible windmilling operating conditions. The flow field was analysed, particularly in terms of the onset of recirculation and the total pressure loss due to the turbulent mixing.

A percentage total pressure loss map was extracted from the results, representing the mixer's off-design performance as a function of the operating condition. This map can be used within an off-design performance solver to include the mixer's off-design performance, which otherwise would be difficult to model accurately. A number of conclusions can be made out of this study:

- A recirculation zone forms when the TMPR reaches a critical value. The formation of this zone creates a sudden increase in total pressure loss across the mixer.
- The most significant parameter in determining the total pressure loss is the TMPR. The total pressure loss increases from 2% at TMPR equal to 1.0 to 17% for TMPR equal to 2.0.
- The NPR has a only a minor influence on the losses. The lowest losses are at a high NPR (2% at NPR = 2.0 and TMPR = 1.0). This increases to 4% as NPR approaches unity.
- The effect of NPR increases with TMPR. The difference in percentage total pressure loss between NPR = 2.0 and 1.3 increases from 1.28% to 2.27% when the TMPR is increased from 1.0 to 1.25. This increases with TMPR.
- A total pressure loss map for the off-design performance of the mixer can be derived from numerical simulations. Such a map can be used within a sub-idle performance solver to capture more faithfully the effect of the pressure losses in the mixer on the whole engine performance. However such a characteristic is specific to the mixer geometry simulated.

Chapter 9

Groundstart Performance of an IP Start Engine

In the introduction (section 1.1), it was mentioned that in trying to increase cycle efficiency, significant changes in engine configuration and architecture are being made. Engine A is one such case. Although similar to other high-bypass three-shaft turbofans, unlike the rest it has an IP start system. This means that the two electric starter/generators and accessories are attached to the IP shaft, not to the HP. This configuration was considered better for more efficient electrical power generation since it is used on a 'more electric' aircraft. With an IP start engine, the IP shaft will rotate first whilst initially the HP shaft remains static. Once the breakaway torque is reached, the HP shaft will windmill and accelerate, driven by the flow generated by the IPC. During initial cranking, the HPC acts as a blockage for the IPC. This forces the IPC pressure ratio to rise dramatically since for a fixed rotational speed, the flow is being limited. This leads to IPC stall. Once the HPC accelerates, it lets enough flow through to reduce the IPC pressure ratio, letting it drop out of stall. Though the engine starts with a stalled IPC, this occurs at a very low power setting. The engine never starts with the HPC in stall.

Current performance solvers are not designed to cater for such a configuration, mainly due to the need to have IPC stalled characteristics introduced to the solver. The following chapter describes the work done to advance the solver's ability to simulate a stalled IPC start, so that future development on such an architecture is possible.

9.1 Analysis of groundstart test data

Groundstart test data was available for this engine. This was analysed to understand exactly what goes on within the engine and identify any factors that can improve the groundstart performance. Further details are also given in Elysee [77]. Since the engine is equipped with electric starters, the starter power can be varied. Lower starting power obviously results in a slower start and longer time-to-idle.

For a standard groundstart, 100% starting power is used to achieve the minimum time-to-idle. However data from test beds was available for the low-powered starts. The transient lines for tests run at 100%, 50%, 40% and 25% are shown in Fig. 9.1. It is immediately noticeable that the transient working line for the different starts, varies significantly. At low power, the pressure ratio reached by the IPC is much lower. It seems that the magnitude of the IPC stall, is less for the low-powered starts. An analysis of the IPC pressure ratio, as shown in Fig. 9.2 indicates more clearly how the oscillations generated by the stall are significant for the high-powered starts, but much lower in amplitude for the low-powered starts. All starts reach the same value of IPC pressure ratio at idle, however as expected the low-powered starts take longer to reach idle condition. The data suggests that since the IPC takes longer to spool-up with low-powered starts, the HPC has more time available to spool-up. The ratio of rotational speeds between the IP and HP spool is more favourable. For high-powered starts, the IPC is forced to spool-up quickly, leaving the HPC to slowly catch-up. In this case, the ratio of rotational speed is not favourable. The IPC tries to flow more air than the HPC can cope with, resulting in IPC stall. Nevertheless, this does not effect the reliability and starting performance. However it is advantageous to know that low-powered starts result in a 'cleaner' start and may be considered when time-to-idle is not an issue. Whilst a low-powered start improves the IPC starting performance, the HPC working line tends to move towards the surge line as starting power decreases, as illustrated in Fig. 9.3. The HPC never actually stalls, however having a small HPC surge margin during a start is undesirable since the HPC is at risk of stalling when the combustor lights-up due to the step pressure rise downstream of the HPC.

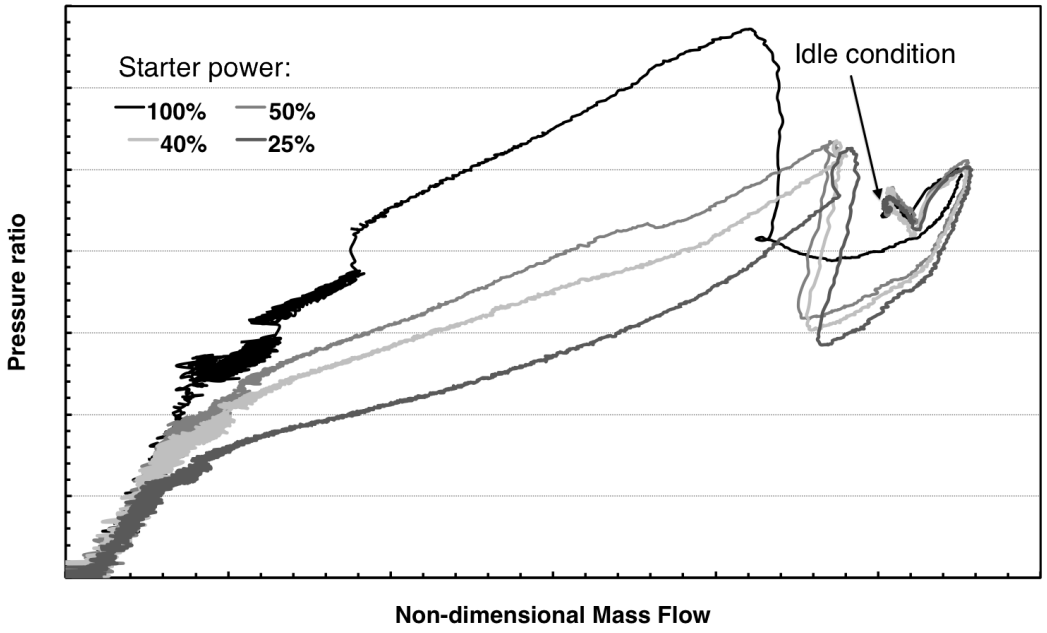

Figure 9.1: IPC transient line during groundstart with different start powers: Rolls-Royce data

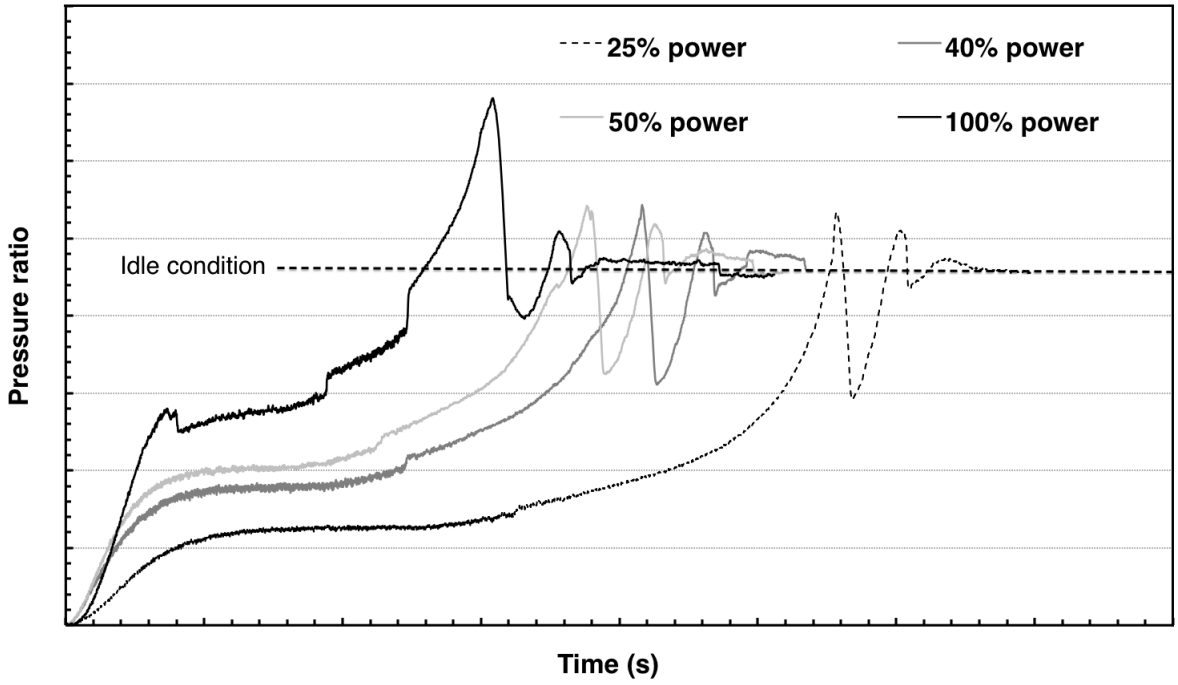

Figure 9.2: IPC pressure ratio during a groundstart for different start powers: Rolls-Royce data

The severity of the IPC stall was also picked up by the IPC VSV angle position sensor. As shown in Figure 9.4, whilst the reading shows the VSV maintaining a constant angle, it also picks up high frequency oscillations. These oscillations are generated by the stalled airflow through the compressor. As the starter power decreases, the amplitude of these oscillations diminishes, indicating less severe stall. This confirms the observation that low powered starts result in less severe IPC stalling.

Similar behaviour is observed on the angle position readings taken for the 2nd stage VSV, shown in Figs. 9.5 and 9.6. This data indicates that the oscillations on the 2nd stage VSV are of an even larger amplitude than on the 1st stage VSV, for both 100% and 50% starting power.

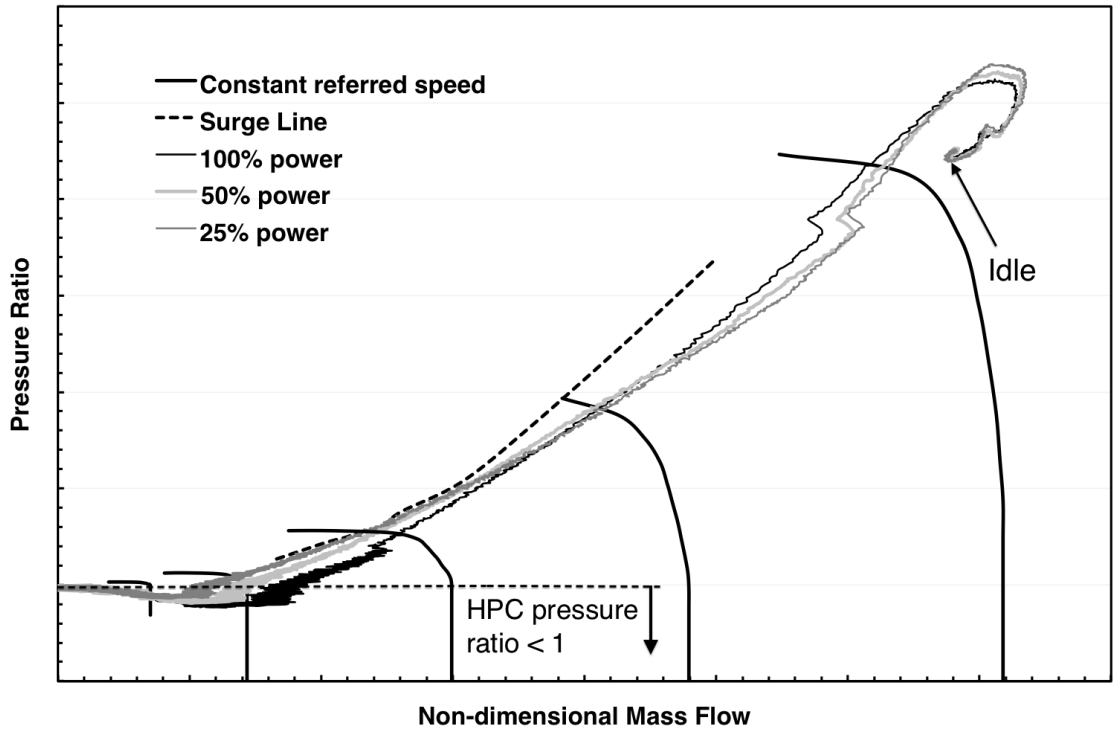

Figure 9.3: HPC working line moves towards surge line as starting power decreases: Rolls-Royce data

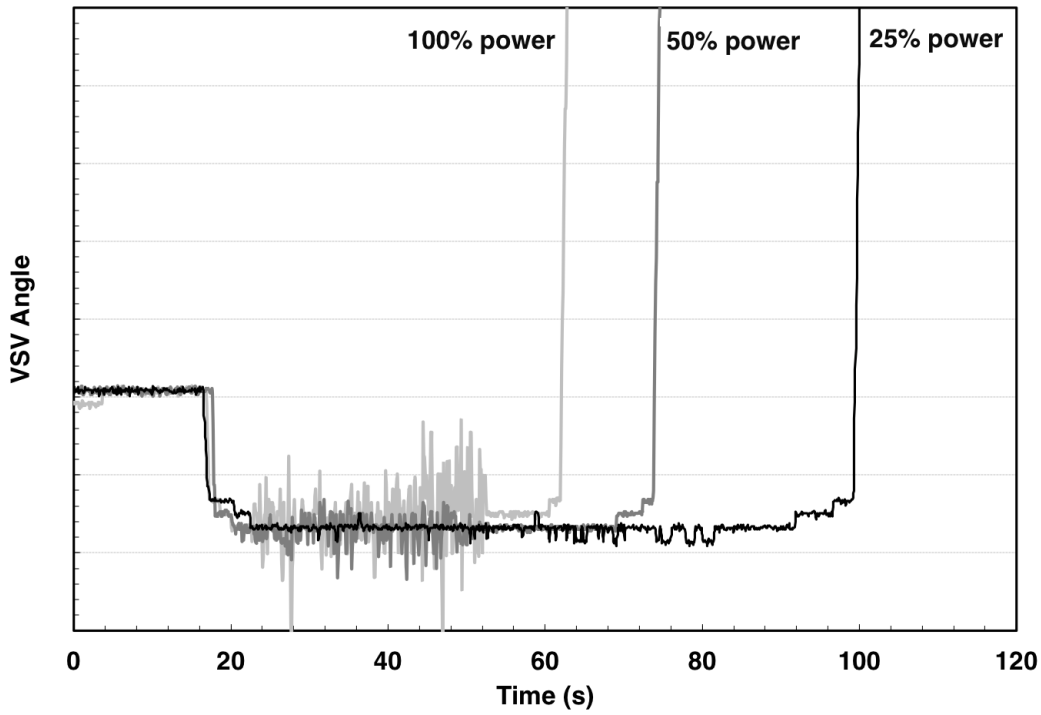

Figure 9.4: Vibration on 1st stage VSV for different starting power: Rolls-Royce data

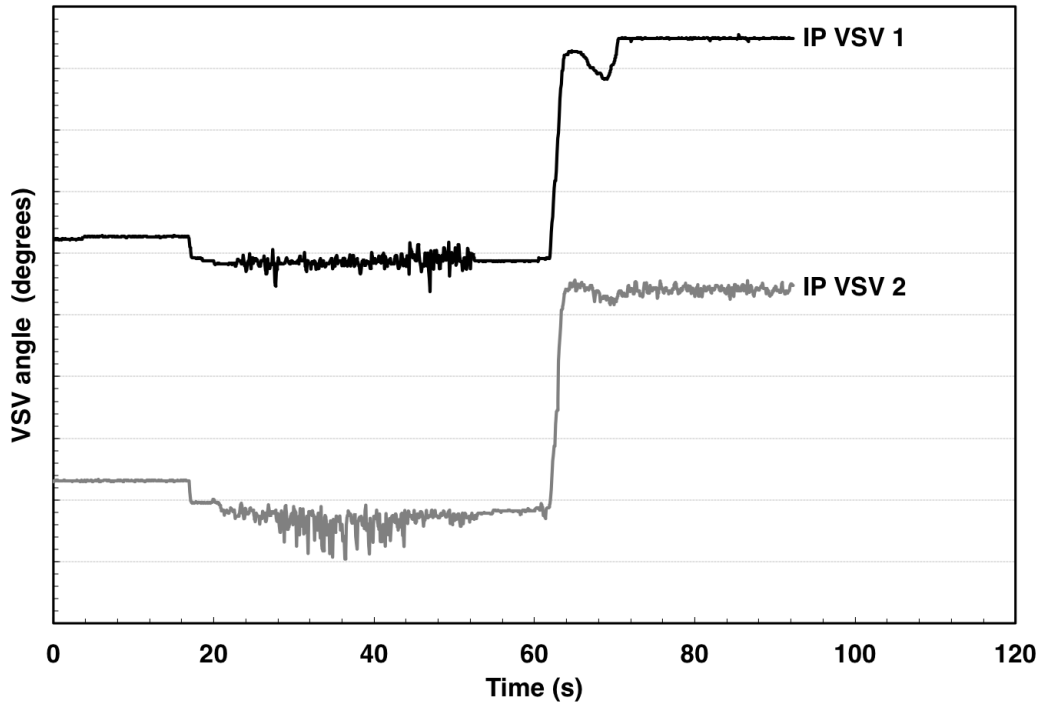

Figure 9.5: Vibration on 1st and 2nd stage VSV at 100% starting power: Rolls-Royce data

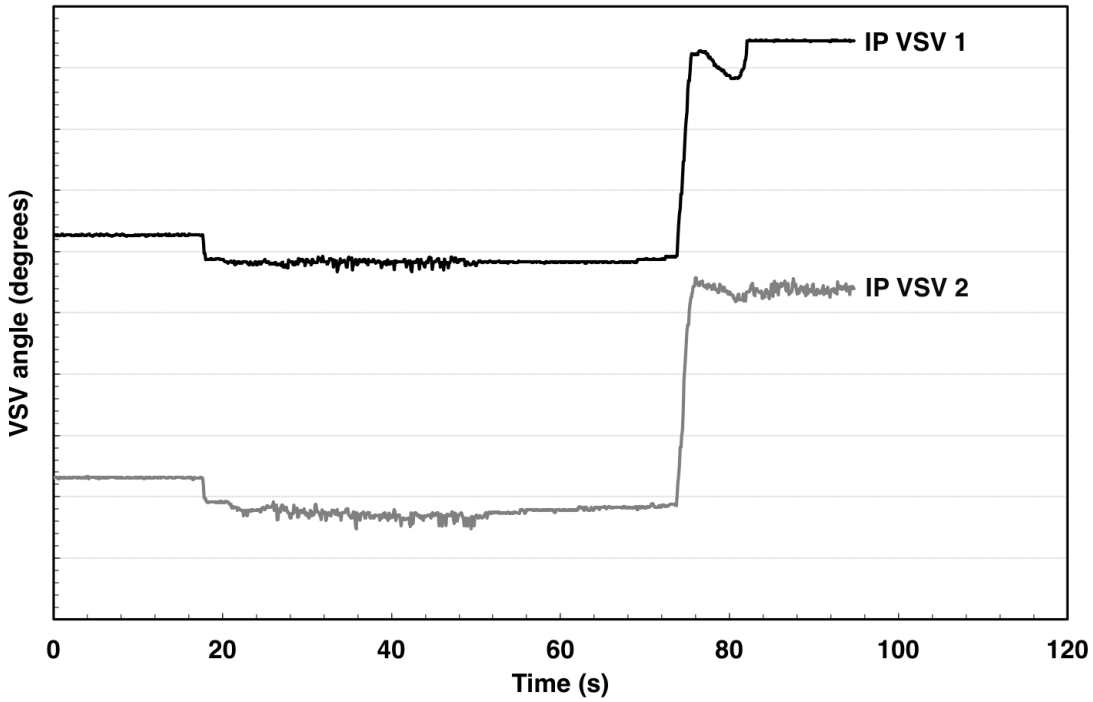

Figure 9.6: Vibration on 1st and 2nd stage VSV at 50% starting power

9.2 Engine model validation

Since the IPC stalls during start-up, the first development version of the engine had a clutch system that connected the IP and HP spools with a reduction gear ratio, called a shaft-power coupling system (SPC). In this manner, the starter system rotated both the IP and HP spools, thus avoiding IPC stall. This eventually was removed since the engine started reliably even with the IPC in stall during the initial phases of the start.

The performance models of the engine were run by the sponsor using the old clutch system, and validated against the development engine data. These simulations were re-run to make sure the model is reliable. For a deadcranking simulation, shown in Fig. 9.7, the model predicts the engine's idle steady state shaft speed within 2% difference. The difference is also within 2% for a groundstart transient, as shown in Fig. 9.8. More validation examples are given by Moxon [23].

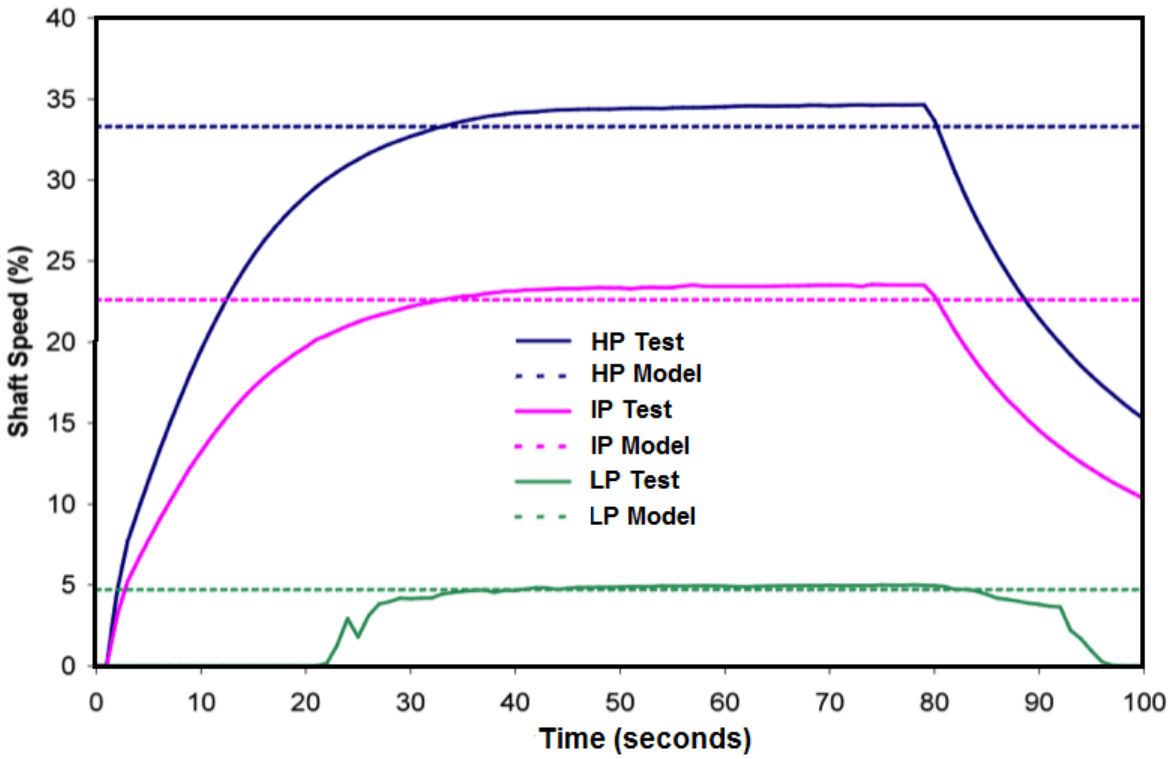

Figure 9.7: Validation of engine model with clutch system - steady state deadcranking speed

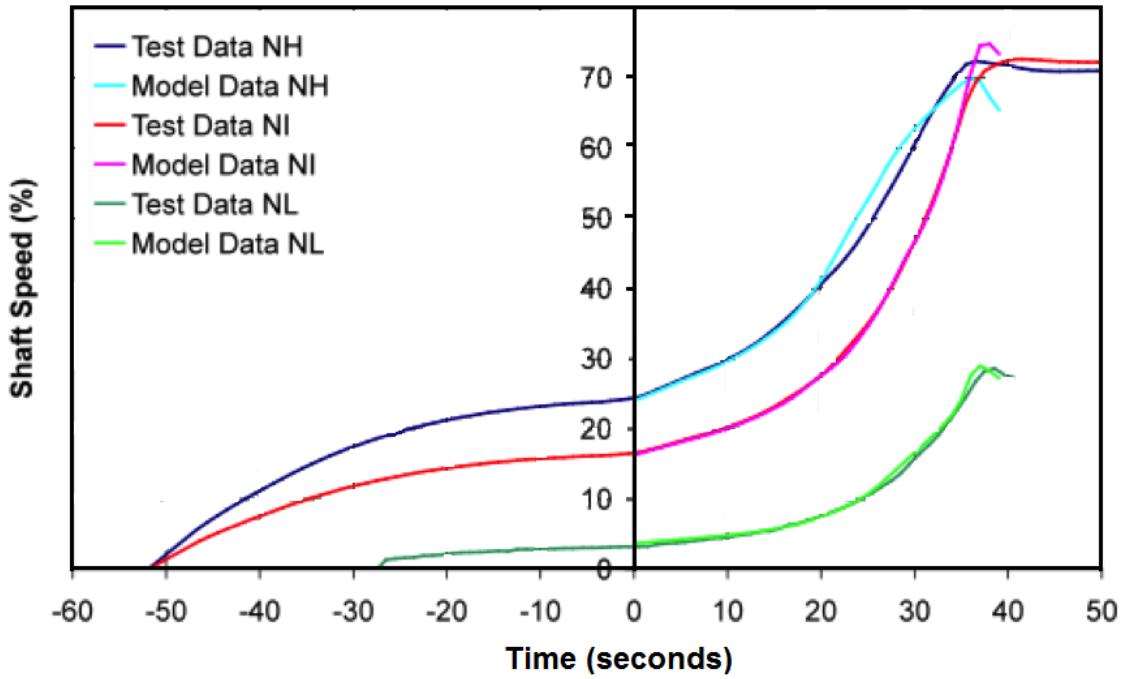

Figure 9.8: Validation of engine model with clutch system - groundstart

However since the current engine has no clutch, it was important to validate the model without the coupling. This was done for two different powered starts: 50% and 100% power, shown in Figs. 9.9 and 9.10 compared against test data from an uncoupled engine. The results show that the uncoupled version of the engine model reproduces the LP shaft speed accurately, whilst there is a 2% error for the IP speed. It is not possible to verify whether the HP speed is predicted accurately since there are no engine dead-cranking tests without the clutch system, that were run long enough for the HP shaft to reach steady state speed.

The difference between a coupled and uncoupled engine during a groundstart is shown in Fig. 9.11.

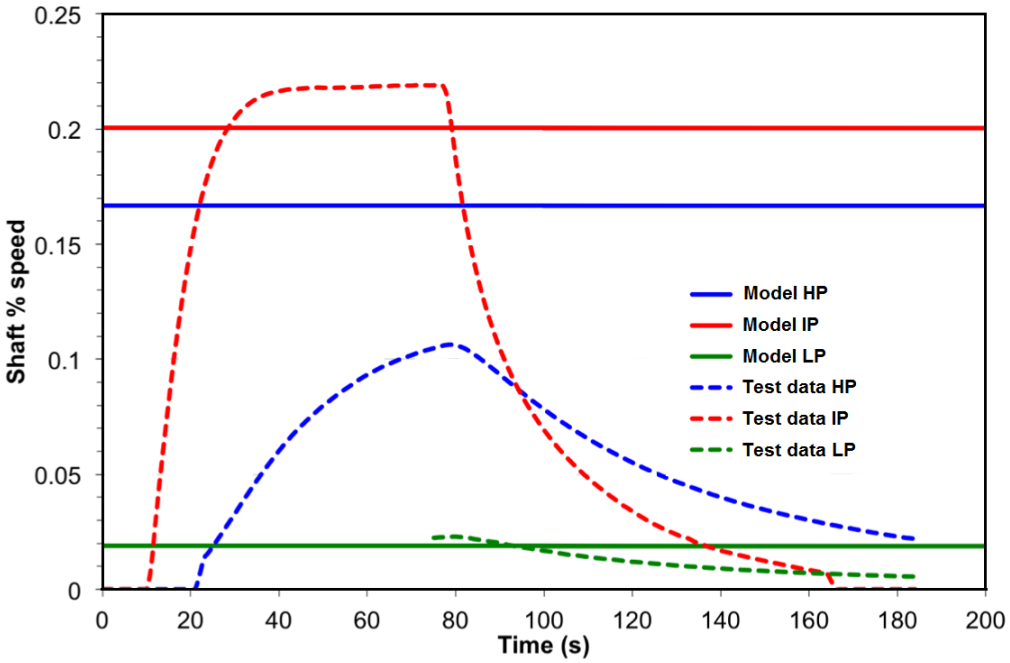

Figure 9.9: Validation of engine model with clutch system - groundstart at 50% starter power

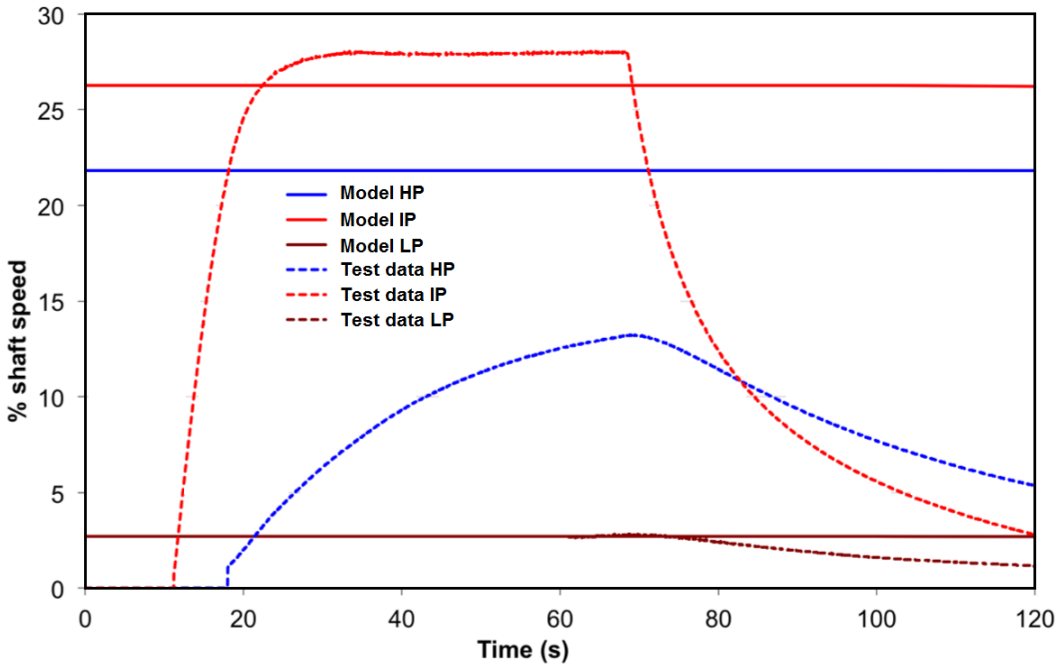

Figure 9.10: Validation of engine model with clutch system - groundstart at 100% starter power

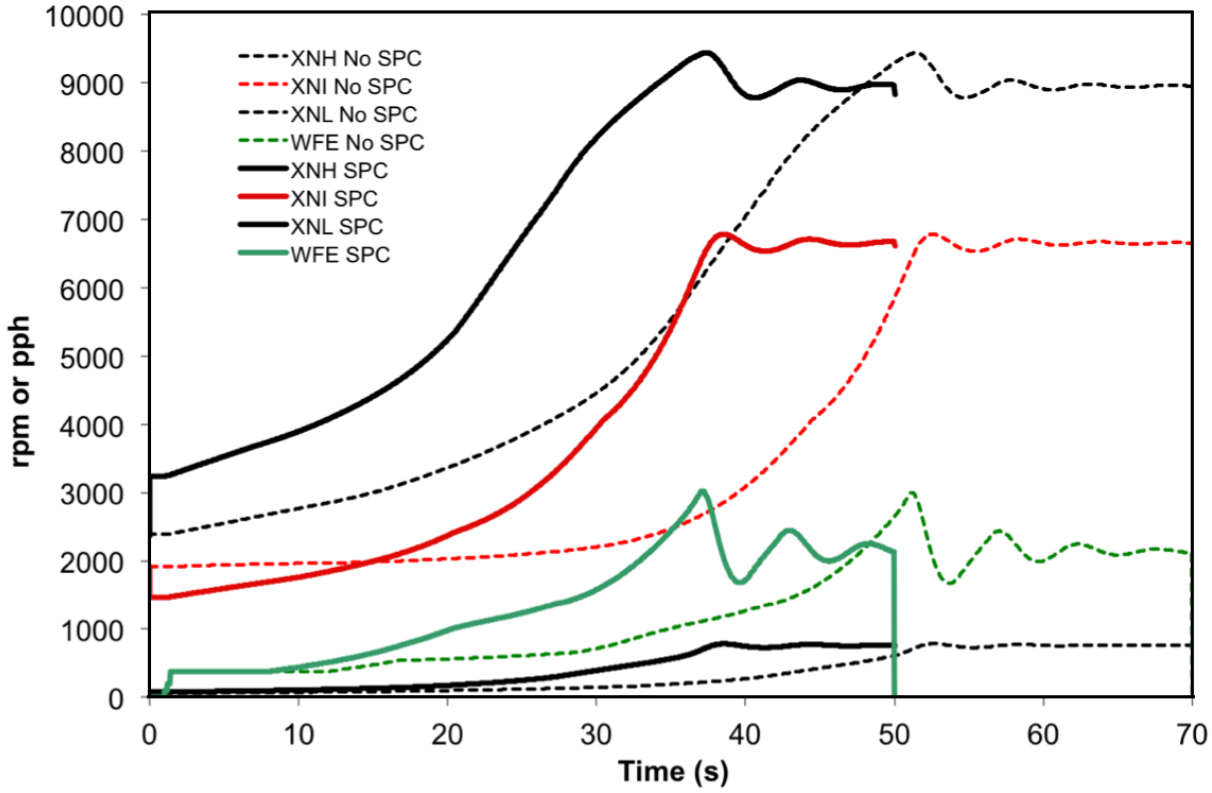

Figure 9.11: Simulation results showing the difference between a coupled (SPC) and uncoupled engine (No SPC) during a groundstart in terms of shaft rotational speeds and fuel flow rate

9.3 IPC stall performance modelling

In order to simulate a groundstart for engine A within a sub-idle performance solver, the stalled part of the transient needs to be accounted for. The first step was to try and generate the compressor's stalled characteristics, as described in section 9.3.1. These were then added to the standard compressor map and used within the solver. To test the new maps, it was attempted to force the IPC into stall by adding a gear ratio between the HPC and IPC, and between the IPC and the starter motor, to force the IPC into stall, as explained in section 9.3.2.

9.3.1 IPC stalled characteristics

The particular design and architecture of engine A means that the compressors can have different transient working lines during a groundstart, depending on the power selection of the electric starters. It is also known that for parts of the transient, the IPC is in stall. It is therefore possible to extract the pressure ratio and non-dimensional mass flow at fixed values of non-dimensional speed ($N/\sqrt{T}$) for each transient. Joining these points together shows the speed lines of the low-speed IPC map even into the stalled region, shown in Fig. 9.12.

However these lines do not show the steady state map characteristics since they are derived from transient data. The values themselves would not be used to generate the stalled part of the compressor sub-idle map. However as a starting point, they useful to roughly estimate the steady state stalled characteristics.

The results shown in Fig. 9.12 show clearly how for a constant speed line, as the non-dimensional mass flow decreases, the pressure ratio increases up to a maximum point beyond which the compressors stall. This point indicates the condition at which the flow becomes detached from the blade leading to a reduction in the compressor's ability to compress air, as seen by the decrease in pressure ratio. Further reduction in flow results in even lower pressure ratios.

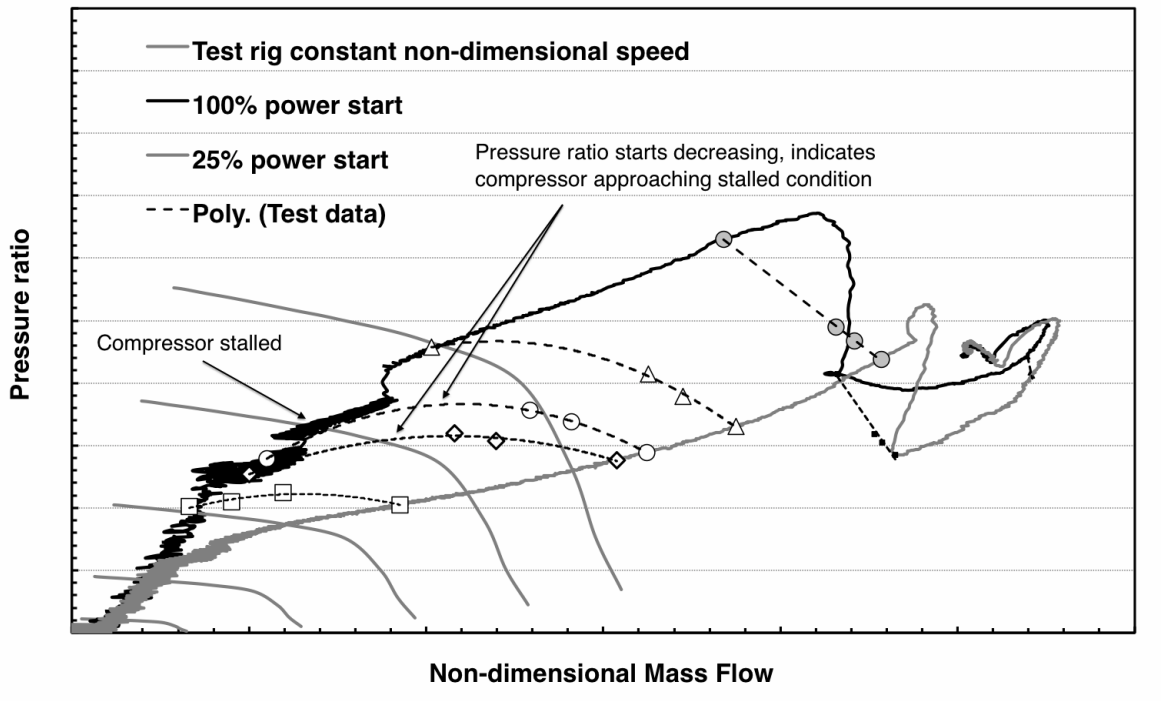

Figure 9.12: Compressor speed lines extracted from the various transients

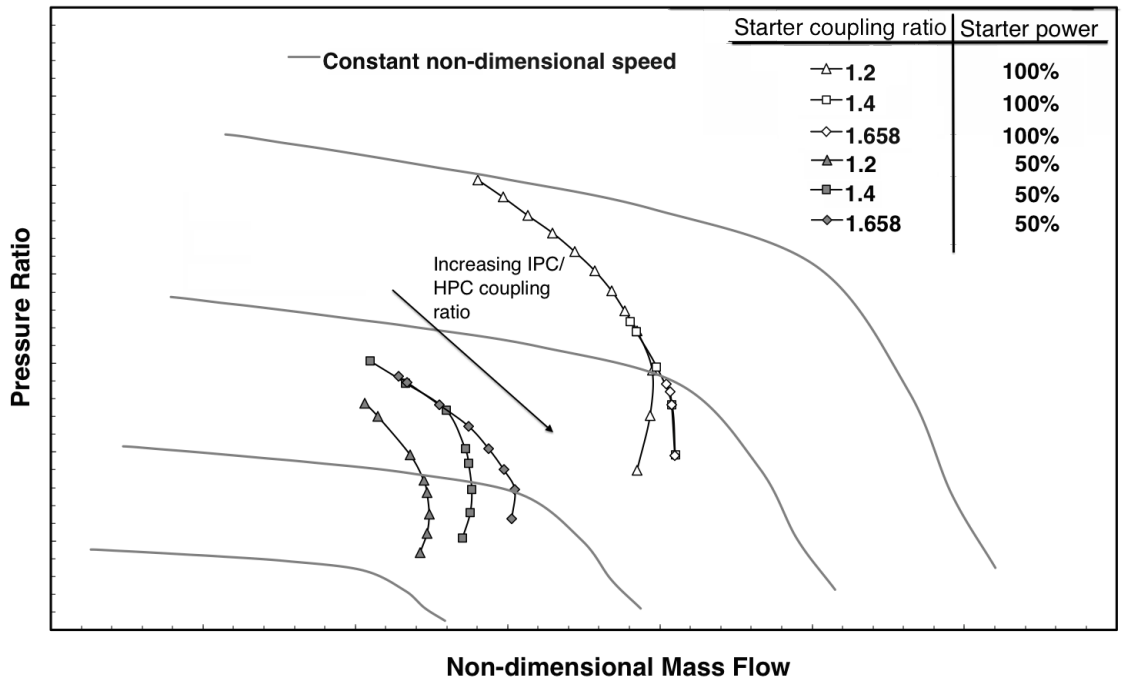

Figure 9.13: IPC operating points simulated for different IP-to-HP spool rotational speed ratios, IP-to-Starter speed ratios, and starter power

9.3.2 Stall attempts

Once the stalled characteristics of the IPC were provided to the solver, steady state simulations were run to attempt to force the IPC into stall and therefore use the newly added characteristics. This was done by adding a forced speed ratio between the IP and HP spools within the performance solver code. A high gear ratio would force the IP to rotate much faster than the HP, forcing the IPC into stall. Additionally, each speed ratio was run at different powered starts and different gear ratios between the starter and the IP shaft. The results are illustrated in Fig 9.13, were the ratio between IP and starter speeds and the percentage starter power are labelled. The speed ratio between the IP and HP was varied between 0.8 and 2.2.

A expected, increasing starter power moves the IPC operating point to a higher speed line, with an increase in pressure ratio and flow. Increasing the gear ratio between the IP spool and the starter also pushes the operating point to a higher pressure ratio. Similarly, increasing the speed ratio between the IP and HP spools moves the IPC to a higher pressure ratio since the HPC starts acting as a throttle downstream of the IPC. The steady state operating points for a constant starter power and IP-starter speed but increasing IP-HP speed ratios shows the IPC non-dimensional mass flow decreasing with increasing pressure ratio, moving towards the stall line. However the last points shown close to the stall line are the last simulations that successfully converged. Any higher speed ratio between the IP and HP spool resulted in the solver failing to converge.

Therefore it was not possible to force the solver to run the IPC in stalled mode and use the new IPC map stalled characteristics. Further work into understanding why the solver couldn't converge was undertaken but not completed in time, and is suggested as future work.

The performance solver always starts a transient simulation from a steady state condition. This means that all the spools would be rotating at a steady state speed when fuel is injected. In most three-shaft engines with HP-start, this is correct. However, in the case of the IP-start engine, the HP spool is still accelerating when ignition occurs. Consequently a groundstart transient for the IP-start engine starts from a steady state condition at which the HP spool is too high. To overcome this, a number of very low-powered starts were attempted in such a way that the starter starts from very low power, and then transitions to maximum power. In this manner, the steady-state starting point would be at a very low speed and closer to the real engine. Figure. 9.14 shows the results when the initial starting power was varied from 50% down to 22%, eventually increasing to 100%. The simulations agree with the observations made in section 9.1, where during a groundstart, the higher the starting power, the more stalled the IPC operates. Eventually all the transient lines meet when the starter reaches 100% power as annotated in Fig. 9.14. However due to the inability of the performance solver to use the stalled IPC map characteristics, it was not possible to run a simulation starting from a completely static HPC, which would have further raised the IPC working line into the stalled region.

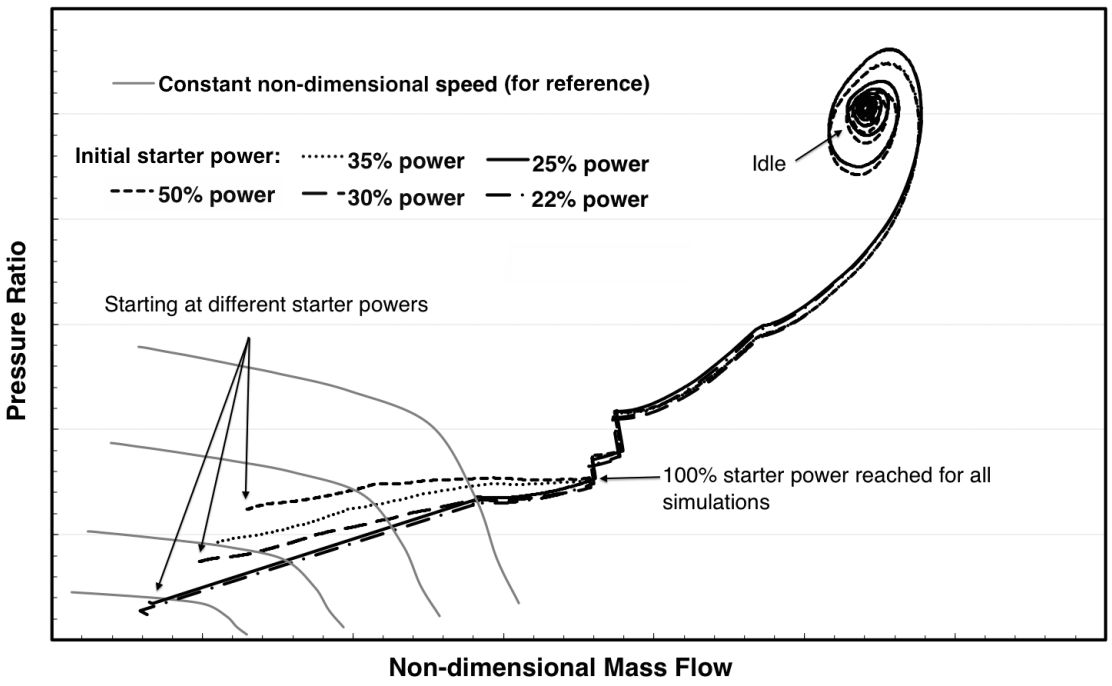

Figure 9.14: IPC transient working lines simulated for different starting power

9.4 Concluding remarks

Analysis of a three-shaft IP start engine test data, has shown that whilst the IPC will always stall due to the presence of the HPC during start, the starting power supplied to the IP shaft has a significant influence on the level of stall the IP will experience. Low-powered starts result in stall of a lower magnitude, verified by the analysis of pressure and flow oscillations, and the detection of vibration on the VIGVs, during different powered starts. This observation is of significant importance, in the view that if IPC deterioration becomes an issue once the engine has been in service for some years, reducing the starting power can be a quick fix to control such deterioration until a permanent solution is studied.

The second part of the work aimed at simulating the groundstarting transient, forcing the solver to simulate also the stalled IPC. Stalled characteristics were added to the IPC map and by manipulating the IPC/HPC speed ratio, IPC/starter speed ratio and the power delivered to the IPC, it was attempted to force the IPC into the stalled region of the map. This however was not successful and further investigation is required to understand why the solver does not converged in the stalled part of the IPC map.

Chapter 10

Conclusions and Future Work

The objective of this research was to improve the accuracy of sub-idle whole engine synthesis solvers. Through numerical and analytical simulations, and understanding the physical phenomena involved, the sub-idle performance of the compressor, combustor, and mixer, was studied resulting in the development of more accurate sub-idle models. A number of these were subsequently introduced into the whole engine performance solver. The majority of the objectives listed in section 1.4, were achieved. Some areas require further research in order to improve the reliability of the models developed.

10.1 Conclusions

Significant contributions were made in the area of aero gas turbine sub-idle performance modelling through the systematic research undertaken on the individual engine components, and the performance solver as a whole. These are listed herein in their respective area of study.

10.1.1 Compressor

A number of studies were undertaken to understand the flow characteristics under locked rotor conditions. An off-design flow deviation model was found to still be valid under conditions of high negative incidence. Numerical simulations were run under compressible flow conditions to extract blade coefficients for high Mach number flows. Due to the highly separated flow, the axial and tangential forces on the blades was measured, from

which the static pressure and tangential force coefficients were extracted, which proved to be a more reliable and accurate method of determining such coefficients. The blockage caused by the highly separated flow was also studied, showing how the flow effective area increases with flow Mach number as the separation is forced to reattach to the blade surface. Contrary to conclusions from previous researchers, after studying the use of Blade Element Theory for locked-rotor conditions at various incidence angles, it was not found to not be accurate enough. A new sub-idle map generation code was developed to include these findings and to run using isentropic flow equations to calculate changes due to compressibility. The new code runs up to the choking point of the zero-speed line, producing a more complete sub-idle compressor map. The code's results were validated against engine test data, producing encouraging results and highlighting areas of further improvement.

The main contributions for the compressor studies are the numerical data gathered in terms of blade characteristics, flow deviation and blockage, together with the new version of the compressor map-generation code.

10.1.2 Performance solver

The whole engine sub-idle performance solver was converted from linearised to torque-based parameters to make it more suitable to handle low-speed compressor and turbine characteristics. Test case runs show that the new torque-based solver gives good results when validated against engine test data. It also gives the same solution as the linearised-based code, showing that the original functionality has not been tampered, with the advantage that it uses parameters better suited for sub-idle simulations. This is a significant contribution towards combining the sub-idle compressor map generating code with the performance solver to ultimately be able to run performance simulations from static conditions.

10.1.3 Combustion

A sub-idle combustion efficiency model was developed through combining a number of established correlations and results from the numerical simulations. The model predicts both reaction-rate and evaporation-rate based combustion efficiency, thus capturing the reduction in efficiency due to poor atomization, which is typical at relight and groundstart conditions. The model was validated against combustor test rig data, and was found to match well, thus resulting in a significant contribution towards moving away from factoring combustion maps, and towards fully predictive combustion efficiency models. The development of the sub-routine and successful validation are therefore considered to be a significant contribution for this field of research.

Numerical simulations with the aim of studying the formation of the recirculation zone under windmilling conditions, first started with a simple axial swirler. The general view was that to simulate various combustor operating conditions, the atomizer flowfield is simply scaled down. The study showed how swirler flowfield velocity profiles are scalable only down to a certain point, thus showing that under relight conditions, scaling the swirler flowfield can introduce significant errors. Further work was done in this area by simulating a whole air-blast atomizer. Results from numerical simulations including fuel injection, were compared against correlations for spray characteristics. The conclusion was that such correlations are insensitive to relight conditions, underestimating the size of the droplets and giving an optimistic calculation of the reaction-based combustion efficiency. These simulations and observations are considered the major contributions within this field, especially since little is known on the aerodynamics and fuel atomization under relight conditions.

The influence of compressor wakes on the atomizer performance during relight was studied, showing that such wakes have a major impact on the atomizer flow field and likely to atomize fuel much better than previously assumed. This is of high scientific and industrial value and is considered a major contribution to knowledge, since it could revolutionise the design methodology for future rich-burn combustors and the testing of combustors for relight conditions.

10.1.4 Mixer

The research on mixed exhaust engine performance focused on investigating low-speed mixing flow phenomena to introduce mixer characteristics within the whole engine performance solver. A percentage total pressure loss map was extracted from the results, representing the mixer's off-design performance as a function of the operating point under windmilling conditions. This map can be used within an off-design performance solver to include the mixer's off-design performance, which otherwise would be difficult to model accurately. A better understanding of the phenomena within the mixer when operating with two highly dissimilar coaxial flows, was obtained. The generation of high-fidelity exhaust mixer performance as function of the operating conditions, is the main contribution of this study.

10.1.5 Engine performance

An analysis of test data from a three-shaft IP start engine, showed that the IPC stalls less severely as starter power is reduced. This forms the main contribution within this area of study, having significant implications in terms of reducing engine damage and deterioration, and better understanding of operability issues. Attempts at simulating these conditions within the performance solver were however unsuccessful, even after providing the stalled compressor map for the solver to use.

10.2 Recommendations for future work

Probably every research produces more questions than answers. This study being no exception, there are various areas that can be further addressed as future work. Sub-idle engine performance modelling is a very complex and wide area of research, offering further investigations into this relatively unexplored engine operation. A number of topics for future work can be taken from this research, which are listed in the following paragraphs.

10.2.1 Performance

- The new torque-based version of the performance solver has the potential to run from a static engine condition. This functionality was not implemented within the time-frame available to this project, and therefore can be set as future work to utilise the full potential of the code.

- A preliminary study on modelling the IPC compressor whilst in stall during a groundstart was conducted. This area of research is still largely unexplored and one can potentially reach the stage were the stalled characteristics can be fully utilised by the solver to simulate an IP start engine more faithfully.

10.2.2 Compressor

- Experimental work

  - Following the experimental work carried out by Zachos [5] and the numerical and analytical work undertaken, the next step is to experimentally investigate the flow through a locked-rotor compressor and create a set of validation data for the code. This project is currently in the proposal stage with the plan of setting up a small axial compressor of which the zero-speed characteristics can be extracted from rig tests. Ideally, measurements should additionally be taken in the interstage gap between the blades. This could hopefully shed more light on the flow field in between the stages. By attaching the rotor to an electric generator, it is also possible to measure the torque, thereby creating the required compressor characteristics that are being investigated.

- Compressor code
  - The compressor code developed still assumes that the flow presented to a blade downstream, is the fully-mixed outlet flow of the blade upstream. This may well be the case, however the interstage gap is too small for this assumption to be realistic. Further work on this topic, which can be a continuation of the work carried out by Ferroglio [20], can improve the accuracy of the compressor code.

10.2.3 Combustor

- Combustion efficiency sub-routine
  - An adaptation of the current standard SMD correlations to align them with the spray characteristics of airblast atomizers during relight. This can be based on the atomizer spray studies conducted in this study.
  - Upgrading of the current sub-routine by introducing more complex gas properties and use of mixtures partial pressures.
- Combustion numerical simulations
  - Introduction of fuel into the whole combustor simulations to analyse the effects of the compressor wakes on the spray properties, especially the uniformity.

10.2.4 Mixer

- Full integration of the sub-routine built within the performance solver and running of engine simulations to validate the effect of the mixer characteristics introduced.

Chapter 11

Project Management and Technology Transfer

11.1 Management

Although the largest part of the project is the technical aspect, because of the multi-disciplinary nature of the project and the collaboration with various parties, the managerial aspect also occupied a significant role. The organisation, the people involved, and the coordination, are illustrated in Fig 11.1. The following lists highlight the nature of the relationships with the people involved.

- Industrial supervisors
  - Agreement on general objectives of the project
  - Technical discussions and guidance on work involved
  - Identify, transfer and ensure security of engine and test data provided
- Academic supervisors
  - Coordination of projects for MSc students
  - Technical discussions on the work involved
  - Discussions on nature and time of placements, and relations with the industrial sponsor

- MSc students
  - Introduced the student to sub-idle research, explained the nature of the project being assigned, provided the important literature and explained which skills would be required
  - Maintained regular contact (through email or face-to-face meetings) with the student, at least once every two weeks, to monitor progress and guide the student towards the final objective
  - Helped troubleshoot any problems encountered such as CFD modelling, meshing, and bugs in codes
  - Analyzed and double-checked the results to ensure their reliability
  - Read the thesis write-up and suggested changes required
  - Coordinated and helped in the writing-up of any publications resulting from the project

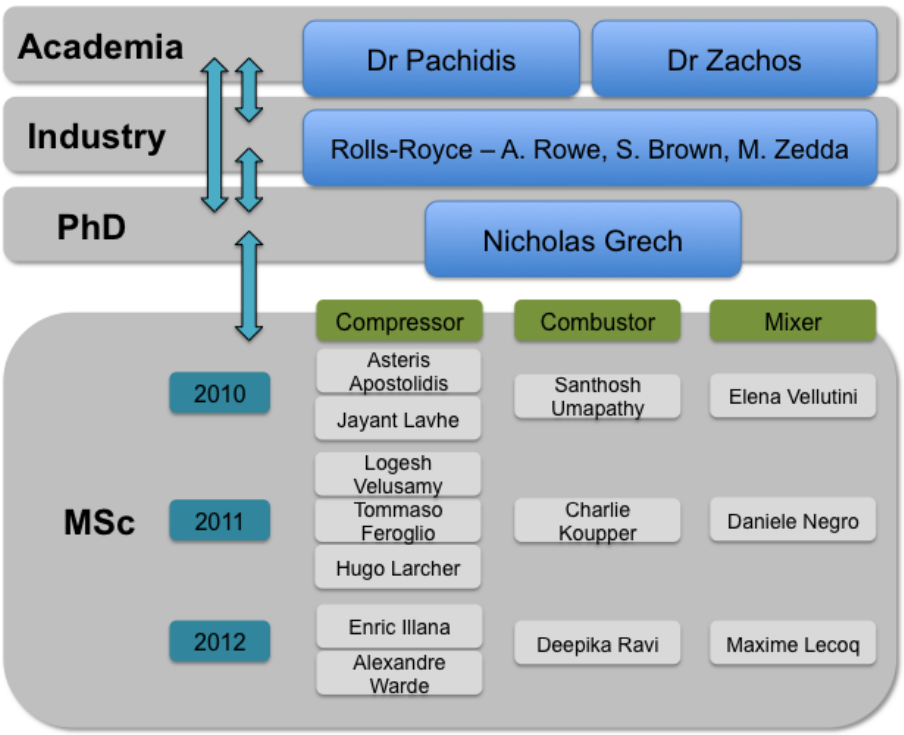

Figure 11.1: Organisation chart

11.2 MSc students' contribution

The author was responsible for the supervision of a number of M.Sc students throughout the duration of the project. In total, thirteen MSc students were supervised: four for the first, five for the second, and four for the last year. The students were assigned projects, of which the title was agreed upon by the author and the academic supervisors, Dr Vassilios Pachidis and Dr Pavlos Zachos. The titles were directly related to the author's work. The projects undertaken by the students within this context, served as their M.Sc thesis project which is a requirement for the successful completion of the MSc Thermal Power course within the Department of Power and Propulsion at Cranfield University.

Overall the experience of working with the M.Sc students was a positive one. A number of students surpassed the author's expectations, delivering work of high quality with minimal supervision, some of which was even published in conferences and journals. However there were cases where the student proved to be less technically able. The author had to dedicate a disproportionate amount of time in advising and guiding the student through each step.

Most of the work assigned to MSc students involved numerical work, where the behaviour of the flow under certain conditions was not known, and therefore needed investigating. The students provided both results of a qualitative nature where knowledge on the flow phenomena was gained, and also of quantitative nature where properties of the flow were extracted and implemented as a database for the codes used.

11.3 Reports and meetings

Meetings with the industrial supervisors were held every two to three months in the form of a short presentation highlighting the progress. Technical meetings were also held when necessary. The Cranfield UTC Annual Review served as an opportunity to present the work done to company employees and academics, promoting discussion and observations.

Each year, a report was presented to the sponsor outlining the progress of the project:

- Cranfield UTC Annual Review Report 2011
- Cranfield UTC Annual Review Report 2012
- Cranfield UTC Annual Review Report 2013

A number of reports on specific work done or deliverables produced, were also presented to the sponsor, namely:

- Engine A Groundstart Performance - Test data analysis of IP compressor performance with various start powers (March 2011)
- Compressor Sub-Idle Map Generation Code - Report and User's Guide (June 2012) - UTC TR 2012-1
- Aero-Engine Mixer Sub-Idle Performance Modelling (November 2012) - UTC TR 2012-6

11.4 Industrial placements

Along the entire duration of the project, the author was given opportunities to undertake some of the work within the sponsoring company. This was a very positive experience from which the author gained highly.

11.4.1 Performance (Derby) - Engine performance modelling

Separate placements which collectively sum up to a number of months, were spent with the performance team at the sponsor's Derby site. The first of these took place during an early stage of the project and served to give the author a better idea on the topic, the tools used, data availability, and the ethics and procedures used within the sponsoring company, as well as interacting with the people involved.

Later placements served to update on the progress, obtain experimental and engine test data, and discuss difficulties. Finally, the last two months of the project were spent with the performance team, integrating the models and code developed over the course of the project, into the sponsor's system.

11.4.2 Combustion (Derby) - Combustor numerical study

Due to IPR restrictions, the combustor numerical modelling was conducted within the Combustion and Casings Aerothermal Methods Team at the sponsor's premises in Derby. A number of factors made this placement very successful:

- There was keen interest on the topic and a great deal of cooperation provided
- The team provided access to a large amount of data and resources, including advice from experienced members of the team
- The team allowed the author to use their dedicated high-performance computing facility, on most occasions allowing access to all their licences and processors available. Since the numerical simulations required a lot of computational power, this was of great advantage

11.4.3 Performance (Bristol) - Performance code

The IT team in Bristol provided support for the codes used and installation of the development and analysis software environments within the Cranfield UTC. The pro-activeness from both sides resulted in a fully autonomous system installed at the Cranfield UTC offices, allowing independent development of the sub-idle code whilst utilising the same environment and codes used by the sponsor.

Two short trips to Bristol were done by the author to help with the coordination of this process and learn as much as possible about the software environment installed. Additionally, members of the IT team visited Cranfield on numerous occasions to install and maintain the system. Whilst this process was beneficial for the current project, it also put the Cranfield UTC group in a better position to transfer and analyse data from the sponsor by utilising the same development platforms.

11.5 Technology transfer

Knowledge transfer between the author and the company was done mainly through presentations, technical discussions and reports. The final placement in Derby served to transfer the results of the research undertaken to the company and gave a chance for explanations and clarifications. Additionally, the Ph.D write-up is also made available to the sponsor for future reference. The project is planned to continue with another Ph.D researcher.

References

[1] Walsh, P., and Fletcher, P., 2004. *Gas Turbine Performance*. Blackwell, 2nd Ed.

[2] Kurzke, J., 1996. "How to get component maps for aircraft gas turbine performance calculations". In International Gas Turbine and Aeroengine Congress and Exhibition, Birmingham, no. 96-GT-164, ASME.

[3] Howell, A., 1942. The Present Basis of Axial Flow Compressor Design, Part 1: Cascade Theory and Performance. Tech. rep., R.A.E. Report E.3946.

[4] Hawthorne, W., 1964. *Aerodynamics of Turbines and Compressors. High Speed Aerodynamics and Jet Propulsion*. Princeton University Press.

[5] Zachos, P., 2010. "Gas turbine sub-idle performance modelling; altitude relight and windmilling". PhD thesis, Cranfield University, School of Engineering.

[6] Leitges, F., 2004. Windmilling - Validation of Component Characteristics in Sub-Idle Conditions. Diploma Thesis, Rolls-Royce Deutschland.

[7] Dixon, S., 1998, 5th Edition. *Fluid Mechanics and Thermodynamics of Turbomachinery*. Elsevier.

[8] Pengue, F., 2008. "Numerical and Experimental Analysis of an HP Compressor Cascade". MSc thesis, Cranfield University, School of Engineering.

[9] *ANSYS Fluent 12.1 User and Theory Guide*.

[10] Zachos, P., Pengue, F., Pachidis, V., and Pilidis, P., 2009. "Flowfield Investigation of a Compressor Cascade at High Incidence - Part 2: Numerical Analysis". *Proc ASME Turbo Expo*(GT2009-59908).

[11] Zachos, P., Grech, N., Pachidis, V., and Singh, R., 2011. "Experimental and Numerical Investigation of a Compressor Cascade at Highly Negative Incidence". *Engineering Applications of Computational Fluid Mechanics,* ***Vol 5***(Issue 1), pp. 26–36.

[12] Reulke, C., 2009. "Experimental/CFD Analysis of the Flow Through a Locked HP Compressor". MSc thesis, Cranfield University, School of Engineering.

[13] Aslanidou, I., 2009. "Physically Enhanced Compressor Map Generation for Sub-Idle Performance Studies". MSc thesis, Cranfield University, School of Engineering.

[14] Robbins, W., Jackson, R., and Lieblein, S., 1955. Aerodynamic Design of Axial-Flow Compressors VII - Blade Element Flow in Annular Cascades. Tech. rep., NACA. RM E55G02.

[15] Larcher, H., 2011. "Improvement of Compressor Map Generation Software for Sub-Idle Performance Studies". MSc thesis, Cranfield University, School of Engineering.

[16] Yocum, A., and O'Brien, W., 1993. "Separated Flow in a Low-Speed Two-Dimensional Cascade: Part 1 - Flow Visualization and Time-Mean Velocity Measurements". *J. Turbomachinery,* ***115***, July.

[17] Creveling, H., and Carmody, R., 1968. Axial Flow Compressor Computer Program for Calculating Off-Design Performance. Tech. Rep. CR-72427, NASA.

[18] Ward, A., 2012. "Numerical Analysis of the Flow through a Windmilling HP Compressor". MSc thesis, Cranfield University, School of Engineering.

[19] Cumpsty, N., 2004. *Compressor Aerodynamics.* Krieger.

[20] Ferroglio, T., 2011. "Numerical Analysis of the Flow Through a Windmilling Compressor". MSc thesis, Cranfield University, School of Engineering.

[21] Maini, G., 2012. Engine A Sub-Idle Matlab Modelling Tool - PTR110688. Tech. rep., Rolls-Royce plc.

[22] Lefebvre, A., 1985. "Fuel effects on gas turbine combustion - ignition, stability, and combustion efficiency". *Journal of Engineering for Gas Turbine and Power,* ***107***, January.

[23] Moxon, A., 2007. Engine A sub-idle performance modelling - PTR109212. Tech. rep., Rolls-Royce plc.

[24] Schmeltz, D., 2006. Improvement and Validation of the Relight Prediction Program CD87. Tech. rep., Rolls-Royce plc DNS 126918.

[25] Rizkalla, A., and Lefebvre, A., 1975. "The influence of air and liquid properties on airblast atomization". *Journal of Fluids Engineering,* ***97***(3).

[26] El-Shanawany, M., and Lefebvre, A., 1980. "Airblast atomization: The effect of linear scale on mean drop size". *Journal of Energy,* ***4***(4).

[27] Fraser, R., Eisenklam, P., Dombrowski, N., and Hasson, D., 1962. "Drop Formation from Rapidly Moving Sheets". *AIChE,* ***8***(5), pp. 672–680.

[28] Lefebvre, A., 1999. *Gas Turbine Combustion.* Taylor & Francis, 2nd Ed.

[29] Lilley, D., 1977. "Swirl Flows in Combustion: A Review". *AIAA Journal,* ***15***(8), August.

[30] Caines, B., Hicks, R., and Wilson, C., 2001. "Influence of sub-atmospheric conditions on the performance of an airblast atomiser". *37th AIAA/ASME/SAE/ASEE Joint Propulsion Conference, Salt Lake City, Utah.*

[31] Beck, J., Lefebvre, A., and Koblish, T., 1989. "Airblast atomization at conditions of low air velocity". *AIAA, 27th Aerspace Sciences Meeting, Reno, Nevada.*

[32] Jasuja, A., 1979. "Atomization of Crude and Residual Fuel Oils". *Journal of Engineering for Power,* ***101***(2), pp. 250–258.

[33] Rosin, P., and Rammler, E., 1933. "The Laws Governing the Fineness of Powdered Coal". *J. Inst. Fuel,* ***7***(31), pp. 29–36.

[34] Ford, C., Carrotte, J., and Walker, A., 2012. "The Impact of Compressor Exit Conditions on Fuel Injector Flows". *Journal of Engineering for Gas Turbines and Power,* ***134***(111504), November.

[35] Frost, T., 1966. "Practical Bypass Mixing Systems for Fan Jet Aero Engines". *The Aeronautical Quarterly*, May, pp. 141–159.

[36] Rehab, H., Villermaux, E., and Hopfinger, E., 1997. "Flow regimes of large-velocity-ratio coaxial jets". *Journal of Fluid Mechanics,* ***345***, pp. 357–381.

[37] Howard, J., 2007. "Sub-idle modelling of gas turbines; altitude relight and windmilling". PhD thesis, Cranfield University, School of Engineering.

[38] Lecoq, M., 2012. "Aero Engine Sub-Idle Mixer Performance Modelling". MSc thesis, Cranfield University, School of Engineering.

[39] Kilik, E., 1976. "The Influence of Swirler Design Parameters on the Aerodynamics of the Downstream Recirculation Region". PhD thesis, Cranfield Institute of Technology.

[40] Vincent, K., Huntely, S., and Wilsted, H., 1952. Comparison of Locked-rotor and Windmilling drag characteristics of an Axial-flow-compressor type Turbojet Engine. Tech. rep., National Advisory Committee for Aeronautics.

[41] Hooker, S., 2007. *Not Much of an Engineer: An Autobiography.* Airlife.

[42] EASA, 2010. Certification Specifications for Engines CS-E. www.easa.eu.int/agency-measures.

[43] Alexiou, A., Roumeliotis, I., Aretakis, N., Tsalavoutas, A., and Mathioudakis, K., 2012. "Modeling Contra-Rotating Turbomachinery Components for Engine Performance Simulations: The Geared Turbofan With Contra-Rotating Core Case". *J. Eng. Gas Turbines Power,* ***134***(111701).

[44] Jones, G., 2002. "Performance Modelling of Windmilling Gas Turbines". PhD thesis, Cranfield University, School of Engineering.

[45] Riegler, C., Bauer, M., and Kurzke, J., 2001. "Some Aspects of Modeling Compressor Behaviour in Gas Turbine Performance Calculations". *Journal of Turbomachinery,* ***123***, April, p. 372.

[46] Rowe, A. Guide to Transient Performance. Tech. rep., Rolls-Royce Performance, PTR 90539.

[47] http://www.airspacemag.com/issues/2006/august- september/flameout.php.

[48] Jones, G., Pilidis, P., and Curnock, B., 2002. "Extrapolation of compressor characteristics to the low-speed region for sub-idle performance modelling". In Proc of ASME Turbo Expo GT-2002-30649.

[49] Jones, G., Pilidis, P., and Curnock, B., 2001. "Compressor characteristics in gas turbine performance modelling". In Proc of ASME Turbo Expo 2001-GT-0384.

[50] Zachos, P., Aslanidou, I., Pachidis, V., and Singh, R., 2011. "A Sub-idle Compressor Characteristic Generation Method With Enhanced Physical Background". *J. Eng. Gas Turbines and Power,* ***133***(8), August.

[51] Hatton, N., 1984. Windmilling Performance of Bypass Engines - Rolls-Royce PTR00736. Tech. rep.

[52] Howell, A., and Carter, A., 1946. "Fluid flow through cascades of aerofoils". In 6th International Congress on Applied Mechanics, Paris.

[53] McKenzie, A., 1997. *Axial Flow Fans and Compressors: Aerodynamic Design and Performance*. Ashgate.

[54] Sing, T., Kim, T., Kim, J., and Ro, S., 2001. "Performance prediction of axial flow compressors using stage characteristics and simultaneous calculation of interstage parameters". *Proc Instn Mech Engrs,* ***215***, pp. 89–98.

[55] Zachos, P., Pachidis, V., Charnley, B., and Pilidis, P., 2009. "Flowfield Investigation of a Compressor Cascade at High Incidence - Part 1: Pnuematic Probe Measurements". *Proc ASME Turbo Expo*(GT2009-59906).

[56] Menter, F., 1993. "Zonal Two Equation k-w Turbulence Models for Aerodynamic Flows". In AIAA 24th Fluid Dynamics Conference, Orlando, Florida -AIAA-93-2906.

[57] Menter, F., 1994. "Two-equation Eddy-viscosity Turbulence Models for Engineering Applications". *AIAA Journal,* ***32***(8), August.

[58] Deutsch, S., and Zierke, W., 1990. "The measurement of boundary layers on a compressor blade in cascade: Part 4 - Flowfields for incidence angles of -1.5 and -8.5 degrees". *ASME Journal of Turbomachinery,* ***112***, pp. 241–255.

[59] Lieblein, S., 1954. Review of High-Performance Axial-Flow-Compressor Blade-Element Theory. Tech. rep., NACA. RM E53L22.

[60] *Ansys CFX User Manual.*

[61] Yocum, A., and O'Brien, W., 1993. "Separated Flow in a Low-Speed Two-Dimensional Cascade: Part 2 - Cascade Performance". *J. Turbomachinery,* ***115***, July.

[62] Carter, A., 1950. The Low Speed Performance of Related Aerofoils in Cascades. Tech. rep., Aeronautical Research Council. ARC Technical Report, CP No 29, 12,883.

[63] Constant, H., 1939. Performance of Cascades of Aerofoils. Tech. rep., R.A.E. ARC 4155, E.3696.

[64] McKenzie, A., 1980. "The Design of Axial Compressor Blading Based on Tests of a Low Speed Compressor". *Proc Instn Mech Engrs,* ***Vol 194***, pp. 103–111.

[65] Cetin, M., Ucer, A., Hirsch, C., and Serovy, G., 1987. Application of Modified Loss and Deviation Correlations to Transonic Axial Compressors. Tech. Rep. 745, AGARD.

[66] Al-Daini, A., 1986. "Loss and Deviation Model for a Compressor Blade Element". *Int. J. Heat Fluid Flow,* ***7***(1), March.

[67] Templalexis, I., Pilidis, P., Pachidis, V., and Kotsiopoulos, P., 2011. "Development of a Two-Dimensional Streamline Curvature Code". *J. Turbomachinery,* ***133***, January.

[68] Boyer, K. "An Improved Streamline Curvature Approach for Off-Design Analysis of Transonic Compression Systems". PhD thesis, Virginia Polytechnic Institute and State University.

[69] Illana, E., 2012. "Study on Flow Separation and Blockage in a Compressor at Locked Rotor Conditions". MSc thesis, Cranfield University, School of Engineering.

[70] Suder, K., 1997. Blockage Development in a Transonic Axial Compressor Rotor. Tech. rep., NASA.

[71] Weber, A., Schreiber, H., Fuchs, R., and Steinert, W., 2002. "3-D Transonic Flow in a Compressor Cascade With Shock-Induced Corner Stall". *J. Eng. Gas Turbine and Power,* ***124***, July.

[72] Khalid, S., Khalsa, A., Waitz, I., Tan, C., Greitzer, E., Cumpsty, N., Adamczyk, J., and Marble, F., 1999. "Endwall Blockage in Axial Compressors". *J. Turbomachinery,* ***121***, July.

[73] Khalsa, A., 1996. "Endwall Blockage in Axial Compressors". PhD thesis, Massachusetts Institute of Technology.

[74] Grech, N., 2012. Compressor Sub-Idle Map Generation Code - Report and User's Guide TR 2012-1. Tech. rep., Cranfield University UTC.

[75] Jenkins, J., 2012. Evaluation of Cranfield UTCâs compressor map extrapolation method - DNS182971. Tech. rep., Rolls-Royce plc.

[76] Maini, G., 2012. Engine A Above-Idle Matlab Modelling Tool - PTR110650. Tech. rep., Rolls-Royce plc.

[77] Elysee, D., 2009. Engine a: Starting test on engine. Tech. Rep. PTR109638, Rolls-Royce Performance, June.

[78] Monticelli, M., 2003. Engine D sub-idle performance modelling - PTR23159. Tech. rep., Rolls-Royce plc.

[79] Meads, R., and Widdowson, D., 2006. Cug 3 shaft turbofan starting synthesis program. Tech. Rep. PTR90900, Rolls-Royce plc.

[80] Brown, S., Seargeant, M., Meads, R., and Widdowson, D. Cug rrap part 1. Tech. rep., Rolls-Royce plc.

[81] Brown, S., Seargeant, M., Meads, R., and Widdowson, D. Cug rrap part 2. Tech. rep., Rolls-Royce plc.

[82] MathWorks. http://www.mathworks.com/help/matlab/ref/triscatteredinterp.html. Matlab online user guide.

[83] Childs, J. H., 1950. Preliminary Correlation of Efficiency of Aircraft Gas-Turbine Combustors for Different Operating Conditions. Tech. rep., NACA RM E50F15.

[84] Lefebvre, A., 1960. Theoretical Aspects of Gas Turbine Combustion Performance, Note Aero No. 163. Tech. rep., College of Aeronautics, Cranfield.

[85] Su, K., and Zhou, C., 1998. "Numerical study of spray parametric effects on gas turbine combustion performance". *ASME Publications*.

[86] Su, K., and Zhou, C., 2000. "Numerical Modelling of Gas Turbine Combustor Integrated with Diffuser". *Proceedings of the 34th National Heat Transfer Conference, Pittsburgh*.

[87] Lefebvre, A., 1989. *Atomization and Sprays*. Taylor and Francis.

[88] Ballal, D., Zedda, M., Jones, B., Singh, R., and Syed, K., 2011. Gas Turbine Combstion - Short Course Notes. Cranfield University.

[89] Aurifeille, E., 2007. Recommended Best Practises for using the Combustion CFD code Precise v4.7. Tech. rep., Rolls-Royce plc DNS 130867.

[90] Kozaily, J., Zachos, P., Pachidis, V., and Singh, R., 2009. "Gas turbine fuel atomization dynamics under sub-atmospheric conditions". *19th ISABE Conference 2009-1160, Montreal, Canada*.

[91] Mehdi, A., Grech, N., Zachos, P., Pachidis, V., and Singh, R., 2011. "Effects of combustor geometry on an airblast atomizer at sub-atmospheric conditions". *20th ISABE Conference, Gothenburg*.

[92] Grech, N., Mehdi, A., Zachos, P., Pachidis, V., and Singh, R., 2012. "Effects of combustor geometry on an airblast atomizer at sub-atmospheric conditions". *Engineering Applications of Computation Fluid Mechanics,* ***6***(2), pp. 203–213.

[93] Sheen, H., Chen, W., Jeng, S., and Huang, T., 1996. "Correlation of Swirl Number for a Radial-Type Swirl Generator". *Experimental Thermal and Fluid Science,* ***12***, pp. 444–451.

[94] Chatterjee, D., Datta, A., Ghosh, A., and Som, S., 2004. "Effects of Inlet Air Swirl and Spray Cone Angle on Combustion and Emission Performance of a Liquid Fuel Spray in a Gas Turbine Combustor". *J. Inst. Eng,* ***26***, pp. 715–722.

[95] Rose, W., 1962. "A Swirling Round Turbulent Jet: 1 - Mean Flow Measurements". *Journal of Applied Mechanics,* ***29***(4), December, pp. 615–625.

[96] Chigier, N., and Chervinsky, A., 1967. "Experimental Investigation of Swirling Vortex Motion in Jets". *Journal of Applied Mechanics,* ***34***(2), June, pp. 443–451.

[97] Beer, J., and Chigier, N., 1972. *Combustion Aerodynamics*. Applied Science Publishers Ltd, London.

[98] Sloan, D., Smith, P., and Smoot, D., 1986. "Modeling of Swirl in Turbulent Flow Systems". *Progress in Energy and Combustion Science,* ***12***(3), pp. 163–250.

[99] Ballal, D., and Lefebvre, A., 1981. "General Model of Spark Ignition for Gaseous and Liquid Fuel/Air Mixtures". In Proceedings of the 18th Symposium (International) on Combustion.

[100] Rao, K., and Lefebvre, A., 1979. "Minimum Ignition Energies in Flowing Kerosine-Air Mixtures". *Combustion and Flame,* ***35***(2), pp. 155–168.

[101] Ballal, D., and Lefebvre, A., 1978. "Ignition if Liquid Fuel Sprays at Subatmospheric Pressures". *Combustion and Flame,* ***31***(2), pp. 115–126.

[102] Widmann, J., Charagundla, S., and Presser, C., 2000. "Aerodynamic Study of a Vane-cascade Swirl Generator". *Chemical Engineering Science,* ***55***(22), pp. 5311–5320.

[103] Brum, R., and Samuelsen, G., 1982. "Two-component laser anemometry measurements in a non-reacting and reacting complex flow model combustor". *Western States Section/The Combustion Institute, Sandia National Laboratories, Livermore, CA*.

[104] Davoudzadeh, F., Liu, N., and Moder, J., 2006. Investigation of Swirling Air Flows Generated by Axial Swirlers in a Flame Tube. Tech. rep., NASA Glenn Research Centre.

[105] Shih, T., Liou, W., Shabbir, A., Yang, Z., and Zhu, J., 1995. "A New $k - \epsilon$ Eddy Viscosity Model for High Reynolds Number Turbulent Flows - Model Development and Validation". *Computer Fluids,* ***24***(3), pp. 227–238.

[106] Escue, A., and Cui, J., 2010. "Comparison of Turbulence Models in Simulating Swirling Pipe Flows". *Applied Mathematical Modelling,* ***34***(10), pp. 2840–2849.

[107] Rocklage-Marliani, G., Schmidts, M., and Ram, I. V., 2003. "Three-dimensional Laser-doppler Velocimeter Measurements in Swirling Turbulent Pipe Flow". *Flow, Turbulence and Combustion,* ***70***, pp. 43–67.

[108] Weber, R., Visser, B., and Boysan, F., 1990. "Assessment of turbulence modeling for engineering prediction of swirling vortices in the near burner zone". *Int. J. Heat and Fluid Flow,* ***11***(3).

[109] Mongia, H., 2008. "Recent progress in comprehensive modelling of gas turbine combustion". In Proceedings of 46th AIAA Aerospace Sciences Meeting and Exhibit, no. 2008-1445.

[110] Wang, S., Yang, V., Hsiao, G., Hsieh, S., and Mongia, H., 2007. "Large-eddy Simulations of a Gas Turbine Swirl Injector Flow Dynamics". *Journal of Fluid Mechanics,* ***583***, pp. 99–122.

[111] Wang, P., and Bai, X., 2005. "Large Eddy Simulations of Turbulent Swirling Flows in a Dump Combustor - A Sensitivity Study". *International Journal for Numerical Methods in Fluids,* ***47***(2), pp. 99–120.

[112] Freitag, M., Klein, M., Gregor, M., Geyer, D., Schneider, C., Dreizler, A., and Janicka, J., 2006. "Mixing Analysis of a Swirling Recirculating Flow using DNS and Experimental Data". *International Journal of Heat and Fluid Flow,* ***27***(4), pp. 636–643.

[113] Wegner, B., Maltsev, A., Schneider, C., Sadiki, A., Dreizler, A., and Janicka, J., 2004. "Assessment of unstready RANS in predicting swirl flow instability based on les and experiments". *International Journal of Heat and Fluid Flow,* ***25***, pp. 528–536.

[114] Read, R., 2008. "Experimental Investigations into High-Altitude Relight of a Gas Turbine". PhD thesis, University of Cambridge.

[115] Kozaily, J., 2008. "Altitude relight performance modelling: Numerical/cfd analysis of an airblast atomizer under sub-atmospheric pressures and low air velocities". MSc thesis, Cranfield University, School of Engineering.

[116] Mehdi, A., 2009. "Altitude relight sub-idle combustion modelling". MSc thesis, Cranfield University, School of Engineering.

[117] Jasuja, A., 1984. "Effects of Airblast Atomizer Design Upon Spray Quality". *AGARD CP No 353.*

[118] Jasuja, A., and Lefebvre, A., 1994. "Influence of ambient pressure on drop-size and velocity distributions in dense sprays". *25th Symposium on Combustion.*

[119] Parsons, J., and Jasuja, A., 1986. "Effect of air pressure upon spray angle/width characteristics of simplex pressure swirl atomizers". *International Journal of Turbo and Jet Engine 3, 207–216.*

[120] Datta, A., and Som, S., 1999. "Effects of Spray Characteristics on Combustion Performance of a Liquid Fuel Spray in a Gas Turbine Combustor". *International Journal of Energy and Research,* ***23***, pp. 217–228.

[121] Rizkalla, A., 1974. "The Influence of Air and Liquid Properties on Airblast Atomization". PhD thesis, Cranfield University, School of Engineering.

[122] Koupper, C., Grech, N., Zachos, P., Pachidis, V., and Singh, R., 2012. "Considerations on the Numerical Modelling and Performance of Axial Swirlers under Relight Conditions". In Proceedings of ASME Turbo Expo 2012, GT2012-68416.

[123] Grech, N., Koupper, C., Zachos, P., Pachidis, V., and Singh, R., 2012. "Considerations on the Numerical Modelling and Performance of Axial Swirlers under Relight Conditions". *Journal of Engineering for Gas Turbines and Power,* ***134***(111505), November.

[124] Technical discussion with Dr M. Zedda, Combustion Aerothermal Methods Team Leader, Rolls-Royce plc.

[125] Barker, A., and Carrotte, J., 2002. "Compressor Exit Conditions and Their Impact on Flame Tube Injector Flows". *Journal of Engineering for Gas Turbines and Power,* ***124***, January.

[126] Walker, A., Carrotte, J., and McGuirk, J., 2009. "The Influence of Dump Gap on External Combustor Aerodynamics at High Fuel Injector Flow Rates". *Journal of Engineering for Gas Turbines and Power,* ***131***(031506), May.

[127] Walker, A., Carrotte, J., and McGuirk, J., 2008. "Compressor/Diffuser/Combustor Aerodynamic Interactions in Lean Module Combustors". *Journal of Engineering for Gas Turbines and Power,* ***130***(011504), January.

[128] Pearson, H., 1962. "Mixing of Exhaust and By-pass Flow in a By-pass Engine". *J. Royal Aeronautical Society,* ***66***, August, pp. 528–530.

[129] Elliot, J., Manning, T., Qiu, Y., Greitzer, E., Tan, C., and Tillman, T., 1992. "Computational and Experimental Studies of Flow in Muli-Lobed Forced Mixers". In AIAA/SAE/ASME/ASEE 28th Joint Propulsion Conference and Exhibit, Nashville, U.S., AIAA 92-3568.

[130] Sanghi, V., Lakshmanan, B., and Sane, S., 2002. "Optimum Mixing of Core and Bypass Streams in High-Bypass Civil Turbofan". *J. Propulsion and Power,* ***18***(4), July - August.

[131] Alexander, E., 1970. Engine Windmilling Characteristics - Significance in Combustion Design. Tech. rep., Rolls-Royce Combustion Research Report CRR 00033.

[132] Gore, R., Crowe, C., and Bejan, A., 1990. "Experimental observations on transition to turbulent flow in mixers". *ASME Fluids Engineering Conference*.

[133] Villermaux, E., and Rehab, H., 2000. "Mixing in coaxial jets". *Journal of Fluid Mechanics,* ***425***, pp. 161–185.

[134] Lima, M., and Palma, J., 2002. "Mixing on coaxial confined jets of high velocity ratio". *Faculdade de Engenharia da Universidade do Porto*.

[135] Saravanamuttoo, H., Rogers, G., and Cohen, H., 2001. *Gas Turbine Theory, 5th Ed.* Prentice Hall.

[136] Mattingley, J., 1996. *Elements of Gas Turbine Propulsion*. McGraw-Hill.

[137] Holmes, M., 1964. An investigation into mixing between bypass air and turbine exhaust gates. Tech. Rep. R-261/262/263/277, National Gas Turbine Establishment.

[138] Russo, F., 2009. "Aero Engine Sub-Idle Mixer Performance Modelling". MSc thesis, Cranfield University, School of Engineering.

[139] Vellutini, E., 2010. "Aero Engine Sub-Idle Mixer Performance Modelling". MSc thesis, Cranfield University, School of Engineering.

[140] Negro, D., 2011. "Aero Engine Sub-Idle Mixer Performance Modelling". MSc thesis, Cranfield University, School of Engineering.

[141] Grech, N., 2012. Aero-engine Mixer Sub-Idle Performance Modelling TR 2012-6. Tech. rep., Cranfield University UTC.

Bibliography

- N.A. Cumpsty, 'Compressor Aerodynamics', Krieger, 2004
- A.H. Lefebvre, 'Gas Turbine Combustion', Taylor & Francis, 1998, 2nd Edition
- A.H. Lefebvre, 'Atomization and Sprays', Taylor & Francis, 1989
- S.L. Dixon, 'Fluid Mechanics and Thermodynamics of Turbomachinery', Elsevier, 1998, 5th Edition
- H.I.H. Saravanamuttoo, G.F.C. Rogers and H. Cohen, 'Gas Turbine Theory', Prentice Hall, 2001, 5th Ed
- W.R. Hawthorne, 'Aerodynamics of Turbines and Compressors. High Speed Aerodynamics and Jet Propulsion', Princeton University Press, 1964
- P. Walsh and P.P. Fletcher, 'Gas Turbine Performance', Blackwell, 2004, 2nd Ed
- J.M.M. Beer and N.A. Chigier, 'Combustion Aerodynamics', Applied Science Publishers Ltd, London, 1972
- G.F.C. Rogers, Y.R. Mayhew, 'Engineering Thermodynamics, Work and Heat Transfer', Longman Scientific, 1992, 4th Edition

Appendix A

Published:

P. Zachos, N. Grech, B. Charnley, V. Pachidis and R. Singh, 2011, 'Experimental and Numerical Investigation of a Compressor Cascade at Highly Negative Incidence', Engineering Applications of Computational Fluid Mechanics, Vol. 5, No. 1, pp.26-36

A. Mehdi, N. Grech, P. Zachos and V. Pachidis, 2011, 'Effect of Combustor Geometry on Performance of Airblast Atomizer under Sub-Atmospheric Conditions', ISABE 2011-1103, Gothenburg, Sweden

N. Grech, A. Mehdi, P.K. Zachos, V. Pachidis, 2012, 'Effect of Combustor Geometry on Performance of Airblast Atomizer under Sub-Atmospheric Conditions', Engineering Applications of Computational Fluid Mechanics, Vol. 6, No. 2, pp.203-213

C. Koupper, N. Grech, P.K. Zachos, V. Pachidis and R. Singh, 2012, 'Considerations on the Numerical Modelling and Performance of Axial Swirlers under Relight Conditions', ASME Turbo Expo 2012 - GT2012-68416, Copenhagen, Denmark

N. Grech, C. Koupper, P.K. Zachos, V. Pachidis and R. Singh, 2012, 'Considerations on the Numerical Modelling and Performance of Axial Swirlers under Relight Conditions' Journal of Engineering for Gas Turbine and Power, November, Vol 134, 111505-1.

Accepted for publication:

N. Grech, M. Lecoq, P.K. Zachos and V. Pachidis, 2013, 'Probabilistic and Numerical Modelling of a Lobed Mixer at Windmilling Conditions', ASME TurboExpo 2013 -

GT2013-94366, San Antonio Texas

N. Grech, E. Illana, P.K. Zachos and V. Pachidis, 'Axial Compressor Aerodynamics under Sub-Idle Conditions', ASME TurboExpo 2013 - GT2013-94368, San Antonio, Texas

N. Grech, P.K. Zachos and V. Pachidis, 'Airblast Atomizer Flow Field Characteristics at Relight Conditions', ISABE 2013-10035, Busan, South Korea

N. Grech, P.K. Zachos and V. Pachidis, 'A Sub-Idle Combustion Efficiency Prediction Code for Gas Turbine Performance Solvers', ISABE 2013-10036, Busan, South Korea

N. Grech, P.K. Zachos and V. Pachidis, 'Axial Compressor Flow Phenomena at Locked-Rotor Conditions', ISABE 2013-10037, Busan, South Korea